

DOKUZ EYLÜL UNIVERSITY
GRADUATE SCHOOL OF NATURAL AND APPLIED
SCIENCES

EXPERIMENTAL AND NUMERICAL
INVESTIGATION OF COLD THERMAL
ENERGY STORAGE SYSTEMS

by
Mehmet Akif EZAN

July, 2011
İZMİR

**EXPERIMENTAL AND NUMERICAL
INVESTIGATION OF COLD THERMAL
ENERGY STORAGE SYSTEMS**

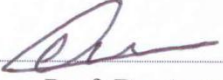
**A Thesis Submitted to the
Graduate School of Natural and Applied Sciences of
Dokuz Eylül University
In Partial Fulfillment of the Requirements for the
Degree of Doctor of Philosophy in
Mechanical Engineering, Thermodynamics Program**

**by
Mehmet Akif EZAN**

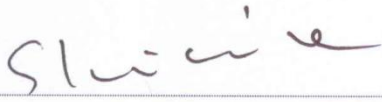
**July, 2011
İZMİR**

Ph.D. THESIS EXAMINATION RESULT FORM

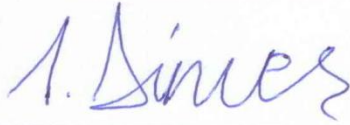
We have read the thesis entitled “**EXPERIMENTAL AND NUMERICAL INVESTIGATION OF COLD THERMAL ENERGY STORAGE SYSTEMS**” completed by **MEHMET AKİF EZAN** under supervision of **ASSOC. PROF. DR. AYTUNÇ EREK** and we certify that in our opinion it is fully adequate, in scope and in quality, as a thesis for the degree of Doctor of Philosophy.


Assoc. Prof. Dr. Aytunç EREK

Supervisor



Assoc. Prof. Dr. Serhan KÜÇÜKA

Thesis Committee Member



Prof. Dr. İbrahim DİNÇER

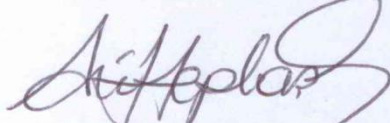
Examining Committee Member


Assoc. Prof. Dr. Zuhul OKTAY

Examining Committee Member

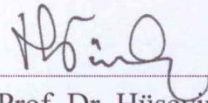

Assoc. Prof. Dr. Mehmet ÇAKMAKÇI

Thesis Committee Member

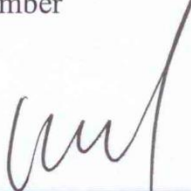


Prof. Dr. Arif HEPBAŞLI

Examining Committee Member


Assist. Prof. Dr. Hüseyin GÜNERHAN

Examining Committee Member


Prof. Dr. Mustafa SABUNCU

Director

Graduate School of Natural and Applied Science

ACKNOWLEDGEMENTS

I feel very fortunate that my co-supervisors Assoc. Prof. Dr. Aytunç EREK and Prof. Dr. İbrahim DİNÇER have given me the opportunity to work with them. Words of thanks alone are insufficient to express my gratitude for the support, patience, understanding, encouraging, and help offered by my dissertation advisors throughout this research.

I would like to thank my thesis committee members, Assoc. Prof. Dr. Serhan KÜÇÜKA, Assoc. Prof. Dr. Mehmet ÇAKMAKCI and Assit. Prof. Dr. Tahsin BAŞARAN for their direction, dedication, and invaluable advice along this dissertation. I would like to express my deep appreciation to Prof. Dr. Arif HEPBAŞLI and Assist. Prof. Dr. Hüseyin GÜNERHAN for their valuable and constructive suggestions during the planning and development of current research work.

I would like to express my gratitude to those who have helped me building the setups that allowed me to run current experiments. Without them, I could not have written this thesis. First, I want to thank my former colleague Muhammet ÖZDOĞAN (MSc) and the technician of the Thermal Science Laboratory, Alim ZORLUOL, for their admirable supports on designing and construction periods of the experimental setups. I would like to acknowledge to Dr. Levent ÇETİN, Dr. Orhan EKREN, and Osman KORKUT (MSc) for their kind supports on constituting the control systems. I am lucky to have worked with Abdullah ADIYAN (MSc) and Tolga ÜSTÜN, who are the owners of Destek Automation and Rast Energy Systems. They helped me to provide the experimental equipment and setup the systems in an affordable manner.

I also wish to express my thanks to my colleagues in Dokuz Eylül University, Department of Mechanical Engineering. Particularly, I want to thank to Ziya Haktan KARADENİZ (MSc) and Dr. Alpaslan TURGUT, for their kind help and guidance during my undergraduate and graduate studies. I am grateful to Mümin GÜNGÖR

(MSc) of his friendship and support in IT services during my studies. I would like to thank my colleagues at University of Ontario Institute of Technology, Canada. I feel very lucky to have met and shared my nine months with; Hakan ÇALIŞKAN, Rami S. EL-EMAM, Dr. Mehmet Fatih ORHAN, Mehmet Kursad COHCE, Ayman KHAFAJA and Nikki LEWIS.

The financial support from the Higher Education Council of Turkey (YÖK) is gratefully acknowledged. This research is supported by Scientific and Technological Research Council of Turkey (TÜBİTAK) under the grant 106M418 and this support is sincerely appreciated.

Most importantly, I would like to thank my mother Kevser EZAN, my brother Atıf Canberk EZAN and my love Aylin FIŞKIN. I am so grateful to them for their patience, endless support, and perseverance.

Mehmet Akif EZAN

EXPERIMENTAL AND NUMERICAL INVESTIGATION OF COLD THERMAL ENERGY STORAGE SYSTEMS

ABSTRACT

In this thesis study, two different types of latent heat thermal energy storage (LHTES) systems are designed and fabricated to investigate the solidification and melting periods of water.

In the shell-and-tube type LHTES system, natural convection dominated phase change process is investigated. An electronic interface measurement method is developed to monitor the solid-liquid interface variations during the phase change. Experimental results indicate that the mean relative difference of the current method is nearly ± 3 percent, in comparison with the photography method. Results designate that, natural convection becomes the dominant heat transfer mechanism after a short heat conduction dominated period. Furthermore, parametric results indicate that the inlet temperature of the heat transfer fluid (HTF) is the most deterministic parameter on the stored and rejected energies. Besides, the natural convection dominated phase change is analyzed in a two-dimensional domain with the aid of FLUENT software. Comparisons are performed in terms of the time wise variations of interface positions and the mean deviation is obtained less than 2 mm.

In the ice-on-coil type LHTES system, four different control strategies are tested to achieve a constant temperature value of the HTF at the inlet section of the tank. More stable inlet temperature of the HTF is achieved for the control with the HTF temperature at the outlet section of the evaporator. Parametric results emphasize that, for the current experimental conditions external melting mode can provide relatively lower outlet temperatures for a longer period. On the other hand, parametric energy and exergy analyses are carried out for the charging period of the system with using the thermal resistance network technique. Time wise variations of the total stored energy, mass of ice and outlet temperature of the HTF are compared with the experimental data. The mean deviation is obtained less than 4 percent in terms of the

total mass of ice. After validation, performance of the system is investigated for several working and design parameters.

Keywords: Thermal energy storage, shell-and-tube, ice-on-coil, phase change, solidification, natural convection, melting, numerical analysis, computational fluid dynamics, experimental analysis, entropy generation, energy analysis, exergy analysis.

SOĞUK ENERJİ DEPOLAMA SİSTEMLERİNİN DENEYSEL VE SAYISAL İNCELENMESİ

ÖZ

Bu tez çalışmasında, suyun katılaşma ve erime süreçlerini incelemek amacıyla, iki farklı gizli ısı enerji depolama (GIED) sistemi tasarlanmış ve imal edilmiştir.

Boru–kovan tipi GIED sisteminde, doğal taşınım etkisindeki faz değişim süreci araştırılmıştır. Faz değişimi sırasında meydana gelen katı–sıvı ara yüzey değişimlerini izlemek amacıyla elektronik ara yüzey ölçüm yöntemi geliştirilmiştir. Mevcut yöntemle fotoğraflama yönteminin karşılaştırmalı deneysel sonuçlarına göre ortalama fark yüzde 3 olarak elde edilmiştir. Kısa bir iletim etkin periyod sonrasında, sistem içerisindeki etkin ısı transferi mekanizmasının doğal taşınım olduğu gözlenmiştir. Parametrik sonuçlara göre, ısı transferi akışkanın giriş sıcaklığı, depolanan ve geri kullanılan enerjilerin belirlenmesinde en etkin parametredir. Ayrıca, doğal taşınım etkisindeki faz değişim süreci iki boyutlu ortamda FLUENT paket programı kullanılarak modellenmiştir. Ara yüzeyin zamana bağlı değişimleri karşılaştırılmış ve sonuçta ortalama farkın 2 mm’den az olduğu bulunmuştur.

Serpantinli GIED sisteminde ısı transferi akışkanının depo girişindeki sıcaklığını sabitlemek için dört farklı kontrol stratejisi test edilmiştir. Isı transferi akışkanının evaporatörden çıkış sıcaklığına göre gerçekleştirilen kontrol durumunda, depo giriş sıcaklığı stabil olarak elde edilmiştir. Mevcut deneysel parametreler için, içten eritmeye kıyasla dıştan eritme durumunda daha düşük çıkış sıcaklıklarının daha uzun süreler için elde edilebildiği gözlenmiştir. Ayrıca, sistem ısı direnç ağları yöntemiyle modellenerek parametrik enerji ve ekserji analizleri gerçekleştirilmiştir. Depolanan enerji, buz kütlesi ve ısı transferi akışkanının tanktan çıkış sıcaklıkları deneysel sonuçlarla karşılaştırılmıştır. Buz kütlesi cinsinden ortalama fark yüzde 4’ten düşük elde edilmiştir. Doğrulamadan sonra, sistem performansı çeşitli çalışma ve tasarım parametreleri için incelenmiştir.

Anahtar sözcükler: Isıl enerji depolama, boru–kovan, serpantin, faz deęiřimi, katılařma, doęal tařımın, erime, sayısal analiz, sayısal akıřkanlar dinamięi, deneysel analiz, entropi üretimi, enerji analizi, ekserji analizi.

CONTENTS

	Page
Ph.D. THESIS EXAMINATION RESULT FORM.....	ii
ACKNOWLEDGEMENTS	iii
ABSTRACT	v
ÖZ.....	vii
CHAPTER ONE – INTRODUCTION	1
1.1 Basics of Thermal Energy Storage	1
1.1.1 Sensible Heat TES	2
1.1.2 Latent Heat TES.....	3
1.1.2.1 Ice Storage Systems	4
1.2 Literature Review	5
1.2.1 Natural Convection Driven Phase Change	6
1.2.1.1 Inside Rectangular Cavities.....	7
1.2.1.2 Around Tubes	10
1.2.1.3 Inside Spherical Capsules	12
1.2.2 Energy Based Parametric Studies of LHTES Systems	13
1.2.2.1 Shell–and–tube Type LHTES Systems.....	13
1.2.2.2 Ice–on–coil Type LHTES Systems	16
1.2.3 Exergy Based Parametric Studies of LHTES Systems	18
1.3 Objectives and Contents of Dissertation.....	19
1.3.1 Objectives	20
1.3.2 Contents of Dissertation	21
CHAPTER TWO – EXPERIMENTAL APPARATUS AND ANALYSES.....	22
2.1 Shell–and–Tube Type LHTES System.....	22
2.1.1 Experimental Procedure	25

2.1.2 Interface Measurement Method	26
2.1.2.1 Theory and Background.....	27
2.1.2.2 Experimental Apparatus and Preliminary Tests	31
2.1.3 Analyses of Experimental Data	36
2.1.3.1 Energy Analysis.....	37
2.1.3.2 Exergy Analysis.....	40
2.1.3.3 Uncertainty Analysis.....	46
2.2. Ice-on-coil Type LHTES System.....	48
2.2.1 Components of Experimental System	48
2.2.1.1 Chiller	51
2.2.1.2 Storage Tank	52
2.2.1.3 Heating Bath.....	57
2.2.1.4 Sensors	57
2.2.2 Experimental Procedures.....	63
2.2.2.1 Procedure of Charging Experiments.....	63
2.2.2.2 Procedure of Discharging Experiments	65
2.2.3 Analyses of Experimental Data	68
2.2.3.1 Energy Analysis.....	68
2.2.3.2 Thermodynamic Analysis of Chiller	71
2.2.3.3 Uncertainty Analysis.....	75
CHAPTER THREE – NUMERICAL ANALYSES	78
3.1 Mathematical Model for Natural Convection Dominated Phase Change	78
3.1.1 Theory and Background.....	78
3.1.2 Fundamental Aspects of CFD.....	85
3.1.2.1 Finite Volume Method.....	87
3.1.2.1.1 One-dimensional Diffusion Problem.....	88
3.1.2.1.2 One-dimensional Convection and Diffusion Problem.....	92
3.1.2.2 SIMPLE Algorithm	95
3.1.3 Local Rate of Entropy Generation in Convective Heat Transfer.....	100
3.2 Numerical Investigation of Ice-on-coil LHTES System	103

3.2.1 Theory and Background	103
3.2.1.1 Period 1 – Sensible Heat Storage	106
3.2.1.2 Period 2 – Sensible and Latent Heat Storage	109
3.2.1.3 Exergy Analysis.....	111
CHAPTER FOUR – RESULTS AND DISCUSSION	113
4.1 Experimental Results of Shell–and–tube Type LHTES System.....	113
4.1.1 Validation of Interface Measurement Method.....	113
4.1.2 Temperature and Interface Variations.....	121
4.1.3 Parametric Results of Shell–and–tube LHTES System.....	130
4.1.3.1 Influences of Flow Parameters of HTF on Charging.....	130
4.1.3.2 Influence of Tube Material on Charging	133
4.1.3.3 Influence of Shell Diameter on Charging	135
4.1.3.4 Influences of Flow Parameters of HTF on Discharging	139
4.2 Experimental Results of Ice–on–coil Type LHTES System.....	143
4.2.1 Temperature and Interface Variations.....	143
4.2.2 Parametric Results of Ice–on–coil LHTES System	148
4.2.2.1 Influence of Control Schemes on Performance of System	150
4.2.2.2 Parametric Results for Charging (Solidification) Experiments.....	159
4.2.2.3 Parametric Results for Discharging (Melting) Experiments.....	160
4.2.2.3.1. Internal Melting Experiments	160
4.2.2.3.2. External Melting Experiments	164
4.3 Numerical Results	166
4.3.1 Natural Convection Dominated Phase Change.....	167
4.3.1.1 Case Studies	167
4.3.1.1.1 One Dimensional Solidification (Case #1).....	167
4.3.1.1.2 Natural Convection of Water (Case #2).	170
4.3.1.1.3 Natural Convection Dominated Melting (Case #3).....	176
4.3.1.1.4 Natural Convection Dominated Solidification (Case #4).....	183
4.3.1.2 Natural Convection Driven Solidification around Tube.....	192
4.1.3.1.1 Description of Mathematical Model and Validation.....	192

4.1.3.1.2 Case Studies.....	199
4.3.2 Numerical Investigation of Ice–on–coil LHTES System.....	211
4.3.2.1 Model Validation.....	211
4.3.2.2 Parametric Energy and Exergy Based Analyses	214
CHAPTER FIVE – CONCLUSIONS AND RECOMMENDATIONS.....	226
REFERENCES	231
APPENDIX	248
A. Nomenclature	248

CHAPTER ONE

INTRODUCTION

In this chapter, first, basic types of thermal energy storage systems are briefly described, and detailed information about the latent heat thermal energy storage system is given. Previously conducted studies, that are motivated the present dissertation are presented in a categorized manner. Finally, objectives and contents of the current dissertation are explained.

1.1 Basics of Thermal Energy Storage

Sustainability of energy is one of the most important problems for using renewable energy resources in the world. Many researchers investigated energy storage systems as a solution for sustainability of renewable energy resources such as solar and wind powers. In the case of using solar power, solar energy is charged while energy sources are widely available (*daytime*), and then the stored energy can be discharged when the sources are limited (*night time*). This procedure can provide sustainable energy usage. Thermal energy storage is essential for using the current energy systems sustainable, efficient, economic, and environmental friendly (Dincer & Rosen, 2002). Thermal energy storage (TES) is a key technology in reducing the mismatch between energy supply and demand for heating and cooling systems (Dincer & Rosen, 2002). TES systems not only provide a balance between supply and demand, but also increase the performance and reliability of the energy systems.

In TES systems, energy can be stored via changing the internal energy of the storage medium as sensible heat, latent heat, thermo chemical or combination of them (Sharma, Tyagi, Chen & Buddhi, 2009). Common TES techniques that are preferred for heating or cooling applications can be described as *sensible heat storage* and *latent heat storage*. In the sensible heat storage systems, energy is stored in a storage medium by means of the temperature difference. Besides, in the latent heat storage systems, energy is stored via changing the phase of the storage medium from one phase to another, by melting (*solid to liquid*) or solidification (*liquid to*

solid). Basic concepts of these methods are described in the following sections.

1.1.1 Sensible Heat TES

Sensible heat storage is performed by increasing (*heating*) or decreasing (*cooling*) the temperature of the storage medium, as seen in Figure 1.1(a). Thus, the amount of heat stored (*or* rejected) in (*or* from) the system depends on the specific heat of the medium, the temperature difference, and the amount of the storage medium. The total energy variation of a sensible heat storage system can be defined as

$$\Delta E = \int_{T_i}^{T_{final}} (mc) dT = (mc) [T_{final} - T_i] \quad (1.1)$$

In the sensible heat storage systems, it is desirable for the storage medium to have high specific heat capacity ($C = \rho c$), long-term stability under number of thermal cycles, availability, and most importantly low cost (Hasnain, 1998a). Sharma et al. (2009) and Hasnain (1998a), reviewed the thermo-physical properties of commonly used solid and liquid materials with pros and cons, and introduced that water is the best liquid for the sensible heat storage systems with high specific heat and lower price.

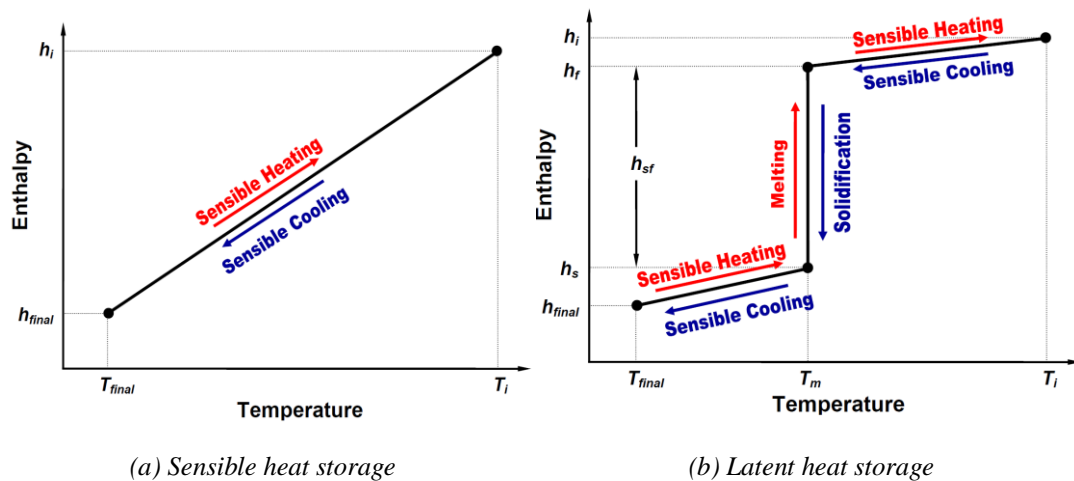


Figure 1.1 Illustration of enthalpy-temperature variations for the sensible and latent heat storage systems.

1.1.2 Latent Heat TES

Latent heat storage bases on heat release (*solidification*) or absorb (*melting*) when a storage medium undergoes a phase change from the solid to liquid, or vice versa (Sharma et al., 2009). Figure 1.1(b) illustrates the typical enthalpy – temperature variation during the latent heat storage process. Initially, storage materials behave like sensible heat storage materials and their temperatures rise (*absorb heat*) or decrease (*release heat*). Unlike the sensible heat storage, when the temperature value of the storage medium reaches its phase change temperature (T_m), phase transformation occurs. The heat releases (*or* absorbs) from the medium by the heat of fusion (h_{sf}) at a constant temperature. When the storage medium changes phase from solid to liquid (or *vice versa*), the corresponding storage materials are named to be phase change materials (PCMs). The storage capacity of the latent heat storage with solid–liquid phase transformation can be defined as follows:

$$\Delta E = \int_{T_i}^{T_m} (mc)_l dT + mh_{sf} + \int_{T_m}^{T_{final}} (mc)_s dT \quad (1.2a)$$

$$\Delta E = (mc)_l [T_m - T_i] + mh_{sf} + (mc)_s [T_{final} - T_m] \quad (1.2b)$$

In the latent heat storage, the value of the heat of fusion (*latent heat*) is much more important than the temperature variations (*sensible heat*). For instance, in the case of water usage as a PCM, the total energy required to melt 1 kg of ice into water is 80 times greater than the energy that is desired to raise the temperature of 1 kg of water by 1°C. It means that the latent heat storage has higher energy storage density in a smaller volume or less material usage, in comparison to the sensible heat storage. Solid–liquid phase change is useful because, relatively large amount of heat can be stored in PCMs over a narrow temperature range, without a corresponding high volume change (Hasnain, 1998a).

Various types of phase change materials have been represented in the previous studies, including *heating* or *cooling* LHTES applications (Abhat, 1983; Dincer & Rosen, 2002; Zalba, Marin, Cabeza & Mehling, 2003; Farid, Khudhair, Razack & Al-Hallaj, 2004; Sharma & Sagara, 2005; Sharma et al., 2009 and Nomura, Okinaka

& Akiyama, 2010). According to these researchers, PCMs should possess some special characteristics to be useful in the latent heat storage systems. Nomura et al. (2010) briefly listed the main characteristics of PCMs as given in Table 1.1. Because of the economic and thermal advantages of water, ice storage applications are the most preferred LHTES systems as cold storage (Hasnain, 1998b). In the following subsection, fundamentals of the ice storage systems are briefly illustrated.

Table 1.1 Characteristics of PCMs.

Thermal Properties	Kinetic or Physical Properties	Chemical Properties	Economic Factors
(1) Suitable phase change temperature range,	(5) Large density,	(8) Long term chemical stability,	(12) Cheap,
(2) Large heat of fusion,	(6) Small volume change during phase change,	(9) Compatibility with construction and container materials,	(13) Abundant,
(3) Large specific heat,	(7) no sub cooling,	(10) Completely reversible phase change,	
(4) Large thermal conductivity in both solid and liquid phases,		(11) non-toxic, non-flammable,	

Source: Nomura et al. (2010)

1.1.2.1 Ice Storage Systems

Hasnain (1998b) designated that principally there are three types of cold storage systems being considered today: *chilled water*, *ice*, and *eutectic salt* storage systems. Hasnain (1998b) also emphasized that the ice storage systems have many advantages over the other cold storage systems as having more suitable storage capacity and being costly effective.

The cooling load variation of a conventional air conditioning system through a day is illustrated in Figure 1.2(a). Cooling load of a building increases depending on the high demand of energy in certain periods of the day, especially at noon. In the ice storage systems, a water filled storage tank can be attached to a chiller to store “cold” at nighttime and use this stored energy during daytime. At nighttime, chiller utilizes to produce large amounts of ice. During daytime, this ice can be melted to use stored cold energy, without utilizing the chiller in peak hours. This method is named as full storage strategy and will balance the load distribution throughout the day as shown in

Figure 1.2(b). Hasnain (1998b) and ASHRAE (1999) introduced all the other thermal energy storage strategies. Various economic and environmental advantages can be achieved by shifting the cooling load from limited and expensive daytime period to a relatively wider and cheaper nighttime period. In comparison to the daytime, energy costs and the condensation temperature of cooling systems are relatively lower at the nighttime; hence, cooling systems can be operated more efficient and economic.

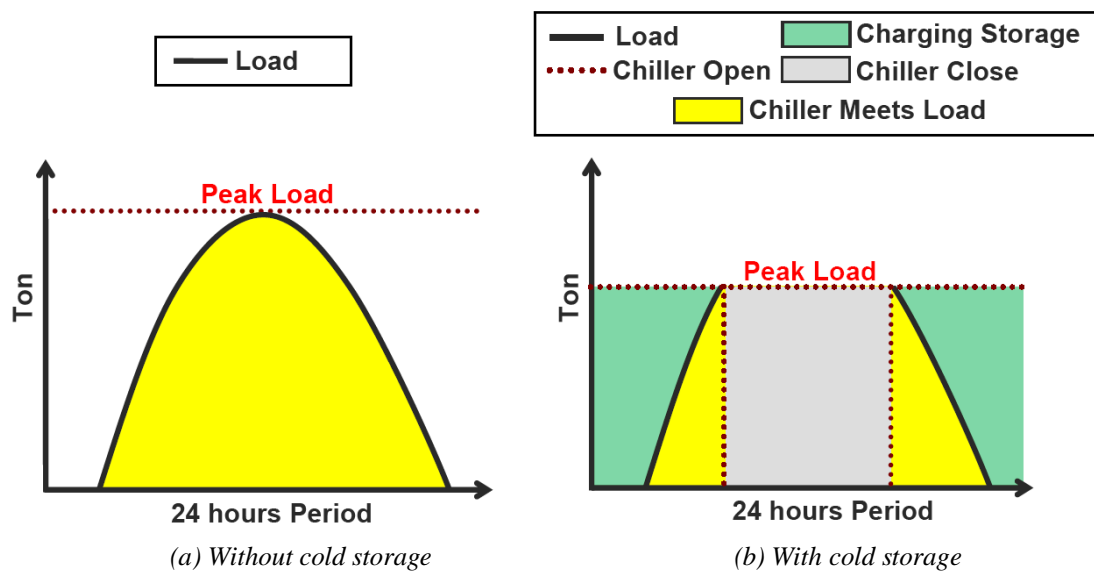


Figure 1.2 Daytime load distribution of an air conditioning unit (*adapted from Hasnain, 1998b*).

Considering the well-known advantages of the LHTES systems, many researchers have performed numerous studies related to the phase change phenomena. In this study, a comprehensive literature review is carried out for understanding the importance of the phase change phenomena. In the following section, previous studies that are motivated this thesis study are presented.

1.2 Literature Review

Understanding of the solidification and melting phenomena has considerable importance in the design period of the LHTES systems. Investigations on the solid-liquid (*charging*) and liquid-solid (*discharging*) processes have been carried out for many decades. Studies related with the phase change have mainly focused on one of the following two purposes: (i) Examining the influence of the natural convection on

solidification and melting processes in a system, or (ii) Parametric assessments of various design and flow parameters on the overall energetic and exergetic performances of the storage system. Hence, literature review is introduced with focusing on these two groups of studies.

1.2.1 Natural Convection Driven Phase Change

There is a linear relationship between the temperature and density for most of the fluids. However, in the case of water, a linear relationship is not justified near the freezing point. The density of water reaches a maximum value at 3.98°C. Before or after this temperature, density of water decreases as illustrated in Figure 1.3.

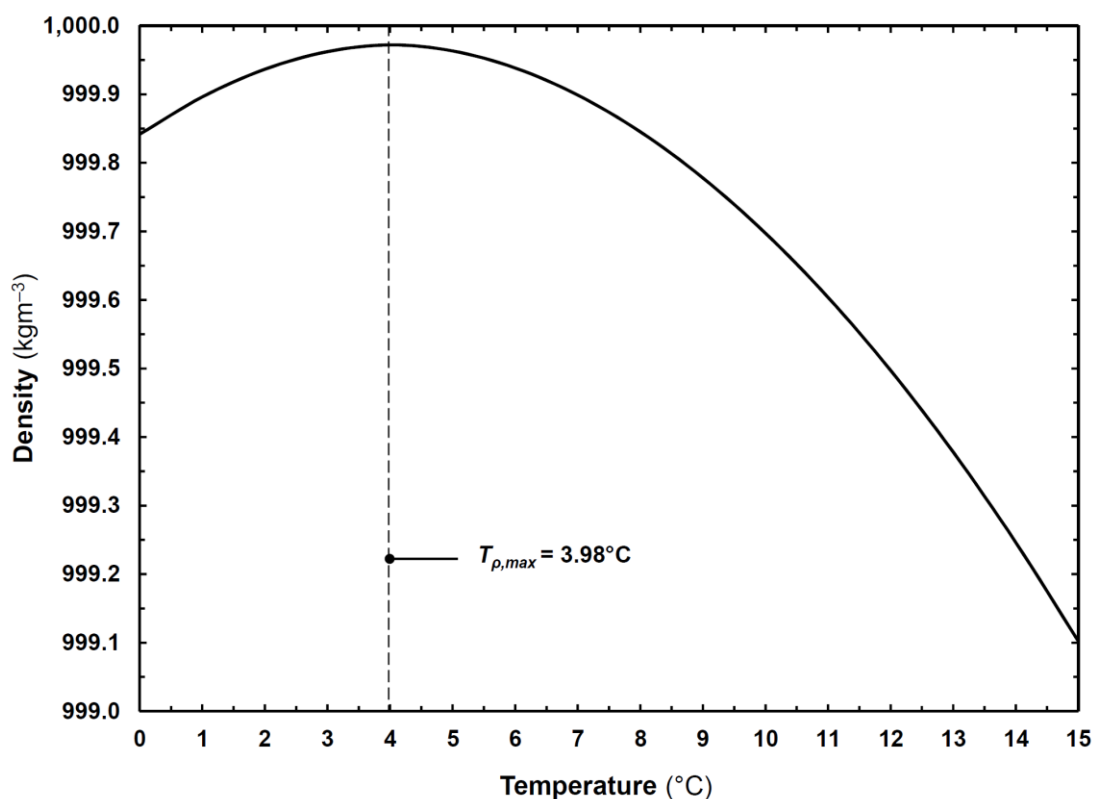


Figure 1.3 Density inversion of water.

Because of this nonlinearity, convective motion in water behaves rather peculiar manner when the temperature encompasses the 3.98°C (Vasseur & Robillard, 1980). Several authors have proposed different correlations for the density of water as a function of temperature (Kell, 1967; Chen & Millero, 1976; Gebhart & Mollendorf,

1977). Lin & Nansteel (1987) indicated that most of these correlations are in a close agreement to each other and, the correlation of Gebhart & Mollendorf (1977) is widely used because of its simple form. Gebhart & Mollendorf (1977) defined a relationship between temperature and density as

$$\rho(T) = \rho_m \left(1 - \omega |T - T_m|^q\right) \quad (1.3)$$

where ρ_m is the maximum density ($\rho_m = 999.972 \text{ kg/m}^3$), $\omega = 9.297173\text{E-}6(\text{°C})^{-q}$, $T_m = 4.0293\text{°C}$ and $q = 1.894816$.

Owing to the effect of density inversion of water, natural convection formation inside systems becomes complicated especially near to the density maximum. Thus, detailed literature review is carried out for the studies that are related to the natural convection of water with and without phase change.

Viskanta (1985) and recently Fukusako & Yamada (1999) performed excellent reviews concerning with the natural convection driven phase change studies. These reviewers designated that the researchers mainly focused on investigation of natural convection problem (*with* or *without* phase change) in three types of geometries:

- *inside rectangular cavities,*
- *around tubes,*
- *inside spherical capsules,*

1.2.1.1 Inside Rectangular Cavities

Either with or without phase change, many researchers have investigated influences of the natural convection inside rectangular or square enclosures, both numerically and experimentally.

Vasseur & Robillard (1980) carried out numerical investigations for transient two-dimensional natural convection of water inside a rectangular enclosure. Numerical solutions are obtained for cases involving different aspect ratios and initial temperature values varying from 4°C to 20°C. Transient streamlines and isotherms are represented to investigate the effect of the density inversion of water

on cooling process. Lin & Nansteel (1987) analyzed the natural convection process inside a square enclosure. The vertical walls of the enclosure are heated and cooled on the opposite directions. They defined a density distribution parameter with extending the inversion parameter that used by Nguyen, Vasseur & Robillard (1982). For the vertical heated or cooled cavity, this parameter designates the position of the maximum density temperature ($T_{\rho,max}$) in respect to the hot and cold wall temperatures. The density inversion parameter is defined as

$$R = \frac{T_{\rho,max} - T_{cold}}{T_{hot} - T_{cold}} \quad (1.4)$$

Lin & Nansteel (1987) stated that the cases $R < 0$ ($T_{hot} > T_{cold} > T_{\rho,max}$) and $R > 1$ ($T_{\rho,max} > T_{hot} > T_{cold}$) result clockwise and counter-clockwise circulation patterns, respectively. On the other hand, when R is in the range of $0 < R < 1$, it indicates that the density inversion point of water lies between the cold wall and hot wall. As a result, there appear two separated circulation cells, separated by the density inversion temperature. Lin & Nansteel (1987) performed numerical analyses for different values of the density distribution parameter; $R = 0.4, 1/2, 0.55, 2/3$ and $3/4$. For $R = 1/2$, symmetrical temperature and flow conditions observed inside the cavity. In addition, with increasing R , the maximum density position moves towards the hot wall, and in contrast, with decreasing R , the maximum density position moves through the cold wall.

Braga & Viskanta (1992a) carried out numerical and experimental studies near the maximum density temperature of water to investigate the transient natural convection heat transfer of water in a rectangular cavity. Experiments are performed for four different initial temperatures of water and, flow patterns are visualized with helium-neon laser. Formations of reverse circulation cells around the density inversion temperature of water are represented in terms of the experimental patterns and numerical predictions for four initial temperatures of water. McDonough & Faghri (1994) presented the transient and steady state natural convection cases of water in a rectangular cavity. Flow patterns are visualized with the aid of the pH indicator technique and experimental patterns are compared with the numerical results. Tong

& Koster (1994) analyzed the density inversion effect in a rectangular enclosure for several aspect ratios. Flow patterns and temperature fields are represented for different boundary conditions of the vertical walls. Kwak, Kuwahara & Hyun (1998), adopted a numerical method to simulate the natural convection of water in a rectangular cavity. First, they validated numerical predictions with comparing their results to the experimental results of Braga & Viskanta (1992a) and then carried out parametric analyses to investigate the influences of the initial temperature of water and, aspect ratio of the cavity on the convective heat transfer of water. Recently, Ho & Tu (2001) investigated the natural convection of water in a tall rectangular enclosure with high Rayleigh numbers, both experimentally and numerically. Hossain & Rees (2005) carried out numerical analysis for transient convection of water inside an enclosure with isothermal walls and heat generation.

Furthermore, the influences of natural convection in the cavities are also investigated with the presence of phase change. Tankin & Farhadieh (1971) observed the formation of ice in a rectangular cavity with the presence of natural convection. Circulation patterns are represented with using Mach–Zehnder interferometer. Brewster & Gebhart (1988) investigated the downward freezing in a rectangular cavity. Upward and downward flow circulations are introduced for various boundary conditions. Cao & Poulikakos (1991), Nishimura, Fujiwara & Hisashi (1991) and Braga & Viskanta (1992b) conducted experimental studies on transient solidification period of water in a rectangular cavity with the presence of natural convection. Cao & Poulikakos (1991) investigated the effect of inclination angle of the cavity on the temperature distribution. Nishimura et al. (1991) visualized the temperature distributions and discussed the formation of the flow patterns. Braga & Viskanta (1992b) carried out experiments for several boundary and initial conditions to investigate the natural convection dominated solidification near the density inversion temperature of water. Time wise flow patterns and temperature variations inside a rectangular cavity are represented. Fukusako, Yamada & Kim (1998) and Kowalewski & Rebow (1999) studied the influence of the natural convection on phase change inside a cavity, for both numerically and experimentally. Fukusako et al. (1998) investigated the melting period of ice in a rectangular cavity and compared

the visualized photographs to the predicted stream functions. Kowalewski & Rebow (1999) represented the variations of transient phase fronts and flow patterns inside a square cavity. Kowalczyk, Hartmann & Delgado (2004) and Scanlon & Stickland (2004) performed numerical analyses for modeling of the solidification problems using the commercial CFD software FLUENT. Seybert & Evans (2005) performed experimental studies using particle–imaging–velocimetry (PIV) to observe the steady–state condition of the solidification inside a rectangular cavity. They compared their results with numerical analysis and investigated the variations of solidification fronts with the temperature and velocity distributions under several wall temperatures. On the other hand, Stickland, Scanlon & MacKenzie (2007) developed an experimental method that allows quantitative measurement of the formation of natural convection driven flow field in a cavity. Banaszek, Jaluri, Kowalewski & Rebow (1999) performed a comprehensive numerical and experimental study. They developed a semi–implicit finite element method (FEM) to simulate solid–liquid phase change controlled by natural convection and conduction. They validated the accuracy of their method with the aid of experimental comparisons. Recently, Tenchev, MacKenzie, Scanlon & Stickland (2005), and Wang, Faghri & Bergman (2010) adopted new numerical methods basis on the moving mesh technique and the consistent update technique, respectively. The validity and the accuracy of these methods are tested via comparing their predictions with the previous experimental and numerical studies.

1.2.1.2 Around Tubes

Either with or without phase change, many researchers have performed numerical and experimental studies to investigate the influences of the natural convection around tubes.

Sasaguchi, Kusano, Kitagawa & Kuwabara (1997), and Sasaguchi, Kuwabara, Kusano & Kitagawa (1998) analyzed the effect of the density inversion point on the cooling process of water around a cylinder. Influences of the initial temperature of

water and the position of the tube are investigated in terms of the angular variation of Nusselt number and the velocity–temperature distributions around tubes.

Bathelt & Viskanta (1980) carried out numerical and experimental studies to introduce the heat transfer during the melting period of n -paraffins (n -heptadecane and n -octadecane) around a cylindrical tube. Velocity profiles and the variation of the local heat transfer coefficient around the tube are represented. Rieger, Projahn & Beer (1982) analyzed the melting process around a tube with using body fitted coordinates. Ho & Viskanta (1984) carried out experimental and numerical investigations for inward melting of n -octadecane inside a cylindrical capsule. Saitoh & Hirose (1984) analyzed the melting process around a cylinder via using multi-point finite difference method with an extended Landau transformation. They compared their predictions with the experimental data of Bathelt & Viskanta (1980) and numerical results of Rieger et al. (1982). Betzel & Beer (1986) presented the time dependent interface variations inside n -octadecane during melting process around the tubes. They carried out experiments for three different types of tubes; plain horizontal tube, axial PVC finned tube and axial copper finned tube. Ho & Chen (1986) analyzed the melting process of water around a cylinder for various wall and initial temperatures. Costa, Oliva & Pérez-Segarra (1997) studied on inward melting period of n -octadecane in the three-dimensional domain. Experimental validations are performed for two different cases. Flow patterns and temperature distributions are represented for different sections along the cylinder. Sasaguchi, Kusano & Viskanta (1997) investigated the effect of the natural convection on the formation of ice with single or double tubes arrangements in a rectangular cavity. Influences of the initial and wall temperature values on the solidified amount of ice are represented for single and double tube cases. Ng, Gong & Mujumdar (1998) analyzed the outward melting period of n -octadecane inside a cylindrical cavity for two different Rayleigh numbers. Khillarkar, Gong & Mujumdar (2000) extended the study of Ng et al. (1998) and analyzed the inward melting around rectangular and circular tubes with various Rayleigh parameters. Ismail & daSilva (2003) developed a numerical method to simulate the melting period of the PCM around a cylinder in

the presence of the natural convection. They represented the variations of Nusselt number on the tube and interface surfaces as functions of time and angle.

Recently, Shih & Chou (2005) carried out numerical simulations with the aid of commercial CFD code FLUENT. They analyzed the solidification period of water around cylindrical tubes for different initial and boundary conditions, with various arrangements of tubes inside a rectangular cavity. They validated the results with comparing the experimental data of Sasaguchi et al. (1997). On the other hand, Sugawara, Komatsu & Beer (2008), Sugawara & Beer (2009), and Sugawara, Komatsu, Makabe & Beer (2010) analyzed solidification and melting periods of water in various geometries with using the commercial CFD code PHOENICS. Sugawara et al. (2008) investigated the solidification and melting around a cylinder, which is located for three different positions, inside a rectangular cavity. Comparative results are represented in terms of the velocity and temperature distributions and amount of the melted or solidified masses of water. Sugawara & Beer (2009) carried out two groups of studies. In the first one, they validated their numerical method with comparing the predictions to the experimental data, for transient and steady-state conditions of the natural convection driven phase change problems inside horizontal and vertical rectangular cavities. After validation, they investigated the influences of natural convection around four vertically arranged cylinders, during the melting and solidification periods. Sugawara et al. (2010) performed experimental and numerical studies to introduce the influence of the natural convection on the solidification in a shell-and-tube type LHTEs system. Numerical analyses are carried out for three-dimensional computational domain. Interface variations are represented for selected sections together with the velocity profiles and the temperature distributions.

1.2.1.3 Inside Spherical Capsules

Khodadadi & Zhang (2001) and Tan, Hosseinzadeh, Khodadadi & Fan (2009) carried out comprehensive studies to introduce the effect of natural convection on melting inside spherical capsules. In these studies, inward melting inside spherical

capsules are investigated under different Rayleigh and Pr number conditions. Tan et al. (2009) performed numerical analyses with the aid of commercial CFD code FLUENT and then validated the results with comparing the time wise temperature distributions for several nodes in the domain. Ettouney, El-Dessouky & Al-Ali (2005) experimentally investigated the melting and solidification processes of paraffin wax inside a spherical shell. They represented the angular variations of interface during melting and solidification, with the aid of thermocouple data. Assis, Katsman, Ziskind & Letan (2007), and Assis, Katsman, Ziskind & Letan (2009) carried out experimental studies to investigate the melting process of paraffin in a spherical capsule with consisting air. Numerical analyses are performed with using FLUENT software to predict the natural convection effects inside the capsule.

As summarize, numerous experimental and numerical studies are conducted to investigate the natural convection phenomena during phase change inside several geometries. These studies briefly mention that, in the early stages of the phase change, heat transfer mechanism is driven by conduction, and the formation of the solid-liquid interface is symmetrical. After buoyancy effects appear, the interface and local Nusselt number variations around the tube (or *inside capsule*) become asymmetric and the influence of the natural convection becomes dominant.

1.2.2 Energy Based Parametric Studies of LHTES Systems

Several researchers have studied on design and flow parameters of LHTES systems for shell-and-tube, ice-on-coil or encapsulated systems. In following sections, detailed reviews are given for *shell-and-tube* and *ice-on-coil* LHTES systems.

1.2.2.1 Shell-and-tube Type LHTES Systems

Shell-and-tube type LHTES systems consist of single or multiple tubes that are settled inside shell geometry. PCM can stand inside either tubes or shell side of the heat exchanger and accordingly this, HTF flows inside the shell or tubes,

respectively. Recently, Agyenim, Hewitt, Eames, & Smyth (2010) carried out detailed literature review and designated that the most intensely analyzed LHTES unit is the shell-and-tube system accounting for more than 70% of the related literature.

Cao & Faghri (1991) numerically modeled the phase change process inside a shell-and-tube type LHTES system as a conjugate problem. They solved the convective heat transfer inside the tube and conductive phase change around tube; finally, they emphasized the importance of the conjugate analysis. Lacroix (1993) developed a numerical model to assess the influences of various thermal and geometric parameters on the heat transfer characteristics of an energy storage system for melting period. The influence of natural convection inside the melting domain is adapted with defining the effective thermal conductivity for the liquid. Validation of the numerical method is performed with comparing the temperature values at various positions inside the medium. Hasan (1994) carried out experimental study to investigate the melting period of palmitic acid inside an energy storage system. Comparative results are represented for various inlet temperatures and flow rates of the HTF. It is indicated that the influence of flow rate is remarkably small in comparison with the inlet temperature. Ismail & Gonçalves (1999) numerically investigated the solidification period of a shell-and-tube type LHTES system with the multi-tube arrangement. A numerical model is developed with neglecting the natural convection effects inside the medium. Time wise variations of effectiveness, amount of solidified PCM, and NTU values are represented for various inlet temperatures of the HTF, Biot numbers and dimensionless shell diameters. Sari & Kaygusuz (2002) experimentally investigated the thermal behaviors of lauric and stearic acid materials in a LHTES system. Experiments are conducted for solidification and melting periods for various Reynolds numbers and inlet temperatures of the HTF. Hamada, Ohtsu & Fukai (2003) carried out numerical and experimental studies on a shell-and-tube type LHTES system with the multi-tube arrangement. The effects of carbon-fibre chips and carbon brushes additives on the thermal conductivity enhancement of phase change materials are investigated. Nagano et al. (2004) studied the performance of charging and discharging periods of

magnesium nitrate hexa-hydrate and magnesium chloride hexa-hydrate mixture as PCMs in a vertical tube LHTES system. Trp, Lenic & Frankovic (2006) analyzed the effects of the thermal parameters of the HTF as well as influences of the length of the tube and the outer radius of the shell on the system performance. Akgün, Aydin & Kaygusuz (2008) carried out experimental investigations for three types of paraffin mixtures. Charging and discharging performances of the materials are tested in a vertical-storage tank with a conical shaped shell. Jian-You (2008) applied the temperature and thermal resistance iteration method for the simulation of solidification/melting processes of PCM in a triplex concentric tube. Several analyses are performed for various flow parameters. Habeebullah (2007) presented the experimental results on solidification of water around long bended tubes and concluded that the thickness of ice increases on the returning bends because of the development of local eddies inside the bends. Recently, Agyenim, Eames & Smyth (2010) experimentally investigated the multi-tube arrangements in a shell-and-tube type LHTES system. The temperature variations in the PCM region is obtained with using sets of thermocouples in 60° intervals around tube.

Above-mentioned researches are studied for bare tube systems. In addition to these studies, influence of fin arrangements and extended surfaces are also investigated for shell-and-tube type LHTES systems.

Yimer & Adami (1997) numerically investigated the LiH based thermal energy storage system for various thermal and geometric parameters. Analyses are performed for bare and finned tubes. Velraj, Seeniraj, Hafner, Faber & Schwarzer (1999) carried out numerical and experimental studies to introduce the influences of two types of heat transfer enhancement strategies. Results are designated that, usage of finned tube and addition of Lessing rings decrease the time for complete solidification in comparison with the bare tube. Ismail, Henriquez, Moura & Ganzarolli (2000) adopted enthalpy method to simulate the solidification process around radially finned tube with neglecting the influence of natural convection. They introduced the effects of usage of different fin materials and geometric parameters of fins, on the performance of the energy storage. Besides Ismail, Alves & Modesto

(2001) carried out companion study to investigate the effect of vertical fin arrangements on solidification process. Analyses are carried out for various thickness, length, angular position, and number of fins. Seeniraj, Velraj & Narasimhan (2002) modeled LHTES system with using enthalpy formulation for charging mode. The influences of geometrical and thermo–physical parameters are studied with considering the effect of fin addition. Lamberg & Sirén (2003) developed an analytical method to solve the solidification process around internal finned tubes. Erek (1999) and Erek, İlken & Acar (2005) experimentally and numerically studied the solidification process around bare and finned tubes, with neglecting the effect of natural convection. They investigated the solidification process in a shell–and–tube heat exchanger for various fin geometries and working conditions. In conjunction with these studies, Ermis, Erek & Dincer (2007) analyzed the same system with using artificial neural network algorithm to predict the influences of parameters in large scale. Castell et al. (2008) developed the heat transfer coefficients for natural convection dominated phase change inside a vertically finned module. Medrano et al. (2009) experimentally investigated the heat transfer processes during solidification and melting for five small heat exchangers working as LHTES systems. Average thermal power values are evaluated for various operating conditions and compared among the heat exchangers studied. Recently, Agyenim, Eames & Smyth (2009), (2010) and (2011) presented the effects of several configurations of fins, on the performance of shell–and–tube type LHTES systems. They investigated the influence of longitudinal fins on the phase change process with several working parameters.

1.2.2.2 Ice–on–coil Type LHTES Systems

Ice–on–coil energy storage systems are popular to use in commercial cooling or heating applications with phase change. There are some corporations about the ice–on–coil LHTES applications, such as Calmac, Evapco and Baltimore Air coil. Web sites of these corporations are cited in references. Ice–on–coil systems simply consist of a storage tank and a coil inside the tank and it is easy to integrate into the conventional cooling systems. In these systems, heat transfer fluid (HTF) flows

inside the coil and phase change material stands in the space between the coil and the tank shell. There are many experimental and numerical studies conducted by several researchers to investigate performance assessments of the systems.

Banaszek, Domanski, Rebow & El-Sagier (1999) designed an air to paraffin wax heat exchanger in Archimedes spiral form. Thermal analyses are carried out to investigate the total time of charging and discharging under several working parameters. Wang, Zhang, Li & Yang (2003) experimentally investigated the external melting period of an ice-on-coil ice storage tank. Time wise temperature distributions inside the tank is represented for various load power, initial ice quantity and inlet temperature and flow rate of HTF. Ereğ & Ezan (2007) carried out numerical and experimental studies for assessing the effects of various inlet conditions of HTF on the storage performance of an ice-on-coil energy storage system.

Several numerical models are developed to predict the time wise solidification process in ice-on-coil storage tanks. Jekel, Mitchell & Klein (1993) developed a mechanistic model based on basic heat transfer and thermodynamic relations. They determined the effectiveness of the storage tank also the rate of heat transfer rejected or delivered from the tank, for both charging and discharging periods. Model is validated by comparing the effectiveness of the ice storage tank with manufacturer's data. Drees & Braun (1995) improved the numerical model of Jekel et al. (1993). In new model, instead of using Nusselt correlations for straight tube, Drees & Braun (1995) computed the internal heat transfer coefficient from the correlations that are developed for curved tubes. They concluded that, in curved tubes, presence of centrifugal forces cause higher velocities and this can increase the overall Nusselt number 500% in some special cases. The validity of this model is tested with more accurate laboratory experiments in terms of charging and discharging heat transfer rates and outlet temperature of the HTF. Vick, Nelson & Yu (1996) developed a new model and computational algorithm to simulate charging and discharging periods of counter-flow ice storage tank. They produced a computer program called IceTES (*Ice thermal energy storage*) and, the validity of this method is represented in a

companion study Nelson, Vick & Yu (1996). Neto & Krarti (1997a, 1997b) described a dynamic model for an internal melt ice-on-coil thermal storage tank, based on a quasi-steady-state analysis and a thermal resistance network technique. Two models are described in Neto & Krarti (1997a) for outward solidification and internal melting processes. Models have abilities to simulate overlapping effects during freezing and melting. Validations of models are represented in Neto & Krarti (1997b) with comparing the time wise variations of predicted outlet temperature, pressure drop and total volumes of phase changed PCM, to the experimental data. Lee & Jones (1996) developed a stand-alone analytical model for an ice-on-coil LHTES system under both charging and discharging modes, and validated the numerical results with comparing the experimental ones. West & Braun (1999) extended their previous study in Drees & Braun (1995) to simulate the partial charging and discharging modes. They represented two models for predicting the thermal behavior of the storage tanks under partial charging and discharging processes. He, Qian, Hu & Zhou (2001) developed a model to simulate the ice formation in an ice-on-coil energy storage system. They applied conduction shape factor to take into account the constrained ice formation. Zhu & Zhang (2001) investigated the effect of ice-water density difference on internal melt ice-on-coil LHTES system.

1.2.3 Exergy Based Parametric Studies of LHTES Systems

Second law analyses of phase change processes are conducted to investigate the entropy generation or exergy efficiency variations during phase change. Entropy generation of a system can be obtained as local or overall. Recently Orhan, Erek & Dincer (2009) and Makhanlall & Liu (2010) investigated the local entropy generation during phase change. Orhan et al. (2009) performed numerical analysis for solidification between two parallel plates with assuming conductive one-dimensional model. Makhanlall & Liu (2010) analyzed the phase change in a two-dimensional square cavity with the presence of natural convection and radiation. Time wise variations of exergy destruction is represented for various parameters and the exergy destruction counters is illustrated.

On the other hand, El-Dessousky & Al-Juwayhel (1997) obtained entropy generation number for various working temperatures and flow rates of the HTF in a LHTES system. Ereke & Dincer (2008) developed a new approach to calculate the entropy generation number in a thermal energy storage system. Ereke & Dincer (2009) extended their previous study and obtained exergy efficiency and effectiveness variations for various working and design parameters of shell-and-tube type LHTES system. McPhee & Dincer (2009) simulated the melting and freezing processes of water in a bed of spherical capsules, to investigate the influence of inlet temperature of HTF on the energy efficiency, exergy efficiency, and exergy destruction. Strub & Bedecarrats (1999) performed numerical study to introduce the influence of inlet temperature of the HTF on discharging process in an encapsulated storage tank.

1.3 Objectives and Contents of Dissertation

In this dissertation, two different types of LHTES systems are designed and fabricated to investigate the solidification and melting phenomena of water. These two systems are named as *shell-and-tube type LHTES* system and *ice-on-coil type LHTES* system. In the shell-and-tube type LHTES system, natural convection dominated phase change process is investigated in a relatively small volume. An electronic interface measurement method is developed to monitor the solid-liquid interface variations during phase change, and this method is validated with the comparisons of visual and temperature data. Influences of natural convection on the formation of solid-liquid interfaces are introduced for solidification and melting modes. Furthermore, thermal behavior of the system is examined during charging and discharging processes for various working and design parameters in terms of total stored and rejected energies also, energy and exergy efficiencies. In the ice-on-coil type LHTES system, interface and temperature variations inside a storage tank are observed in a large scaled storage tank, during melting and solidification processes. Storage tank is designed as counter flow and staggered tube arrangement. In system, PID algorithm controlled the pumps, the chiller, and the heating tank to minimize the oscillations of flow rate and inlet temperature of HTF. Several control

strategies are tested to obtain a constant temperature value of HTF at the inlet section of the tank. In addition, influences of working parameters of HTF on charging/discharging capability of the system are investigated. Discharging experiments are performed for internal and external melting cases.

Besides, numerical analyses are conducted to simulate these two types of storage systems. Natural convection dominated phase change in a shell-and-tube type system is analyzed in two-dimensional domain with the aid of commercial CFD code FLUENT. First, several preliminary case studies are selected from literature and comparisons are conducted to validate the numerical methodology. Afterwards, current shell-and-tube type LHTES system is numerically modeled in a two-dimensional domain and, comparisons are performed for current experimental data. Finally, influences of natural convection on solidification and local entropy generation are represented for three different initial temperatures of water. On the other hand, energy and entropy analyses are carried out for charging period of an ice-on-coil LHTES system with using thermal resistance network technique. First, the time-dependent variations of predicted total stored energy, mass of ice and outlet temperature of HTF from storage tank are compared with experimental data. Then, performance of the ice-on-coil LHTES system is investigated for several working and design parameters. The results of the comparative study are represented with variations of the heat transfer rate, total stored energy, dimensionless energetic and exergetic effectiveness, also, energy and exergy efficiency.

1.3.1 Objectives

Several items can be listed to specify the objectives of the current dissertation. Here are the specific objectives of this thesis study:

- Design and fabricate a shell-and-tube type LHTES system to perform charging and discharging experiments;
 - *Design and validate an interface measurement method for water,*
 - *Investigate the influence of natural convection during phase change,*

- *Perform parametric experiments to introduce the energetic and exergetic assessment of the system,*
- Design and fabricate an ice–on–coil type LHTES system to perform charging and discharging experiments;
 - *Design and validate interface measurement method,*
 - *Investigate the influence of control schemes on the inlet temperature of HTF to the storage tank,*
 - *Perform parametric experiments to introduce the energetic and thermodynamic assessment of the system,*
- Perform numerical investigations on phase change, with and without natural convection;
 - *Adapt a numerical methodology to predict natural convection dominated phase change around tube. Validate the methodology and perform parametric energy and entropy based investigations,*
 - *Adapt a numerical method for ice–on–coil LHTES system to predict the influence of working parameters on the charging performance. Validate the method and perform parametric energy and entropy–based investigations.*

1.3.2 Contents of Dissertation

In the second chapter of the dissertation, experimental apparatus and analyses are described for the shell–and–tube and ice–on–coil LHTES systems. In the third chapter, numerical methodologies and corresponding models are defined. In the fourth chapter, experimental and numerical results are represented in a categorized manner. Finally, in the fifth chapter contributions of current dissertation are summarized. Besides, uncertainty analyses are performed for two experimental studies and second law analyses (*entropy* and *exergy*) are carried out in both experimental and numerical studies, so, basic definitions and formulations about uncertainty and second law analyses are represented in the corresponding chapters.

CHAPTER TWO

EXPERIMENTAL APPARATUS AND ANALYSES

In this thesis study, two different types of LHTES systems are designed and fabricated to examine the solidification and melting phenomena of water. These two systems are named as *shell-and-tube type LHTES* system and *ice-on-coil type LHTES* system. In this chapter, corresponding experimental apparatus and measurement systems are introduced in the following subsections.

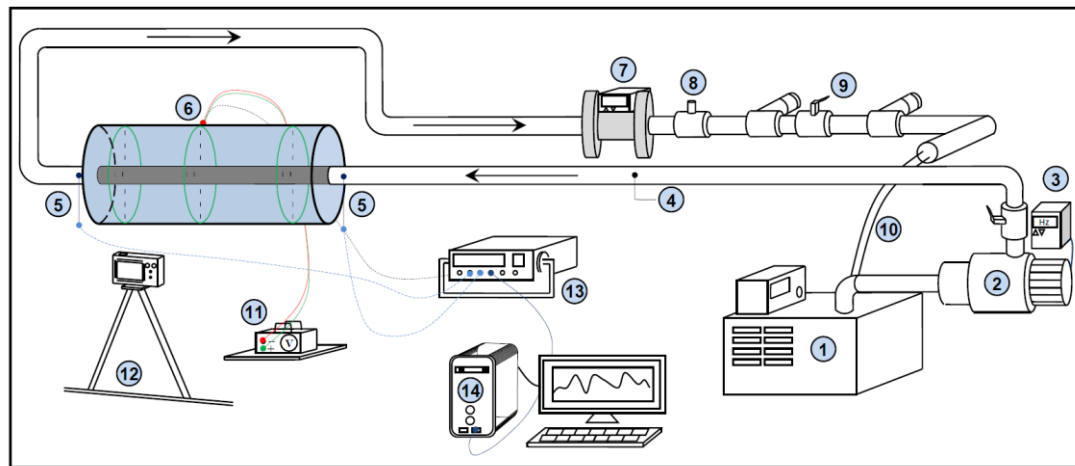
2.1 Shell-and-Tube Type LHTES System

A shell-and-tube type latent heat thermal energy storage system is designed and fabricated, in order to investigate the thermal behavior of a LHTES system for both charging (*solidification*) and discharging (*melting*) periods. Figure 2.1 illustrates a schematic diagram of the current experimental setup. System consists of a flow control system, the heat exchanger section, and the measurement system.

The parts comprising the flow system are; the thermostatic bath Polyscience (*Naperville, IL, USA*) (1), with an accuracy of $\pm 0.01^\circ\text{C}$, that controls the inlet temperature of the HTF, a centrifugal pump Wilo (*Dortmund, Germany*) (2) which is driven by the frequency controller (3), pipe line (4) which provides fully developed flow conditions at the inlet of the heat exchanger section, Bürkert (*Ingelfingen, Germany*) electromagnetic flow meter (7) and Bürkert electronically controlled proportional valve (8) to regulate the flow rate of the HTF. Consequently, the flow system provides the required constant inlet temperature and flow rate of the HTF to the heat exchanger section.

The heat exchanger section is composed of two concentric tubes as shown in Figure 2.2. The interior cylindrical tube has a length of $\ell = 400$ mm with inner and outer diameters of $D_i = 15$ mm and $D_o = 25$ mm, respectively. Plexiglas (*acrylic*) is preferred as a shell material because of its transparency. Polyamide shutters are

fastened with O-rings to provide sealing of the shell. Ethylene glycol–water solution is used as a heat transfer fluid and water fills the annulus between the tube and the shell, as PCM. Since the volume of water increases as it solidifies for a constant mass, an overflowing connection is mounted on the side of the annulus. Figure 2.3 shows the un-insulated heat exchanger section of the system.



(1) Refrigerated Bath, (2) Pump, (3) Motor Speed Controller, (4) Pipeline, (5) Pt-100 Sensor, (6) Measurement Cards, (7) Electromagnetic Flowmeter, (8) Electronically Controlled Valve, (9) By-pass, (10) Return Connection, (11) Electronic Circuit, (12) Camera, (13) Data Acquisition Unit, (14) Computer

Figure 2.1 Schematic diagram for the shell-and-tube LHTES system.

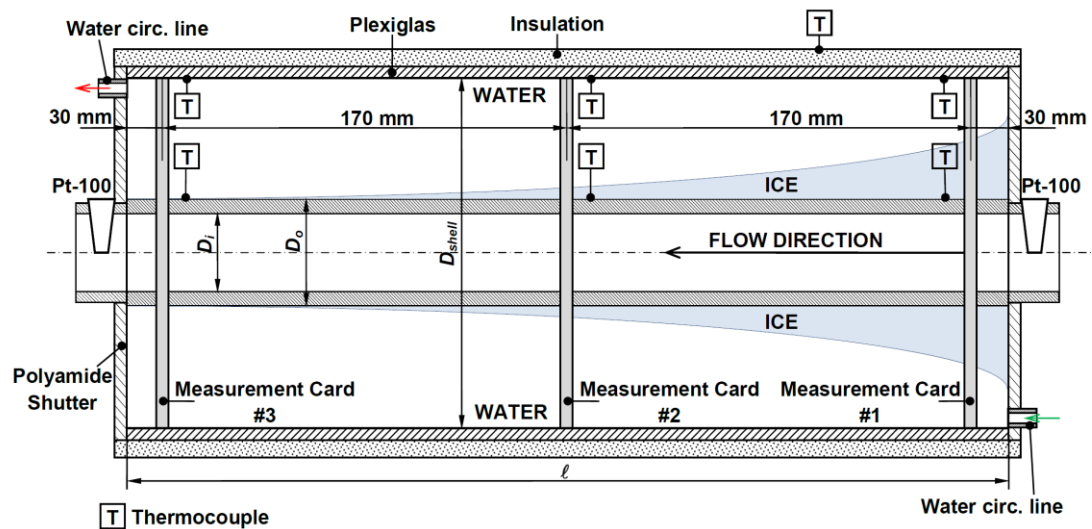


Figure 2.2 The geometry of the shell-and-tube heat exchanger.

Three different tubes, which are made of copper, stainless steel, and polyethylene (PE-32) materials, have been used in the experimental study. In addition, two exterior cylindrical tubes with different diameters have been used. In order to reduce

the heat gain from the surroundings, the outer surface of the exterior cylindrical tube has been insulated with a 15 mm thick layer of armafex and a 30 mm thick layer of glass wool. At the middle section of the tank, two openings have been attached on the front and backsides of the insulation, as monitoring windows, for visualization.

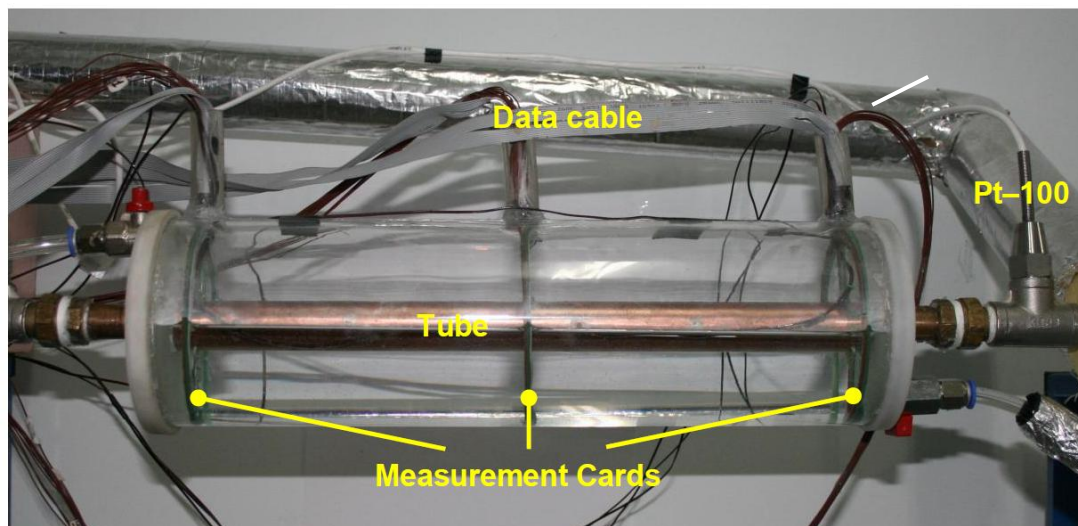


Figure 2.3 Heat exchanger section of the system – *without insulation*.

Three measurement cards are settled inside the PCM to observe the solidification interface. Cards are located at the inlet, middle, and outlet sections along the flow direction. Further details about these cards and the interface measurement method are given in the following section. Four thermocouples, 30-gauge and T-type, are mounted on each three directions of the cards. Hence, a total of 36 thermocouples is used to establish the temperature distribution inside the PCM. In addition, outer surface temperature of the interior tube and inner surface temperature of the shell are measured at 18 points with 24-gauge T-type thermocouples. Thermocouples are calibrated in a constant temperature bath between the range of -15°C and $+25^{\circ}\text{C}$. Inlet and outlet temperature values of the HTF to the storage tank are measured by Pt-100 probes with an accuracy of $\pm 0.01^{\circ}\text{C}$. While temperature and flow rate readings are collected in a computer via Agilent 34970A (Santa Clara, CA, USA) data acquisition system, the voltage measurements from the pair of electrodes are transmitted to the computer with a device that is specially designed and produced for this study.

2.1.1 Experimental Procedure

In all charging experiments, the initial mean temperature of the water is decreased nearly to the phase change temperature. In order to achieve that, a small pump is integrated to the system to circulate cold water from a separated tank, containing ice–water mixture, to the annulus space. As soon as the mean temperature of the system reaches below 0.5°C, ethylene–glycol water solution (*40% Ethylene glycol by volume*) is pumped through the thermostatic bath with a definite flow rate and inlet temperature. Charging experiments are continued since the water almost completely converts to ice, and discharging experiments are carried out after the solidification experiments are completed.

During the experiments, temperature and volumetric flow rate measurements are determined by means of the data acquisition system at one–minute interval and recorded in the computer via an RS232 interface. The solidified or melted mass amount of PCM is essential for calculation of the latent energy stored/rejected for a LHTES system. As is known, the solid–liquid interface varies through the flow direction and around the tube. In order to capture these variations, the interface measurement is carried out at three different sections along the flow direction with the electronic measurement cards (*see Fig. 2.2*). The cards are connected to the data acquisition system that scans all measurement nodes on three cards in one–minute interval. Photography method is also implemented for validating the accuracy of the measurement method. A camera is located in front of the middle section of the system, and photographs are taken at every 15 minutes by opening the covers on the insulation.

The total heat gain from surroundings is calculated both theoretically and experimentally. In the experimental approach, the liquid water turned into ice and leaved for melting under environmental conditions. During melting of ice, temperature and measurement card data are collected in the computer, until all of ice fully changed into the liquid phase. The Total internal energy variation of the system should be equal to the heat gain. Internal energy variation of the system is computed

with using a control volume approach. The details about the control volume approach are given in the following sections. Total heat gain from the surroundings can be written as

$$Q_{gain}(t) = \bar{U}A \int_{t=0}^t (\bar{T}_{outer} - \bar{T}_{inner}) dt \quad (2.1)$$

where \bar{U} is the overall heat transfer coefficient of the system and can be obtained as a function of mean temperature difference between the outer surface of the insulation and the inner surface of the shell. On the other hand, in theoretical approach, overall heat transfer coefficient is obtained with using the thermal resistance networks for lateral and peripheral surfaces of the shell.

2.1.2 Interface Measurement Method

The rate of energy stored in a LHTES system mostly depends on time wise variations of the volume fractions of liquid and solid phases of the PCM, rather than the temperature variations. Hence, measurement of volume fractions of liquid and solid phases is very important for energy and exergy analyses. In earlier experimental studies, solid and liquid volumes of PCM in a LHTES system have been calculated with using one of the following methods. Taking photographs (Yamada, Fukusako, Kawanami & Watanabe, 1997; Erek, 1999; Erek et al., 2005, Tan et al., 2009), measuring with thermocouples at different sections or points (Medrona et al., 2009; Ayenim et al., 2009; Ayenim et al., 2010) or using other physical measurement methods such as caliper (Habebullah, 2007; Erek & Ezan, 2007). Recently, Shi, Wang & Li (2005) summarized all of the possible measurement methods for an ice storage system and showed the accordance of an electronic measurement method which bases on monitoring the difference of electrical characteristics of liquid and solid phases of the PCM.

This study aims to design a measurement setup for monitoring whether a specific spatial point (*measurement node*) is inside the *solid* or *liquid* phases of the water. Measurement method bases on the observation of the electrical conductivity of phase change medium, since electrical conductivity of water changes dramatically while it

freezes (Knight & Cox, 2006; Xiaoping, Spitzer & Sudmeier, 2007; Li, Li & Wu, 2001; Jay & Lehr, 2005). In the following section, detailed information about the theory of the current method is given.

2.1.2.1 Theory and Background

Electrical conductivity characteristics of liquid and solid phases of water vary noticeably. This fact allows designing an indicator system for monitoring phase for a specific point. The electrical conductivity measurement methods, which can be used for monitoring ice formation, are generally represented as following setups:

- *Resistance based measurement setups:* the amperometric method (Palleschi & Biagiotti, 2008) and the potentiometric method, which implement Ohm's law on alternating and direct current circuits (Mark, 2009),
- *Inductance based measurement setup,* which uses a toroid shape inductive probe (De Jong, Ballantyne, Cameron & Read, 1979),
- *Capacitance based measurement methods,* which utilizes dielectric effect of ice between probes (Daily & Ramirez, 2004).

Last two methods exploit frequency based modeling and analysis of measurement setups since both require AC input voltage. Measurement outputs are then received as periodic steady state signals. Amplitude and phase shift in the output signal is utilized to identify system parameters that are an inductance or a capacitance parallel or series to a resistance. Resistance based measurement systems are relatively simple than the others to analyze, because there is only a proportional relationship referring to electrical circuit form. The difference between the amperometric and potentiometric method is that the potentiometric method uses alternating voltage as input, and calculates the ratio between output and input signal amplitudes. Potentiometric method implements Ohm's law to calculate resistance of the system with DC input voltage. A major fallback of DC input voltage is that electrolysis occurs between probes.

Electrical conductivity, the reciprocal of the electrical resistivity, is the ability of a medium to conduct electric current. In order for anything to conduct electricity, matter must have charge carriers. In metals, they are weak-bounded electrons, and in solutions, they are ionic contents. The electrical conductivity is used to monitor the characteristics of a medium concerning the changes in it. As instance for phase change, Knight & Cox (2006), and for purity, Palleschi & Biagiotti (2008) can be investigated. Pure water is an excellent insulator. However, water is also a good solvent, and it often has some solute dissolved in it. If water has any amount of an impurity, it conducts electricity. Since impurities, e.g. salt, separate into free ions in aqueous solution by which an electric current can flow. In Figures 2.4 and 2.5, the variations of the resistivity and the conductivity of water are given as functions of temperature. It is clear that the electrical conductivity is affected by temperature. When the temperature of water rises, the viscosity decreases and movement of ions become easier (Xiaoping et al., 2007; Li et al., 2001).

The electrical conductivity of water is defined as

$$S = \rho \sum \lambda_i c_i \quad (2.2)$$

where S is electrical conductivity, and c_i is the concentration of the i^{th} ion, λ_i is the equivalent ionic conductance of ion i , and ρ is the density of the water (Jay & Lehr, 2005). Since the ionic conductance and density values of water vary with temperature, the conductivity of water becomes also temperature dependent. Typical conductivity and resistivity values are given in Table 2.1 for different types of water.

Table 2.1 Typical conductivity and resistivity values for different types of water.

Type of Water	Conductivity	Resistivity
	(S/m)	(Ω /m)
Ultra pure water	5.5E-6	181818.18
Drinking water	0.005 – 0.05	200 – 20
Sea water	5	0.2

While liquid water freezes into the solid phase, solid phase becomes more pure than the liquid one. This is because of the crystal lattice of the ice, which tries to form a uniform structure and, this uniform structure force the impurities

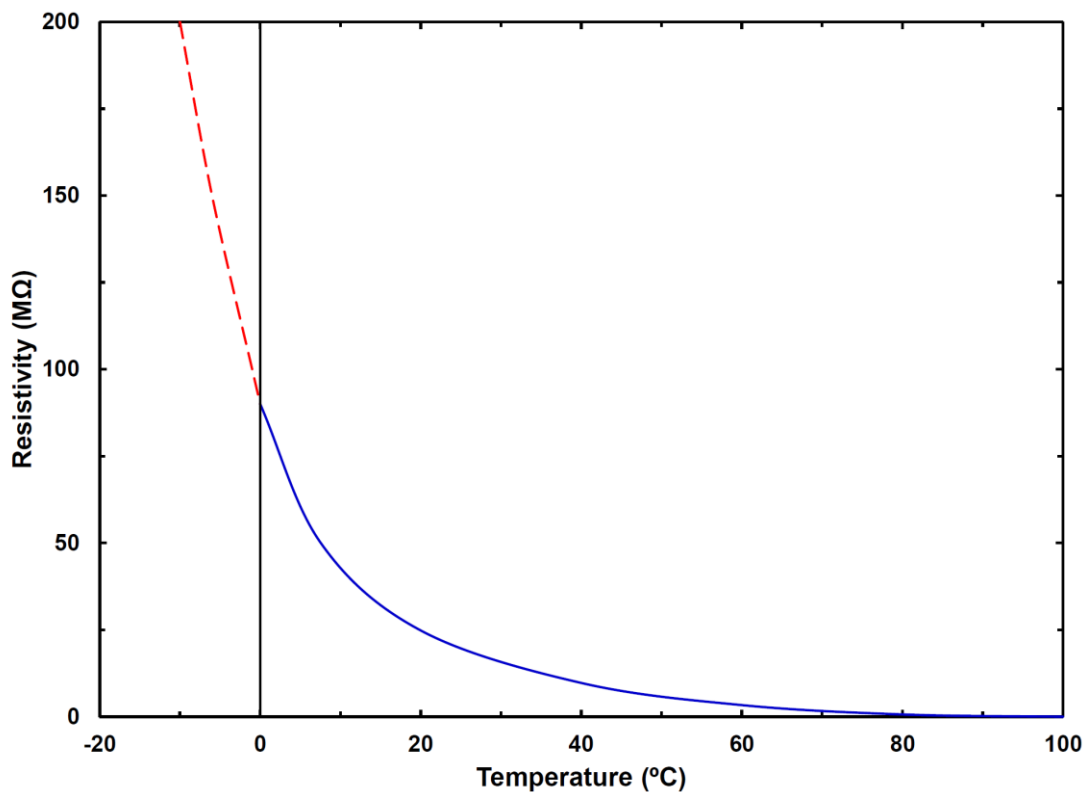


Figure 2.4 Variation of the resistivity of water with temperature (*adapted from Light, Licht, Bevilacqua & Morash, 2005*).

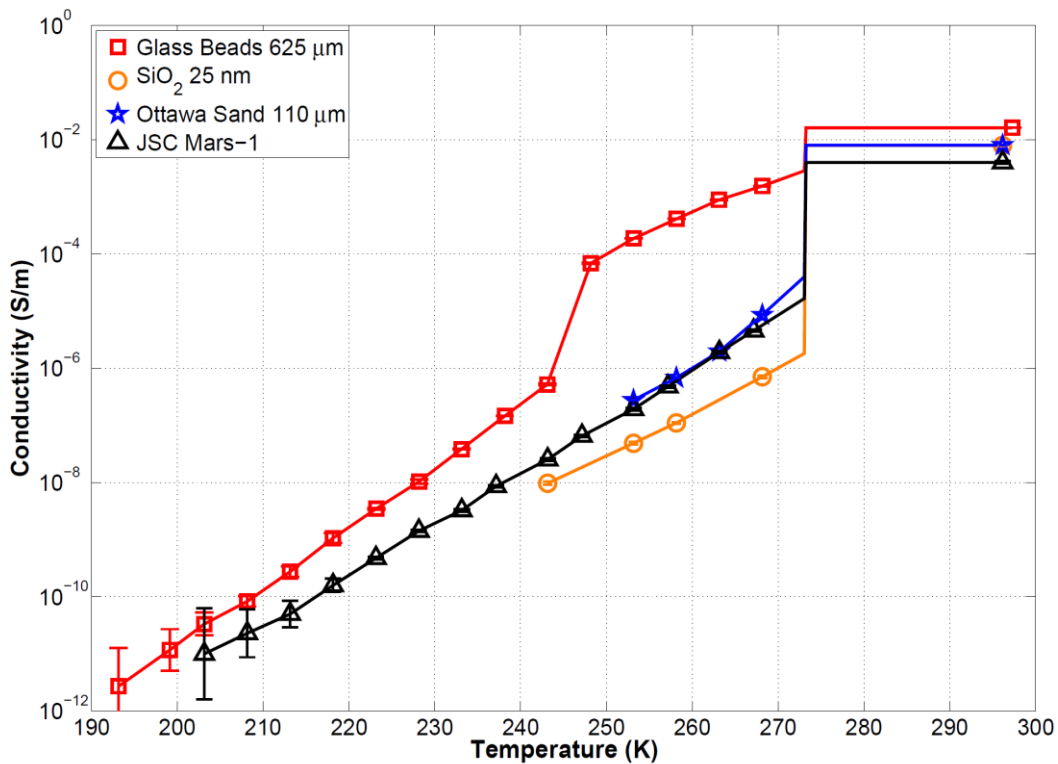


Figure 2.5 The decrease in the resistivity of impure ice, with silicate, via temperature (*Stillman & Grimm, 2007*).

out (Hori, Kako & Hayashi, 2006). This effect causes a decrease in the electrical conductivity of ice. When ice becomes de-ionized, the molecules and ions cannot move anymore (Hori et al. 2006). Even if the liquid water initially has charge carriers, during the freezing process, the mobility of these carriers becomes significantly diminished. Thus, the electrical conductivity drops dramatically during the phase change (Figure 2.5).

The basic electrical conductivity measurement methods, which can be used for monitoring of ice formation, can be detailed as follows:

In amperometric measurement setup, the probe is used to measure the conductivity with two electrodes spaced apart from each other and protrude inside the media. The amperometric method applies a known voltage value to the pair of electrodes and measures the current. According to Ohm's law, monitoring current allows recovery of the conductivity of the medium (Palleschi & Biagiotti, 2008).

The potentiometric method employs four rings; the two outer rings are used to apply an alternating voltage and induce a current loop in the solution, while the inner rings measure the voltage drop induced by the current loop. This measurement is directly dependent upon the conductivity of the solution (Mark, 2009).

Another method of conductivity measurement is using an inductive probe. The sensor is a toroid on a stick. The advantage of this technology is the measurement without any electrical contact between the electrode and the process medium. The probe uses two toroidal transformers, which are inductively coupled side by side and encased in a plastic sheath. The measurement is made by applying a high frequency reference voltage to generate a strong magnetic field. When the media in toroid shaped probe changes, current flows through sensing windings proportional to the voltage induced by the magnetic field. The conductance is proportional to the specific conductivity of the fluid and a constant factor determined by the geometry and installation of the sensor (De Jong et al. 1979). Although this method is used

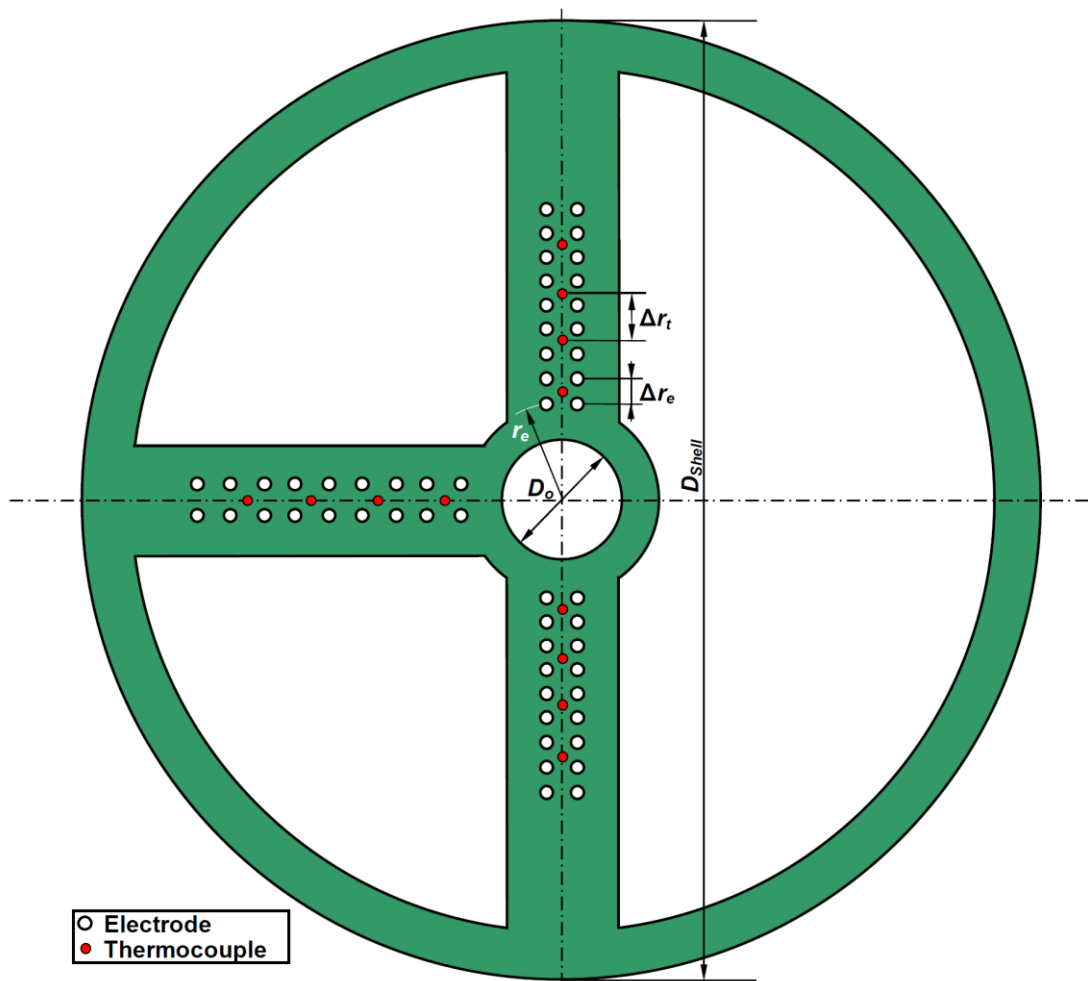
widely in industrial applications, it does not provide data referring to a specific point because of the sensor geometry.

One inverse approach, for estimating conductivity of medium to define its current state is to measure the dielectric effect of probes, which are basically have the same setup with amperimetric measurement (Daily & Ramirez, 2004). The term dielectric is used when considering the effect of alternating electric fields on the substance. When the conductivity of the medium reduces, dielectric effect of the probes becomes dominant, and the capacitance value of the system increases. Hence, the phase of the output signal shifts.

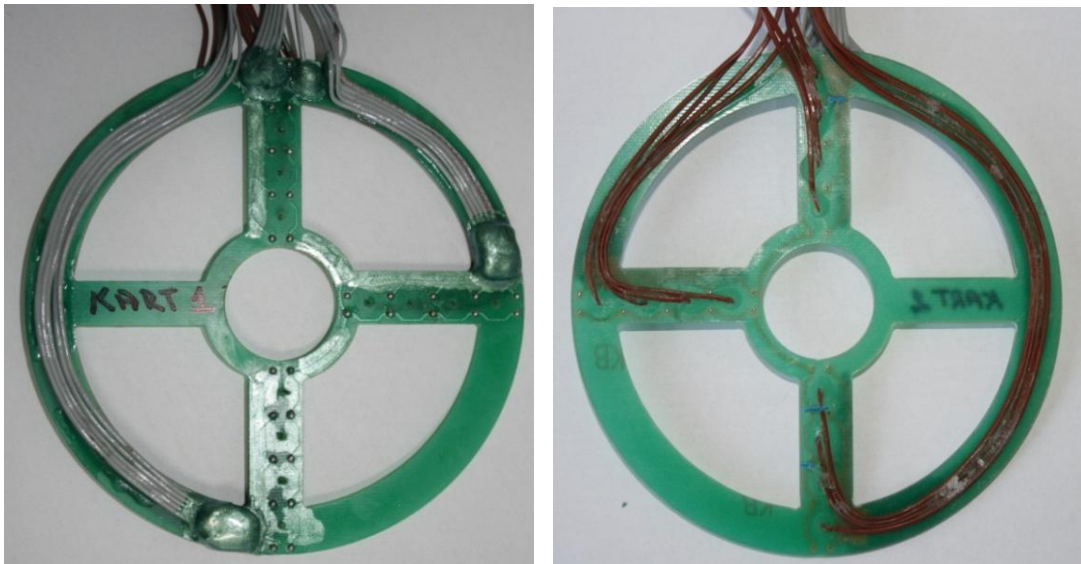
2.1.2.2 Experimental Apparatus and Preliminary Tests

The probe dimensions and the positions of the electrodes on the board are illustrated in Figure 2.6. Electrodes on the printed board are designed as small circular pads with the diameter of 1 mm. Generally, in ampreimetric measurement setups, the electrodes protrude inside the medium and this causes capacitive effects on the system. Because, the conductivity decreases and they become capacitors rather than resistors (Shi et al. 2005). These quasi-2D electrodes have no parallel plate arrangement in measurement setup and the capacitive effect on measurement is omitted.

The distance between the pair of electrodes is 2.54 mm (0.1 inch) and 10 mm, in axial and radial directions, respectively. Therefore, the measurement uncertainty occurring from geometry is ± 0.38 mm. As is intended to measure the time wise interface variations, it is necessary to use several nodes of measurement. The distances between the pair of electrodes on radial direction and the total number of electrodes on measurement cards differ with the shell diameter. Depending on the shell diameter, there are 5 to 9 measuring nodes on three radial directions at $\theta = 90^\circ$, 0° and -90° , and hence, totally 15 to 27 electrodes exist on each card. Furthermore, there are also four thermocouples mounted on each direction of the probe and 36 thermocouples are used to establish the temperature distribution of PCM. Figure 2.6(a)



(a) Technical drawing



(b) Photography

Figure 2.6 Layout of the electrodes and thermocouples on the measurement cards.

shows the technical drawing of a measurement card for a shell diameter of 190 mm, and the corresponding geometrical parameters of the cards are given in Table 2.2 for two different shell diameters. Besides, in Figure 2.6(b) illustrative pictures are given for front and back views of the measurement card.

PIC 16f877 micro controller is used as a main processor unit. It has three peripheral circuits: *measurement circuit*, *serial communication circuit*, and *multiplexers*. Measurement circuit has a pre-resistance (R_p) of 1 K Ω to limit the current in the above-mentioned probe design. Multiplexers are used to direct input output node connections to analog to digital (A/D) converter pin and digital output pin. Communication circuit is an IC to convert levels of voltages of microcontroller and computer (Figure 2.7).

Table 2.2 Geometrical parameters of the measurement cards.

Parameter	$D_{shell} = 114 \text{ mm}$	$D_{shell} = 190 \text{ mm}$
r_e	15 mm	20 mm
Δr_e	10 mm	5 mm
Δr_t	10 mm	
n_e	45 nodes	81 nodes
n_t	12 thermocouples	

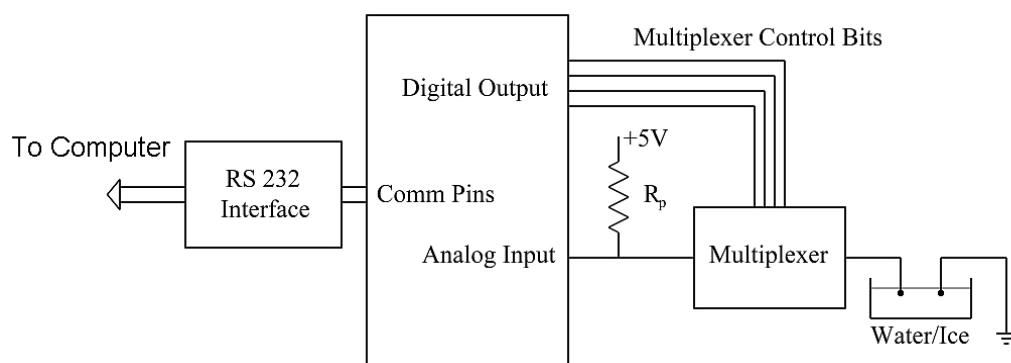


Figure 2.7 Measurement circuit for conductivity.

Micro controller operates in timer driven routines at a specific operation period of which a digital output port becomes active for 20 ms. This evokes an A/D measurement, and the program records the read values to a summing register. A/D measurement is repeated 50 times. The sum of all the values is then transferred to a

computer to create a log (Figure 2.8). The described measurement loop is repeated for all 45/81 measurement nodes. Scanning method for measurement is as follows: First, the nodes on the same radial level closest to the pipe are scanned. Afterwards, this scan continues to distant nodes. Microcontroller uses timer interrupts for providing consistency in sampling time, and controls multiplexers to enlarge input–output ports.

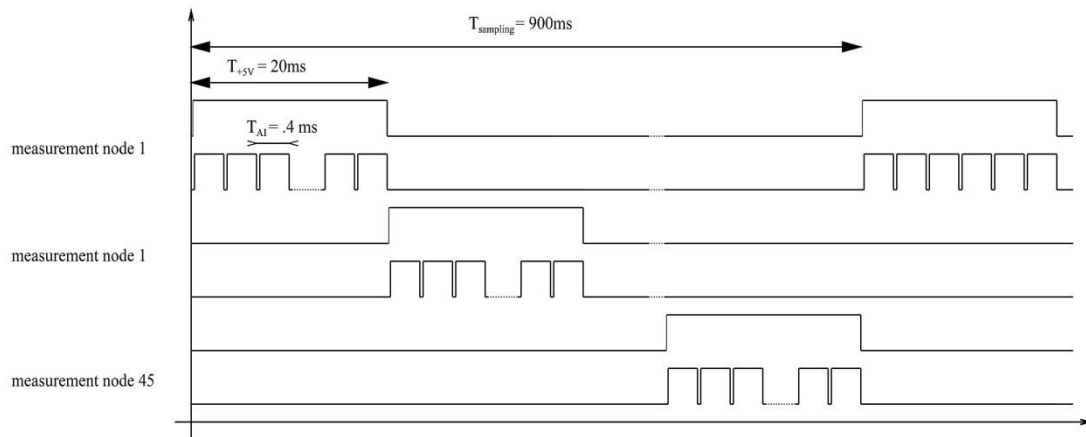


Figure 2.8 Timing diagram.

Since there exist 45/81 measurement points, it is not possible to measure all points at the same time with using only one microprocessor. Data measurements are performed synchronously to construct instantaneous ice formation (Figure 2.8). Concerning slow time response of ice formation system, which has a time constant of a few seconds, microprocessor based measurement system with a time constant in milliseconds satisfies Nyquist frequency criterion for constructing real signal from sampled values (Proakis & Manolakis, 1996).

The electrolysis on measurement nodes is an important issue of concern for planning sampling times, because ion deposition on the electrodes due to electrolysis can vary the resistance and can also cause corrosion which leads to defected probes. Therefore, the measurement system is designed to avoid electrolysis effects; it applies input voltage only during the measurement period (Figure 2.8).

Before installation of the experimental apparatus, the characteristic of electrical signal variations with time or temperature was determined experimentally. First, signal variation of a single measurement node is observed as a function of temperature. A prototype measurement card is prepared with one pair of the electrode and two thermocouples. Prototype is located inside a water-filled pot, and then pot is cooled down inside a cooling bath. During solidification, temperature and voltage values are logged in a computer. As a result, the variation of voltage is obtained as a function of temperature as seen in Figure 2.9. This results match with the resistivity variation as given in Figures 2.5. While temperature value of the measurement node decreases, the monitored voltage (*proportional to resistance between electrodes*) also decreases.

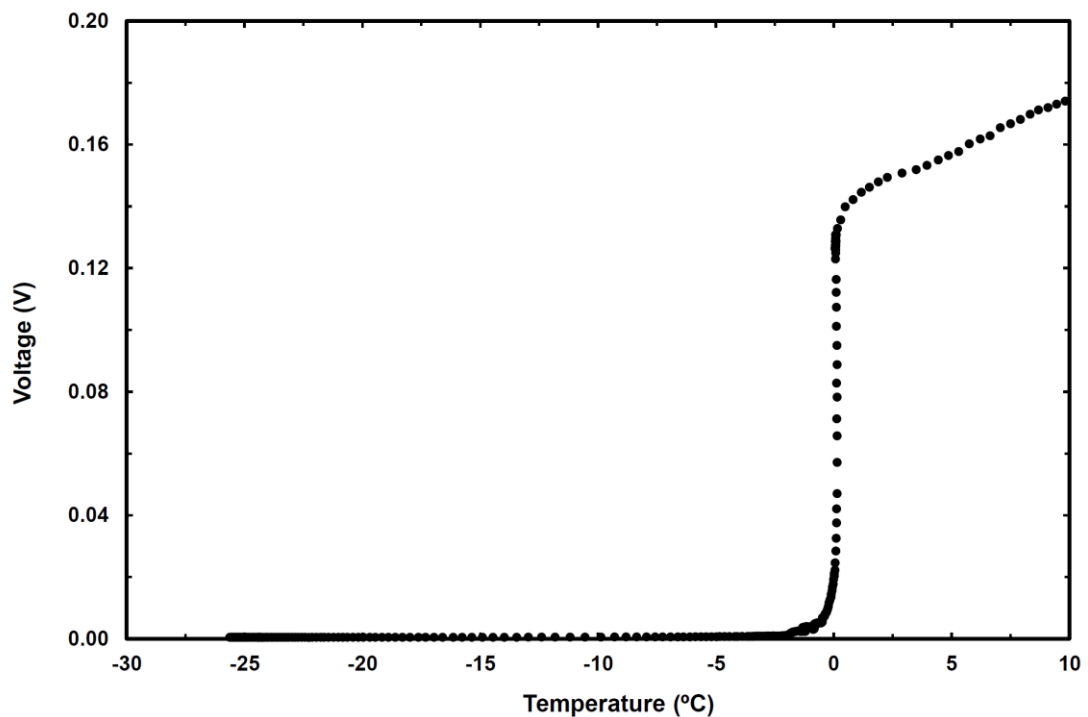


Figure 2.9 Variation of the voltage with the temperature for a single measurement node.

Then, time wise variations of the electrical resistance values are monitored for one direction ($\theta = 90^\circ$) of a measurement card. Card is located on the tube inside the heat exchanger section. The time wise variations of resistance values for the nine measurement nodes are monitored during outward solidification around the tube. As

seen in Figure 2.10, resistance values change dramatically, when ice is formed at the measurement node, while the circuit becomes electrically open.

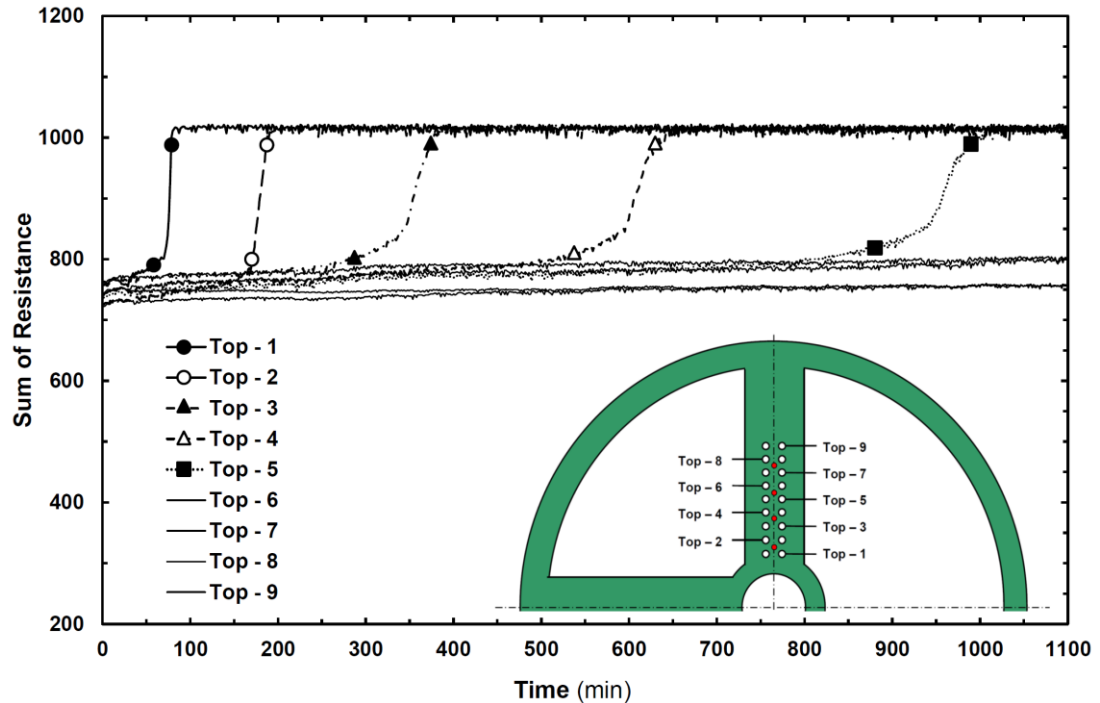


Figure 2.10 Time wise variations of the electrical resistance values.

As a conclusion, these results verify that the implemented measurement system can act as an indicator to provide discrete data, while the current phase of the measurement point is ice or water. Transition times of the curves designate the beginning of phase change. These transition points can be obtained with applying the first derivative for each curve.

2.1.3 Analyses of Experimental Data

The performance of LHTES systems can be evaluated through two approaches; with applying energy conservation principle (*first law of thermodynamics*) or exergy principle (*second law of thermodynamics*). In this section, methodologies for energy and exergy analyses are addressed in the following subsections.

2.1.3.1 Energy Analysis

Generally, computations of sensible and latent energies in a LHTES system are performed in terms of the average temperature values with the mean solid and liquid volumes of PCM. In this study, the sensible and latent stored/rejected energy values are calculated with using a control volume approach for PCM section of the heat exchanger. As there are three measurement cards at three different sections of the tank, the solid–liquid interface and temperature distributions can be calculated for radial and axial directions, as functions of time. The space including PCM is divided into control volumes in polar coordinates with intervals of $dr = 1$ mm and $d\theta = 2^\circ$ for more detailed experimental calculations as illustrated in Figure 2.11. The solid–liquid interface is obtained from the data of measurement cards. The temperature distributions inside the solid and liquid phases of the PCM are determined for each card section with the aid of sixteen thermocouples fixed on the card and the tube and shell surfaces. The thermocouples are symbolized with solid circles in Figure 2.11. Thermocouples are located at $r_{t0} = 12.5$ mm, $r_{t1} = 22.5$ mm, $r_{t2} = 32.5$ mm, $r_{t3} = 42.5$ mm, $r_{t4} = 52.5$ mm and $r_{t5} = 95$ mm positions for $D_{shell} = 190$ mm. On the other hand for $D_{shell} = 114$ mm, thermocouples are fixed at $r_{t0} = 12.5$ mm, $r_{t1} = 20$ mm, $r_{t2} = 30$ mm, $r_{t3} = 40$ mm, $r_{t4} = 50$ mm and $r_{t5} = 57$ mm positions.

The temperature distribution in a cylindrical domain can be determined with solving the following energy equation for a known velocity field,

$$\rho c_p \left(\frac{\partial T}{\partial t} + v_r \frac{\partial T}{\partial r} + \frac{v_\theta}{r} \frac{\partial T}{\partial \theta} \right) = \frac{1}{r} \frac{\partial}{\partial r} \left(kr \frac{\partial T}{\partial r} \right) + \frac{1}{r^2} \frac{\partial}{\partial \theta} \left(k \frac{\partial T}{\partial \theta} \right) \quad (2.3)$$

where left hand side of the equation represents the unsteady and advection terms, right hand side of the equation specifies conduction terms. In the current study, owing to the slow nature of phase change process and relatively small velocity components, energy equation can be simplified as quasi–steady–state heat conduction equation in cylindrical geometry. First, the temperature values at each node for all directions can be evaluated by using quasi–steady–state heat conduction equation, by considering the two discrete thermocouple values,

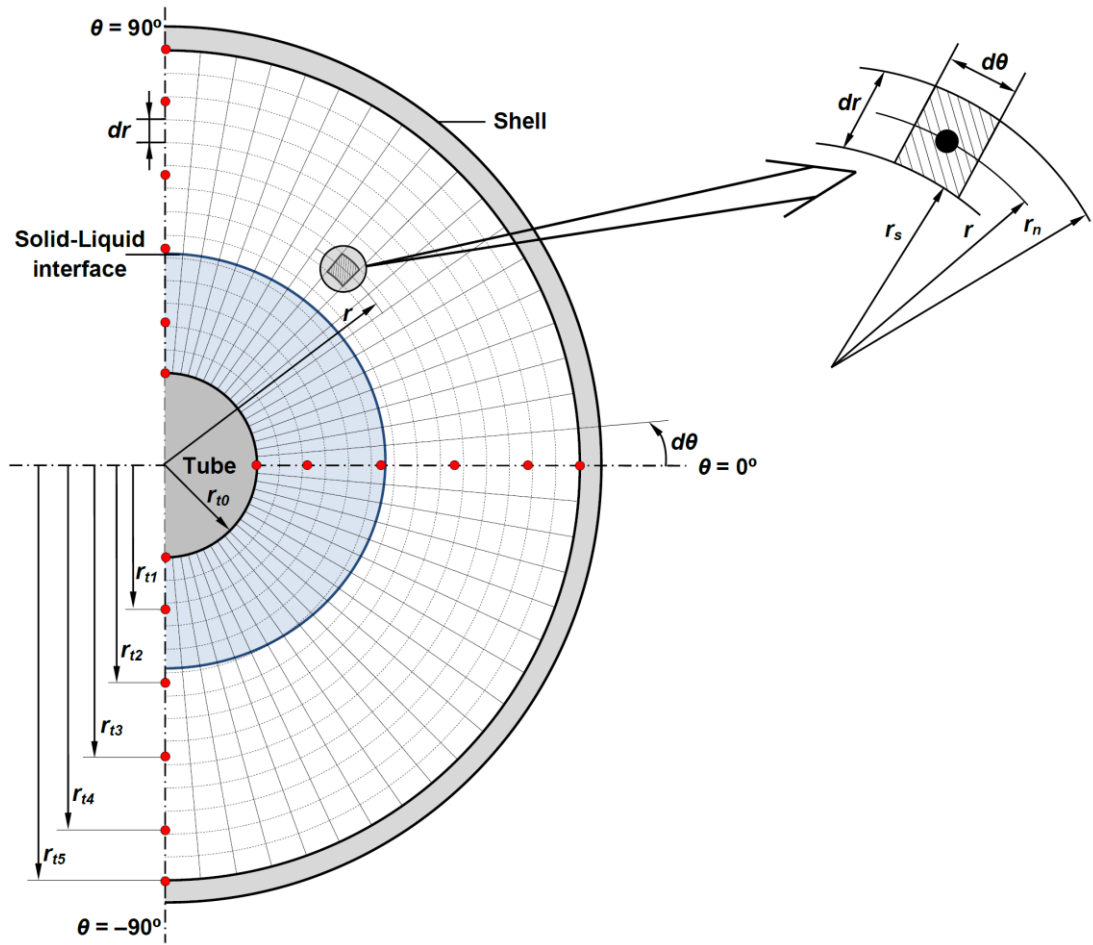


Figure 2.11 Computational domain.

$$T(r_{i \rightarrow t(i+1)}) = \frac{T_{r_i} - T_{r_{t(i+1)}}}{\ln(r_i / r_{t(i+1)})} \ln\left(\frac{r}{r_{t(i+1)}}\right) + T_{r_{t(i+1)}} \quad (i = 0, 1, 2, 3, 4) \quad (2.4)$$

afterwards, an angular interpolation can be applied to compute the temperature values for all interior nodes between $\theta = 90^\circ : 0^\circ$ or $\theta = -90^\circ : 0^\circ$.

Solid–liquid interface differs along the flow direction and, it is not symmetrical around the tube. Thus, the total energy of the system for an instant time can be defined as integration of the specific energies for each control volume over the domain, rather than taking average values,

$$E_{system}(t) = \iiint_V e(r, \theta, x, t) dV \quad (2.5)$$

where $e(r, \theta, x, t)$ is the specific energy of an arbitrary control volume for an instant time and has two components as follows:

$$e(r, \theta, x, t) = e_{sensible}(r, \theta, x, t) + e_{latent}(r, \theta, x, t) \quad (2.6)$$

The sensible and latent components can be defined for the solidification process as

$$e_{sensible}(r, \theta, x, t) = \begin{cases} C_{water} T(r, \theta, x, t) & (r > r_{ice}) \\ C_{ice} T(r, \theta, x, t) & (r < r_{ice}) \end{cases} \quad (2.7a)$$

$$e_{latent}(r, \theta, x, t) = \rho_{ice} f(r, \theta, x, t) h_{sf} \quad (2.7b)$$

where C is the heat capacity ($C = \rho c$), h_{sf} is the heat of fusion and $f(r, \theta, x, t)$ is the fraction of ice volume in each control volume. Finally, the total stored/rejected energy can be written in terms of internal energy variation of the system as

$$\Delta E_{system}(t) = E_{system}(t) - E_{system,i} \quad (2.8)$$

Energy efficiencies of the system for charging, storing, and discharging periods can be defined as follows:

$$\eta_{charging}(t) = \frac{\Delta E_{system}(t)}{E_{HTF}(t)} \quad (2.9)$$

$$\eta_{storing}(t) = \frac{\Delta E_{system}(t) + Q_{gain}}{E_{HTF}(t)} \quad (2.10)$$

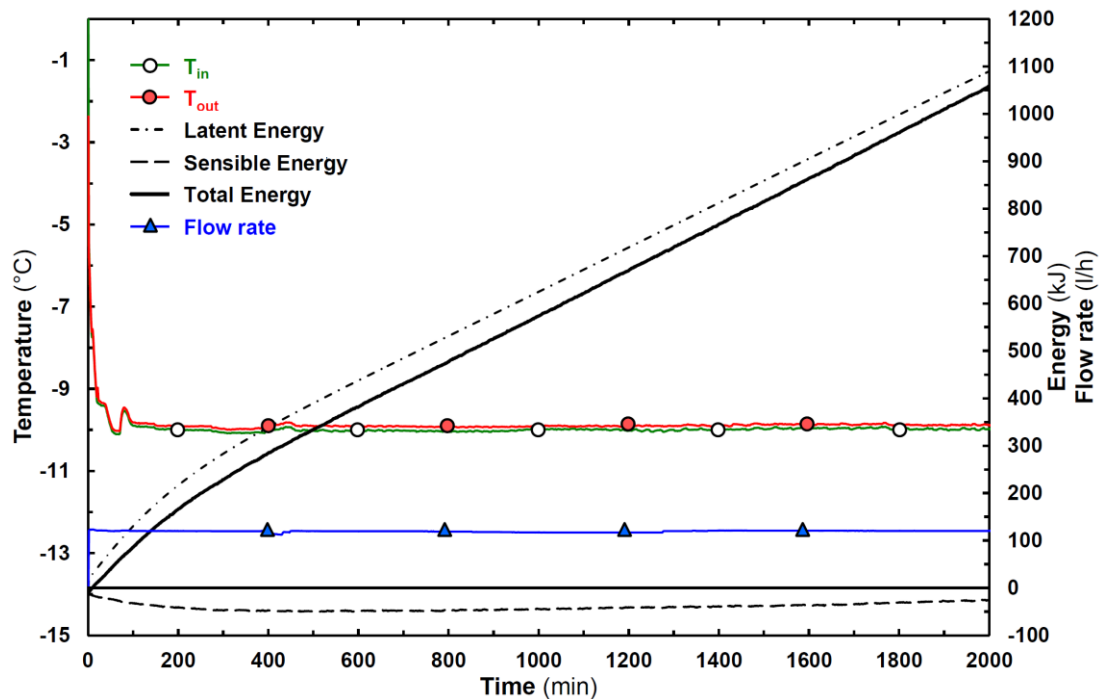
$$\eta_{discharging}(t) = \frac{E_{HTF}(t)}{\Delta E_{system}(t)} \quad (2.11)$$

where $\eta(t)$ symbolize total energy efficiency and $E_{HTF}(t)$ designates the total energy transferred to/from the system by the HTF. Total energy rejected/extracted from the HTF can be written in terms of enthalpy variation between the inlet and outlet of the heat exchanger or as the temperature difference to be;

$$E_{HTF}(t) = \int_{t=0}^t (\dot{m}c)_{HTF} [T_{in}(t) - T_{out}(t)] dt \quad (2.12)$$

where T_{in} , T_{out} and \dot{m} are the temperature values of the HTF at the inlet and outlet sections of the tank, and mass flow rate of the HTF, respectively.

Control volume approach is applied to all parametric experiments (*totally 46*). For this purpose, a numerical procedure is coded as a VBA (*Visual Basic Application*) subroutine inside MS Excel software. For each experiment, temperature and measurement card data are imported into Excel files to obtain time wise temperature and interface variations as well as total sensible and latent energies. As an instance, in Figure 2.12, time wise variations of total stored, sensible, and latent energies are given together with the inlet–outlet temperatures and volumetric flow rate variations.



($D_{shell} = 190 \text{ mm}$, $T_{in} = -10^\circ\text{C}$ and $\dot{V} = 2 \text{ l/min}$)

Figure 2.12 Temperature, flow rate and energy variations for a selected experiment.

2.1.3.2 Exergy Analysis

Unlike to the first law of thermodynamics, second law of thermodynamics quantifies the “*quality of energy*”. The quality of energy is measured from the state of the system in relation with its surroundings conditions (Jegadheeswaran, Pohekar & Kousksou, 2010). The quality or usefulness of energy is termed as “*availability*” or “*exergy*”. Exergy represents the measure of a system’s “*capacity to perform work*” (Kestin, 1980). Since second law of thermodynamics introduces exergy, the analysis

based on the second law is widely called “*exergy analysis*” (Jegadheeswaran et al., 2010). Unlike to energy, exergy cannot be conversed rather it destroyed. However, exergy can be conserved if the process takes place in a reversible manner. It is well known that all real processes are irreversible and irreversibilities related with the process are exposed exergy destruction. Hence, exergy balance of a system with heat gain can be expressed as follows:

$$\left\{ \begin{array}{c} \text{Exergy} \\ \text{Input} \end{array} \right\} - \left\{ \begin{array}{c} \text{Exergy} \\ \text{Output} \end{array} \right\} + \left\{ \begin{array}{c} \text{Exergy} \\ \text{Gain} \end{array} \right\} - \left\{ \begin{array}{c} \text{Exergy} \\ \text{Destruction} \end{array} \right\} = \left\{ \begin{array}{c} \text{Exergy} \\ \text{Change in System} \end{array} \right\}$$

or

$$\left(\dot{E}x_{in} - \dot{E}x_{out} \right)_{HTF} + \dot{E}x_{gain} - \dot{E}x_d = \left(\frac{dEx}{dt} \right)_{system} \quad (2.13)$$

where *in* and *out* subscripts designate the exergy values of the HTF at the inlet and outlet sections of the heat exchanger, respectively. On the other hand, subscripts “*gain*” and “*d*” represent the exergy input to the system via heat transfer and amount of exergy destruction in the system, respectively. Exergy destruction corresponds to the degree of irreversibilities and proportional to the entropy generation in the system. For the current study, we can consider a control volume as illustrated in Figure 2.13. Here, the heat transfer fluid enters to the system with a definite temperature and flow rate of T_{in} and \dot{m} , respectively. At the outlet section of the system, the temperature of the fluid is measured as T_{out} and the system has a constant heat gain from surroundings as \dot{Q}_{gain} . Rates of exergy at the inlet and outlet sections of heat transfer fluid can be expressed as

$$\dot{E}x_{HTF, in} = (h_{HTF, in} - h_o) - T_o (s_{HTF, in} - s_o) \quad (2.14a)$$

$$\dot{E}x_{HTF, out} = (h_{HTF, out} - h_o) - T_o (s_{HTF, out} - s_o) \quad (2.14b)$$

Hence, the net rate of exergy involved with HTF can be arranged as

$$\left(\dot{E}x_{in} - \dot{E}x_{out} \right)_{HTF} = \dot{m}_{HTF} \left[(h_{in} - h_{out})_{HTF} - T_o (s_{in} - s_{out})_{HTF} \right] \quad (2.15)$$

assuming that the specific volume and specific heat of the HTF remains constant from inlet to outlet of the system, entropy and enthalpy variations can be obtained with using following fundamental thermodynamic relations,

$$dh = c dT \rightarrow \int_{in}^{out} dh = c \int_{in}^{out} dT \rightarrow (h_{in} - h_{out})_{HTF} = c_{HTF} (T_{HTF,in} - T_{HTF,out}) \quad (2.16)$$

$$ds = \frac{dh}{T} \rightarrow \int_{in}^{out} ds = c \int_{in}^{out} \frac{dT}{T} \rightarrow (s_{in} - s_{out})_{HTF} = c_{HTF} \ln \left(\frac{T_{HTF,in}}{T_{HTF,out}} \right) \quad (2.17)$$

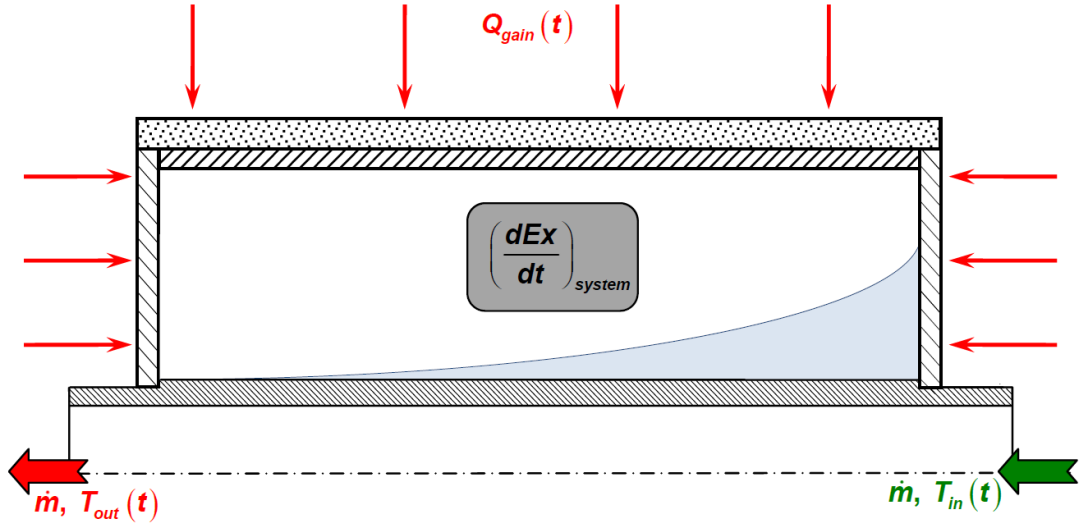


Figure 2.13 Control volume of the system.

Substituting the Eqs. (2.16) and (2.17) into Eq. (2.15) yields,

$$\left(\dot{E}x_{in} - \dot{E}x_{out} \right)_{HTF} = (\dot{m}c)_{HTF} \left[(T_{HTF,in} - T_{HTF,out}) - T_o \ln \left(\frac{T_{HTF,in}}{T_{HTF,out}} \right) \right] \quad (2.18)$$

Eq. (2.18) represents the rate of exergy variation in the HTF. Net exergy variation of the HTF can be defined by:

$$\Delta Ex_{HTF}(t) = \int_{t=0}^t \dot{m}(t) c_{HTF} \left\{ [T_{in}(t) - T_{out}(t)] - T_o(t) \ln \left(\frac{T_{in}(t)}{T_{out}(t)} \right) \right\} dt \quad (2.19)$$

On the other hand, exergy variation in the system can be defined as follows:

$$\left(\frac{dEx}{dt} \right)_{system} = \frac{Ex_{system}^n - Ex_{system}^{n-1}}{\Delta t} \quad (2.20)$$

exergy terms for the current time, n , and previous time, $n - 1$, can be defined in terms of the total enthalpy and entropy variations,

$$Ex_{system}^n = (H_{system}^n - H_o) - T_o (S_{system}^n - S_o) \quad (2.21a)$$

$$Ex_{system}^{n-1} = (H_{system}^{n-1} - H_o) - T_o (S_{system}^{n-1} - S_o) \quad (2.21b)$$

In the current study, the variation of internal energy in the system is related with sensible and latent cooling (*charging*) or heating (*discharging*). For charging process, water with an initial temperature of T_i , cools down via HTF. First superheated water cools down to the melting temperature, T_m , and then turns into ice. Enthalpy variation of this process can be illustrated as in Figure 2.14. Here, T_{final} designates the final temperature of sub-cooled ice.

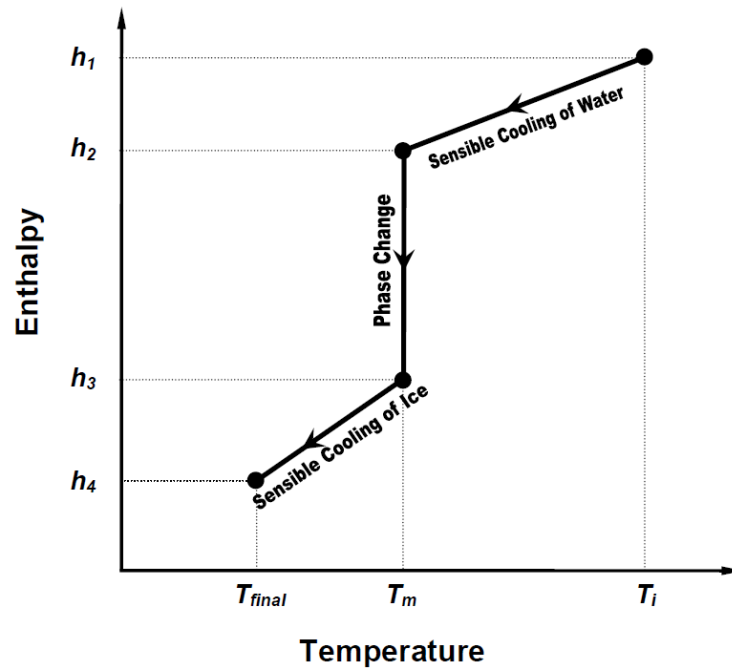


Figure 2.14 Enthalpy variation of water during phase change.

Substituting the Eqs. (2.21a) and (2.21b) into Eq. (2.20) yields,

$$\left(\frac{dEx}{dt}\right)_{system} = \left(\frac{\Delta Ex}{\Delta t}\right)_{system} = \left(\frac{H^n - H^{n-1}}{\Delta t}\right)_{system} - T_o \left(\frac{S^n - S^{n-1}}{\Delta t}\right)_{system} \quad (2.22)$$

For the process illustrated in Figure 2.14, enthalpy and entropy variations can be defined as

$$\left(\frac{H^n - H^{n-1}}{\Delta t}\right)_{system} = \frac{1}{\Delta t} \left\{ (mc)_{water} (T_m - T_i) - h_{sf} \Delta m_{ice} + (mc)_{ice} (T_{final} - T_m) \right\} \quad (2.23a)$$

$$\left(\frac{S^n - S^{n-1}}{\Delta t}\right)_{system} = \frac{1}{\Delta t} \left\{ (mc)_{water} \ln\left(\frac{T_m}{T_i}\right) - h_{sf} \frac{\Delta m_{ice}}{T_m} + (mc)_{ice} \ln\left(\frac{T_{final}}{T_m}\right) \right\} \quad (2.23b)$$

Hence, exergy variation in the system can be obtained as

$$\begin{aligned} \Delta Ex_{system} = & (mc)_{water} \left\{ (T_m - T_{in}) - T_o \ln\left(\frac{T_m}{T_i}\right) \right\} + \Delta m_{ice} h_{sf} \left\{ -1 + \frac{T_o}{T_m} \right\} \\ & + (mc)_{ice} \left\{ (T_{final} - T_m) - T_o \ln\left(\frac{T_{final}}{T_m}\right) \right\} \end{aligned} \quad (2.24)$$

where the first term on the right-hand side of the equation represents the exergy variation due to sensible cooling of water, second term designates the exergy variation resulting from the phase change and the last term corresponds the sub cooling of the ice. Here, mass amounts of ice and water assumed to be equal that the system goes into ice fully. If partial phase transformation occurs and the temperature of water drops down to a temperature higher than melting temperature point (T_{water}), following term should be added into Eq. (2.24),

$$\Delta Ex_{sensible, water} = (mc)_{water} \left\{ (T_{water} - T_i) - T_o \ln\left(\frac{T_{water}}{T_i}\right) \right\} \quad (2.25)$$

With combining the Eqs. (2.24) and (2.25), following equation can be obtained to define the net exergy variation of the system for charging period as

$$\begin{aligned} \Delta Ex_{system} = & m_{ice}(t) c_{ice} \left\{ (\bar{T}_{ice}(t) - T_m) - T_\infty(t) \ln \frac{\bar{T}_{ice}(t)}{T_m} \right\} \\ & + m_{water}(t) c_{water} \left\{ (\bar{T}_{water}(t) - \bar{T}_{water,i}) - T_\infty(t) \ln \frac{\bar{T}_{water}(t)}{\bar{T}_{water,i}} \right\} \\ & + m_{ice}(t) c_{water} \left\{ (T_m - \bar{T}_{water,i}) - T_\infty(t) \ln \frac{T_m}{\bar{T}_{water,i}} \right\} \\ & + m_{ice}(t) \left\{ -h_{sf} + T_\infty(t) \frac{h_{sf}}{T_m} \right\} \end{aligned} \quad (2.26)$$

where the first two terms signify the exergy variations inside the solid and liquid phases of water due to sensible cooling. The third term represents the exergy change arises from the cooling of superheated water that transformed into ice. Last term indicates the exergy variation arise from phase change. On the other hand, the net exergy variation of the system for discharging period can be written as follows:

$$\begin{aligned}
\Delta Ex_{system} = & m_{ice}(t) c_{ice} \left\{ \left[\bar{T}_{ice}(t) - \bar{T}_{ice,i} \right] - T_{\infty}(t) \ln \frac{\bar{T}_{ice}(t)}{\bar{T}_{ice,i}} \right\} \\
& + m_{water}(t) c_{water} \left\{ \left[\bar{T}_{water}(t) - T_m \right] - T_{\infty}(t) \ln \frac{\bar{T}_{water}(t)}{T_m} \right\} \\
& + m_{water}(t) c_{ice} \left\{ \left[T_m - \bar{T}_{ice,i} \right] - T_{\infty}(t) \ln \frac{T_m}{\bar{T}_{ice,i}} \right\} \\
& + m_{water}(t) \left\{ h_{sf} + T_{\infty}(t) \frac{h_{sf}}{T_m} \right\}
\end{aligned} \tag{2.27}$$

where the first two terms signify the exergy variation inside the solid and liquid phases of water due to sensible heating. The third term represents the exergy change arises from the heating of sub cooled ice that transformed into water. Last term indicates the exergy variation arise from phase change.

On the other hand, exergy associated with heat gain can be defined as follows:

$$\dot{Ex}_{gain} = \dot{Q}_{gain} \left(1 - \frac{T_o}{T_m} \right) \tag{2.28}$$

Exergy destruction is related with the entropy generation during the process. In all real processes while entropy is always generated, exergy is destroyed. Relationship between the entropy generation and exergy destruction (or *irreversibility*) is defined by Gousy–Stodala theorem (Bejan, 1995), and expressed in following mathematical form,

$$\dot{Ex}_d = T_o \dot{S}_{gen} \tag{2.29}$$

Exergy efficiency of the charging process is defined as the fraction of the net exergy variation in the system to the exergy variation of the HTF to be;

$$\psi_{\text{charging}}(t) = \frac{\Delta E_{x_{\text{system}}}(t)}{\Delta E_{x_{\text{HTF}}}(t)} \quad (2.30)$$

Besides, for discharging period, exergy efficiency is defined as the inverse of the charging period as follows:

$$\psi_{\text{discharging}}(t) = \frac{\Delta E_{x_{\text{HTF}}}(t)}{\Delta E_{x_{\text{system}}}(t)} \quad (2.31)$$

2.1.3.3 Uncertainty Analysis

Experimental studies, naturally, cause some uncertainties and unpredictable errors. Such diversions may arise due to human nature reading errors, instrumental manufacturing errors, environmental condition effects or calibration errors and none of which can be taken into account for evaluating the experimental results. Recently many studies were performed about the uncertainty theory, to investigate the accuracy of the estimations for experiments, experimental setup and instruments (Holman 2001, Hepbasli & Akdemir, 2004).

In this study, uncertainties are calculated with using the methodology given in Holman (2001). Suppose a set of measurements are performed to determine some desired results of the experiments. Overall uncertainty of the calculated results will be basis on the uncertainties in the primary measurements. The result R is a given function of the independent variables $x_1, x_2, x_3 \dots x_n$. Thus,

$$R = R(x_1, x_2, x_3 \dots x_n) \quad (2.32)$$

Let w_r be the uncertainty in the result and $x_1, x_2, x_3 \dots x_n$ be the uncertainties of the independent variables. Hence, the overall uncertainty in the result can be obtained as

$$w_R = \left[\left(\frac{\partial R}{\partial x_1} w_1 \right)^2 + \left(\frac{\partial R}{\partial x_2} w_2 \right)^2 + \dots + \left(\frac{\partial R}{\partial x_n} w_n \right)^2 \right]^{1/2} \quad (2.33)$$

For an instant time, total energy stored in the system can be written in terms of the mean values of temperature and radius of ice,

$$\begin{aligned} \Delta E_{system} = & \pi \left(r_{ice}^2(t) - r_{tube}^2 \right) \rho_{ice} \ell \left[c_{water} \Delta \bar{T}_{ice}(t) - h_{sf} \right] \\ & + \pi \left(r_{shell}^2(t) - r_{ice}^2 \right) \rho_{water} \ell \left[c_{water} \Delta \bar{T}_{water}(t) \right] \end{aligned} \quad (2.34)$$

In this study, following uncertainties affect computations of the total energy stored/rejected in shell-and-tube type LHTES system,

uncertainties arise from,

- the geometry of the heat exchanger ($r_{tube}, r_{shell}, \ell$),
- temperature and ice radius measurement sensors ($\Delta \bar{T}_{water}, \Delta \bar{T}_{ice}, r_{ice}$),
- selection of the thermo-physical properties of PCM ($\rho_{ice}, \rho_{water}, c_{ice}, c_{water}, h_{sf}$)

Total energy stored can be written as a function of these independent variables as

$$E = E(t, r_{ice}, r_{tube}, r_{shell}, \ell, \rho_{ice}, \rho_{water}, c_{ice}, c_{water}, \Delta \bar{T}_{water}, \Delta \bar{T}_{ice}, h_{sf}) \quad (2.35)$$

Measuring ranges and uncertainties of individual parameters are given in Table 2.3. To determine the overall uncertainty that affects the computation of the total energy stored, Eq. (2.35) can be written in partial derivatives in terms of individual uncertainties,

$$w_E = \left[\begin{aligned} & \left(\frac{\partial E}{\partial r_{ice}} w_{r_{ice}} \right)^2 + \left(\frac{\partial E}{\partial r_{tube}} w_{r_{tube}} \right)^2 + \left(\frac{\partial E}{\partial r_{shell}} w_{r_{shell}} \right)^2 + \left(\frac{\partial E}{\partial \ell} w_{\ell} \right)^2 \\ & + \left(\frac{\partial E}{\partial c_{water}} w_{c_{water}} \right)^2 + \left(\frac{\partial E}{\partial c_{ice}} w_{c_{ice}} \right)^2 + \left(\frac{\partial E}{\partial \rho_{water}} w_{\rho_{water}} \right)^2 \\ & + \left(\frac{\partial E}{\partial \rho_{ice}} w_{\rho_{ice}} \right)^2 + \left(\frac{\partial E}{\partial h_{sf}} w_{h_{sf}} \right)^2 + \left(\frac{\partial E}{\partial \Delta \bar{T}_{water}} w_{\Delta \bar{T}_{water}} \right)^2 \\ & + \left(\frac{\partial E}{\partial \Delta \bar{T}_{ice}} w_{\Delta \bar{T}_{ice}} \right)^2 \end{aligned} \right]^{1/2} \quad (2.36)$$

As a result, overall uncertainty for computing the total energy stored can be obtained as $\pm 3.0\%$.

Table 2.3 Uncertainties of parameters for the shell-and-tube type LHTES system.

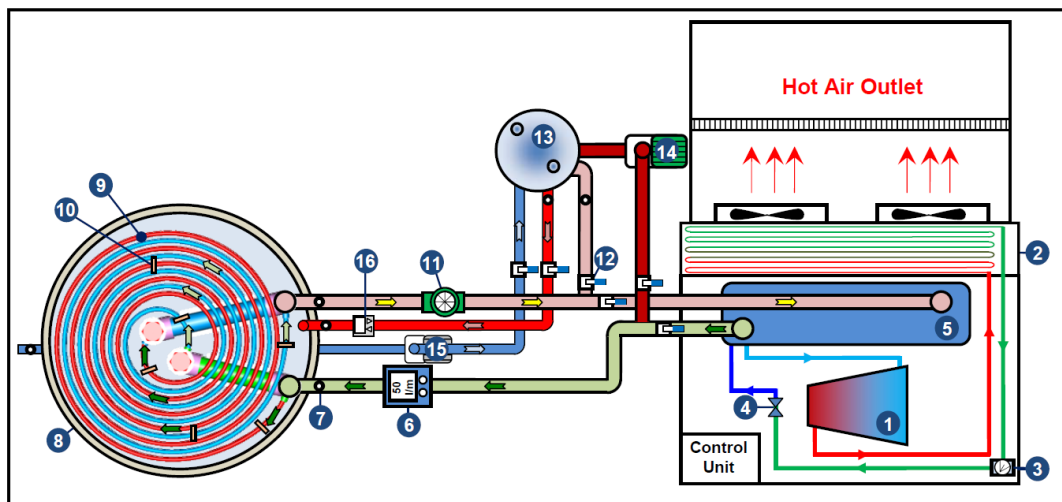
Parameter	Value	Uncertainty	Comment
Radius of ice, r_{ice}	12.5 mm – 50 mm	± 0.38 mm	Uncertainty arise from electronic measurement method
Radius of tube, r_{tube}	12.5 mm		
Radius of shell, r_{shell}	57 mm or 95 mm	$\pm 1\%$	Uncertainty arise from geometry of heat exchanger
Length of tube, l	400 mm		
Density of ice, ρ_{ice}	920 kg/m ³	<i>neglected</i>	
Density of water, ρ_{water}	1000 kg/m ³	$\pm 0.02\%$	
Specific heat of water, c_{water}	4218 J/kgK	$\pm 0.3\%$	Uncertainty arise from the selection of thermo-physical properties of the PCM
Specific heat of ice, c_{ice}	2040 J/kgK	$\pm 0.3\%$	
Heat of fusion, h_{sf}	333400 J/kg	<i>neglected</i>	
Temperature differences, $\Delta\bar{T}_{ice}, \Delta\bar{T}_{water}$	$-2.5^{\circ}\text{C} \leftrightarrow +2.5^{\circ}\text{C}$	$\pm 0.5^{\circ}\text{C}$	Uncertainty arise from the thermocouple measurements

2.2. Ice-on-coil Type LHTES System

After completing the investigations about the shell-and-tube type LHTES system, phase change process is studied in large scaled LHTES system. An ice-on-coil LHTES system is designed and constructed at Dokuz Eylül University Thermal Science Laboratory.

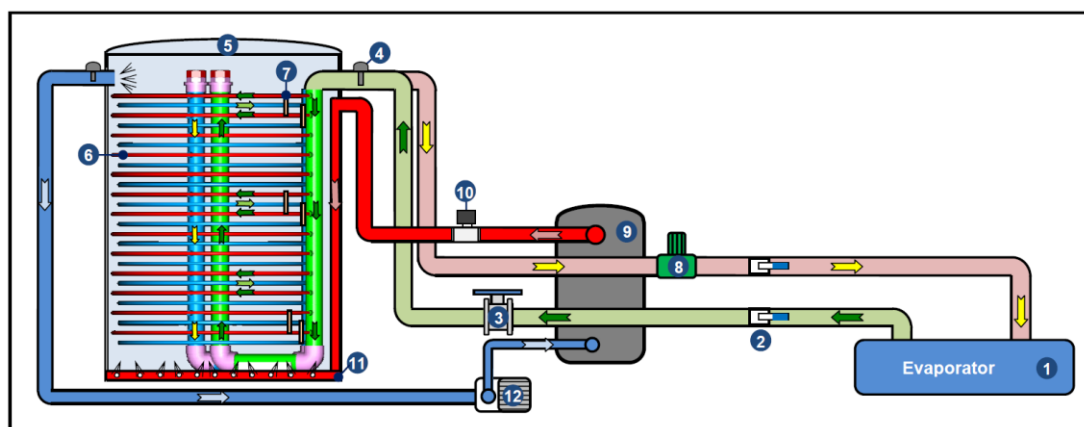
2.2.1 Components of Experimental System

The schematic diagram of the experimental setup is illustrated in Figure 2.15 for top and front views. Besides pictures of the current experimental system is given in Figure 2.16. System mainly consists of a chiller, a storage tank and a heating bath. In following subsections, detailed information about the design and working parameters of each component is represented.



(1) Compressor, (2) Condenser, (3) Flow meter (*R404A*), (4) Expansion valve, (5) Evaporator, (6) Flow meter (*Brine*), (7) Pt-100, (8) Storage Tank, (9) Coil, (10) Measurement Cards, (11) Pump, (12) Valves, (13) Heating Tank, (14) Pump (*Brine*), (15) Pump (*Water*), (16) Flow meter (*Water*)

(a) Top view



(1) Evaporator, (2) Valves, (3) Flow meter (*Brine*), (4) Pt-100, (5) Storage tank, (6) Coil, (7) Measurement Card, (8) Pump (*Brine*), (9) Heating tank, (10) Flow meter (*Water*), (11) Diffuser (*Water*), (12) Pump (*Water*)

(b) Front view

Figure 2.15 Schematic representation of ice-on-coil LHTES system.



(a) Storage tank and measurement systems

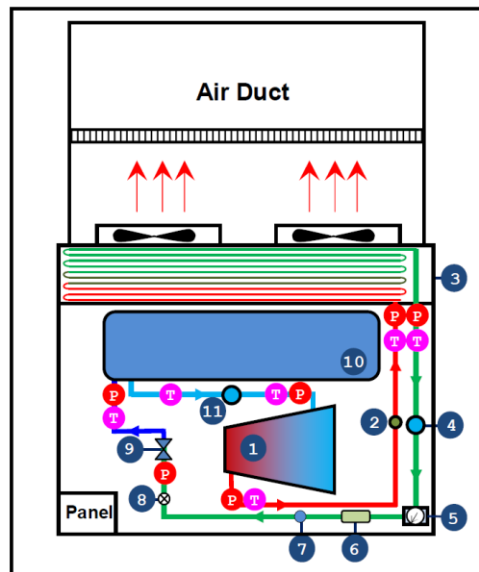


(b) Chiller and components

Figure 2.16 Photography of ice-on-coil LHTES system.

2.2.1.1 Chiller

Chiller has vapour compression refrigeration cycle and working with the refrigerant R404A. The components of the refrigeration system and the positions of the measurement sensors on the cycle are illustrated in Figure 2.17.



(1) Compressor, (2) Oil separator, (3) Condenser, (4) Liquid tank, (5) Flow meter (R404A), (6) Dryer, (7) Sight glass, (8) Solenoid valve, (9) Electronic expansion valve, (10) Evaporator, (11) Accumulator

Figure 2.17 Components of the chiller.

System consists of a semi-hermetic reciprocating compressor, a shell-and-tube type evaporator, and an air-cooled condenser. HTF is cooled down at the evaporator side of the chiller. Depending on the control schemes, compressor is driven either variable speed or on/off. In variable speed control scheme, the speed of the compressor is varied in a range of 20 to 80 Hz; besides, in on/off control scheme the speed of the compressor is fixed at 50 Hz. Chiller has also filter drier, solenoid valve, accumulator, liquid tank and oil separator as auxiliary equipment. An electronic expansion valve (EEV) is used in the system to increase the cycle efficiency and to ease controlling the set value of the HTF at the inlet section of the tank.

In Figure 2.17, positions of temperature and pressure sensors are designated with “T” and “P” letters, respectively. Totally six Pt-100 probes and six ratio-metric type

pressure transducers are settled on the refrigeration cycle to monitor the time wise variations of temperature and pressure data. Pt-100 probes are located at the inlet and outlet sections of the compressor, evaporator, and condenser. Besides, pressure transducers are settled at the inlet and outlet sections of the compressor, condenser, and expansion valve. Temperature and pressure data is collected in five seconds interval with the aid of HIOKI (*Nagano, Japan*) data acquisition unit. In addition, power consumption of the compressor and flow rate of R404A are measured with using MOD-BUS algorithm and these data are collected in computer in one-minute interval. Specifications for the components of the chiller are given in Table 2.4.

2.2.1.2 Storage Tank

The storage tank has an immersed coil inside the PCM. In system, water is used as PCM inside the storage tank, and ethylene glycol–water solution (*40% ethylene glycol by volume*) is circulated in the coil as the heat transfer fluid (HTF).

The design parameters of the storage tank are determined with considering a space that needs an average cooling load of 6 kW for ten hours (9⁰⁰ to 19⁰⁰). With considering a full storage strategy, total amount of cooling load should be stored in off pick hours. Considering the particular case of Turkey, low electric tariff period is eight hours. Hence, storage tank is designed for eight hours charging period.

According to these parameters, the total volume of the tank can be obtained as in the following procedure. First, the total amount of stored energy can be calculated with considering the specified cooling load of the space as follows:

$$\Delta E_{system}(t) = \dot{Q}\Delta t \quad (2.37)$$

where $\Delta E_{system}(t)$ designates the internal energy variation of the system and Δt is the total charging time of system. As is known, in LHTES systems, internal energy variation of the system primarily depending on the amount of phase-changed

Table 2.4 Specifications for the equipment of chiller.

Compressor	Type : Semi-hermetic reciprocating (R404A refrigerant) Capacity : 10kW, 380 V, 20–80 Hz
Condenser	Type : Air cooled
Evaporator	Type : Shell-and-tube liquid
Expansion valve	Type : Electronic Port size : 1.8 mm Operating range : 0–480 pulse Rated voltage : DC 12 V Output signal : 4–20 mA
Pressure Transducer	Type : Carel SPKT, Ratio-metric Range : Low pressure: –1 and 9 bar absolute High pressure: 0 and 45 bar absolute Output signal : 4–20 mA Accuracy : ±1.2% of full scale
Pt-100	Type : Stainless steel sensor, 24V DC supply Range : –15 and 50°C Output signal : 4–20 mA Accuracy : ±0.15% of full scale
Wattmeter	Type : EPM-07S (10–300V AC 45–65 Hz) Range : 220/600 V , 50/60 Hz Output signal : 4–20 mA Accuracy : ±0.5% of full scale
Inverter	Type : PWM Capacity : 10 kW Frequency Range : 0–100 Hz Output signal : 4–20 mA Accuracy : ± 1 % of full scale
R404A flow meter	Type : Krohne H250 Range : 0 – 15 l/min Output signal : 4–20 mA Accuracy : ±1.6% of full scale

material rather than temperature difference of PCM. Hence, the required amount of water can be obtained in terms of total stored energy and latent heat of water as follows:

$$m_{PCM} = \frac{\Delta E_{system}(t)}{h_{sf}} \quad (2.38)$$

where m_{PCM} is the total amount of phase-changed PCM. Based on the above-mentioned conditions, m_{PCM} is obtained as ~650 kg. With considering the volumes of pipes and supporting elements, the useful volume of the tank is assumed as 75–80%

of overall volume of the tank. Hence, the volume of the storage tank is designed as to be more than 1 m^3 . Design process of the tank is carried out with using commercial three-dimensional designing software, I-DEAS.

A cylindrical storage tank is designed with the height and diameter of $h_{\text{tank}} = 1.6 \text{ m}$ and $D_{\text{tank}} = 1 \text{ m}$, respectively. Polyethylene tubes with inner and outer diameters of $D_i = 12 \text{ mm}$ and $D_o = 16 \text{ mm}$ are used in the coil. Depending on the parametric results of shell-and-tube type LHTES system, the radius of ice reaches nearly 30 – 35 mm at the end of eight hours. Hence, the horizontal difference between the tubes is set as 60 mm in coil. Archimedes spiral form is applied to obtain a coil with a constant pitch in the radial direction. In Archimedes spiral form, the relationship between the radius of curvature (r) and the rotation angle (θ) is defined as

$$r(\theta) = a + b\theta \quad (2.39)$$

where a indicates the center point and b is used to determine the difference between the spirals. In Figure 2.18, the Archimedes spiral with a radial pitch of 60 mm is illustrated. Here, a and b parameters are set as 0 and 9.5496, respectively.

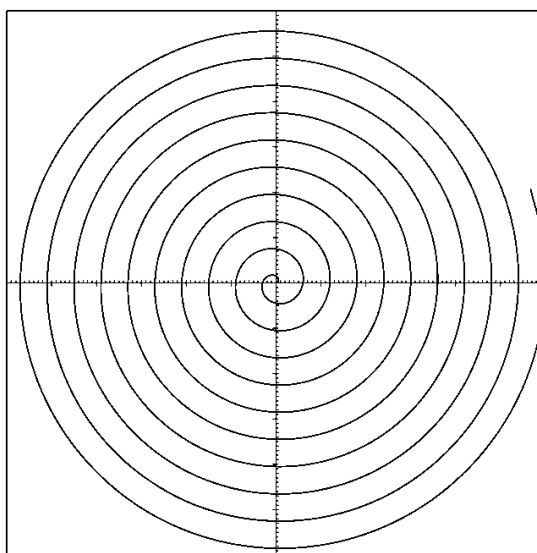


Figure 2.18 Archimedes spiral form.

The coil is designed as staggered pipe arrangement with counter flow to achieve a homogenous solidification/melting process. Figure 2.19 compares aligned and staggered pipe arrangements. As seen in this Figure, the volume of the tank can be

used more efficiently for phase change process with using staggered pipe arrangement instead of using aligned pipe arrangement. For this reason, staggered pipe arrangement is preferred for the current system. In Figure 2.20, staggered pipe arrangement of the coil is given. Here, the vertical and horizontal pitches should be differing to obtain a constant radius of ice around tubes. For the current system vertical and horizontal pitches are defined as $\Delta h = 45$ mm and $\Delta r = 60$ mm, respectively.

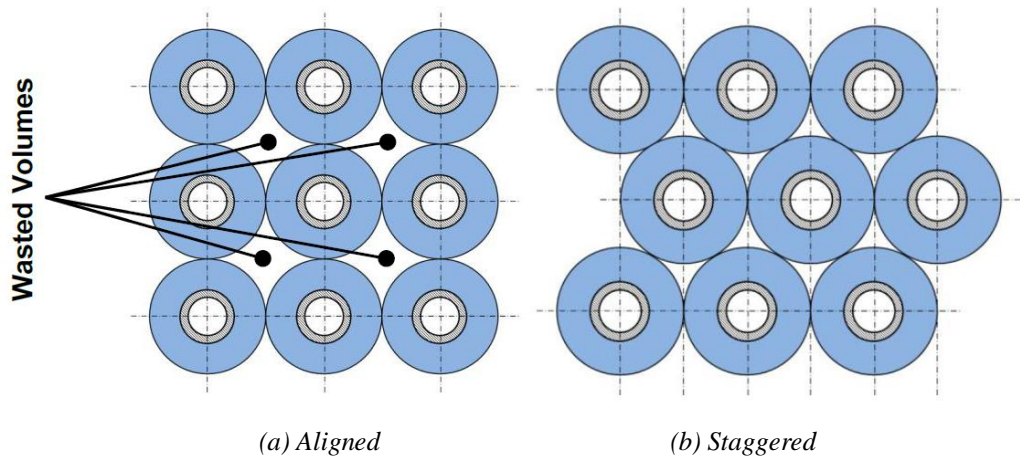


Figure 2.19 Aligned and staggered pipe arrangements.

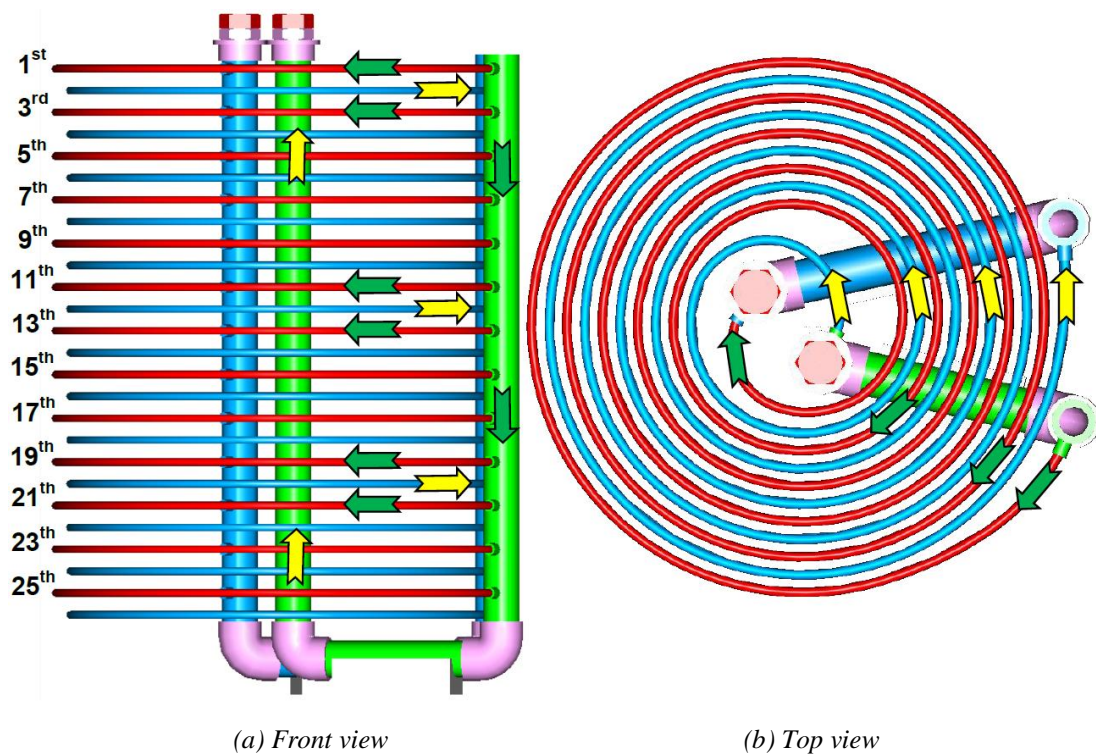


Figure 2.20 Staggered and counter-flow pipe arrangements.

In both solidification and melting mode, interface varies along the flow direction due to the varying wall temperatures. In Figure 2.21, the variations of ice radius along the flow direction are illustrated for parallel and counter flow cases. In comparison to the counter-flow, there are wasted spaces at the outlet sections of the tubes in parallel flow. Thus, in the current system, coil is designed as counter-flow to reduce the wasted spaces and use the tank volume more efficiently.

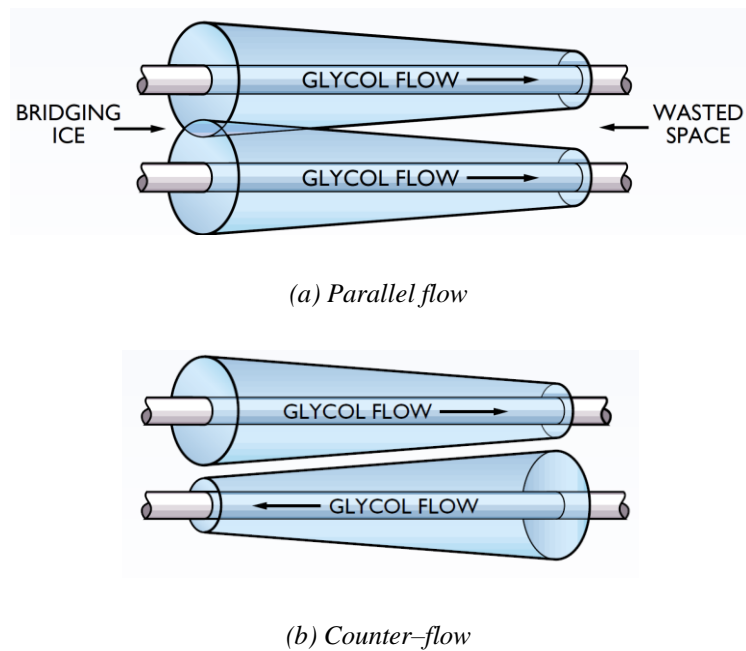
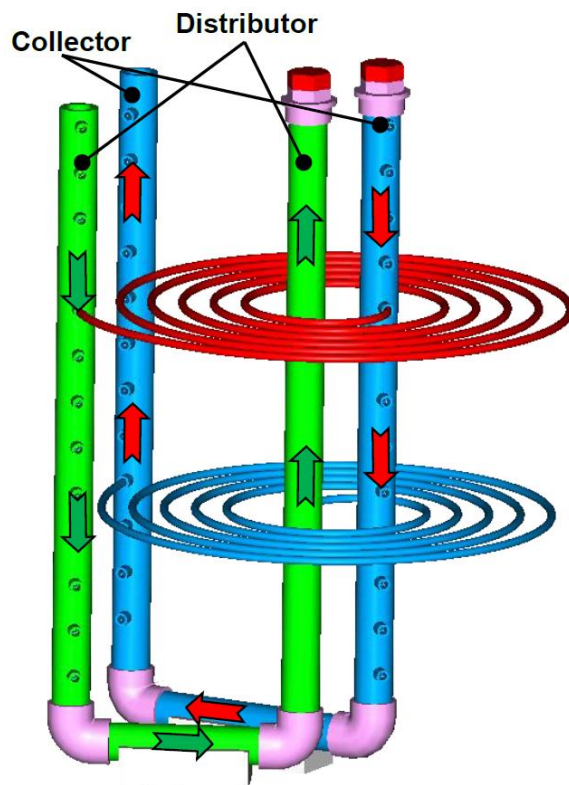


Figure 2.21 Counter-flow pipe arrangements.

For the current system, the principles of the counter flow are illustrated in Figures 2.20 and 2.22. In red colored pipes, heat transfer fluid flows from the outer side of the tank to the inside, besides, in the blue colored pipes, flow direction is from inside to the outer side of the tank. Bundle consists of totally 26 vertically arranged spirals. From top to bottom, flow direction is from outside to inside direction for the odd numbered pipes. In contrast, for the remaining pipes flow direction is from inside to outside direction of the tank. To achieve the proper distribution and collection of the HTF, collector and distributor pipes are designed as “U” shaped as seen in Figure 2.22.



(a) Design



(b) Photography

Figure 2.22 Positions of the distributor and collector pipes.

2.2.1.3 Heating Bath

Discharging experiments are carried out with using a heating bath. As seen in Figure 2.23, the bath is designed as a shell-and-tube type heat exchanger. An electrical resistance heater is fixed at the center of the tank to supply the required heating power during the discharging experiments. Water and HTF stands on the shell and tube sides of the exchanger, respectively. Hence, bath is used for both internal and external melting experiments without making any modifications inside the bath. Heater is controlled via PID unit to obtain either constant heat load or constant inlet temperature values at the inlet section of the storage tank.

2.2.1.4 Sensors

A total of 15 interface measurement cards and 56 temperature sensors are used to observe time wise variations of the solid/liquid interface and temperature on

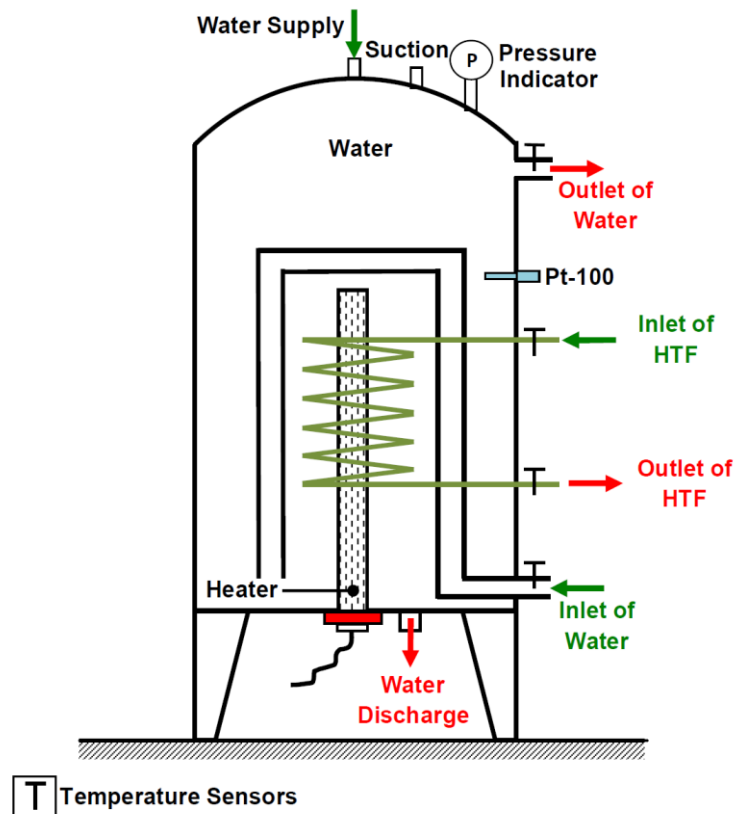


Figure 2.23 Heating bath.

different sections of the tank. Temperature variations inside the PCM and on the surfaces of the tank and coil are measured via 52 thermocouples. On the other hand, inlet and outlet temperature values of the HTF and PCM are monitored with the Pt-100 probes.

An interface measurement method is applied to watch the solid/liquid interface variations inside the storage tank. Detailed information about the interface measurement method is given in Section 2.1.2. For the current system, measurement cards are designed to place between two tubes in the vertical direction. In Figure 2.24, the geometric parameters of the measurement cards are given together with an illustrative picture for the location of the card on the coil. Each card has totally eight pairs of electrodes and three thermocouples. In Figure 2.24, electrode and thermocouple positions are symbolized with hollow and solid circles, respectively. Cards are designed to obtain the variations of solid/liquid interfaces for both upper and lower tubes. For this purpose, four electrodes are settled near the upper tube and

the other four electrodes are settled near the lower tube. Electrodes are located at $r_1 = 15$ mm, $r_2 = 20$ mm, $r_3 = 25$ mm and $r_4 = 30$ mm positions from the centers of the tubes. Besides, three thermocouples are settled on the cards, at distances of $r_{top} = 22.5$ mm, $r_{bottom} = 22.5$ mm and $r_{middle} = 45$ mm from the centers of the tubes.

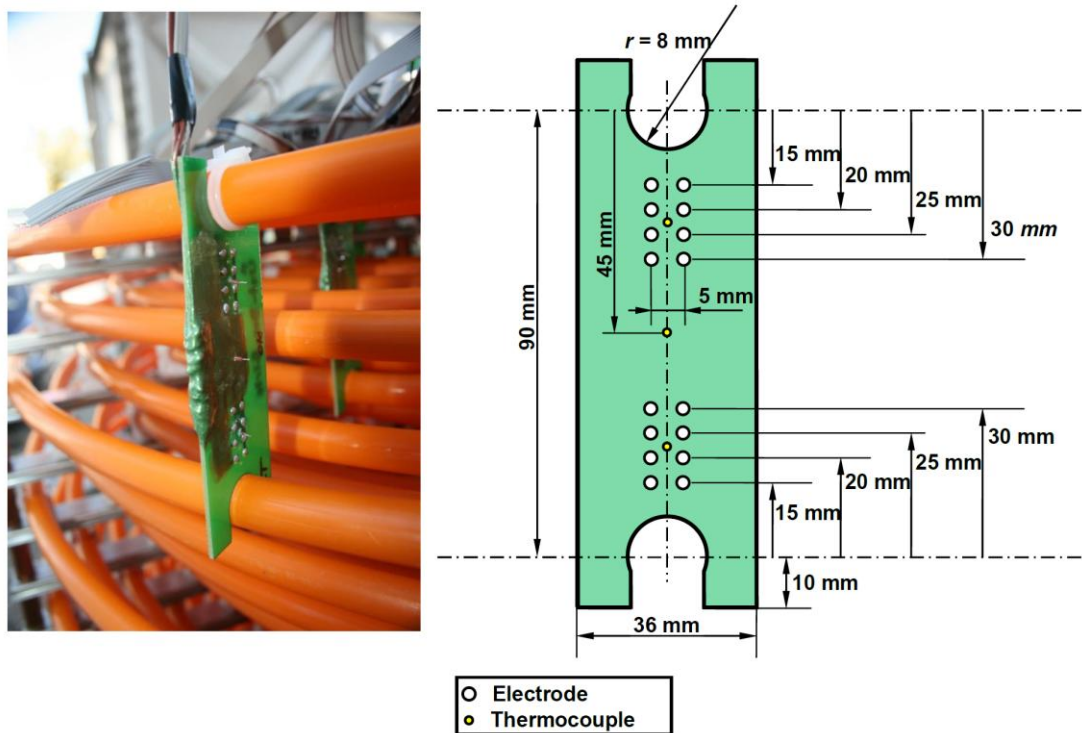


Figure 2.24 Layout of the electrodes and thermocouples on the measurement cards.

As described in Section 2.1.2, the current interface measurement method is based on observation of the variations in the electrical conductivity of phase change medium, since the electrical conductivity of water changes dramatically while it freezes. The signal variations are watched during the experiments, and when the pair of electrodes is covered by ice, signal makes a sudden change. The altering time of the signal designates the solidification time for each electrode position. As an illustration, in Figure 2.25 the signal variations of a measurement card are given for eight electrode pairs, which are settled near the upper and lower tubes.

Cards are located at the several sections in the vertical direction of the tank and through the flow direction of the HTF. In the vertical direction, cards are located at

the *top*, *center* and *bottom* sections of the tank. On the other hand, through the flow direction of the HTF, cards are settled at the *inlet*, *middle*, and *outlet* sections. Figure 2.26 represents the layout of the interface measurement cards inside the tank. Abbreviations for measurement cards are given in Table 2.5.

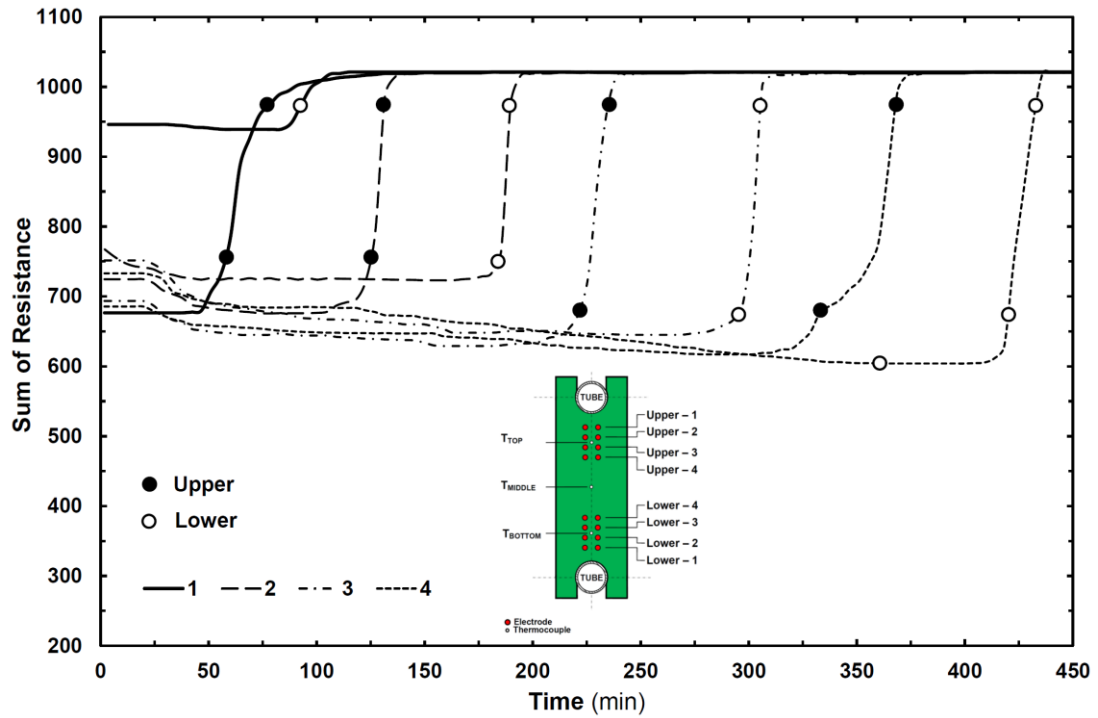


Figure 2.25 Time wise variations of the electrical resistance values.

Table 2.5 Abbreviations for the measurement cards.

Flow Direction	Vertical Direction					
	Top		Center		Bottom	
	Inner Distribution	Outer Distribution	Inner Distribution	Outer Distribution	Inner Distribution	Outer Distribution
Inlet	T-I-I	T-O-I	C-I-I	C-O-I	B-I-I	B-O-I
Middle	T-I-M	T-O-M	-	-	-	B-O-M
Outlet	T-I-O	T-O-O	C-I-O	C-O-O	B-I-O	B-O-O

A total of 120 pairs of electrodes is scanned during the experiments. The same methodology and the device is utilized to capture the signals as described in Section 2.1.2.2. The duration of scanning for all 120 electrodes take nearly 1.5 minutes, and the scanning process continue until the experiments are finalized.

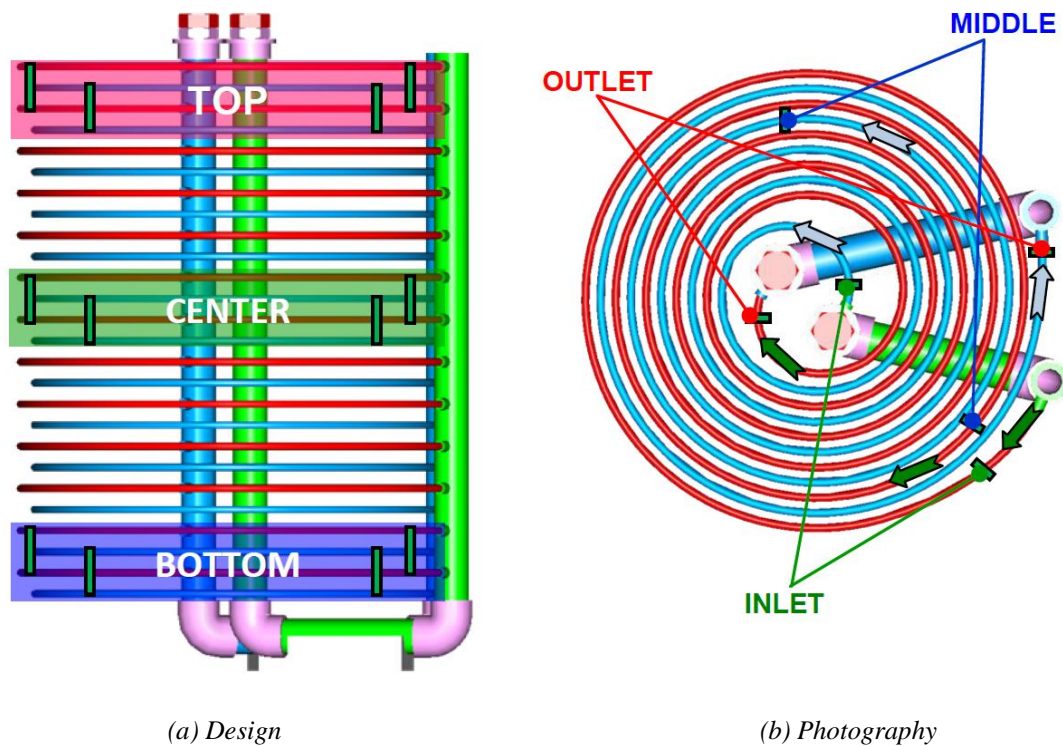


Figure 2.26 Layout of the measurement cards inside the storage tank.

Temperature sensors are placed on the surfaces of the tank and tubes inside the PCM and at the inlet and outlet sections of the storage tank for the HTF or PCM. A total of 56 temperature sensors is used to monitor the heat transfer interactions inside the tank. Inlet and outlet temperatures of the HTF (*or* PCM) to the storage tank are measured with the Pt-100 temperature sensors. On the other hand, three thermocouples are placed on the eight measurement cards to attain the temperature variations inside the solid and liquid phases of the water. Hence, a total of 24 thermocouples (30-Gauge, T-type) is placed inside the PCM. Besides, the surface temperature values of the tubes are measured at the inlet, middle, and outlet sections of the first two tubes in the vertical direction. All temperature data are collected on computer for every 30 seconds via Agilent 34970A (*Santa Clara, CA, USA*) data acquisition unit.

Energy storage tank is covered with double-layered insulation coating. R-flex insulation material is applied with a total thickness of 38 mm. Even though, all external surfaces of the tank are well insulated; there occurs heat gain (*loss*) from (*to*)

surroundings. Thermocouples are fixed at the inner and outer surfaces of the insulation coating on the top, bottom and lateral surfaces of the tank to compute the amount of heat transfer from surroundings to the tank. A total of twenty-one thermocouples is used to calculate the rate of heat transfer passes through the insulation. Positions of the thermocouples on the tank surface and measurement card are illustrated in Figure 2.27. With considering the possible thermal differentiation along the angular and vertical directions of the tank, thermocouples are settled at three different angular sections (A, B, C) and four vertical positions in each angular section.

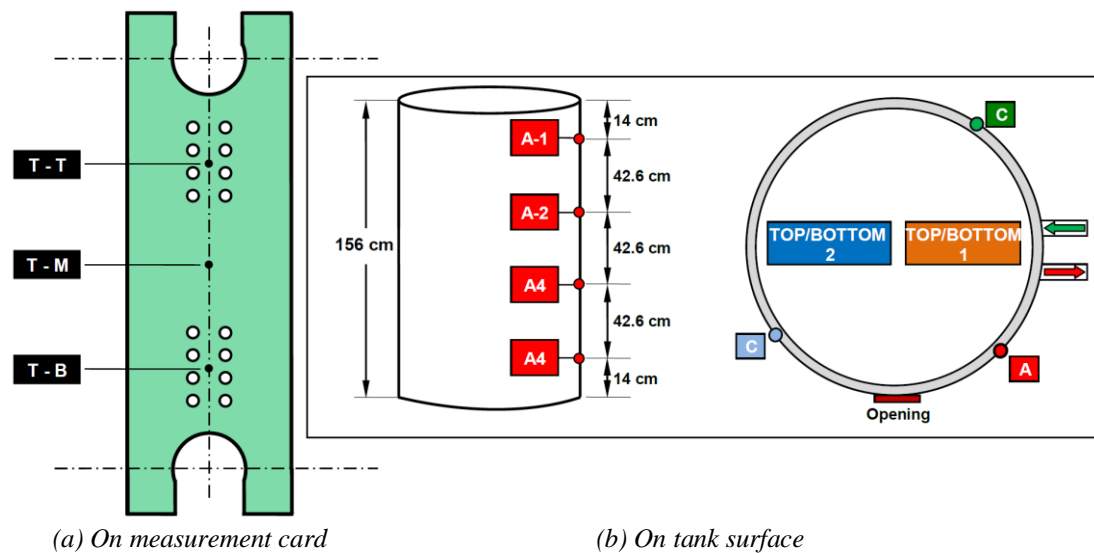


Figure 2.27 Positions of the thermocouples.

Chiller, heating bath, and pumps are controlled by PID algorithm to minimize the oscillations of the inlet temperature and flow rate of HTF (*or* PCM). On this account, chiller is controlled via variable speed compressor together with an electronic expansion valve, besides; pumps are controlled with the motor speed controller. The working parameters for compressor, pumps, and flow meters are obtained with the aid of MOD-BUS data transmission algorithm in 15 seconds interval. For compressor; torque, frequency, and amount of the power consumption data are obtained from the motor speed controller. On the other hand, flow rate of HTF (*or* PCM) is collected as digital output signals from the electromagnetic flow meter.

2.2.2 Experimental Procedures

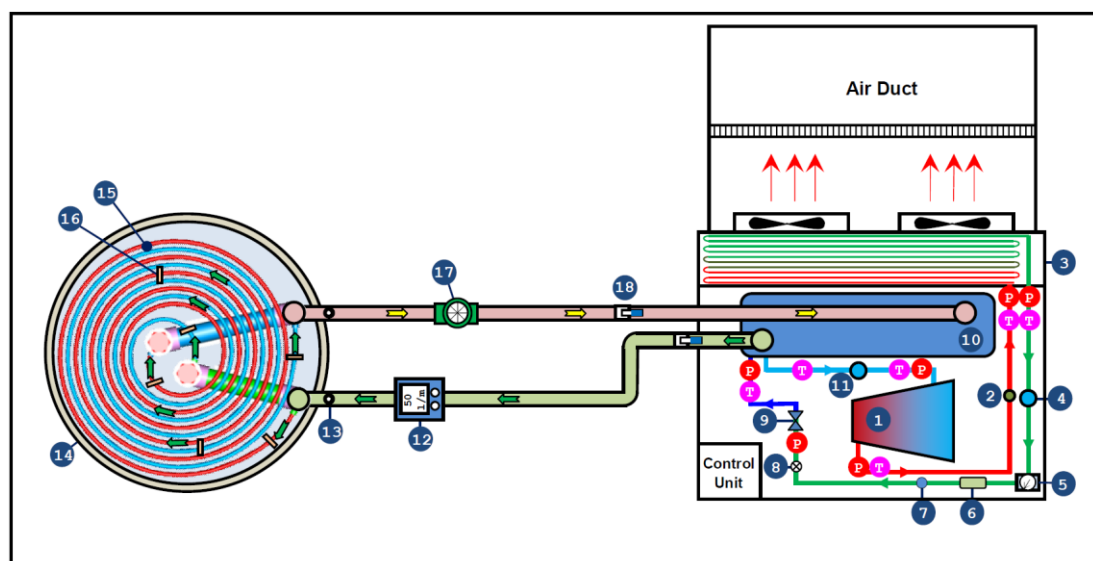
In this study, charging and discharging experiments are conducted for an ice-on-coil type LHTES system. Detailed information about the experimental procedures is illustrated in following subsections.

2.2.2.1 Procedure of Charging Experiments

In Figure 2.28, schematic representation of the experimental setup is simplified to illustrate only charging process. In all charging experiments, the initial mean temperature of the water is decreased under 4°C to minimize the natural convection effects in the system. In order to achieve that, HTF is cooled down at the evaporator side of the chiller and circulated inside the coil to decrease the temperature of water homogenously before experiments. Temperature variations on the tube surfaces are observed to avoid the formation of ice on the surface of the tubes. In addition, tube and collector surfaces are checked before starting the experiments for possible ice formations. As soon as the mean temperature value of the water reached below or close to 4°C, experiments are initiated for proper working parameters. HTF is cooled down at the evaporator (1) side of the chiller and passes through the KROHNE flow meter (3) and KROHNE Pt-100 (4) temperature sensor before reach the storage tank (5). Inside the tank, HTF is distributed into coil (6) to perform an outward solidification around tubes. Time wise variations of the interface positions and the temperature values of the solid and liquid phases of water are observed with the aid of measurement cards (7). At the outlet section of the tank, temperature value of the HTF is measured by KROHNE Pt-100 (4) temperature sensor. WILO suction pump (8) is placed at the return pipeline to circulate HTF inside the system.

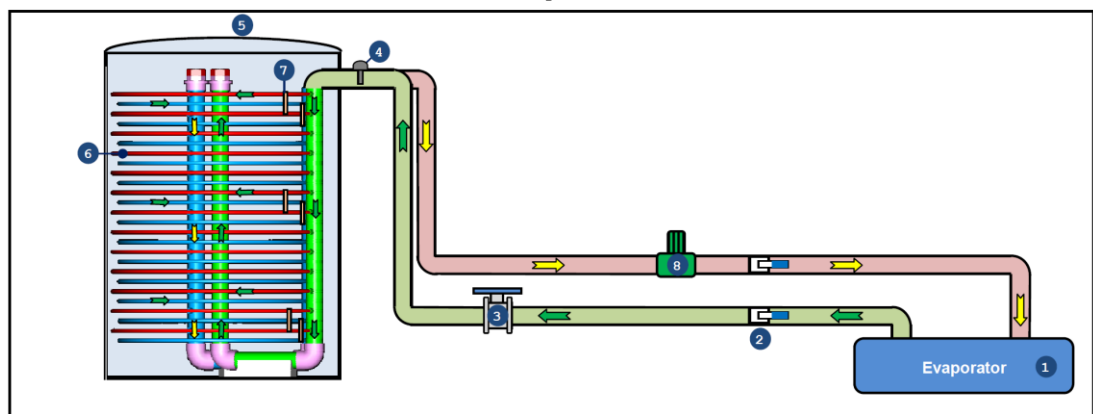
Chiller and pump are controlled by PID algorithm to obtain a constant flow rate of HTF and a constant temperature value of HTF at the inlet section of the tank. Speed of the pump is regulated with the aid of motor speed controller, depending on the output signal value of the flow meter. On the other hand, four different control strategies are tried out to obtain a constant inlet temperature of HTF at the inlet

section of the tank. Control system of the chiller consists of a semi-hermetic reciprocating compressor, a microcontroller with PID subroutine and a PWM (Pulse-Width-Modulated) inverter. The output signal of the PID microcontroller is supplied to the inverter to modulate the compressor speed in a range of 20 to 80 Hz according to the monitored value. The monitored value is a function of the error between the set and monitored values of the temperature or pressure. In the current study, chiller is controlled via four different control strategies to achieve a constant inlet temperature at the inlet section of the tank.



(1) Compressor, (2) Oil separator, (3) Condenser, (4) Liquid tank, (5) Flow meter (*R404A*), (6) Dryer, (7) Sight glass, (8) Solenoid valve, (9) Electronic expansion valve, (10) Evaporator, (11) Accumulator, (12) Flow meter (*Brine*), (13) Pt-100, (14) Storage tank, (15) Coil, (16) Measurement card, (17) Pump, (18) Valves

(a) Top view



(1) Evaporator, (2) Valve, (3) Flow meter, (4) Pt-100, (5) Storage tank, (6) Coil, (7) Measurement card, (8) Pump

(b) Front view

Figure 2.28 Schematic representation of the charging process.

Three different monitored values are used in the PID subroutines; (i) evaporation temperature of R404A, (ii) temperature of the HTF at the outlet section of the evaporator, and (iii) suction pressure of the compressor. In these three control strategies, compressor is driven depending on the monitored value with the aid of PID subroutine and inverter. On the other hand, in the refrigeration cycle, refrigerant flow rate varies when the compressor speed changes. Expansion devices regulate the flow rate of the refrigerant, in order to provide stable superheat value at the evaporator. In the current study, an electronic expansion valve (EEV) is used to stabilize the super heat temperature in the evaporator. In addition to these variable speed control strategies, relatively simple (iv) on–off control strategy is also tested to compare the performance of all possible control strategies.

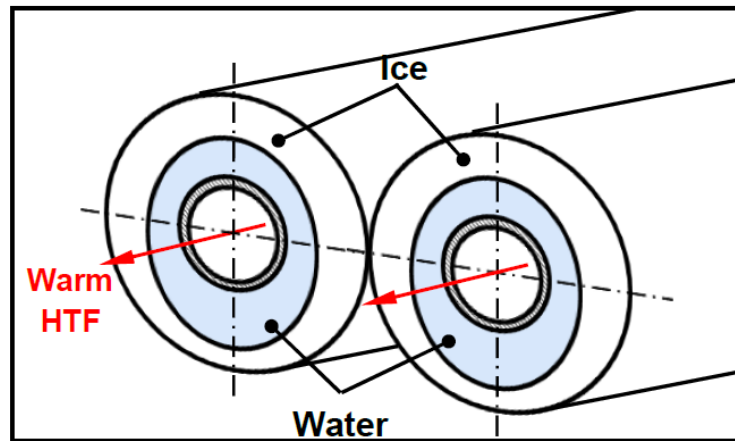
The positions of the control sensors for each scheme are listed below:

- Scheme (i):* Temperature value of R404A is measured at the outlet section of the evaporator with the aid of NTC type temperature sensor (0 – 10 VDC output).
- Scheme (ii):* Temperature value of the HTF is measured at the outlet section of the evaporator with the aid of NTC type temperature sensor (0 – 10 VDC output).
- Scheme (iii):* Pressure of R404A is measured at the suction section of the compressor with the aid of ratio metric type pressure transducer (4 – 20mA output).
- Scheme (iv):* Temperature value of the HTF is measured at the outlet section of the evaporator with the aid of NTC type temperature sensor (0 – 10 VDC output).

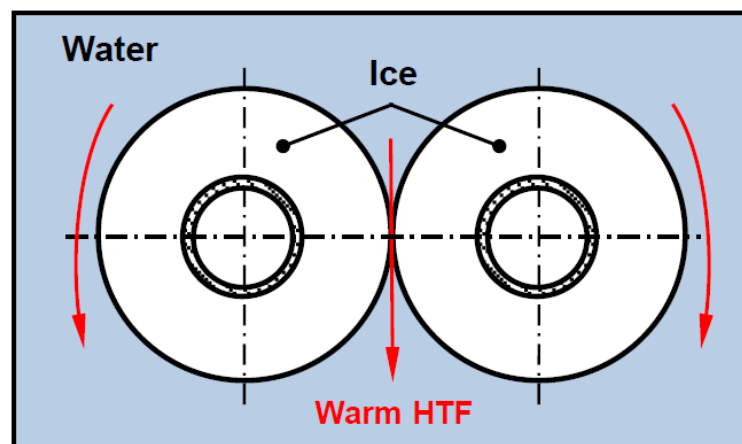
2.2.2.2 Procedure of Discharging Experiments

In literature, discharging experiments are generally carried out either inwards (*external*) or outwards (*internal*) directions. Internal and external melting modes are illustrated schematically in Figure 2.29. In the internal melting mode, relatively

warm brine circulates inside the tubes and melts ice outward. In contrast, for the external melting mode, relatively warm water circulates at the outer surface of ice and melts ice inwards.



(a) Internal melting mode



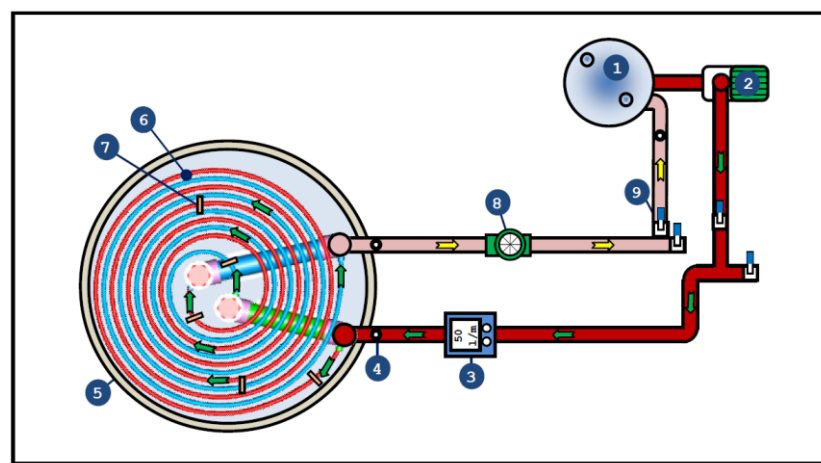
(b) External melting mode

Figure 2.29 Discharging modes.

In the current study, discharging experiments are performed for both internal and external melting modes. After the charging experiments completed, chiller side of the system is disabled by closing the valves, and discharging experiments are initiated.

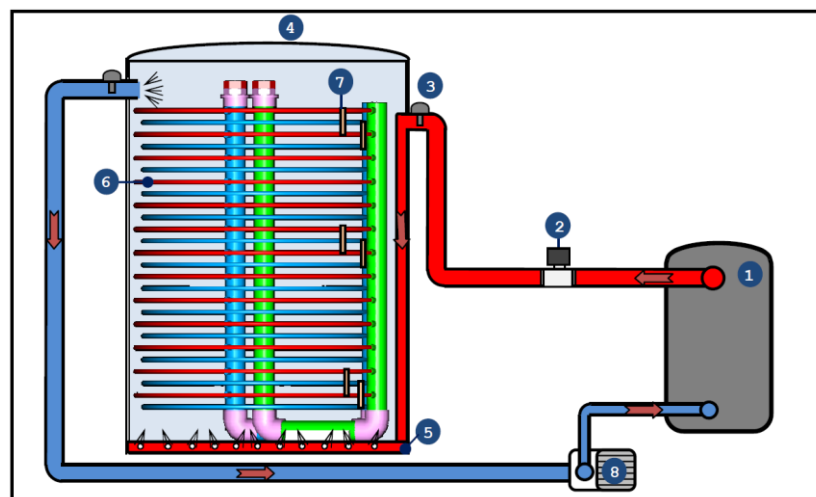
A schematic representation of the internal melting mode is illustrated in Figure 2.30(a). In the internal melting experiments, the HTF is heated in the heating tank (1) and then pumped (2) through the coil (6) to melt ice outwards. Internal melting

experiments are carried out for constant heat load and constant inlet temperature conditions. For this purpose, outlet temperature of the heating bath is controlled by PID controller. On the other hand, schematic representation of external melting mode is illustrated in Figure 2.30(b). In external melting experiments, water is heated in the heating tank (1) and then pumped through the bottom of the tank to the diffuser (5). From the holes of the diffuser, water is distributed inside the tank and flows around the ice to make an inward melting. Then, water is collected from the side of the tank and circulated back to heating bath.



(1) Heating tank, (2) Pump, (3) Flow meter (Water), (4) Pt-100, (5) Storage tank, (6) Coil, (7) Measurement card, (8) Pump, (9) Valves

(a) *Internal melting mode*



(1) Heating tank, (2) Flow meter, (3) Pt-100, (4) Storage tank, (5) Diffuser, (6) Coil, (7) Measurement card, (8) Pump

(b) *External melting mode*

Figure 2.30 Schematic representation of the discharging process.

The external melting experiments are performed for only constant heat load condition unlike the internal melting experiments. Because, at the beginning of the external melting experiments the average temperature of the water is very close to the phase change temperature. Thus, a higher amount of heat power is needed to increase this low temperature to a definite set temperature and keep it constant during experiments.

2.2.3 Analyses of Experimental Data

In this section, methodology for the energy, thermodynamic, and uncertainty analyses of the ice-on-coil LHTES system are addressed in three subsections.

2.2.3.1 Energy Analysis

Energy balance of the storage tank can be written with considering the storage tank as thermodynamically open system, as shown in Figure 2.31. Energy balance of the system can be written in general form as follows:

$$\left\{ \begin{array}{c} \text{Energy} \\ \text{Input} \end{array} \right\} - \left\{ \begin{array}{c} \text{Energy} \\ \text{Output} \end{array} \right\} \pm \left\{ \begin{array}{c} \text{Energy} \\ \text{Gain / Loss} \end{array} \right\} = \left\{ \begin{array}{c} \text{Energy} \\ \text{Change in System} \end{array} \right\}$$

or

$$E_{HTF}(t) \pm Q_{gain/loss}(t) = \Delta E_{system}(t) \quad (2.40)$$

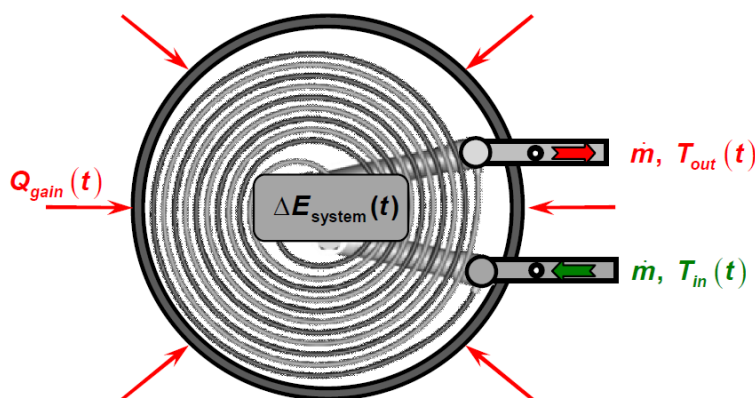


Figure 2.31 Energy balance for the storage tank.

where the first term on the left hand side represents the energy variation of the HTF; second term designates the heat gain (*loss*) from (*to*) surroundings. Right hand side of the equation points out the net energy variation inside the storage tank. The internal energy variation of the tank is composed of latent and sensible components and can be written to be:

$$\Delta E_{system}(t) = \left\{ \left[\left[m(t)c \right]_{water} \bar{T}_{water}(t) \right] - \left[\left[mc \right]_{water,i} \bar{T}_{water,i} \right] \right\} + \left\{ \left[m(t)c \right]_{ice} \left(\bar{T}_{ice}(t) - T_m \right) \right\} - \left\{ m(t)_{ice} h_{sf} \right\} \quad (2.41)$$

where the first two brackets represent the sensible energy variations inside the liquid and solid phases of the PCM. Moreover, the last term indicates the latent energy variation of the PCM. In the equation, $\bar{T}_{water,i}$, $\bar{T}_{water}(t)$ and $\bar{T}_{ice}(t)$ denote the mean temperature values of water and ice at initial and certain times of the experiments, respectively.

Energy variation of the HTF can be written in the form of temperature difference between the inlet and outlet sections of the tank as

$$E_{HTF}(t) = \int_{t=0}^t \left[\dot{m}(t)c \right]_{HTF} \left[T_{in}(t) - T_{out}(t) \right] dt \quad (2.42)$$

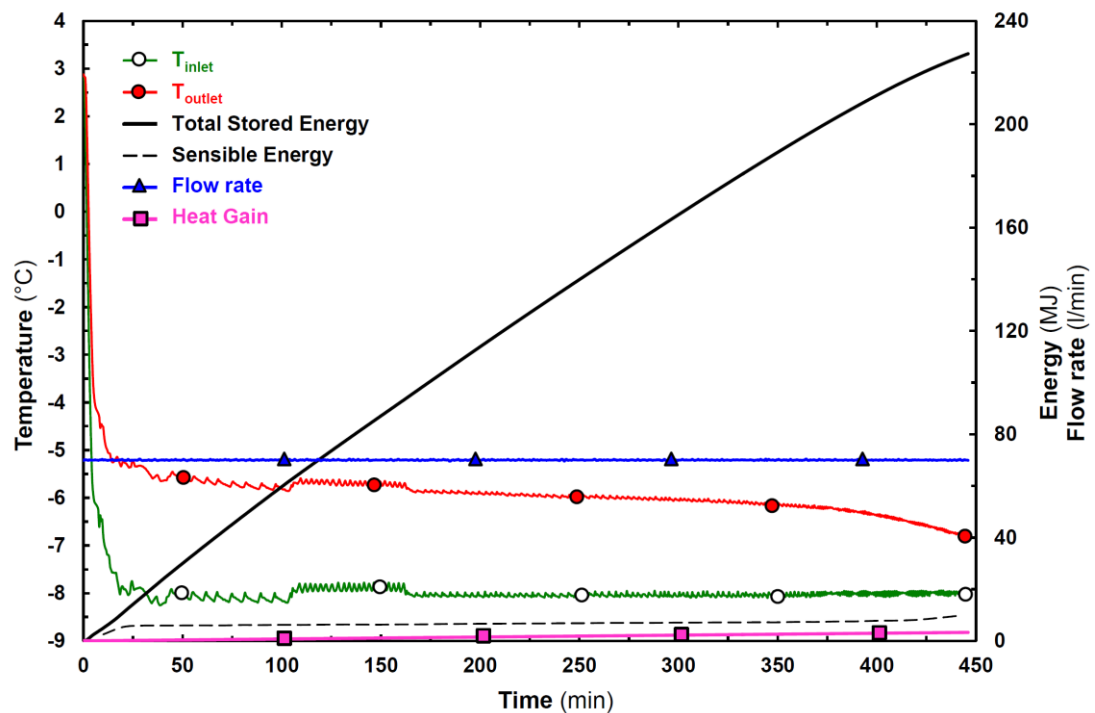
where $\dot{m}_{HTF}(t)$, $T_{in}(t)$ and $T_{out}(t)$ represent the mass flow rate of the HTF and the temperature values of the HTF at the inlet and outlet sections of the storage tank, respectively.

The heat gain or loss from surroundings is computed from the integration of the time dependent heat transfer rate from surroundings to the tank to be;

$$Q_{gain}(t) = \int_{t=0}^t \dot{Q}_{gain}(t) dt \quad (2.43)$$

In Figure 2.32, time wise variations of the total stored, sensible, and latent energies are given together with the variations of the inlet–outlet temperature values and volumetric flow rate of the HTF for a selected experiment. It can be seen that the inlet temperature and the flow rate of the HTF are almost constant during the experiment. Besides, the outlet temperature of the HTF gets close to the inlet temperature and the total stored energy value approximates to its maximum while

solidification process becomes completed at the end of the experiments. This indicates that, the heat transfer rate decreases with increasing the radius of ice. On the other hand, the sensible energy and the heat gain from surroundings have very small influence in comparison with the latent energy variations. As an average, total sensible energy and total heat gain are nearly 3% and 1.5% of the total stored energy, respectively.



($T_{in} = -8^{\circ}\text{C}$ and $\dot{V} = 70 \text{ l/min}$)

Figure 2.32 Temperature, flow rate and energy variations.

Conservation of energy can be verified with comparing the total stored energies computed from the flow side to the internal energy variations. In Figure 2.33, total stored energy variations are given for two different computation methods with two different flow rates ($\dot{V} = 50 \text{ l/min}$ and $\dot{V} = 60 \text{ l/min}$) of $T_{in} = -8^{\circ}\text{C}$. While filled circles and triangles represent the results of the internal energy variations of the storage tank (*internal*), hollow ones indicate enthalpy variation of the HTF through the storage tank (*flow side*). Energy variations seem to be close for two calculation methods, and the mean difference is less than 5%.

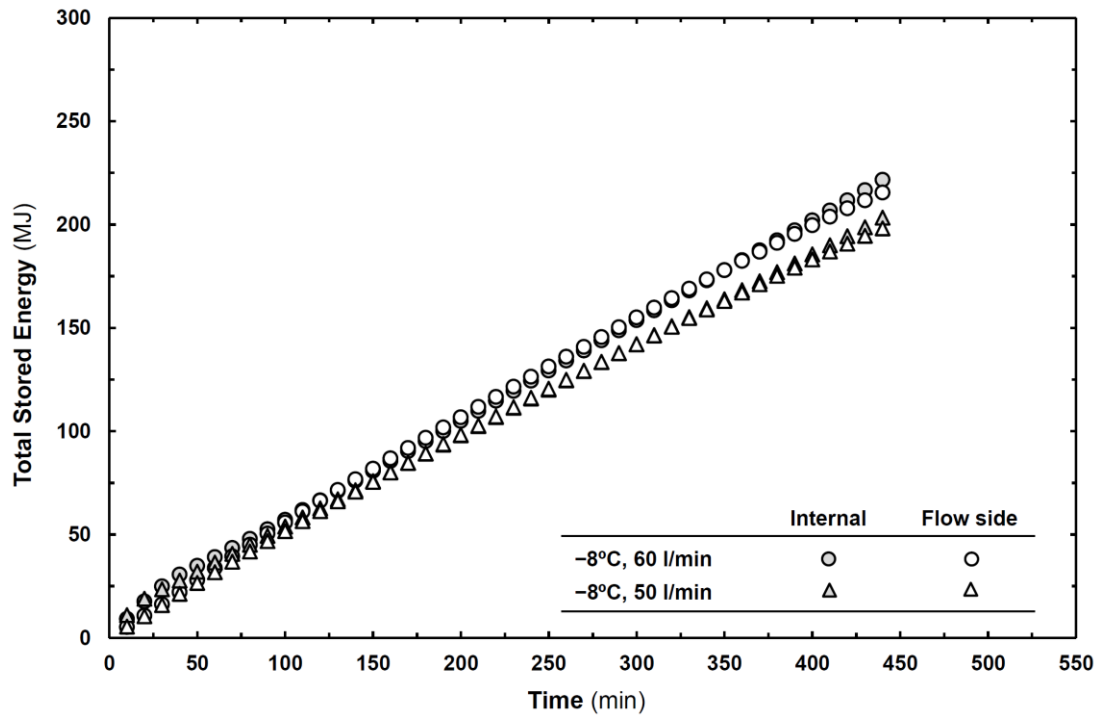


Figure 2.33 Total stored energy variations in comparison with the total rejected energy.

Finally, energy efficiencies of the system can be written for charging and discharging periods as follows:

$$\eta_{\text{charging}}(t) = \frac{\Delta E_{\text{system}}(t)}{E_{\text{HTF}}(t)} \quad (2.44)$$

$$\eta_{\text{discharging}}(t) = \frac{E_{\text{HTF}}(t)}{\Delta E_{\text{system}}(t)} \quad (2.45)$$

where $\eta(t)$ symbolize total energy efficiency of the system.

2.2.3.2 Thermodynamic Analysis of Chiller

In the refrigeration cycle, time wise variations of the enthalpy values of R404A are determined with depending on the temperature and pressure values at the inlet and outlet sections of the components. Sözen, Arcaklioglu & Menlik (2010) obtained enthalpy functions in both saturated liquid–vapor and superheated vapor regions with using Artificial Neural Network (ANN). ANN is a system resembling the human brain in two points; the knowledge is acquired by the network through a learning

process and inter–neuron connection strengths known as synaptic weights are used to store the knowledge (Sözen et al., 2010). Sözen et al. (2010) presented the enthalpy functions as follows:

$$h_l = \frac{1}{1 + e^{-(58.2766F_1 - 38.4775F_2 - 7.1084F_3 - 23.2643F_4 - 70.6907F_5 - 0.7067F_6 + 3.414F_7 + 50.1514)}} \quad (2.46)$$

$$h_v = \frac{1}{1 + e^{-(29.7715 F_1 + 63.042 F_2 - 0.4046 F_3 - 0.0972 F_4 + 29.2497 F_5 + 0.1112 F_6 - 0.2735 F_7 + 0.8612)}} \quad (2.47)$$

where l and v subscripts symbolize the saturated liquid–vapor and superheated vapour regions, respectively. F_i is the transfer functions and can be defined as

$$F_i = \frac{1}{1 + e^{-E_i}} \quad (2.48)$$

where E_i values are given in Table 2.6.

Table 2.6 Weight values obtained from ANN.

Components (i)	Phase					
	Saturated liquid–vapor region $E_i = C_{1i}T + C_{2i}x + C_{3i}$			Superheated vapor region $E_i = C_{1i}T + C_{2i}P + C_{3i}$		
	C_{1i}	C_{2i}	C_{3i}	C_{1i}	C_{2i}	C_{3i}
1	-4.3925	-0.3801	7.1726	0.7469	-1.4623	3.4859
2	-4.7218	0.6069	6.6522	3.7094	-0.1897	-6.3462
3	3.4022	2.0406	-1.1320	1.2867	-21.2796	-2.4877
4	-2.2480	-1.4765	-0.8275	-0.9031	121.8597	-9.0938
5	-0.3683	-0.3160	2.2345	1.7780	-1.6304	3.0104
6	16.9481	-1.4439	0.9324	-2.0343	691.4332	-65.7969
7	-3.3502	2.9187	-4.8559	-4.2591	3.0793	2.9128

Source: Sözen et al. (2010)

Evaporator and compressor capacities are calculated with considering the enthalpy variations of R404A. Compressor and evaporator capacities can be obtained from

$$\dot{W}_{comp} = \dot{m}_{ref} (h_{out} - h_{in})_{comp} \quad (2.49)$$

$$\dot{Q}_{evap} = \dot{m}_{ref} (h_{out} - h_{in})_{evap} \quad (2.50)$$

where h_{in} and h_{out} represent the enthalpy values of the refrigerant at the inlet and the outlet sections of the evaporator (or compressor), respectively. \dot{m}_{ref} is the mass flow rate of the refrigerant R404A. Furthermore, evaporator capacity of the chiller can be calculated with considering the enthalpy variation of the heat transfer fluid,

$$\dot{Q}_{HTF} = (\dot{m}c)_{HTF} (T_{out} - T_{in}) \quad (2.51)$$

where \dot{m}_{HTF} is the mass flow rate of the heat transfer fluid, c_{HTF} is the specific heat value of the HTF and T_{in} and T_{out} indicate the temperature values of the HTF at the inlet and outlet sections of the evaporator, respectively.

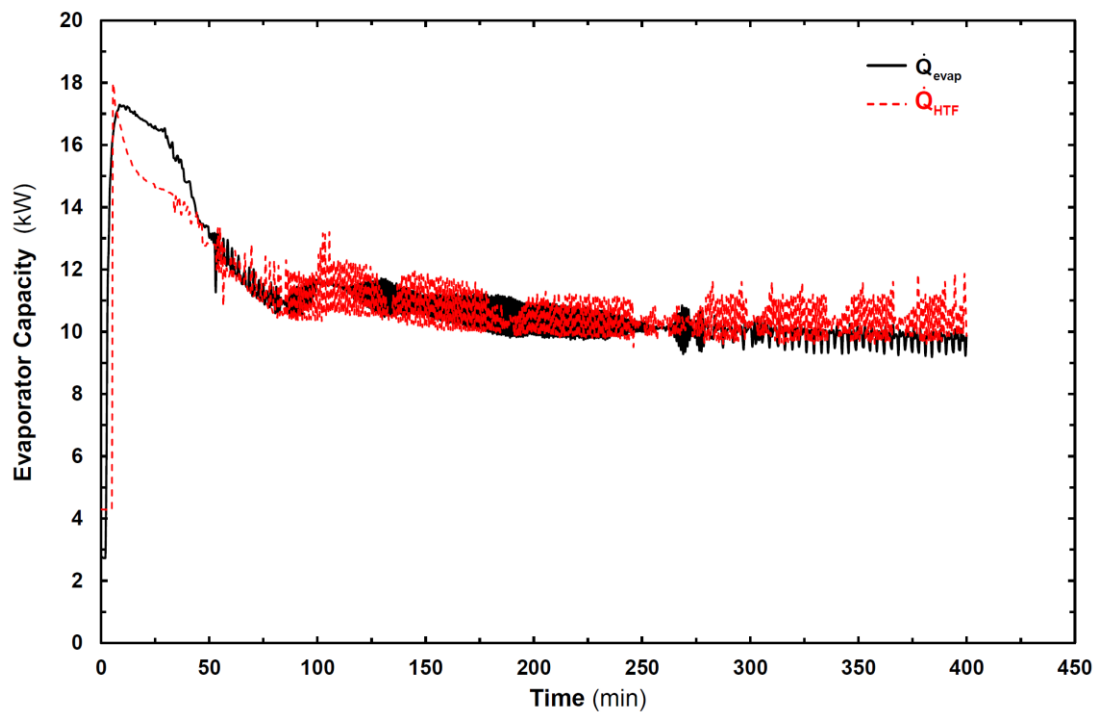
The coefficient of performance (COP) of the storage system can be defined as the ratio of the total stored energy to the power consumption of the compressor as follows:

$$COP_{system}(t) = \frac{E_{system}(t) - E_{system}(t - \Delta t)}{\dot{W}_{comp}(t) \Delta t} \quad (2.52)$$

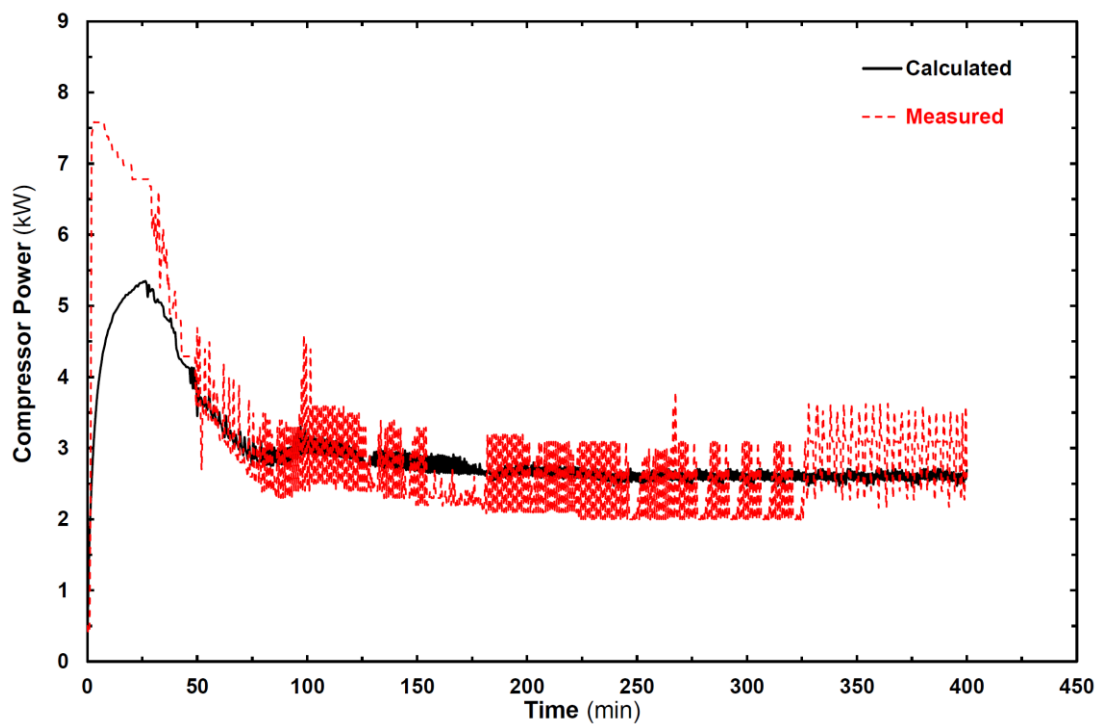
where the nominator and denominator designate the rate of energy stored in the system and consumed as the compressor work.

Energy balance of the refrigeration system can be checked for the evaporator and the compressor components. Time wise variations of the evaporator capacity can be obtained for R404A and HTF sides, as defined in Eqs. (2.50) and (2.51). Also, variations of the power consumption of the compressor can be determined using the enthalpy variation of R404A and wattmeter measurements. In Figure 2.34(a) and (b), comparative results are given for the evaporator capacity and compressor power consumption. Results indicate that the energy balance is almost provided for two components. The difference between the measured and calculated values may arise due to the presence of the heat loss (or *gain*) to (or *from*) surroundings, efficiency of the compressor or the possible measurement uncertainties.

While energy analysis is performed for all parametric experiments, thermodynamic based analysis is carried out for only some group of experiments. For this purpose, a numerical procedure is coded as a VBA (*Visual Basic Application*) subroutine inside MS Excel software. First, experimental data from measurement cards, temperature and pressure sensors are imported into Excel files for each experiment. Then, time wise temperature and interface variations as well as total sensible, latent energies are attained with the aid of VBA code.



(a) Energy balance for the evaporator



(b) Energy balance for the compressor

(Scheme (ii), $T_{in} = -7^{\circ}\text{C}$ and $\dot{V} = 60 \text{ l/min}$)

Figure 2.34 Comparisons of the evaporator capacity and compressor consumption.

2.2.3.3 Uncertainty Analysis

Experimental studies, naturally, cause some uncertainties and unpredictable errors. Such diversions may arise due to human nature reading errors, instrumental manufacturing errors, environmental condition effects or calibration errors and none of which can be taken into account for evaluating the experimental results. Recently many studies were performed about the uncertainty theory, to investigate the accuracy of the estimations for experiments, experimental setup and instruments (Holman 2001, Hepbasli & Akdemir, 2004).

In this study, uncertainties are calculated with using the methodology given in Holman (2001). Suppose a set of measurements is performed to determine some desired results of the experiments. Overall uncertainty of the calculated results will basis on the uncertainties in the primary measurements. The result R is a given function of the independent variables $x_1, x_2, x_3 \dots x_n$. Thus,

$$R = R(x_1, x_2, x_3 \dots x_n) \quad (2.53)$$

Let w_r be the uncertainty in the result and $x_1, x_2, x_3 \dots x_n$ be the uncertainties of the independent variables. Hence, the overall uncertainty in the result can be obtained as

$$w_R = \left[\left(\frac{\partial R}{\partial x_1} w_1 \right)^2 + \left(\frac{\partial R}{\partial x_2} w_2 \right)^2 + \dots + \left(\frac{\partial R}{\partial x_n} w_n \right)^2 \right]^{1/2} \quad (2.54)$$

For an instant time, total energy stored in the system can be written in terms of the mean values of temperature and radius of ice,

$$E_{system}(t) - E_{system,i} = [m(t)c\Delta T(t)]_{water} + m_{ice}(t)h_{sf} + [m(t)c\Delta T(t)]_{ice} \quad (2.55)$$

or, in terms of individual parameters,

$$E_{system}(t) - E_{system,i} = \rho_{water} \left\{ V_{water,i} - \pi [r_{ice}^{-2}(t) - r_o^2] l \right\} c_{water} \Delta \bar{T}_{water}(t) + \rho_{ice} \left\{ \pi [r_{ice}^{-2}(t) - r_o^2] l \right\} [h_{sf} + c_{ice} \Delta \bar{T}_{ice}(t)] \quad (2.56)$$

where $V_{i,w}$ is the initial volume of water in the tank ($\sim 0.96 \text{ m}^3$). On the other hand, total delivered energy by the HTF is,

$$E_{HTF} = \int_{t=0}^t \dot{m}_{HTF}(t) c_{HTF} \Delta T_{HTF}(t) dt \quad (2.57)$$

or, in terms of individual parameters,

$$E_{HTF} = \int_{t=0}^t \rho_{HTF} \dot{V}(t) c_{HTF} \Delta T_{HTF}(t) dt \quad (2.58)$$

In this study, following uncertainties affect computations of the total stored or delivered energies in ice–on–coil type LHTES system,

uncertainties arise from,

- the geometry of the storage tank and coils ($V_{water,i}, r_o, \ell$),
- temperature and ice radius measurement sensors ($\bar{\Delta T}_w, \bar{\Delta T}_{ice}, \Delta T_{HTF}, \bar{r}_{ice}$),
- selection of the thermo–physical properties of PCM
($\rho_{ice}, \rho_{water}, \rho_{HTF}, c_{ice}, c_{HTF}, c_{water}, h_{sf}$),
- measurement of volumetric flow rate (\dot{V}_{HTF})

Total stored and delivered energies can be written as functions of these independent variables as

$$E_{system} = E(t, r_{ice}, r_o, V_{water,i}, \ell, \rho_{ice}, \rho_{water}, c_{ice}, c_{water}, \bar{\Delta T}_w, \bar{\Delta T}_{ice}, h_{sf}) \quad (2.59)$$

$$E_{HTF} = E(t, \rho_{HTF}, \dot{V}_{HTF}, c_{HTF}, \Delta T_{HTF}) \quad (2.60)$$

Measuring ranges and uncertainties of individual parameters are given in Table 2.7. To determine the overall uncertainties those affect the computation of total stored and delivered energies, Eqs. (2.59) and (2.60) can be written in partial derivatives in terms of individual uncertainties,

$$w_{E_{HTF}} = \left[\left(\frac{\partial E_{HTF}}{\partial c_{HTF}} w_{c_{HTF}} \right)^2 + \left(\frac{\partial E_{HTF}}{\partial \rho_{HTF}} w_{\rho_{HTF}} \right)^2 + \left(\frac{\partial E_{HTF}}{\partial \dot{V}_{HTF}} w_{\dot{V}_{HTF}} \right)^2 + \left(\frac{\partial E_{HTF}}{\partial \Delta T_{HTF}} w_{\Delta T_{HTF}} \right)^2 \right]^{1/2} \quad (2.61)$$

$$w_{E_{system}} = \left[\begin{aligned} & \left(\frac{\partial E_{system}}{\partial r_{ice}} w_{r_{ice}} \right)^2 + \left(\frac{\partial E_{system}}{\partial r_o} w_{r_o} \right)^2 + \left(\frac{\partial E_{system}}{\partial V_{water,i}} w_{V_{water,i}} \right)^2 \\ & + \left(\frac{\partial E_{system}}{\partial \ell} w_{\ell} \right)^2 + \left(\frac{\partial E_{system}}{\partial c_{water}} w_{c_{water}} \right)^2 + \left(\frac{\partial E_{system}}{\partial c_{ice}} w_{c_{ice}} \right)^2 \\ & + \left(\frac{\partial E_{system}}{\partial \rho_{water}} w_{\rho_{water}} \right)^2 + \left(\frac{\partial E_{system}}{\partial \rho_{ice}} w_{\rho_{ice}} \right)^2 + \left(\frac{\partial E_{system}}{\partial h_{sf}} w_{h_{sf}} \right)^2 \\ & + \left(\frac{\partial E_{system}}{\partial \Delta T_{water}} w_{\Delta T_{water}} \right)^2 + \left(\frac{\partial E_{system}}{\partial \Delta T_{ice}} w_{\Delta T_{ice}} \right)^2 \end{aligned} \right]^{1/2} \quad (2.62)$$

As a result, overall uncertainty for computing total stored and delivered energies can be obtained as $\pm 2.8\%$ and $\pm 2.2\%$ respectively.

Table 2.7 Uncertainties of parameters for ice-on-coil type LHTES system.

Parameter	Value	Uncertainty	Comment
Radius of ice, r_{ice}	8 mm – 30 mm	± 0.38 mm	Uncertainty arise from electronic measurement method
Radius of tube, r_o	8 mm		
Volume of tank, $V_{water,i}$	0.96 m ³	$\pm 1\%$	Uncertainty arise from geometry of storage tank and coils
Length of tube, ℓ	10 m		
Density of ice, ρ_{ice}	920 kg/m ³	<i>neglected</i>	
Density of water, ρ_{water}	1000 kg/m ³	$\pm 0.02\%$	
Density of HTF, ρ_{HTF}	1070 kg/m ³	$\pm 0.02\%$	
Specific heat of water, c_{water}	4218 J/kgK	$\pm 0.3\%$	Uncertainty arise from the selection of thermo-physical properties of the PCM
Specific heat of ice, c_{ice}	2040 J/kgK	$\pm 0.3\%$	
Specific heat of HTF, c_{HTF}	3350 J/kgK	$\pm 0.3\%$	
Latent heat, h_{sf}	333400 J/kg	<i>neglected</i>	
Temperature differences, $\Delta \bar{T}_{ice}, \Delta \bar{T}_{water}$	$-2.5^\circ\text{C} \leftrightarrow +2.5^\circ\text{C}$	$\pm 0.5^\circ\text{C}$	Uncertainty arise from the thermocouple measurements
Temperature differences, $\Delta \bar{T}_{HTF}$	$0.5^\circ\text{C} \leftrightarrow +5^\circ\text{C}$	$\pm 0.05^\circ\text{C}$	Uncertainty arise from the Pt-100 measurements
Flow rate, \dot{V}_{HTF}	60 l min ⁻¹ \leftrightarrow 70 l min ⁻¹	$\pm 2\%$	Uncertainty arise from volumetric flow rate measurement

CHAPTER THREE

NUMERICAL ANALYSES

In parallel to the experimental studies, two sets of numerical analyses are carried out to introduce further details about the shell-and-tube type and ice-on-coil type LHTES systems. Natural convection dominated phase change in the shell-and-tube type system is analyzed in two-dimensional computational domain with the aid of commercial CFD code FLUENT. On the other hand, energy and exergy analyses are carried out for the charging period of an ice-on-coil LHTES system with using thermal resistance network technique. In this chapter, corresponding mathematical models are introduced in two subsections.

3.1 Mathematical Model for Natural Convection Dominated Phase Change

As designated in the literature review, solid-liquid phase change in the presence of natural convection is investigated by many researchers. Here, the primary purpose of the current analyses is the adaption of the temperature transforming method, which is developed by Cao & Faghri (1990), into the commercial CFD code FLUENT, for simulating the conduction/convection dominated phase change problems.

3.1.1 Theory and Background

Numerical analyses are performed via using the commercial CFD code FLUENT, with defining some additional sub-routines. In modeling of the buoyancy driven phase change problems, usage of FLUENT solidification/melting module may cause some convergence difficulties, as it is reported by Pinelli & Piva (2003). Scanlon & Stickland (2004) suggested that, to overcome these difficulties, some special subroutines could be defined to adopt the effect of phase change, rather than using solidification/melting module.

In the current study, the methodology developed by Scanlon & Stickland (2004) is extended to apply the temperature transforming method proposed by Cao & Faghri (1990) in FLUENT. Before going through the details about temperature transforming method, related governing equations are defined under several assumptions. In numerical analyses, following main assumptions are adopted,

- (1) PCMs (*water* or *n-octadecane*) are treated as the Newtonian and incompressible fluid,
- (2) Natural convection of water (or *n-octadecane*) is laminar without viscous dissipation and radiation effects,
- (3) Thermo-physical properties of PCMs differ for solid and liquid phases and properties are temperature independent for identical phases. Only density and dynamic viscosity of liquid water are defined as temperature dependent,
- (4) No-slip conditions ($u = 0, v = 0$) are valid for all boundaries,
- (5) Except the constant temperature boundaries, all other surfaces are adiabatic if there is not any contrary designation.

under these assumptions, the time-dependent governing equations for two-dimensional Cartesian coordinate system can be expressed as

For mass:

$$\frac{\partial}{\partial t}(\rho) + \frac{\partial}{\partial x}(\rho u) + \frac{\partial}{\partial y}(\rho v) = 0 \quad (3.1)$$

For x-momentum:

$$\frac{\partial}{\partial t}(\rho u) + \frac{\partial}{\partial x}(\rho uu) + \frac{\partial}{\partial y}(\rho uv) = -\frac{\partial p}{\partial x} + \frac{\partial}{\partial x}\left(\mu \frac{\partial u}{\partial x}\right) + \frac{\partial}{\partial y}\left(\mu \frac{\partial u}{\partial y}\right) \quad (3.2)$$

For y-momentum:

$$\frac{\partial}{\partial t}(\rho v) + \frac{\partial}{\partial x}(\rho uv) + \frac{\partial}{\partial y}(\rho vv) = -\frac{\partial p}{\partial y} + \frac{\partial}{\partial x}\left(\mu \frac{\partial v}{\partial x}\right) + \frac{\partial}{\partial y}\left(\mu \frac{\partial v}{\partial y}\right) + \rho g(T - T_m) \quad (3.3)$$

For energy:

$$\frac{\partial}{\partial t}(H) + \frac{\partial}{\partial x}(uH) + \frac{\partial}{\partial y}(vH) = \frac{\partial}{\partial x}\left(k \frac{\partial T}{\partial x}\right) + \frac{\partial}{\partial y}\left(k \frac{\partial T}{\partial y}\right) \quad (3.4)$$

Temperature transformation method is applied into the energy equation to convert enthalpy definitions into the temperature-based form. The enthalpy value of a material can be computed as the sum of the sensible and the latent heat components by;

$$H = h + \rho h_{sf} f \quad (3.5)$$

where h is the sensible enthalpy, f is the liquid fraction and h_{sf} is the latent heat. Sensible enthalpy can be defined in terms of the specific heat as follows:

$$\frac{dh}{dT} = \rho c \quad (3.6)$$

hence, the sensible enthalpy can be derived as

$$h = h_{ref} + \int_{T_{ref}}^T (\rho c) dT \quad (3.7)$$

Temperature transformation method is based on the equivalent heat capacity method (Morgan, 1981). In that method, to account for the latent heat effect on the liquid–solid interface, an equivalent heat capacity is introduced assuming that the phase change process occurs over a temperature range. The equivalent heat capacity method has the advantage of being simple for programming but also have many difficulties in the selection of the time step size, mesh size, and the phase–change temperature range (Cao & Faghri, 1990).

Cao & Faghri, (1990) proposed new temperature–based fixed grid formulization to overcome these weak points of the former method. Likely to the heat capacity method, this new model also assumes that, phase change process occurs over a range of phase change temperature from $T_m - \delta T_m$ to $T_m + \delta T_m$, rather than a fixed temperature and the enthalpy variation of the material is assumed to be linear in the mushy region. Here, $T_m - \delta T_m$ and $T_m + \delta T_m$ designate the phase transformation temperatures for the solid and the liquid states of the material, respectively. Hence, in addition to the *solid* and *liquid* phases, there is a transition phase takes place called *mushy*, as shown in Figure 3.1.

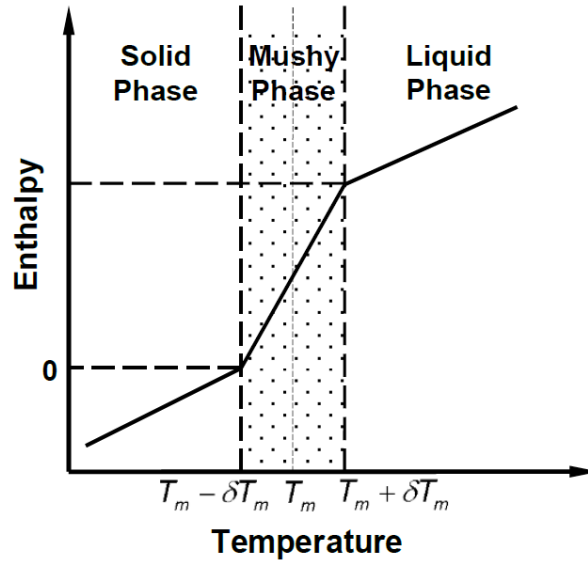


Figure 3.1 Illustration of enthalpy – temperature relationship.

The relationship between the enthalpy and temperature can be obtained with assuming linear variations. For three different phase regions, the relationship between total enthalpy and temperature can be obtained as follows:

Solid phase, ($T < T_m - \delta T_m$)

$$H(T) = (\rho c)_s (T - T_m + \delta T_m) \quad (3.8)$$

Mushy phase, ($T_m - \delta T_m \leq T \leq T_m + \delta T_m$)

$$H(T) = (\rho c)_m (T - T_m) + \rho \frac{h_{sf}}{2\delta T_m} (T - T_m) + (\rho c)_m \delta T_m + \rho \frac{h_{sf}}{2} \quad (3.9)$$

Liquid phase, ($T > T_m + \delta T_m$)

$$H(T) = (\rho c)_l (T - T_m) + (\rho c)_s \delta T_m + \rho h_{sf} \quad (3.10)$$

Hence, the relationship between the enthalpy and temperature can be expressed as

$$H(T) = \begin{cases} C_s (T - T_m) + C_s \delta T_m & T < T_m - \delta T_m \\ \left(C_m + \rho \frac{h_{sf}}{2\delta T_m} \right) (T - T_m + \delta T_m) & T_m - \delta T_m \leq T \leq T_m + \delta T_m \\ C_l (T - T_m) + C_s \delta T_m + \rho h_{sf} & T > T_m + \delta T_m \end{cases} \quad (3.11)$$

where C represents the heat capacity ($C = \rho c$) and C_m is the heat capacity for the mushy region. C_m is defined as the average of the solid and liquid phase values, $C_m = 0.5(C_s + C_l)$.

Cao & Faghri (1990), introduced a linear temperature dependent function to define the enthalpy to be;

$$H = CT + S \quad (3.12)$$

where S represents the source term. Enthalpy can be written in terms of C and S terms as follows:

$$C = C(T) = \begin{cases} C_s & T < T_m - \delta T_m & \text{Solid Phase} \\ C_m + \rho \frac{h_{sf}}{2\delta T_m} & T_m - \delta T_m \leq T \leq T_m + \delta T_m & \text{Mushy Phase} \\ C_l & T > T_m + \delta T_m & \text{Liquid Phase} \end{cases} \quad (3.13)$$

$$S = S(T) = \begin{cases} C_s (\delta T_m - T_m) & T < T_m - \delta T_m & \text{Solid Phase} \\ \left(C_m + \rho \frac{h_{sf}}{2\delta T_m} \right) (\delta T_m - T_m) & T_m - \delta T_m \leq T \leq T_m + \delta T_m & \text{Mushy Phase} \\ C_s \delta T_m - C_l T_m + \rho h_{sf} & T > T_m + \delta T_m & \text{Liquid Phase} \end{cases} \quad (3.14)$$

In the light of Eq. (3.12), Eq. (3.4) can be re-arranged to obtain the energy equation in the temperature-based form as follows:

$$\begin{aligned} \frac{\partial}{\partial t}(CT) + \frac{\partial}{\partial x}(uCT) + \frac{\partial}{\partial y}(vCT) &= \frac{\partial}{\partial x} \left(k \frac{\partial T}{\partial x} \right) + \frac{\partial}{\partial y} \left(k \frac{\partial T}{\partial y} \right) \\ &\quad - \frac{\partial}{\partial t}(S) - \frac{\partial}{\partial x}(uS) - \frac{\partial}{\partial y}(vS) \end{aligned} \quad (3.15)$$

In Eq. (3.15), the last three terms on the right hand side are named as source terms. As mentioned by Wang et al. (2010), S term is constant inside the liquid phase ($-\partial S/\partial x = 0, -\partial S/\partial y = 0$) and moreover velocity components are both zero in the solid and mushy regions, so the last two terms drop and only the time-dependent term remains as the source term of energy equation. This time-dependent source term is integrated over the control volume with using finite volume approach (Versteeg & Malalesekera, 2007) as

$$-\iint_{t,v} \frac{\partial}{\partial t}(S) dV dt \approx -\frac{(S)^n - (S)^{n-1}}{\Delta t} \Delta V \quad (3.16)$$

and a UDS (*User Defined Scalar*) sub-routine is defined into FLUENT code, to apply this source term into energy equation. Furthermore, two additional source terms are added into momentum equations to simulate the “zero” velocity inside the *solid* and *mushy* phases as

$$\varphi_x = -Bu \text{ and } \varphi_y = -Bv \quad (3.17)$$

where the coefficient B , is selected as $B = 10^9$ (Scanlon & Stickland, 2004). UDF (*User Defined Function*) sub-routines are defined to adapt these source terms into momentum equations.

Physically, pure substances, e.g. *pure water*, solidify without a mushy region. However, previous numerical studies indicated that, with selecting a relatively small mushy region temperature ranges, this method can be applied for simulation of the solid–liquid phase transformation of water (Erek, 1999; Erek et al., 2005; Ermis et al., 2007; Scanlon & Stickland, 2004; Shih & Chou, 2005). With using this small temperature range, the large differences between the solid and liquid heat capacities can be handled and the possible inconsistencies on the numerical calculations can be eliminated. Because of the code structure of the commercial CFD software’s, mushy zone temperature range should be defined carefully. Sugawara et al. (2010) simulated the solidification process of the water with the aid of commercial software package PHOENICS. It is designated that, for reliable calculations, the phase change temperature range should be taken small values, such as $0.1^\circ\text{C} < 2\delta T_m < 1^\circ\text{C}$. Kowalczyk et al. (2004) carried out numerical analysis for solidification of the water inside a rectangular domain with using ANSYS CFX software. They introduced that pure substances, e.g. *pure water*, solidify without a mushy region, nevertheless, for phase change of pure water, the temperature difference between T_{liquid} and T_{solid} is defined for numerical convenience and amounts up to 0.5 K.

Cao and Faghri (1990) tested the consistency of their own temperature transforming method for varies dimensionless phase change temperature ranges, $\delta T_m^* = \delta T_m / (T_{hot} - T_{cold})$. They changed δT_m^* value between 0.001 to 0.1 and it is concluded

that the method is insensitive to the phase change temperature range. In current numerical study, several phase change temperature range values are tested for both one- and two- dimensional cases, to investigate the influence of the phase change temperature range. Numerical analyses are performed for a range of 0.02 K to 1 K, to select an optimum temperature value for the phase change range. Unlike to the results of Cao & Faghri (1990), for relatively small values of mushy temperature range, numerical inconsistencies and convergence difficulties occur in FLUENT, because of the higher heat capacity values for mushy region. Hence, to determine the optimum mushy region temperature range for water, author also investigated the recent studies that are performed with using commercial software. Sugawara et al. (2010) simulated the solidification period of water with the aid of commercial software package PHOENICS. In those analyses, they selected the temperature range as 0.2°C. Scanlon & Stickland (2004) carried out numerical analysis for simulation of similar problem in FLUENT software with a temperature range of 0.51K.

Considering these previous studies, phase change temperature range for water is defined as 0.51K with referring to Scanlon & Stickland (2004) with, $T_m - \delta T_m = 272.66$ K and $T_m + \delta T_m = 273.16$ K. The specific heat and thermal conductivity values of water are defined as constants for the three regions. Density and viscosity of water are determined as temperature (K) dependent polynomial functions as defined in Seybert & Evans (2005), for buoyancy driven cases. Thermo-physical properties of water used in current analyses are given in Table 3.1 for each phase.

Table 3.1 Thermo-physical properties of water (PCM).

Property	Phase		Unit
	Liquid	Solid	
<i>Density, (ρ)</i>	$456.49 + 3.925T - 0.007085T^2$	917	kg/m ³
<i>Dynamic viscosity, (μ)</i>	$0.08771 - 5.724E-4T + 9.437E-7T^2$	–	kg/ms
<i>Specific heat, (c)</i>	4180	2217	J/kgK
<i>Thermal conductivity, (k)</i>	0.578	1.918	W/mK
<i>Heat of fusion, (h_{sf})</i>	333000		J/kg

In numerical procedure, Power Law differencing scheme (Patankar, 1980) is used for discretization of the momentum and energy equations, PRESTO (*PRE*ssure

STaggering Option) scheme is applied as pressure correction and SIMPLE (*Semi-Implicit Method for Pressure-Linked Equations*) algorithm is preferred for solving the governing equations. Basic aspects of finite volume method and discretization schemes are illustrated in the following subsection.

3.1.2 Fundamental Aspects of CFD

For two-dimensional transient convection-diffusion process, transport equations can be written as in Eqs. (3.1) to (3.4). Analytical solutions for these partial differential equations can be obtained for only some simplified problems. As an instance in Section 4.3.1.1.1, analytical solution of one-dimensional solidification problem is illustrated. Ozisik (1980) defined the temperature variations inside the solid and liquid phases in terms of x -position. Analytical solutions make it possible to express the field variables, e.g. u , v , T , etc., as functions of spatial locations of x , y . Nevertheless, in real fluid flows, because of the two- or three-dimensional nature of problems, analytical relationships are not easily achievable. Even the problem reduced into two-dimensional problem, it is difficult to obtain analytical results for convection diffusion problems, except some simple cases.

Rather than attaining closed-form analytical expressions, with using Computational Fluid Dynamics (CFD) methods, transport equations can be solved for the discrete locations. In CFD methodology, first, partial differential equations are replaced into algebraic equations and then, the discrete values of the flow field variables are computed with solving the sets of algebraic equations or matrices.

There are many computational methods for discretization of the transport equations for a computational domain. Commonly, following methods are preferred for CFD applications (Tu, Yeoh & Liu, 2008); finite difference method, finite element method, spectral methods and finite volume (*control volume*) method. Detailed discussions about the cons and pros of each approach can be found elsewhere (Versteeg & Malalasekera, 2007; Tu et al., 2008). As an overview, solution procedure for these CFD methods is illustrated in Figure 3.2.

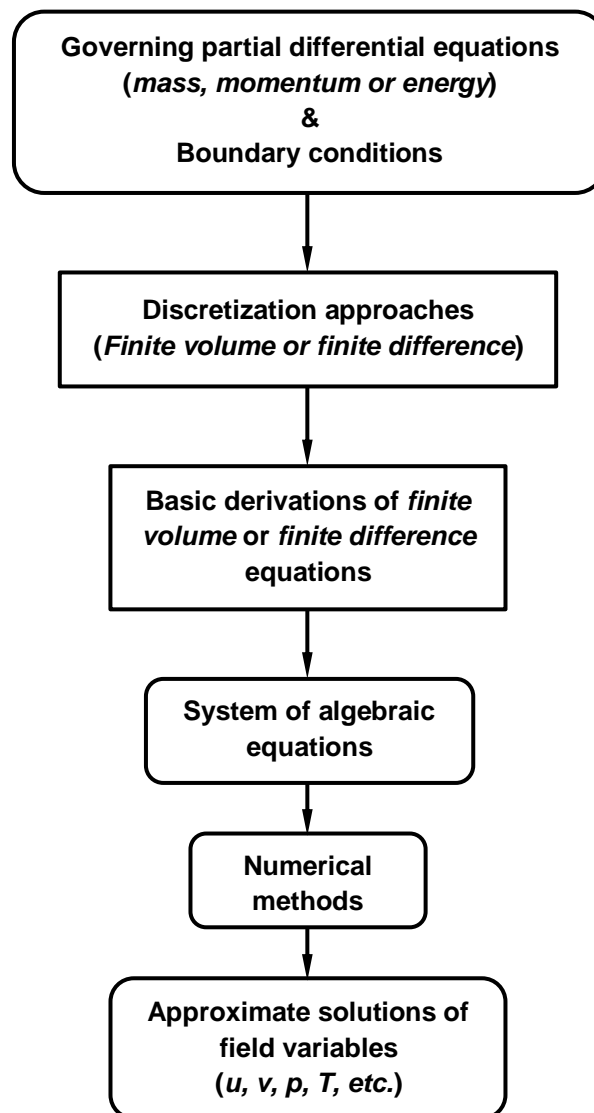


Figure 3.2 Overview of the computational solution procedure for CFD problems (*adapted from Tu et al., 2008*).

Tu et al. (2008) designated that nowadays, majority of all commercial CFD codes basis on the finite volume method. In current study, FLUENT commercial CFD software is utilized to predict the natural convection dominated phase change problem in various geometries. As indicated above, FLUENT software is basis on the finite volume approach. Hence, in following the sub-section, fundamentals of the finite volume approach are explained.

3.1.2.1 Finite Volume Method

Finite volume approach (or *control volume method*) is useful tool for discretizing the differential equations (Patankar 1980). The most attractive feature of the control–volume formulation is that the resulting solution would imply that the integral conservation of the quantities such as mass, momentum, and energy is exactly satisfied over any group of control volumes and, naturally, over the whole calculation domain (Patankar 1980).

In this method, the calculation domain is divided into a number of non–overlapping control volumes (Figure 3.3) such that there is one control volume surrounding each grid point.

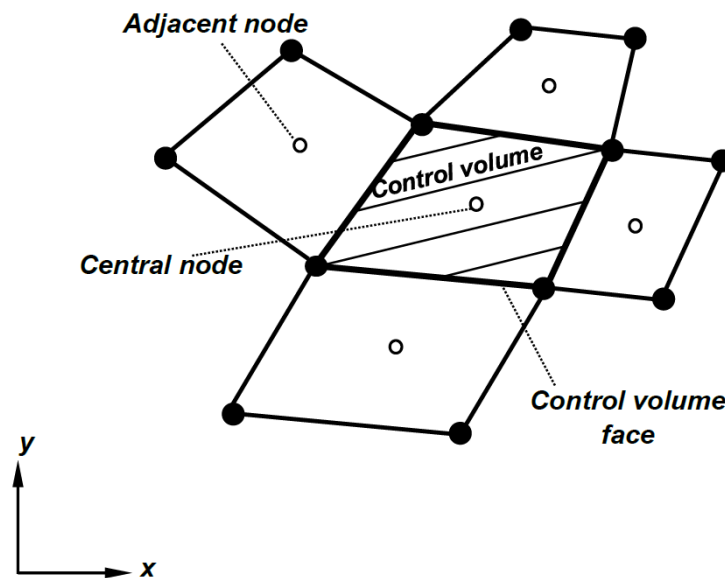


Figure 3.3 Representation of the structured grid arrangement (*open symbols at the center of the control volumes denote computational node*) (adapted from Tu et al., 2008).

All transport equations can be written in terms of generic variable of ϕ as follows:

$$\frac{\partial}{\partial t}(\rho\phi) + \text{div}(\rho\phi\mathbf{u}) = \text{div}(\Gamma\text{grad}\phi) + S_\phi \quad (3.18)$$

or in words,

$$\left[\begin{array}{l} \text{Rate of change of} \\ \phi \text{ in the control volume} \\ \text{with respect time} \end{array} \right] + \left[\begin{array}{l} \text{Net flux of } \phi \text{ due} \\ \text{to convection out of} \\ \text{the control volume} \end{array} \right] + \left[\begin{array}{l} \text{Net flux of } \phi \text{ due} \\ \text{to diffusion into} \\ \text{the control volume} \end{array} \right] + \left[\begin{array}{l} \text{Net rate of creation of} \\ \phi \text{ inside the control} \\ \text{volume} \end{array} \right]$$

Eq. (3.18) clearly highlights the various transport processes, such as, the rate of change terms and the convective term on the left hand side. The diffusive term (Γ : *diffusion coefficient*) and the source term are on the right hand side (Versteeg & Malalasekera, 2007). The transport equation can be integrated over each control volume to achieve the discretization equation as follows:

$$\int_{CV} \frac{\partial}{\partial t} (\rho\phi) dV + \int_{CV} \text{div}(\rho\phi\mathbf{u}) dV = \int_{CV} \text{div}(\Gamma \text{grad}\phi) dV + \int_{CV} S_{\phi} dV \quad (3.19)$$

Piecewise profiles expressing the variation of ϕ between the grid points are used to evaluate the required integrals. The result is the discretization equation containing the values of ϕ for a group of grid points. The discretization equation obtained in this manner expresses the conservation principle for ϕ for the finite control volume, just as the differential equation expresses it for an infinitesimal control volume (Patankar 1980).

Numerical procedure of finite volume is developed by considering the illustrative examples that are defined by Versteeg & Malalasekera (2007) and Patankar (1980). Problems are associated with: (1) *Steady one-dimensional diffusion problem* and (2) *Steady one-dimensional convection and diffusion problem*.

3.1.2.1.1 One-dimensional Diffusion Problem. Consider a one-dimensional domain defined in Figure 3.4. The governing equation for this steady pure diffusion problem can be expressed as

$$\frac{\partial}{\partial x} \left(\Gamma \frac{\partial \phi}{\partial x} \right) + S = 0 \quad (3.20)$$

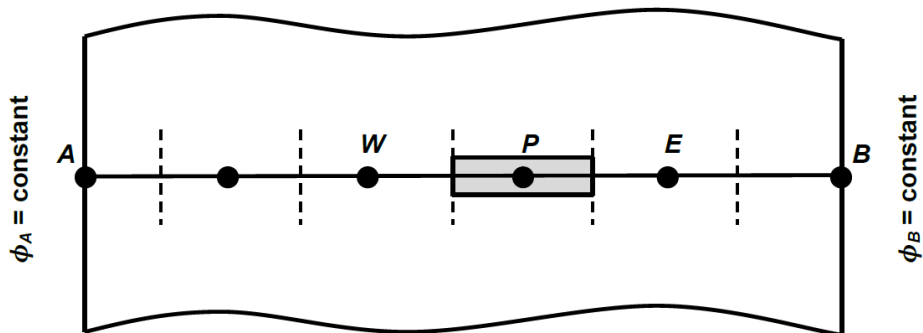


Figure 3.4 Geometry and boundary conditions of the one-dimensional diffusion problem.

where ϕ is the diffusion property, *e.g.* temperature, Γ is the diffusion coefficient, *e.g.* thermal conductivity and S is the source term, *e.g.* the rate of heat generation per unit volume.

The first step in the finite volume method is to divide the domain into discrete control volumes. Discretization equation can be derived for the grid-point cluster, shown in Figure 3.5. Here, the central point of the control volume is indicated with P , besides, W and E identify the nodes to the west and east, respectively. Bold borderlines show the faces of the control volume, and denoted with e and w .

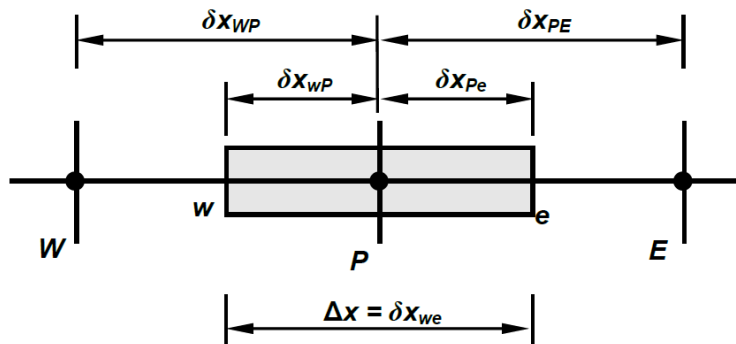


Figure 3.5 Control volume and grid nodes for one-dimensional domain.

The key step of the finite volume is the integration of the governing equation (or equations) over a control volume to yield a discretized equation at its nodal point P (Versteeg & Malalasekera, 2007). Integration of the Eq. (3.20) over the control volume, can be written as follows:

$$\int_{\Delta V} \frac{d}{dx} \left(\Gamma \frac{d\phi}{dx} \right) dV + \int_{\Delta V} S dV = 0 \quad (3.21)$$

Here, linear interpolation functions are used between the grid points, hence, derivative $d\phi/dx$ can be expressed as the piecewise linear profile by;

$$\left[\left(\Gamma A \frac{d\phi}{dx} \right)_e - \left(\Gamma \frac{d\phi}{dx} \right)_w \right] + \bar{S} \Delta V = 0 \quad (3.22)$$

where \bar{S} is the average value of the source over the control volume, and the diffuse flux terms are evaluated as

$$\left(\Gamma A \frac{d\phi}{dx} \right)_e = \Gamma_e A_e \left(\frac{\phi_E - \phi_P}{\delta x_{PE}} \right) \quad (3.23a)$$

$$\left(\Gamma A \frac{d\phi}{dx} \right)_w = \Gamma_w A_w \left(\frac{\phi_P - \phi_W}{\delta x_{WP}} \right) \quad (3.23b)$$

The source term \bar{S} may be a function of the dependent variable, in such cases, the finite volume method approximates the source term by means of a linear form as

$$\bar{S} \Delta V = S_u + S_P \phi_P \quad (3.24)$$

Eqs. (3.23) and (3.24) can be arranged in Eq. (3.22) to be;

$$\Gamma_e A_e \left(\frac{\phi_E - \phi_P}{\delta x_{PE}} \right) - \Gamma_w A_w \left(\frac{\phi_P - \phi_W}{\delta x_{WP}} \right) + (S_u + S_P \phi_P) = 0 \quad (3.25)$$

where Γ is used to represent the value of Γ pertaining to the particular control face, e.g. Γ_e refers to interface e . If the diffusion coefficient Γ is a function of x , then the value of Γ must be known at the grid points W , E and P (Erek, 1999).

The interpolation factor f_e is a ratio defined in terms of the distances in Figure 3.6,

$$f_e = \frac{\delta x_{eE}}{\delta x_{PE}} \quad (3.26)$$

if the interface e is the midway between the grid points, f_e would be 0.5, and Γ_e would be arithmetic mean of Γ_E and Γ_P .

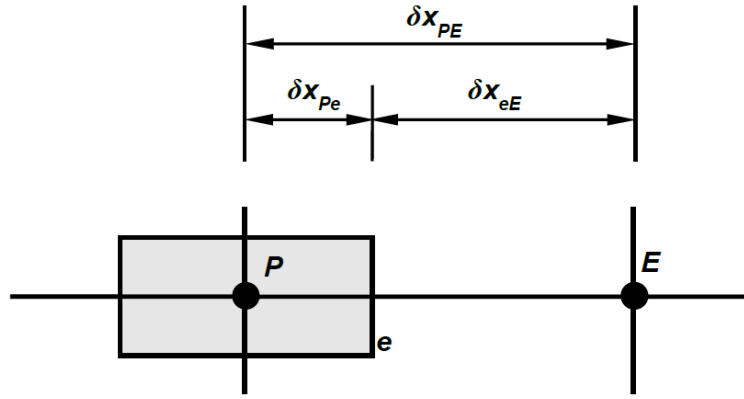


Figure 3.6 Distances for interface “e”.

Heat flux at the interface “e” can be obtained as

$$q_e'' = \Gamma_e \left(\frac{T_P - T_E}{\delta x_{PE}} \right) \quad (3.27)$$

and another heat flux equation can be written, if the control volume that surround the grid point P is filled with a material of uniform diffusion coefficient Γ_P , and the one around E with a material of diffusion coefficient Γ_E , so the steady heat flux for the composite slab between the points P and E leads to be;

$$q_e'' = \frac{T_P - T_E}{\delta x_{PE}/\Gamma_P + \delta x_{eE}/\Gamma_E} \quad (3.28)$$

Eqs. (3.26) to (3.28) can be arranged to express the desired Γ_e as

$$\Gamma_e = \left(\frac{1 - f_e}{\Gamma_P} + \frac{f_e}{\Gamma_E} \right)^{-1} \quad (3.29)$$

As a particular grid structure, if the interface e is placed midway between P and E , then interpolation factor becomes, $f_e = 0.5$. For this particular case, the Eq. (3.29) can be re-arranged as follows:

$$\Gamma_e^{-1} = 0.5 \left(\frac{1}{\Gamma_P} + \frac{1}{\Gamma_E} \right) \quad \text{or} \quad \Gamma_e = \frac{2\Gamma_P\Gamma_E}{\Gamma_P + \Gamma_E} \quad (3.30)$$

Thus, Γ_e is gained as a harmonic mean of Γ_P and Γ_E , rather than the arithmetic mean, for a uniform grid structure (Patankar 1980).

Eq. (3.25) can be re-arranged to obtain the general form as

$$\left(\frac{\Gamma_e}{\delta x_{PE}} A_e + \frac{\Gamma_w}{\delta x_{WP}} A_w - S_P \right) \phi_P = \left(\frac{\Gamma_w}{\delta x_{WP}} A_w \right) \phi_W + \left(\frac{\Gamma_e}{\delta x_{PE}} A_e \right) \phi_E + S_u \quad (3.31)$$

where the coefficients of ϕ_W and ϕ_E can be defined as a_W and a_E , respectively. In addition, the coefficient of ϕ_P is named as a_P , hence the general form of the discretized equation can be written as

$$a_P \phi_P = a_W \phi_W + a_E \phi_E + b \quad (3.32)$$

The coefficients of Eq. (3.32) are given in Table 3.2. The values of S_u and S_P can be obtained from the source model as given in Eq. (3.24). Eqs. (3.31) and (3.32) represent the discretized form of the Eq. (3.20) (Patankar 1980).

Table 3.2 Coefficients for one-dimensional diffusion problem.

a_W	a_E	a_P	b
$\frac{\Gamma_w}{\delta x_{WP}} A_w$	$\frac{\Gamma_e}{\delta x_{PE}} A_e$	$a_W + a_E - S_P$	S_u

3.1.2.1.2 One-dimensional Convection and Diffusion Problem. In the absence of the source terms, the governing equation for steady state convection-diffusion problem can be expressed as

$$\frac{\partial}{\partial x} (\rho u \phi) = \frac{\partial}{\partial x} \left(\Gamma \frac{\partial \phi}{\partial x} \right) \quad (3.33)$$

where u represents the velocity in the x -direction. Besides, the continuity equation becomes to be;

$$\frac{\partial}{\partial x} (\rho u) = 0 \quad (3.34)$$

With applying the finite volume method based on the control volume shown in Figure 3.7, the algebraic form of the Eq. (3.33) can be written as

$$(\rho u \phi A)_e - (\rho u \phi A)_w = \left(\Gamma A \frac{\partial \phi}{\partial x} \right)_e - \left(\Gamma A \frac{\partial \phi}{\partial x} \right)_w \quad (3.35)$$

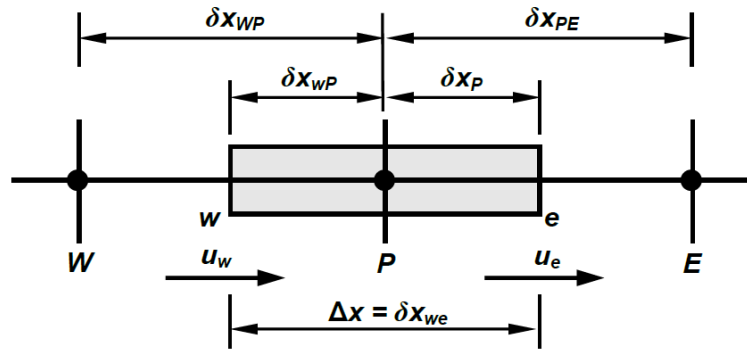


Figure 3.7 A control volume around node “P”.

Before discretization of the Eq. (3.35), it is convenient to define the variables of F and D to represent the convective mass flux per area and the diffusion conductance at cell face as

$$F = \rho u \quad (3.36a)$$

$$D = \frac{\Gamma}{\delta x} \quad (3.36b)$$

With respect to Eq. (3.35), F and D variables for the cell faces can be expressed as follows:

$$F_w = (\rho u)_w, \quad F_e = (\rho u)_e \quad (3.37a)$$

$$D_w = \frac{\Gamma_w}{\delta x_{WP}}, \quad D_e = \frac{\Gamma_e}{\delta x_{PE}} \quad (3.37b)$$

where it is assumed that the areas of the control volume surfaces are equal ($A_w = A_e$). The right hand side of the equation represents the diffusion term, $\Gamma d\phi/dx$, and it can be discretized with using the central differencing approach as in previous example. With considering the Eq. (3.37), integrated convection–diffusion equation, Eq. (3.35), can be re–arranged as follows:

$$F_e \phi_e - F_w \phi_w = D_e (\phi_E - \phi_P) - D_w (\phi_P - \phi_W) \quad (3.38)$$

Besides, continuity equation can be integrated over the control volume as

$$(\rho u A)_e - (\rho u A)_w = 0 \quad (3.39)$$

In the light of Eq. (3.37), continuity equation becomes to be;

$$F_e - F_w = 0 \quad (3.40)$$

General form of the discretized equation is defined as

$$a_P \phi_P = a_W \phi_W + a_E \phi_E + b \quad (3.41)$$

and to transform the Eq. (3.38) into this form, there are several possibilities to be applied. Well-known differencing schemes can be listed as; central, upwind, power law, and QUICK (*Quadratic Upstream Interpolation for Convective Kinetics*) schemes. Patankar (1980) summarized the coefficients of the Eq. (3.41) for central, upwind, and power schemes as follows:

$$a_E = D_e A(|P_e|) + \max[-F_e, 0] \quad (3.42a)$$

$$a_W = D_w A(|P_w|) + \max[F_w, 0] \quad (3.42b)$$

$$a_P = a_E + a_W + (F_e - F_w) \quad (3.42c)$$

where the function of $A(|P|)$ differs for each differencing schemes. In Table 3.3, expressions for $A(|P|)$ are listed for three common used differencing schemes.

Table 3.3 Function of $A(|P|)$ for different schemes.

Scheme	Formula for $A(P)$
Central difference	$1 - 0.5 P $
Upwind	1
Power law	$\max[0, (1 - 0.1 P)^5]$

In this problem, velocity field is assumed as known and the transport property of ϕ is calculated in domain. The transport property (e.g. *temperature*) depends on the magnitude and direction of the velocity field. However, in real engineering applications, the velocity field is not known. Therefore, to compute the transport property variation inside the domain, the first step is determining the flow field. There are some popular algorithms to predict the velocity field and the most popular one is known as SIMPLE algorithm. SIMPLE (*Semi-Implicit Method for Pressure-Linkage Equations*) algorithm was developed by Patankar & Spalding (1972). In following section, details about the SIMPLE algorithm and the usage of staggered grid arrangement are represented.

3.1.2.2 SIMPLE Algorithm

Transport equations for each velocity component, x - and y -momentum equations, can be derived from the general transport equation given in Eq. (3.18). By replacing the variable ϕ into u and v , following governing equations can be obtained for two-dimensional, laminar, and steady flow with incompressible fluid,

For mass:

$$\frac{\partial}{\partial x}(\rho u) + \frac{\partial}{\partial y}(\rho v) = 0 \quad (3.43)$$

For x -momentum:

$$\frac{\partial}{\partial x}(\rho uu) + \frac{\partial}{\partial y}(\rho vu) = -\frac{\partial p}{\partial x} + \frac{\partial}{\partial x}\left(\mu \frac{\partial u}{\partial x}\right) + \frac{\partial}{\partial y}\left(\mu \frac{\partial u}{\partial y}\right) \quad (3.44)$$

For y -momentum:

$$\frac{\partial}{\partial x}(\rho uv) + \frac{\partial}{\partial y}(\rho vv) = -\frac{\partial p}{\partial y} + \frac{\partial}{\partial x}\left(\mu \frac{\partial v}{\partial x}\right) + \frac{\partial}{\partial y}\left(\mu \frac{\partial v}{\partial y}\right) \quad (3.45)$$

The discretization procedure illustrated in previous section is valid to solve these transport equations. The real difficulty in the calculation of the velocity field lies in the unknown pressure field (Patankar, 1980). Governing equations can be discretized for the domain with utilizing the finite volume approach. The first step of the SIMPLE algorithm is defining the proper control volumes for scalar variables, such as, pressure, temperature, density, etc. Among many grid arrangements, staggered arrangement is the most popular and wide accepted method to obtain realistic pressure and velocity field inside the computational domain. In staggered grid arrangement, while the velocity components are defined at the control volume faces, the rest of variables, or *scalars*, are stored at the central node of the control volume. A typical staggered grid arrangement is represented in Figure 3.8 and 3.9 for two-dimensional computational domain. The horizontal velocity component from the x -momentum equation is evaluated at the east, e , and the west, w , faces of the control volume (Figure 3.8). Besides, the vertical velocity component from the y -momentum equation is defined at the north, n , and south, s , faces of the control volume (Figure 3.9).

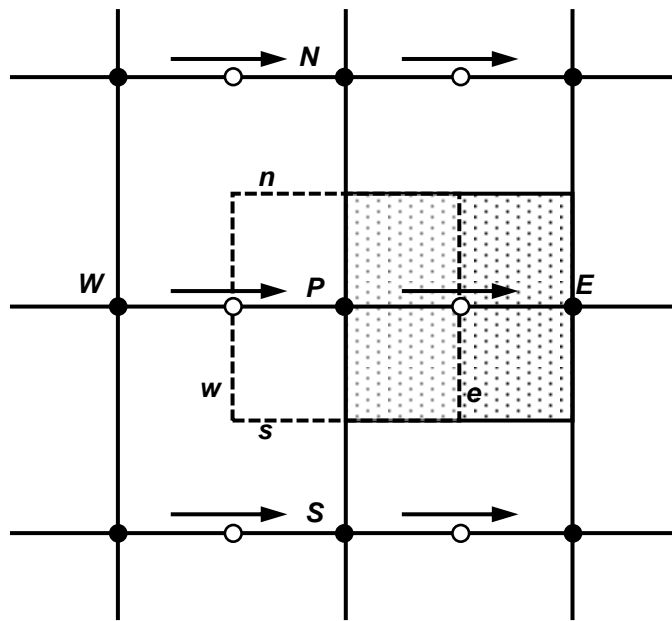


Figure 3.8 Control volume for x -velocity component.

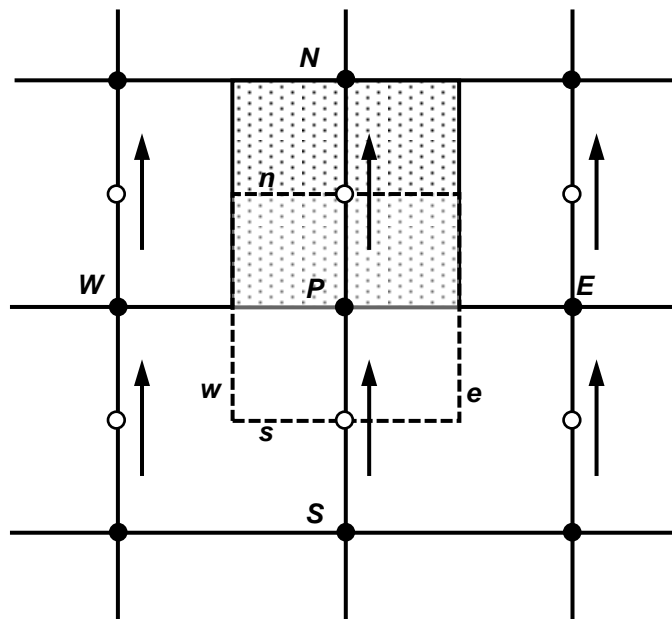


Figure 3.9 Control volume for y -velocity component.

The PRESTO (*PREssure STaggering Option*) scheme uses the discrete continuity balance for a “*staggered*” control volume about the face to compute the “*staggered*” (i.e., *face*) pressure. This procedure is similar in spirit to the staggered-grid schemes used with structured meshes (ANSYS Inc., 2009).

For staggered grid, discretized x - and y -momentum equations can be expressed as follows:

$$a_e u_e = \sum a_{nb} u_{nb} + b + (p_P - p_E) A_e \quad (3.46a)$$

$$a_n v_n = \sum a_{nb} v_{nb} + b + (p_P - p_N) A_n \quad (3.46b)$$

where nb subscript indicated the neighbor cell coefficients. a_e , a_n , and a_{nb} contain combinations of the convective flux per unit mass, F , and the diffusive conductance, D , at the u - and v -control cell faces.

Discretized momentum equations, Eq. (3.46), can be solved only when the pressure field is given, or is somehow estimated. To initiate the SIMPLE algorithm, momentum equations are solved using the guessed pressure field, p^* , to obtain the guessed velocities, u^* and v^* , which are called as “starred velocities”

$$a_e u_e^* = \sum a_{nb} u_{nb}^* + b + (p_P^* - p_E^*) A_e \quad (3.47a)$$

$$a_n v_n^* = \sum a_{nb} v_{nb}^* + b + (p_P^* - p_N^*) A_n \quad (3.47b)$$

After computing the estimated velocity field, next step is applying the pressure and velocity correction for estimated the velocity and pressure values as follows:

$$p = p^* + p' \quad (3.48a)$$

$$u = u^* + u' \quad (3.48b)$$

$$v = v^* + v' \quad (3.48c)$$

where u , v and p designate the corrected the velocity components and pressure. On the other hand, u' , v' , and p' are the corrections for the velocity and pressure.

Eqs. (3.47a) and (3.47b) can be subtracted from Eqs. (3.46a) and (3.46b) and re-arranged with considering the correction Eq. (3.48) to be;

$$a_e u_e' = \sum a_{nb} u_{nb}' + b + (p_P' - p_E') A_e \quad (3.49a)$$

$$a_n v_n' = \sum a_{nb} v_{nb}' + b + (p_P' - p_N') A_n \quad (3.49b)$$

where the $\sum a_{nb} u_{nb}'$ and $\sum a_{nb} v_{nb}'$ terms are dropped as discussed in Patankar (1980). Omission of these terms is the main approximation of the SIMPLE algorithm

(Versteeg & Malalasekera, 2007). With dropping these two terms, velocity correction equations can be written as

$$u_e = u_e^* + d_e (p'_P - p'_E) \quad (3.50a)$$

$$v_n = v_n^* + d_n (p'_P - p'_N) \quad (3.50b)$$

where $d_e = A_e/a_e$ and $d_n = A_n/a_n$. Finally, continuity equation, Eq. (3.43) can be discretized to yield an equation for pressure correction as

$$a_P p'_P = a_E p'_E + a_W p'_W + b' \quad (3.51)$$

General solution procedure for SIMPLE algorithm is illustrated in Figure 3.10. Method is based on an iterative solution procedure. In FLUENT CFD code, each governing equation is solved “*decoupled*” or “*segregated*” from other equations, hence this solution algorithm is named as segregated.

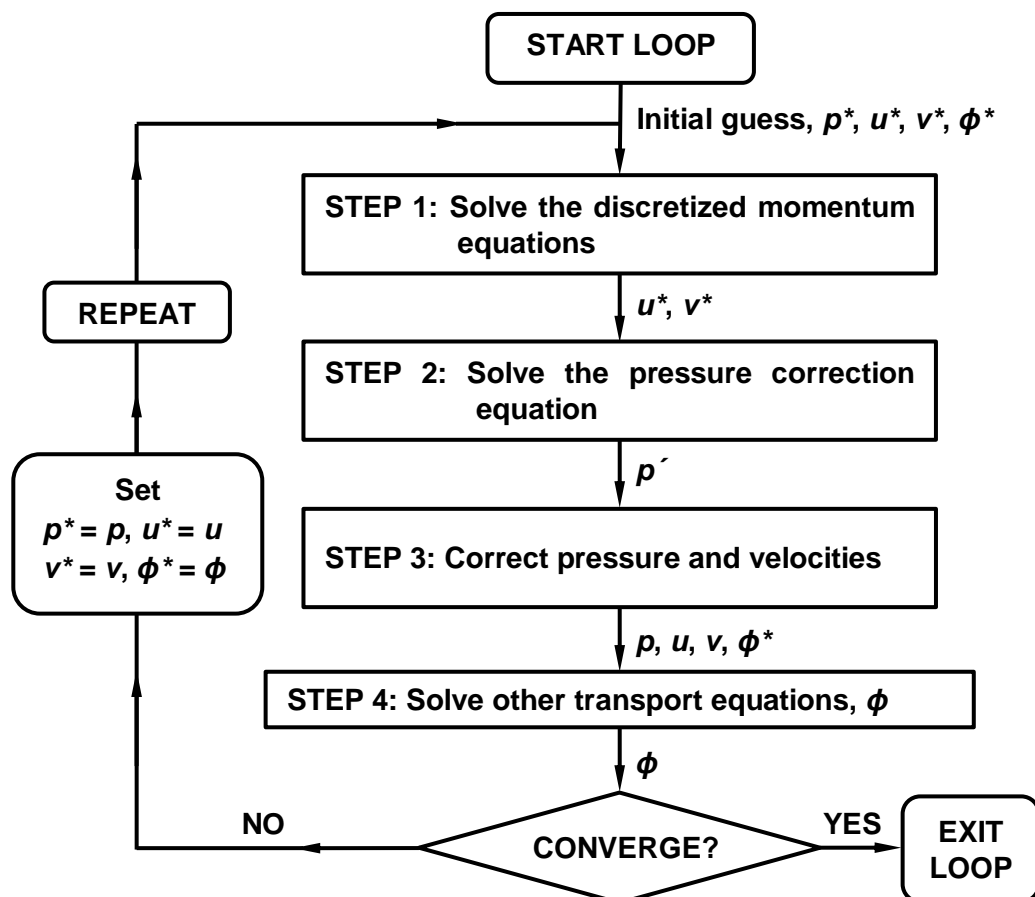


Figure 3.10 Flow chart of the SIMPLE algorithm.

The segregated algorithm is memory-efficient, since the discretized equations need only be stored in the memory one at a time. However, the solution convergence is relatively slow, in as much as the equations are solved in a decoupled manner (ANSYS Inc., 2009). In Figure 3.11, solution procedure of FLUENT code is illustrated in the case of usage of UDFs (*User Defined Functions*).

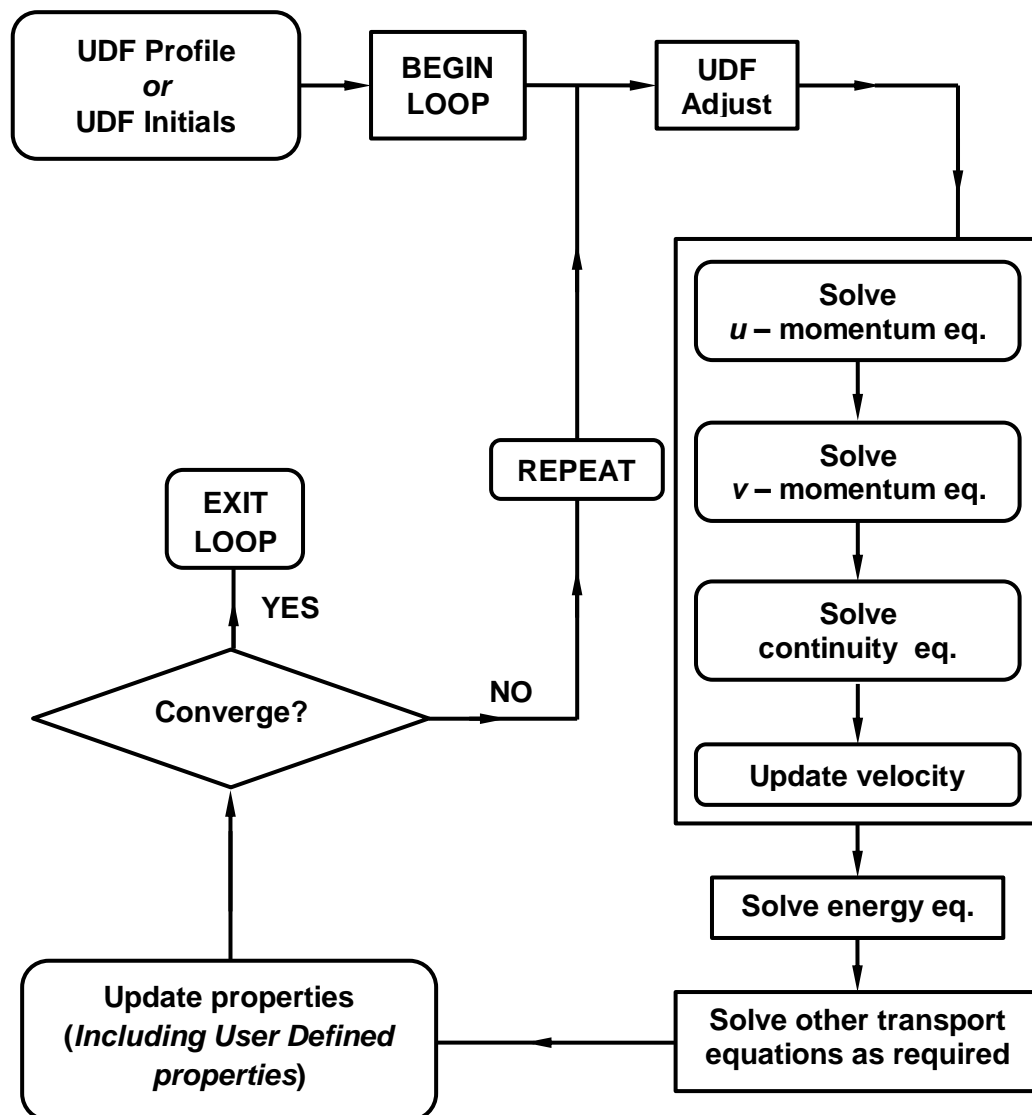


Figure 3.11 Solution procedure of FLUENT CFD code (adapted from ANSYS Inc., 2009).

3.1.3 Local Rate of Entropy Generation in Convective Heat Transfer

Considering two-dimensional flow, a small differential element with dimensions of “ $dxdy$ ” can be select as given in Figure 3.12. For this differential element, entropy generation rate per unit volume \dot{S}_{gen}''' [$\text{Wm}^{-3}\text{K}^{-1}$] can be define as

$$\dot{S}_{gen}'''(dxdy) = \frac{\partial(\rho s)}{\partial t} dxdy + (\dot{S}_{out} - \dot{S}_{in}) \quad (3.52)$$

where $(\dot{S}_{out} - \dot{S}_{in})$ consist of diffusion and advection components,

$$\dot{S}_{out} - \dot{S}_{in} = (\dot{S}_{out} - \dot{S}_{in})_{adv} + (\dot{S}_{out} - \dot{S}_{in})_{diff} \quad (3.53)$$

Advection component of entropy can be written as

$$(\dot{S}_{out} - \dot{S}_{in})_{adv} = (\dot{m}s)_{out} - (\dot{m}s)_{in} \quad (3.54)$$

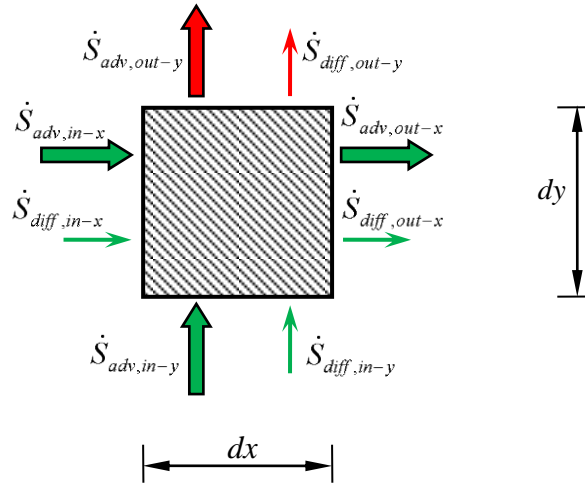


Figure 3.12 Differential element for entropy balance.

For two-dimensional control volume convective entropy define as

$$\begin{aligned} (\dot{S}_{out} - \dot{S}_{in})_{adv} = & \left\{ \left[(\dot{m}s)_x + \frac{\partial(\dot{m}s)_x}{\partial x} dx \right] - (\dot{m}s)_x \right\} \\ & + \left\{ \left[(\dot{m}s)_y + \frac{\partial(\dot{m}s)_y}{\partial y} dy \right] - (\dot{m}s)_y \right\} \end{aligned} \quad (3.55)$$

where $\dot{m}_x = (\rho u) dy$ and $\dot{m}_y = (\rho v) dx$

$$(\dot{S}_{out} - \dot{S}_{in})_{adv} = \frac{\partial(\rho us)}{\partial x} dxdy + \frac{\partial(\rho vs)}{\partial y} dxdy \quad (3.56)$$

hence, advection competent becomes,

$$(\dot{S}_{out} - \dot{S}_{in})_{adv} = \left[\rho s \frac{\partial(u)}{\partial x} + \rho u \frac{\partial(s)}{\partial x} + \rho s \frac{\partial(v)}{\partial y} + \rho v \frac{\partial(s)}{\partial y} \right] dx dy \quad (3.57)$$

Diffusion component of entropy can be written as

$$(\dot{S}_{out} - \dot{S}_{in})_{diff} = \left(\frac{Q}{T} \right)_{out} - \left(\frac{Q}{T} \right)_{in} \quad (3.58)$$

for two-dimensional control volume entropy transfer with diffusion yields,

$$(\dot{S}_{out} - \dot{S}_{in})_{diff} = \left[\left(q_x + \frac{\partial q_x}{\partial x} dx \right) \frac{dy}{T + \frac{\partial T}{\partial x} dx} - \frac{q_x}{T} dy \right] + \left[\left(q_y + \frac{\partial q_y}{\partial y} dy \right) \frac{dx}{T + \frac{\partial T}{\partial y} dy} - \frac{q_y}{T} dx \right] \quad (3.59)$$

with assuming $T + (\partial T / \partial x) dx \approx T$, diffusion component obtained as

$$(\dot{S}_{out} - \dot{S}_{in})_{diff} = \left[\frac{1}{T} \left(\frac{\partial q_x}{\partial x} + \frac{\partial q_y}{\partial y} \right) - \frac{1}{T^2} \left(q_x \frac{\partial T}{\partial x} + q_y \frac{\partial T}{\partial y} \right) \right] dx dy \quad (3.60)$$

Substituting Eqs. (3.57) and (3.60) into Eq. (3.52) yields,

$$\begin{aligned} \dot{S}_{gen}^m(dx dy) = & \frac{\partial(\rho s)}{\partial t} dx dy + \left[\frac{1}{T} \left(\frac{\partial q_x}{\partial x} + \frac{\partial q_y}{\partial y} \right) - \frac{1}{T^2} \left(q_x \frac{\partial T}{\partial x} + q_y \frac{\partial T}{\partial y} \right) \right] dx dy \\ & + \left[\rho s \frac{\partial(u)}{\partial x} + \rho u \frac{\partial(s)}{\partial x} + \rho s \frac{\partial(v)}{\partial y} + \rho v \frac{\partial(s)}{\partial y} \right] dx dy \end{aligned} \quad (3.61)$$

$$\begin{aligned} \dot{S}_{gen}^m = & \frac{1}{T} \left(\frac{\partial q_x}{\partial x} + \frac{\partial q_y}{\partial y} \right) - \frac{1}{T^2} \left(q_x \frac{\partial T}{\partial x} + q_y \frac{\partial T}{\partial y} \right) + s \left[\frac{\partial(\rho)}{\partial t} \rho \frac{\partial(u)}{\partial x} + \rho \frac{\partial(v)}{\partial y} \right] \\ & + \rho \left[\frac{\partial(s)}{\partial t} + u \frac{\partial(s)}{\partial x} + v \frac{\partial(s)}{\partial y} \right] \end{aligned} \quad (3.62)$$

Owing to the continuity equation, the third term in Eq. (3.62) drops,

$$\dot{S}_{gen}^m = \frac{1}{T} \left(\frac{\partial q_x}{\partial x} + \frac{\partial q_y}{\partial y} \right) - \frac{1}{T^2} \left(q_x \frac{\partial T}{\partial x} + q_y \frac{\partial T}{\partial y} \right) + \rho \left[\frac{\partial(s)}{\partial t} + u \frac{\partial(s)}{\partial x} + v \frac{\partial(s)}{\partial y} \right] \quad (3.63)$$

in vector notation, the volumetric rate of entropy generation can be expressed as

$$\dot{S}_{gen}^m = \frac{1}{T} \nabla \cdot \mathbf{q} - \frac{1}{T^2} \mathbf{q} \cdot \nabla T + \rho \frac{Ds}{Dt} \quad (3.64)$$

From the first law of thermodynamics,

$$\rho \frac{Du}{Dt} = -\nabla \cdot \mathbf{q} - P(\nabla \cdot \mathbf{v}) + \mu \Phi \quad (3.65)$$

and internal energy can be written as in terms of entropy as

$$du = Tds - Pd(1/\rho) \quad (3.66)$$

hence,

$$\rho \frac{Ds}{Dt} = \frac{\rho}{T} \frac{Du}{Dt} + \frac{P}{\rho T} \frac{D\rho}{Dt} \quad (3.67)$$

Combining Eqs. (3.65) and (3.67) into Eq. (3.64),

$$\dot{S}_{gen}^m = \frac{1}{T} \nabla \cdot \mathbf{q} - \frac{1}{T^2} \mathbf{q} \cdot \nabla T + \frac{1}{T} [-\nabla \cdot \mathbf{q} - P(\nabla \cdot \mathbf{v}) + \mu \Phi] + \frac{P}{\rho T} \frac{D\rho}{Dt} \quad (3.68)$$

Finally, volumetric entropy generation can be written as follows:

$$\dot{S}_{gen}^m = -\frac{1}{T^2} \mathbf{q} \cdot \nabla T + \frac{\mu}{T} \Phi \quad (3.69)$$

from Fourier Law,

$$\mathbf{q} = -k \nabla T \quad (3.70)$$

hence, volumetric entropy generation becomes,

$$\dot{S}_{gen}^m = \frac{k}{T^2} (\nabla T)^2 + \frac{\mu}{T} \Phi \quad (3.71)$$

or,

$$\dot{S}_{gen}^m = \frac{k}{T^2} \left[\left(\frac{\partial T}{\partial x} \right)^2 + \left(\frac{\partial T}{\partial y} \right)^2 \right] + \frac{\mu}{T} \left\{ 2 \left[\left(\frac{\partial u}{\partial x} \right)^2 + \left(\frac{\partial v}{\partial y} \right)^2 \right] + \left(\frac{\partial u}{\partial y} + \frac{\partial v}{\partial x} \right)^2 \right\} \quad (3.72)$$

3.2 Numerical Investigation of Ice–on–coil LHTES System

In this part of the dissertation, energy, and entropy analyses are carried out for charging period of an ice–on–coil LHTES system with using thermal resistance network technique (Jekel et al. 1993, Drees & Braun, 1995, Neto & Krarti, 1997a).

3.2.1 Theory and Background

Numerical predictions are performed with utilizing the thermal resistance network technique developed by Jekel et al. (1993), Drees & Braun (1995), and Neto & Krarti (1997a). According to these reference works, following basic assumptions are conducted in the current analysis,

- (1) Quasi–steady state condition is valid for each segment,
- (2) Heat gain from surroundings to the tank is uniformly distributed into the system,
- (3) Sensible heat storage inside the tube material and the heat transfer fluid (HTF) are small enough to be neglected,
- (4) Thermo–physical properties of ethylene–glycol/water mixture are defined as functions of the inlet temperature of the HTF. On the other hand, for water, only density and thermal expansion coefficient are selected as temperature dependent. Thermo–physical properties of ethylene–glycol/water mixture (40% of ethylene glycol by volume) are given in Table 3.4, for selected temperature values.

Table 3.4 Thermo–physical properties of the ethylene glycol – water mixture.

Temperature	Density, ρ	Viscosity, μ	Specific Heat, c	Thermal Conductivity, k
(°C)	(kg/m ³)	(kg/ms)	(kJ/kgK)	(W/mK)
–20	1071.98	0.01575	3.334	0.371
–15	1070.87	0.01174	3.351	0.377
–10	1069.63	0.00906	3.367	0.383
–5	1068.28	0.00718	3.384	0.389
0	1066.80	0.00583	3.401	0.395

Source: ASHRAE (1997)

In the model, the coil is divided into small segments as seen in Figure 3.13. Quasi-steady state energy balance is applied for each segment and, time step to simulate the solidification process around coil. First, the radius of ice is determined iteratively for each segment. Then, the temperature value of the HTF at the outlet section of each segment is calculated and set as the inlet temperature of the next segment.

The energy balance for an individual segment (i) can be written in general form as

$$E_{HTF,i}(t) \pm Q_{gain,i}(t) = \Delta E_{segment,i}(t) \quad (3.73a)$$

or

$$\dot{Q}_{in,i} - \dot{Q}_{out,i} + \dot{Q}_{gain,i} = \left(\frac{dH}{dt} \right)_{segment,i} \quad (3.73b)$$

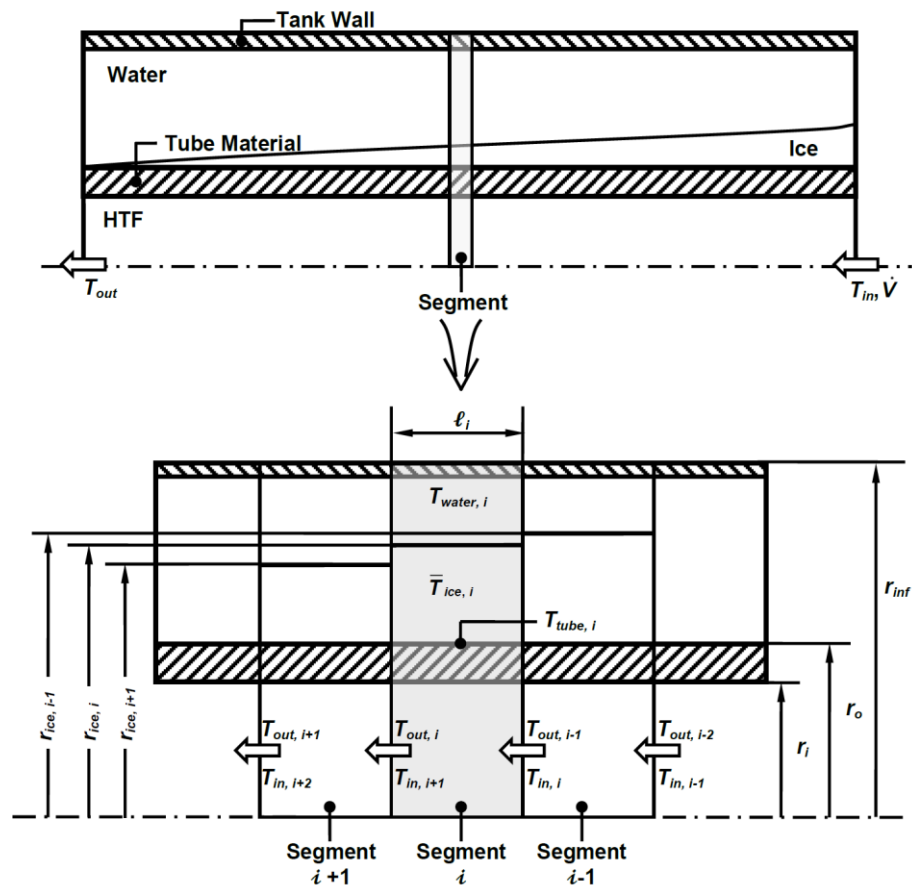


Figure 3.13 Mathematical model of the ice-on-coil LHTES system.

In terms of the sensible and latent heat capacitances, the energy equation becomes to be;

$$\begin{aligned} \dot{Q}_{gain,i} - \dot{Q}_{HTF,i} = & \left(mc \frac{dT}{dt} \right)_{water,i} + h_{sf} \left(\frac{dm}{dt} \right)_{ice,i} + \left(mc \frac{dT}{dt} \right)_{ice,i} \\ & + \left(mc \frac{dT}{dt} \right)_{HTF,i} + \left(mc \frac{dT}{dt} \right)_{tube,i} \end{aligned} \quad (3.74)$$

where $\dot{Q}_{gain,i}$ is the instant heat gain from surroundings to segment and $\dot{Q}_{HTF,i}$ is the net rejected rate of heat transfer from the segment. Right hand side of the equation designates the total internal energy variations inside the PCM, HTF, and tube material, respectively. In comparison with the total mass of water, total masses of the tube material and HTF are small enough to be neglected. Therefore, in analyses, last two terms in Eq. (3.74) can be reduced. Only sensible and latent heat transfer variations of the PCM are taken into account in current computations.

Energy balance equations are solved for each circular computational segments with dimensions of, $r_{inf} = \Delta r/2$ and $\ell_i = \ell/N_{segment}$. Here, Δr indicates the distance between the centers of the tubes, *pitch*, in horizontal or vertical directions. In the light of the current experimental system, r_{inf} is set as 0.03 m. On the other hand, ℓ and $N_{segment}$ designate the length of tubes and the number of segments in the tube, respectively.

The storage process can be divided into three individual periods. In the first period, super-heated water cools down (*sensible heat storage*) through the phase change temperature. In the second period, un-constrained ice formation occurs together with the cooling of the solid and the liquid phases of water (*sensible and latent heat storage*). Lastly, in the third period, radius of ice reaches to the r_{inf} value so, only sub-cooling of ice taking into account inside the corresponding segment. As the main concepts for the first and third periods are similar, detailed formulations and thermal network representations are illustrated only for the first and second periods of the storage.

3.2.1.1 Period 1 – Sensible Heat Storage

In Figure 3.14, the components of Eq. (3.74) are represented as thermal resistance network in general form. For simplicity, internal energy variations in the tube material and HTF can be neglected. Hence, energy equation becomes to be;

$$\dot{Q}_{gain,i} - \dot{Q}_{HTF,i} = \left(mc \frac{dT}{dt} \right)_{water,i} \quad (3.75)$$

or

$$\dot{Q}_{gain,i} - \dot{Q}_{HTF,i} = \dot{Q}_{water, sen, i} \quad (3.76)$$

The heat transfer rate between the HTF and water can be defined with using the enthalpy variation of the HTF as

$$\dot{Q}_{HTF,i} = (\dot{m}c)_{HTF} [T_{out,i} - T_{in,i}] \quad (3.77)$$

or with using the overall heat transfer coefficient definition as follows:

$$\dot{Q}_{HTF,i} = (UA)_{water \rightarrow HTF} [T_{water,i} - \bar{T}_{HTF,i}] \quad (3.78)$$

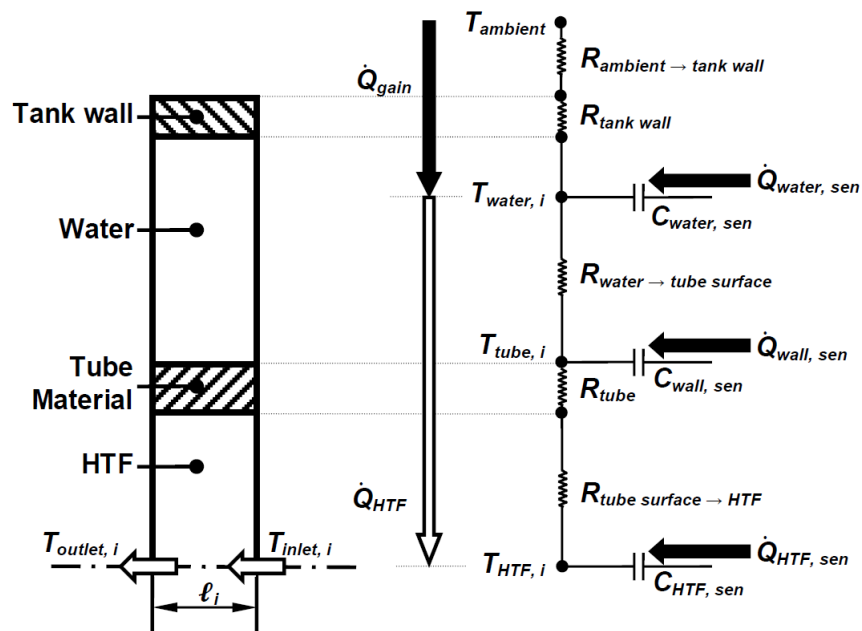


Figure 3.14 Thermal resistance networks for Period 1.

where $\bar{T}_{HTF,i}$ represents the mean temperature value of the HTF, $(T_{in,i} + T_{out,i})/2$. Overall heat transfer coefficient, $(UA)_{water \rightarrow HTF}$, can be obtained with using the thermal resistance network given in Figure 3.14, as

$$(UA)_{water \rightarrow HTF} = \left[R_{tube\ surface \rightarrow HTF} + R_{tube} + R_{water \rightarrow tube\ surface} \right]^{-1} \quad (3.79)$$

The thermal resistances of $R_{tube\ surface \rightarrow HTF}$, R_{tube} and $R_{water \rightarrow tube\ surface}$ are calculated with using the following equations:

$$R_{tube\ surface \rightarrow HTF} = \left[2\pi r_i \ell_i h_{HTF} \right]^{-1} \quad (3.80a)$$

$$R_{tube} = \frac{\ln(r_o/r_i)}{2\pi k_{tube} \ell_i} \quad (3.80b)$$

$$R_{water \rightarrow tube\ surface} = \left[2\pi r_o \ell_i h_{water} \right]^{-1} \quad (3.80c)$$

where h_{HTF} and h_{water} designate the heat transfer coefficients for the *HTF* and *water*, respectively.

Even though Jekel et al. (1993) analyzed the solidification process for a spiral shaped coil, they computed the heat transfer coefficient of the HTF, h_{HTF} , with assuming a straight pipe. On the other hand, Drees & Braun (1995) defined the heat transfer coefficient of the HTF for a curved tube. They concluded that, in the curved tubes, the presence of the centrifugal forces causes higher velocities, and this can increase the overall Nusselt number 500% in some special cases. Hence, in the current analysis, the heat transfer coefficient for the internal flow inside the curved pipe is determined with using the Nusselt correlations represented by Seban & McLaughlin (1963). Seban & McLaughlin defined the Nusselt correlations for laminar and turbulent flow conditions inside the curved spirals. Laminar condition is valid under the following range:

$$11.6 < \text{Re} \sqrt{\frac{D_i}{D_H}} < 2000 \quad (3.81)$$

and for the laminar region, Nusselt correlation is defined as follows:

$$\overline{\text{Nu}} = 0.13 \left[\frac{f}{8} \text{Re}^2 \right]^{1/3} \text{Pr}^{1/3} \quad (3.82)$$

where f is the Darcy–Weisbach friction factor and defined as

$$\frac{f}{f_s} = \left\{ 1 - \left[1 - \left(\frac{11.6}{\text{Re} \sqrt{D_i/D_H}} \right)^{0.45} \right]^{2.22} \right\}^{-1} \quad (3.83)$$

with $f_s = 64/\text{Re}$. Besides, the initial point of the turbulent flow determined by the critical Reynolds number as

$$\text{Re}_{cr} = 2 \times 10^4 \left(\frac{D_i}{D_H} \right)^{0.32} \quad (3.84)$$

and the following Nusselt correlation is valid for $\text{Re}(D_i/D_H)^2 > 6$

$$\overline{\text{Nu}} = \frac{f}{8} \text{Re} \text{Pr}^{0.4} \quad (3.85)$$

On the other hand, the heat transfer coefficient of water at the outer surface of the tube is determined with using the Churchill and Chu correlation, which is cited by Incropera & DeWitt (2002),

$$\overline{\text{Nu}}_D = \left\{ 0.60 + \frac{0.387 \text{Ra}_D^{1/6}}{\left[1 + (0.559/\text{Pr})^{9/16} \right]^{8/27}} \right\}^2 \quad (3.86)$$

An iterative procedure can be utilized for the Eqs. (3.77) and (3.78) to obtain the outlet temperature value of the HTF from each segment. Afterwards, the outer surface temperature values of the tube can be updated with defining the following energy balance equation between the tube surface and the HTF as

$$\dot{Q}_{HTF,i} = (UA)_{tube\ surface \rightarrow HTF} \left[T_{tube,i} - \bar{T}_{HTF,i} \right] \quad (3.87)$$

where the overall heat transfer coefficient between the HTF and the outer surface of tube, $(UA)_{tube\ surface \rightarrow HTF}$, can be obtained with using the thermal resistance network given in Figure 3.14. On the other hand, the variation of the mean temperature value of water can be obtained with rearranging Eq. (3.75) to be;

$$T_{water,i} = T_{water,i}^0 + \frac{(\dot{Q}_{gain} - \dot{Q}_{HTF}) \Delta t}{(\rho V c)_{water}} \quad (3.88)$$

where $T_{water,i}$ and $T_{water,i}^0$ indicate mean temperature values of water for the current and previous time steps, respectively.

3.2.1.2 Period 2 – Sensible and Latent Heat Storage

For phase change period, energy equation, Eq. (3.74), can be written as

$$\dot{Q}_{gain,i} - \dot{Q}_{HTF,i} = \dot{Q}_{water, sen, i} + \dot{Q}_{latent, i} + \dot{Q}_{ice, sen, i} + \dot{Q}_{HTF, sen, i} + \dot{Q}_{wall, sen, i} \quad (3.89)$$

The right-hand side of the equation represents the sensible and latent energy variations inside the segment. In Figure 3.15, the components of the Eq. (3.89) are illustrated in thermal resistance network.

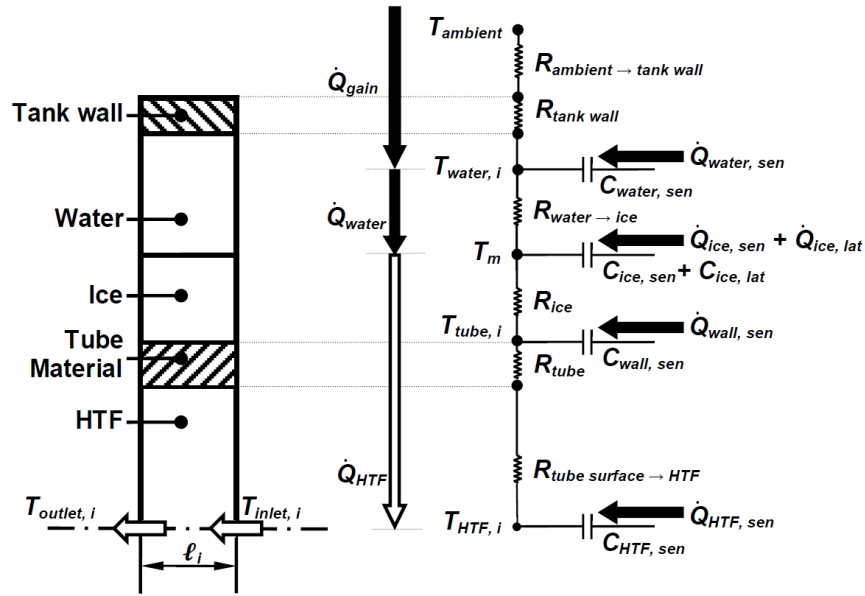


Figure 3.15 Thermal resistance networks for Period 2.

Similar to the Period 1, sensible heat variations inside the tube material and HTF are neglected for the Period 2. Hence, the energy equation reduced as

$$\dot{Q}_{gain,i} - \dot{Q}_{HTF,i} = \dot{Q}_{water, i} + \dot{Q}_{latent, i} + \dot{Q}_{ice, sen, i} \quad (3.90)$$

where components of the Eq. (3.90) can be written as follows:

$$\dot{Q}_{HTF,i} = (UA)_{ice \rightarrow HTF} [T_m - \bar{T}_{HTF,i}] \quad (3.91a)$$

$$\dot{Q}_{water,i} = (2\pi r_{ice,i} \ell_i) h_{water} [T_{water,i} - T_m] \quad (3.91b)$$

$$\dot{Q}_{latent,i} = h_{sf} \frac{m_{ice,i} - m_{ice,i}^0}{\Delta t} \quad (3.91c)$$

$$\dot{Q}_{ice, sen,i} = (mc)_{ice,i} \frac{\bar{T}_{ice,i} - \bar{T}_{ice,i}^0}{\Delta t} \quad (3.91d)$$

The heat transfer coefficient between the heat transfer fluid and the surface of ice, $(UA)_{ice \rightarrow HTF}$, can be obtained with using the thermal resistance network given in Figure 3.15. On the other hand, for quasi-steady state conditions, the mean temperature value of ice can be calculated as

$$\bar{T}_{ice} = T_{tube,i} + (T_{tube,i} - T_m) \left[\frac{1}{2 \ln(r_{ice,i}/r_o)} - \frac{r_{ice,i}^2}{r_{ice,i}^2 - r_o^2} \right] \quad (3.92)$$

The iterative solution procedure can be applied to the Eqs. (3.90) and (3.91) to obtain the radius values of ice, for each segment. Afterwards, the surface temperature of the tube can be updated with defining the energy balance between the tube surface and the HTF, as in Eq. (3.87). The mean temperature of water can be obtained with defining the following energy balance:

$$T_{water,i} = T_{water,i}^0 + \frac{(\dot{Q}_{gain} - \dot{Q}_{water,i}) \Delta t}{(\rho V c)_{water}} \quad (3.93)$$

Internal energy variation inside the tank can be obtained by Eq. (3.74) as

$$\Delta E_{system} = \sum_{t=0}^t \sum_{i=1}^n \left\{ [mc(T - T^0)]_{water,i} + h_{sf} (m - m^0)_{ice,i} + [mc(T - T^0)]_{water,i} \right\} \quad (3.94)$$

where superscript "0" designate the previous time step, and n indicates the number of segments. On the other hand, the total energy delivered by the heat transfer fluid is determined with the integration of Eq. (3.77) to be;

$$E_{HTF}(t) = (\dot{m}c)_{HTF} \int_{t=0}^t [T_{out} - T_{in}] dt \quad (3.95)$$

The energetic effectiveness and energy efficiency are computed to compare the performance of the system in dimensionless scale. Erek & Dincer (2009) defined the energetic effectiveness of the LHTES system, ε_{en} , as the ratio of the actual total stored energy to the maximum possible energy to be stored. Maximum possible stored energy can be obtained when the final temperature of the system reaches to the inlet temperature value of the HTF as

$$\varepsilon_{en} = \frac{\Delta E_{system}(t)}{\Delta E_{system,max}} = \frac{E_{system}(t) - E_{system,i}}{E_{system}(t \rightarrow \infty) - E_{system,i}} \quad (3.96)$$

In addition, energy efficiency can be defined as the ratio of the total stored energy to the total delivered energy to the system by the HTF as

$$\eta = \frac{\Delta E_{system}(t)}{E_{HTF}(t)} \quad (3.97)$$

3.2.1.3 Exergy Analysis

The entropy balance for an individual segment can be written in the following general form,

$$\dot{S}_{in,i} - \dot{S}_{out,i} + \frac{\dot{Q}_{gain}}{T_m} + \dot{S}_{gen,i} = \left(\frac{dS}{dt} \right)_{segment,i} \quad (3.98)$$

hence, entropy generation can be define as

$$\dot{S}_{gen,i} = \left(\dot{S}_{out,i} - \dot{S}_{in,i} \right)_{HTF} - \frac{\dot{Q}_{gain}}{T_m} + \left(\frac{dS}{dt} \right)_{PCM,i} + \left(\frac{dS}{dt} \right)_{wall,i} + \left(\frac{dS}{dt} \right)_{HTF,i} \quad (3.99)$$

The first two terms on the right-hand side of the Eq. (3.99) represent the rate of entropy transfer due to the HTF and the heat gain, respectively. The last three terms correspond to the entropy variations inside the PCM, wall thickness, and the HTF, respectively. In comparison to the total mass of water, masses of the tube material and HTF are small enough to be neglected in entropy generation equation.

The entropy transfer rate of the HTF and entropy storage rate of the PCM can be written as follows:

$$\left(\dot{S}_{out,i} - \dot{S}_{in,i}\right)_{HTF} = (\dot{m}c)_{HTF} \ln\left(\frac{T_{HTF,out,i}}{T_{HTF,in,i}}\right) \quad (3.100)$$

$$\left(\frac{dS}{dt}\right)_{PCM,i} = \frac{S - S^0}{\Delta t} = \frac{\left[mc \ln\left(\frac{T}{T^0}\right) \right]_{water,i} + \frac{h_{sf}}{T_m} (m - m^0)_{ice,i} + \left[mc \ln\left(\frac{T}{T^0}\right) \right]_{ice,i}}{\Delta t} \quad (3.101)$$

where S and S^0 indicate the total entropy values for the present and previous time steps, respectively. Finally, the total entropy generation can be determined by integrating the Eq. (3.99) over time to be;

$$\dot{S}_{gen,i} = \int_{t=0}^t \left[\left(\dot{S}_{out,i} - \dot{S}_{in,i}\right)_{HTF} - \frac{\dot{Q}_{gain}}{T_m} + \left(\frac{dS}{dt}\right)_{PCM,i} \right] dt \quad (3.102)$$

The entropy generation number (N_s) for the storage tank can be defined as the ratio of the total irreversibility to the net exergy input with the HTF (Bejan, 1995) as

$$N_s = \frac{T_o \dot{S}_{gen}}{\dot{E}x_{HTF}} \quad (3.103)$$

where $\dot{E}x_{HTF}$ is the net exergy variation of the HTF and defined as follows:

$$\dot{E}x_{HTF} = \left(\dot{E}x_{in} - \dot{E}x_{out}\right)_{HTF} = (\dot{m}c)_{HTF} \left[\left(T_{HTF,in} - T_{HTF,out}\right) - T_o \ln\left(\frac{T_{HTF,in}}{T_{HTF,out}}\right) \right] \quad (3.104)$$

The exergy efficiency can be defined in terms of the entropy generation number as following (Erek & Dincer, 2008),

$$\psi = 1 - N_s \quad (3.105)$$

On the other hand, exergetic effectiveness of the system is defined as the ratio of the actual total exergy stored to the maximum possible exergy stored (Erek & Dincer, 2009). The exergetic effectiveness can be written as

$$\varepsilon_{ex} = \frac{\Delta Ex_{system}(t)}{\Delta Ex_{system,max}} = \frac{Ex_{system}(t) - Ex_{system,i}}{Ex_{system}(t \rightarrow \infty) - Ex_{system,i}} \quad (3.106)$$

CHAPTER FOUR

RESULTS AND DISCUSSION

In this chapter, experimental and numerical results of the current dissertation are represented in a categorized manner.

4.1 Experimental Results of Shell-and-tube Type LHTES System

For the shell-and-tube type system, first the validation of the interface measurement method is performed by the comparisons of the visual and temperature data. Then, the influence of the natural convection on the formation of solid-liquid interface is introduced for the solidification and melting modes. Furthermore, thermal behavior of the system is investigated during charging and discharging processes for various working and design parameters in terms of the total stored and rejected energies with energy and exergy efficiencies.

4.1.1 Validation of Interface Measurement Method

According to the earlier experimental studies, the most commonly preferred method to obtain the solid-liquid interface in LHTES systems is the photography method (Erek et al., 2005; Khodadadi & Zhang, 2001; Ho & Chen, 1986). Hence, in this study, the photography method is implemented for validating the accuracy of the measurement method. A camera is located in front of the middle section of the system, and photographs are taken at every 15 minutes by opening the covers on the insulation. The radii of ice at the top and bottom directions are scaled from photographs with the aid of the diameter of the tube, as illustrated in Figure 4.1.

Two sets of comparisons are performed for the systems with the shell diameters of 114 mm and 190 mm. For the former one, $D_{shell} = 114$ mm, comparisons between the photograph and measurement probes are obtained for two different flow rates of -5°C inlet temperature experiments. In each experiment, solidification is observed until the 4th electrodes penetrate into the ice. For the latter one, $D_{shell} = 190$ mm,

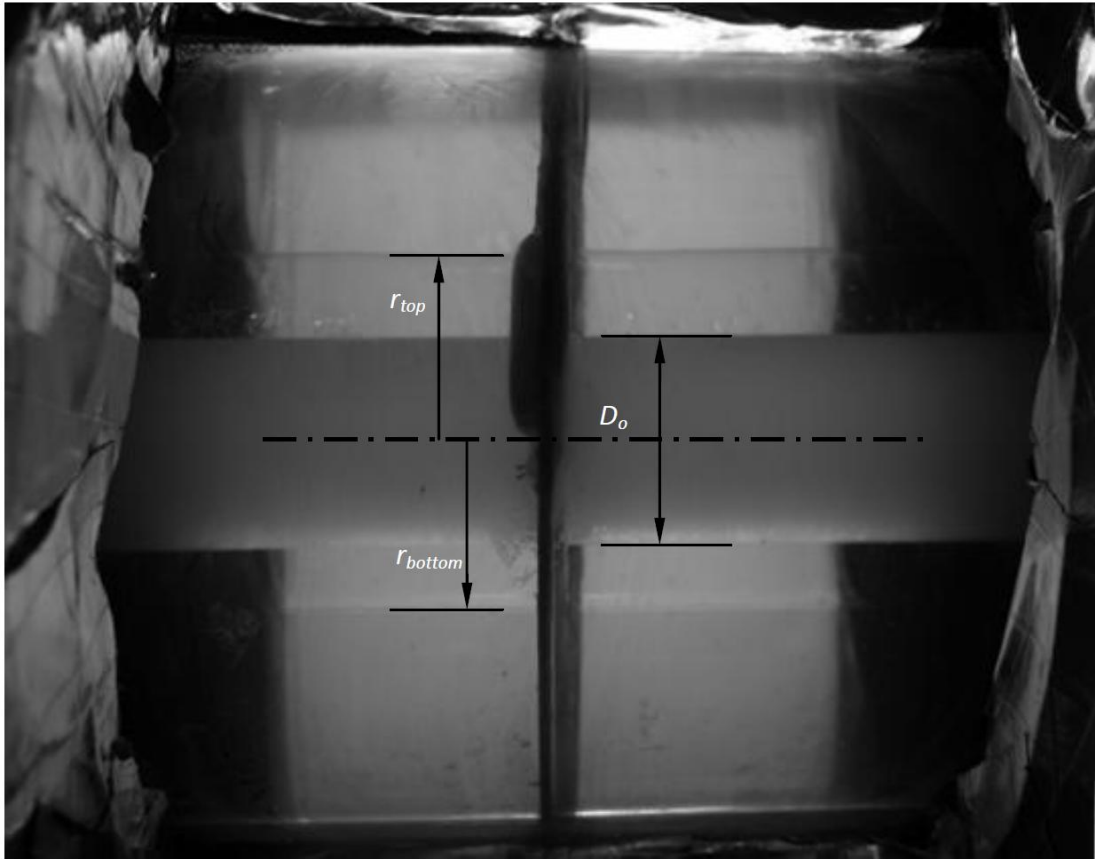


Figure 4.1 Scaling for the top and the bottom radii of the ice with the aid of the pipe diameter.

comparisons are performed for the two flow rates of -10°C inlet temperature experiments.

In Figures 4.2 and 4.3, the radii of ice calculated from the measurement card are given as functions of time for $D_{shell} = 114$ mm case in comparison with the photography data. Four different curves can be seen in each figure, which are; *top* ($\theta = 90^{\circ}$) and *bottom* ($\theta = -90^{\circ}$) radius values obtained from the photography and the electronic measurement methods. In Figures, hollow triangles and circles illustrate the photography data and the solid ones denote the measurement card results. A dynamic curve fitting method (*Exponential Rise to Maximum – 5 Parameters*) is applied to four nodes of the measurement card data to obtain the fitted curves, which are shown as dashed lines. The fitted curves are defined as follows:

$$r(t) = y_0 + a[1 - \exp(-bt)] + c[1 - \exp(-dt)] \quad (4.1)$$

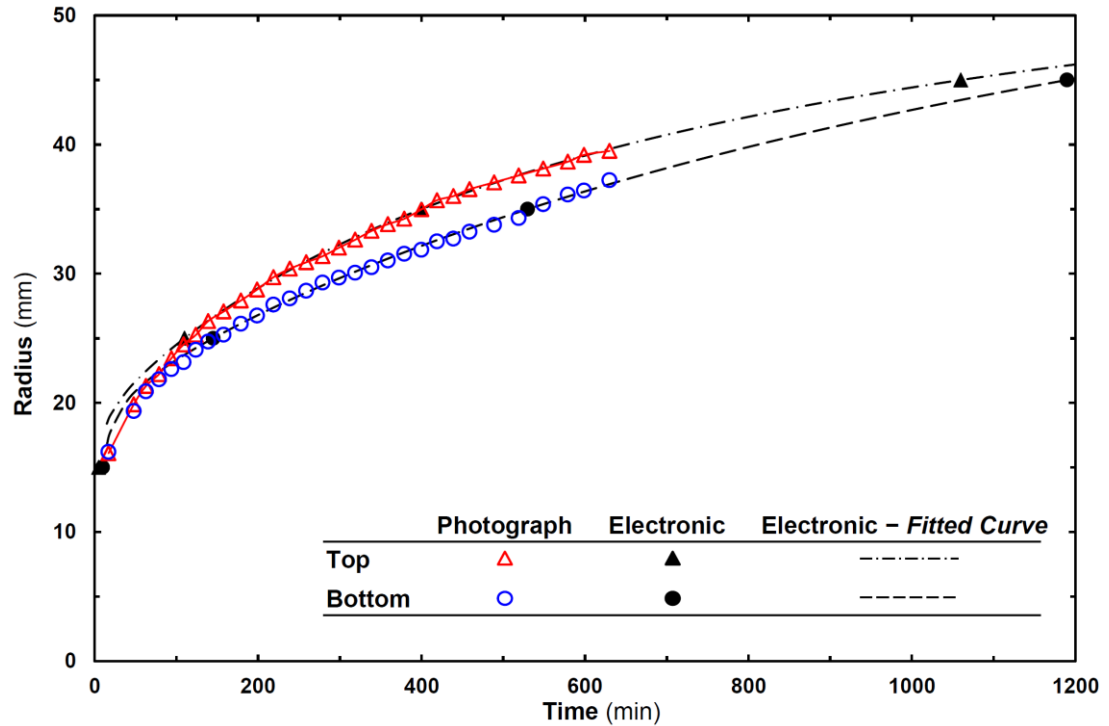
where y_0 , a , b , c and d are the five parameters of the equation and the corresponding values of these parameters are given in Table 4.1.

Table 4.1 Coefficients in Eq. (4.1).

Curves		y_0	a	b	c	d
Figure 4.2	Top	12.5	10.59	0.0111	30.14	0.0010
	Bottom	12.5	7.96	0.0374	34.90	0.0011
Figure 4.3	Top	12.5	14.20	0.011	28.96	0.0011
	Bottom	12.5	10.20	0.014	43.00	0.0008
Figure 4.4	Top	12.5	12.17	0.0073	69.30	2.84E-4
	Bottom	12.5	9.54	0.0122	71.97	1.97E-4
Figure 4.5	Top	12.5	16.57	0.0060	64.71	2.71E-4
	Bottom	12.5	73.04	0.0002	9.39	0.0143

From Figures 4.2 and 4.3, it can be seen that there is a good agreement between two measurement methods. At the top and bottom directions, the solidification tendencies are nearly same. On the other hand, to introduce the relative differences between these two methods, corresponding measurement data are given in Tables 4.2 and 4.3. At the beginning of the solidification, there appear relatively higher differences, but as an average, the relative difference is less than $\pm 3\%$.

On the other hand, for $D_{shell} = 190$ mm case, solid-liquid interface is determined with three different ways; (1) with the electronic measurement cards, (2) with the temperature values of thermocouples, and (3) with scaling of photographs. Time wise variations of the ice radii values are given in Figures 4.4 and 4.5. Six different curves can be seen in each figure, representing, top ($\theta = 90^\circ$) and bottom ($\theta = -90^\circ$) radius values obtained from photography, thermocouples and electronic measurement method. In figures, hollow triangles and circles illustrate the photography results; solid ones denote electronic measurement results. Besides, hollow/solid rectangles designate the results of the thermocouple data. From the Figures 4.4 and 4.5, it can be seen that solidification tendencies have good agreement between the results of the three methods. The solidification tendencies are nearly same at the top and bottom sides of the tube. The relative differences between the photography and the electronic measurement methods are given in Tables 4.4 and 4.5. As an average, the relative difference between photography and electronic method is less than $\pm 4\%$.



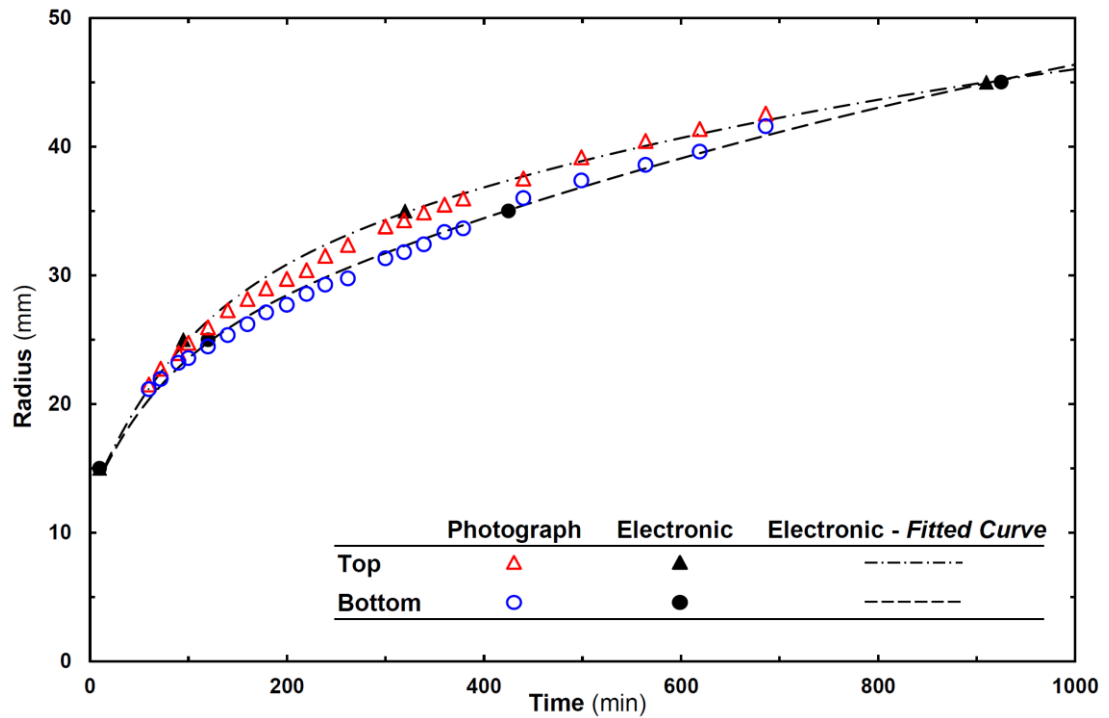
($D_{shell} = 114 \text{ mm}$, $T_{in} = -5^{\circ}\text{C}$ and $\dot{V} = 2 \text{ l/min}$)

Figure 4.2 Validation of the interface measurement method.

Table 4.2 Comparison of the measured radius values with the relative errors.

Time	Top Direction ($\theta = 90^{\circ}$)				Bottom Direction ($\theta = -90^{\circ}$)			
	Radius of Ice		Absolute Difference	Relative Difference	Radius of Ice		Absolute Difference	Relative Difference
	Photo	Electronic			Photo	Electronic		
(min)	(mm)	(mm)	(mm)	%	(mm)	(mm)	(mm)	%
63	22.5	21.3	1.2	5.4	21.6	20.9	0.7	3.5
79	23.4	22.2	1.2	5.2	22.4	21.8	0.6	2.8
94	24.2	23.5	0.7	3.1	23.1	22.6	0.5	2.1
109	25.0	24.5	0.4	1.8	23.7	23.1	0.5	2.3
124	25.7	25.3	0.4	1.6	24.2	24.1	0.2	0.6
139	26.4	26.3	0.0	0.1	24.8	24.7	0.1	0.2
158	27.2	27.1	0.1	0.4	25.4	25.3	0.2	0.7
179	28.1	27.9	0.1	0.5	26.1	26.1	0.0	0.1
199	28.8	28.8	0.1	0.2	26.8	26.8	0.0	0.0
219	29.6	29.7	0.2	0.5	27.4	27.6	0.2	0.8
239	30.3	30.4	0.1	0.3	28.0	28.1	0.1	0.4
259	31.0	30.9	0.1	0.3	28.5	28.7	0.1	0.5
299	32.2	32.0	0.2	0.7	29.6	29.7	0.1	0.2
319	32.8	32.6	0.2	0.6	30.2	30.1	0.1	0.3
339	33.4	33.3	0.1	0.3	30.7	30.5	0.2	0.6
359	33.9	33.8	0.1	0.3	31.2	31.0	0.2	0.5
379	34.5	34.3	0.2	0.6	31.7	31.5	0.1	0.4
439	35.9	36.0	0.1	0.2	33.1	32.7	0.3	1.0
489	37.0	37.1	0.0	0.1	34.1	33.8	0.4	1.1
579	38.8	38.7	0.1	0.3	36.0	36.1	0.1	0.4
599	39.1	39.2	0.1	0.2	36.4	36.4	0.1	0.2

($D_{shell} = 114 \text{ mm}$, $T_{in} = -5^{\circ}\text{C}$ and $\dot{V} = 2 \text{ l/min}$)



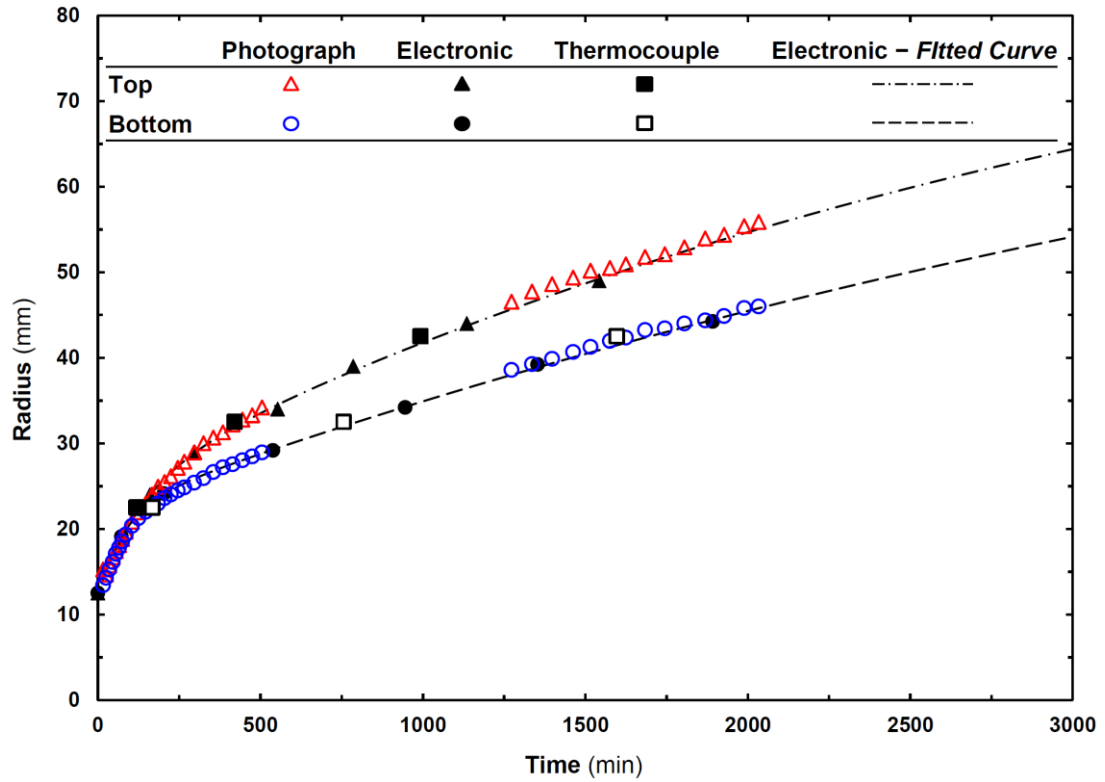
($D_{shell} = 114 \text{ mm}$, $T_{in} = -5^\circ\text{C}$ and $\dot{V} = 4 \text{ l/min}$)

Figure 4.3 Validation of the interface measurement method.

Table 4.3 Comparison of the measured radius values with the relative errors.

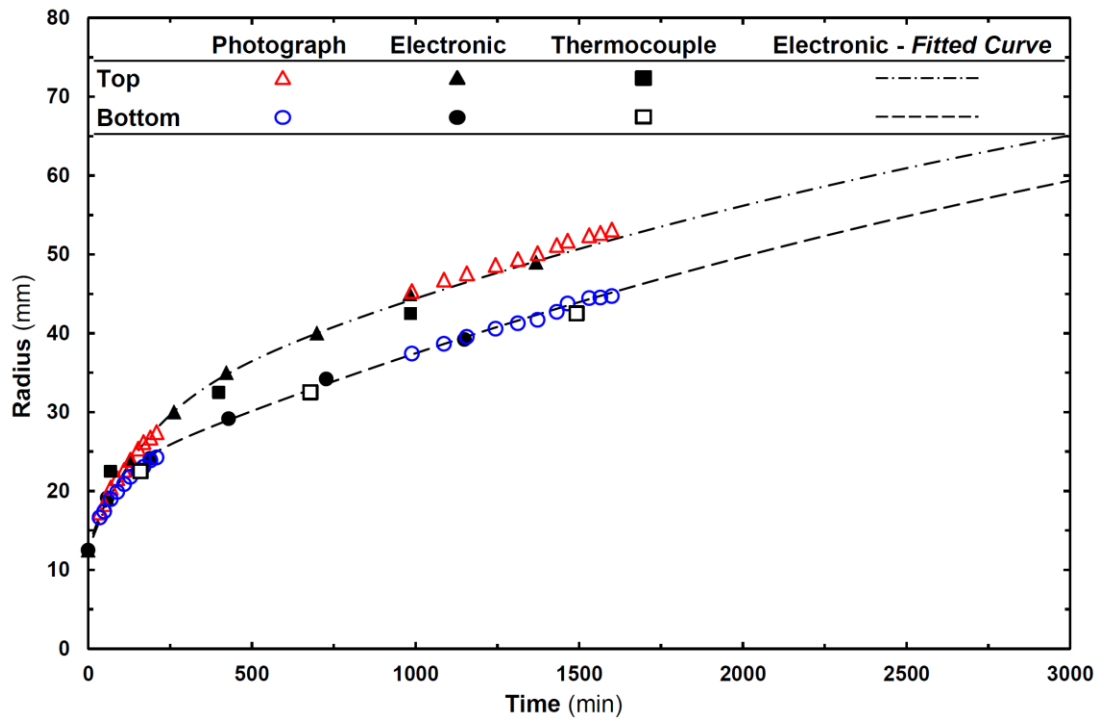
Time	Top Direction ($\theta = 90^\circ$)				Bottom Direction ($\theta = -90^\circ$)			
	Radius of Ice		Absolute Difference	Relative Difference	Radius of Ice		Absolute Difference	Relative Difference
	Photo	Electronic			Photo	Electronic		
(min)	(mm)	(mm)	(mm)	%	(mm)	(mm)	(mm)	%
60	21.2	21.5	0.3	1.4	20.4	21.1	0.8	3.7
72	22.5	22.7	0.3	1.2	21.4	21.9	0.5	2.3
90	24.6	23.9	0.2	0.9	22.9	23.2	0.3	1.5
100	25.0	24.8	0.2	1.0	23.5	23.6	0.0	0.1
120	26.5	26.0	0.5	2.1	24.8	24.5	0.3	1.3
140	27.8	27.3	0.5	1.9	25.9	25.4	0.5	2.0
160	28.9	28.2	0.8	2.8	26.8	26.2	0.6	2.4
179	29.9	29.0	0.9	3.1	27.6	27.1	0.5	1.9
200	30.6	29.7	1.1	3.8	28.5	27.7	0.8	2.7
220	31.7	30.4	1.3	4.2	29.2	28.5	0.6	2.3
239	32.4	31.5	0.9	2.7	29.8	29.3	0.6	2.0
262	33.2	32.4	0.8	2.5	30.6	29.7	0.8	2.8
300	34.3	33.8	0.5	1.5	31.7	31.3	0.4	1.3
319	34.9	34.3	0.6	1.7	32.3	31.8	0.5	1.5
339	35.4	34.9	0.5	1.4	32.8	32.4	0.4	1.4
360	35.9	35.5	0.4	1.2	33.4	33.4	0.0	0.1
379	36.4	36.0	0.4	1.1	33.9	33.6	0.3	0.8
440	37.7	37.5	0.2	0.5	35.4	36.0	0.6	1.5
499	38.9	39.2	0.3	0.8	36.9	37.4	0.5	1.4
564	40.1	40.4	0.4	0.9	38.3	38.6	0.3	0.7
619	41.0	41.4	0.4	0.9	39.5	39.6	0.1	0.3

($D_{shell} = 114 \text{ mm}$, $T_{in} = -5^\circ\text{C}$ and $\dot{V} = 4 \text{ l/min}$)



($D_{shell} = 190$ mm, $T_{in} = -10^{\circ}\text{C}$ and $\dot{V} = 2$ l/min)

Figure 4.4 Validation of the interface measurement method.



($D_{shell} = 190$ mm, $T_{in} = -10^{\circ}\text{C}$ and $\dot{V} = 8$ l/min)

Figure 4.5 Validation of the interface measurement method.

Table 4.4 Comparison of the measured radius values with the relative errors.

Time	Top Direction ($\theta = 90^\circ$)				Bottom Direction ($\theta = -90^\circ$)			
	Radius of Ice		Absolute Difference	Relative Difference	Radius of Ice		Absolute Difference	Relative Difference
	Photo	Electronic			Photo	Electronic		
(min)	(mm)	(mm)	(mm)	%	(mm)	(mm)	(mm)	%
16	15.3	14.2	1.1	7.3	13.4	14.4	1.0	7.4
25	14.7	15.0	0.3	2.4	14.3	15.4	1.1	7.5
35	15.7	15.9	0.2	1.3	15.3	16.3	1.1	6.9
46	16.7	16.9	0.2	1.1	16.1	17.2	1.1	6.9
55	17.4	17.6	0.2	1.1	17.1	17.9	0.9	5.0
65	18.1	18.4	0.3	1.5	17.8	18.6	0.8	4.7
75	18.8	19.1	0.3	1.4	18.5	19.3	0.7	4.0
86	19.7	19.8	0.2	0.9	19.3	19.9	0.6	3.0
105	20.8	21.1	0.2	1.0	20.4	20.9	0.5	2.5
125	21.9	22.2	0.3	1.2	21.3	21.7	0.4	2.1
147	23.0	23.3	0.4	1.7	22.0	22.5	0.5	2.3
167	24.0	24.3	0.3	1.2	22.4	23.1	0.7	3.1
185	24.9	25.1	0.1	0.6	23.0	23.6	0.7	2.9
205	25.5	25.9	0.4	1.5	23.6	24.1	0.5	2.2
225	26.2	26.6	0.4	1.7	24.0	24.5	0.5	2.2
246	27.1	27.3	0.2	0.7	24.5	25.0	0.5	2.0
266	27.9	28.0	0.1	0.4	24.8	25.3	0.5	2.0
296	28.9	28.9	0.1	0.3	25.4	25.9	0.5	1.9
325	30.0	29.6	0.4	1.3	25.9	26.3	0.4	1.5
355	30.7	30.4	0.3	0.9	26.7	26.8	0.1	0.5
385	31.3	31.1	0.2	0.6	27.2	27.2	0.0	0.1
415	32.2	31.8	0.4	1.3	27.6	27.6	0.1	0.3
445	32.8	32.4	0.4	1.1	28.0	28.0	0.0	0.1
475	33.3	33.0	0.2	0.7	28.5	28.4	0.0	0.1
505	34.2	33.6	0.6	1.6	28.9	28.8	0.1	0.3
1273	46.5	45.7	0.9	1.8	38.6	38.0	0.6	1.5
1336	48.8	46.5	2.3	4.7	39.3	38.7	0.6	1.6
1398	49.6	47.4	2.2	4.5	39.9	39.4	0.5	1.3
1463	50.5	48.2	2.3	4.5	40.6	40.1	0.5	1.3
1516	51.0	48.9	2.1	4.1	41.3	40.6	0.7	1.6
1576	51.8	49.7	2.1	4.1	42.0	41.3	0.8	1.8
1625	52.3	50.3	2.0	3.9	42.4	41.8	0.6	1.5
1684	53.2	51.0	2.2	4.2	43.1	42.4	0.7	1.7
1745	52.1	51.7	0.4	0.7	43.4	43.0	0.5	1.0
1805	52.9	52.4	0.5	0.9	44.0	43.6	0.4	1.0
1869	53.9	53.2	0.7	1.4	44.4	44.2	0.2	0.3
1927	54.4	53.9	0.5	1.0	44.9	44.8	0.1	0.2
1989	55.4	54.6	0.8	1.5	45.8	45.4	0.4	1.0
2034	55.9	55.1	0.8	1.5	46.0	45.8	0.2	0.4

($D_{shell} = 190$ mm, $T_{in} = -10^\circ\text{C}$ and $\dot{V} = 2$ l/min)

Table 4.5 Comparison of the measured radius values with the relative errors.

Time	Top Direction ($\theta = 90^\circ$)				Bottom Direction ($\theta = -90^\circ$)			
	Radius of Ice		Absolute Difference	Relative Difference	Radius of Ice		Absolute Difference	Relative Difference
	Photo	Electronic			Photo	Electronic		
(min)	(mm)	(mm)	(mm)	%	(mm)	(mm)	(mm)	%
35	17.3	16.3	1.0	5.9	16.6	16.8	0.2	1.0
49	18.3	17.6	0.7	4.0	17.4	18.1	0.7	4.1
69	20.4	19.3	1.1	5.4	19.0	19.6	0.6	3.3
89	21.6	20.9	0.7	3.3	19.9	20.8	0.9	4.7
110	22.7	22.4	0.3	1.1	20.9	21.8	1.0	4.7
129	24.0	23.7	0.3	1.2	21.8	22.6	0.9	4.0
153	25.4	25.1	0.3	1.0	22.5	23.5	1.0	4.4
169	26.2	26.0	0.2	0.9	23.0	24.0	0.9	4.0
190	26.8	27.0	0.3	1.0	23.9	24.5	0.6	2.7
209	27.5	27.9	0.5	1.7	24.2	25.0	0.8	3.1
989	45.3	44.3	1.1	2.4	37.4	37.3	0.1	0.3
1087	46.9	45.6	1.2	2.6	38.7	38.7	0.0	0.0
1157	47.6	46.5	1.1	2.4	39.5	39.6	0.1	0.2
1245	48.7	47.6	1.1	2.2	40.6	40.7	0.1	0.4
1313	49.4	48.5	1.0	1.9	41.2	41.6	0.4	0.9
1373	50.1	49.2	1.0	1.9	41.7	42.4	0.7	1.6
1432	51.2	49.9	1.3	2.5	42.7	43.1	0.4	0.1
1465	51.7	50.3	1.5	2.8	43.8	43.5	0.2	0.5
1531	52.4	51.1	1.4	2.6	44.5	44.3	0.1	0.3
1565	52.7	51.5	1.3	2.4	44.5	44.7	0.2	0.5
1600	53.2	51.9	1.3	2.4	44.7	45.2	0.5	1.0

($D_{shell} = 190$ mm, $T_{in} = -10^\circ\text{C}$ and $\dot{V} = 8$ l/min)

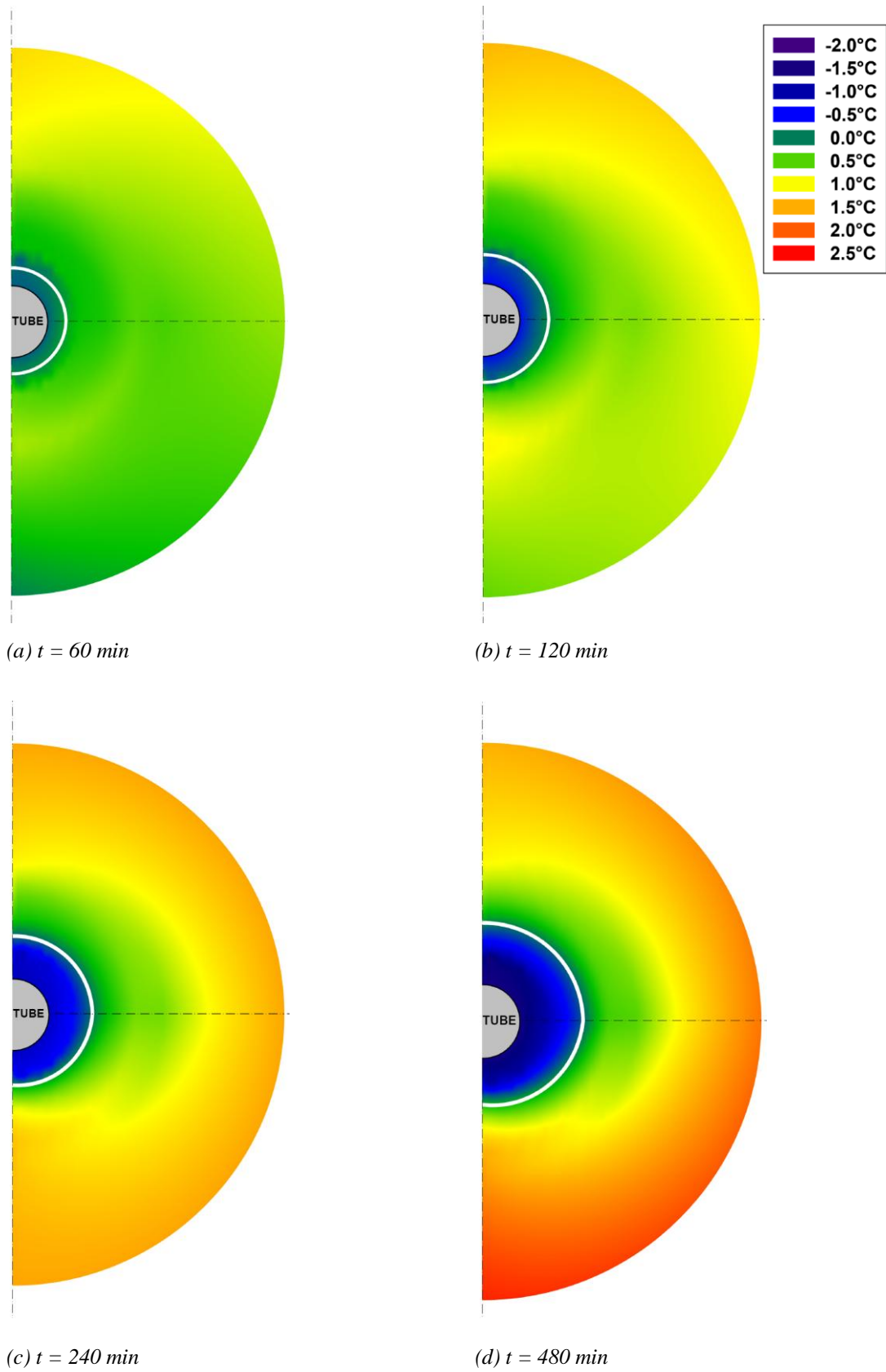
The mean relative difference of the current method is nearly $\pm 3\%$, in comparison with the traditional method of photography. In terms of the absolute difference, the discrepancy between photography and measurement card results is less than ± 1 mm. Comparative results indicate that the current measurement method is applicable to obtain the solid–liquid interface for a LHTES system. In practice, current method has many advantages in contrast with the photography method, such as, eliminating the heat gain from surroundings that caused by opening covers on insulation at specific times. In addition, electronic interface measuring method can be used to observe solidification front where photography method cannot be applicable, such as monitoring several sections inside a LHTES system, especially in closed and large–scale storage tanks.

Experimental results for the charging and discharging periods of the shell-and-tube heat type LHTES system are represented in two subsections; *temperature–interface variations* and *parametric energy and exergy based assessments of system*. In the former one, influence of the natural convection inside the system is discussed for solidification and melting modes, in terms of the interface and temperature variations. In the latter one, effects of several working and design parameters on the charging and discharging capability of the system are investigated.

4.1.2 Temperature and Interface Variations

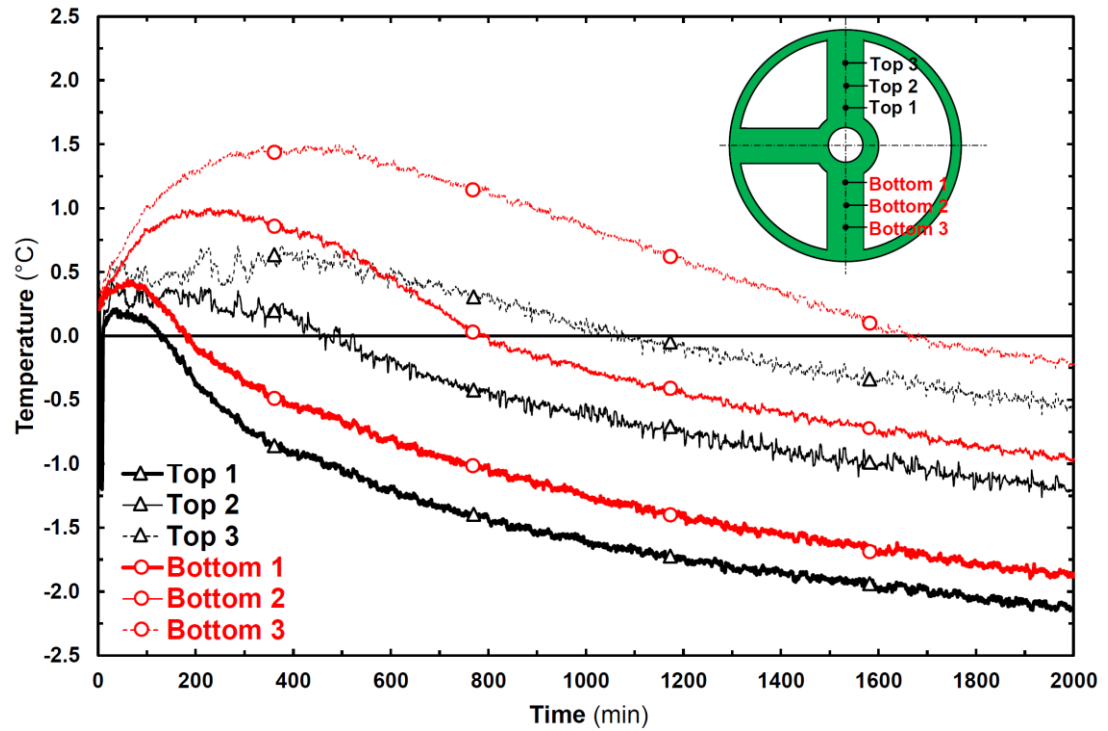
Temperature contours and solid–liquid interface variations allow to examine the influences of the natural convection during solidification and melting processes. In Figure 4.6, typical temperature contours at the middle section of the annuli are given with the solid–liquid interfaces at $t = 60$ min, 120 min, 240 min and 480 min, for a selected charging experiment ($T_{in} = -10^{\circ}\text{C}$, $\dot{V} = 2$ l/min). In these figures, bold white lines designate the solid–liquid interface positions obtained from the measurement card. As seen from the figures, for both melting and solidification processes, natural convection affects the shape of the interface and the temperature gradients. Similar variations are obtained in previous studies by many researchers (Viskanta, 1985; Ssaguchi et al., 1997; Ho & Viskanta, 1984; Tan et al., 2009).

As shown in Figure 4.6(a), at the beginning of the solidification process, $t = 60$ min, water stands in the annulus almost at a uniform temperature. In progressing time, the density of water around tube decreases with the cooling effect and cause an upward flow from tube surface to the shell. Near the shell surface, because of the heat gain from surroundings, the temperature of water increases and relatively hot water with higher density drops down to the bottom side of the annuli. Hence, natural convection dominated sub region appear at the top side of domain and thermally stratified subsection at the bottom side of the tube. Thermal stratification slows down the solidification speed in progressing time. The disparity between the solidification speeds of top ($\theta = 90^{\circ}$) and the bottom ($\theta = -90^{\circ}$) sides can be seen from the time wise temperature and solidification thickness variations in Figures 4.7 and 4.8.



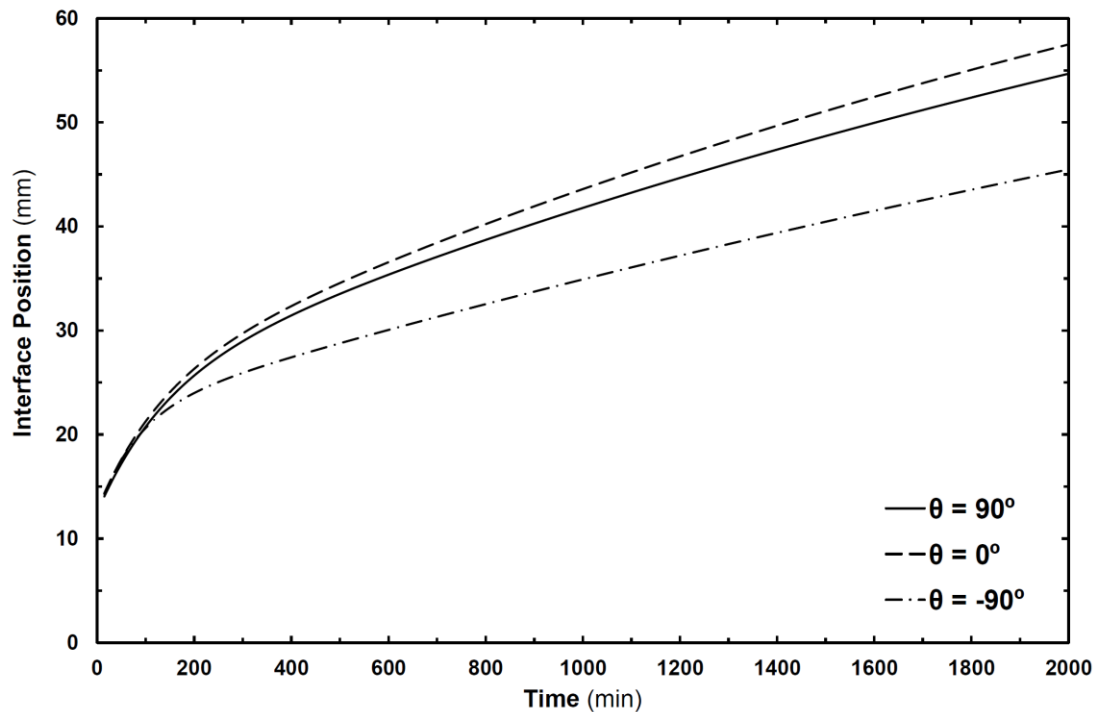
($D_{shell} = 190 \text{ mm}$, $T_{in} = -10^\circ\text{C}$ and $\dot{V} = 2 \text{ l/min}$)

Figure 4.6 Temperature contours for solidification mode.



($D_{shell} = 190 \text{ mm}$, $T_{in} = -10^\circ\text{C}$ and $\dot{V} = 2 \text{ l/min}$)

Figure 4.7 Temperature variations at the top and bottom sides of the tube.



($D_{shell} = 190 \text{ mm}$, $T_{in} = -10^\circ\text{C}$ and $\dot{V} = 2 \text{ l/min}$)

Figure 4.8 Time wise variation of the interface position around the tube for solidification mode.

In Figure 4.7, temperature variations of three top and bottom thermocouples are given together. At the top side of the annuli, temperature values of water almost remain constant until the solidification occurs. On the contrary, at the bottom side, the temperature of water rises more than 1°C above the initial values. This effect slows down the solidification speed at the bottom side of the annuli for declining times, and the solid–liquid interface becomes asymmetric. Angular variation of the radius of ice around the tube is illustrated in Figure 4.8. Here it can be seen that the time wise solidification tendencies are close at $\theta = 0^{\circ}$ and $\theta = 90^{\circ}$, where the natural convection is effective. On the other hand, at $\theta = -90^{\circ}$ solidification tendency differs at the top side of the tube.

Hence, it is clear that two independent thermal sub–regions occur around the interface. The top side of the tube can be called as the natural convection dominant region, while the bottom side of the tube is the conduction dominant, as reported in the earlier studies (Viskanta, 1985; Tan et al., 2009). In Figure 4.9, these sub–regions are illustrated schematically. As is known, density of the water has an inversion point at $T_{\rho,max} \approx 4^{\circ}\text{C}$. Density of the water increases between the melting temperature ($T_m = 0^{\circ}\text{C}$) and the inversion temperature ($T_{\rho,max} \approx 4^{\circ}\text{C}$) with increasing temperature. Above 4°C , density of water tends to drop. In the current solidification experiments, temperature of water always remains under 4°C , so hot water with relatively higher density stays at the bottom of side the tube and forms a thermal stratification region at the bottom side of the annulus. On the other hand, at the top side of the tube, the temperature difference between the hot shell surface ($T_{shell} > T_m$) and the ice surface ($T_m = 0$) causes buoyancy effects. Hot water with relatively higher density near the shell surface flows down through the interface surface and because of the ice surface, temperature of water decreases. With decreasing temperature, density of water also decreases around the interface and cold water with relatively low density flows through the shell surface.

The shape of ice is also affected by the axial flow direction. The solidification front varies along the flow direction, because, the wall temperature of the tube differs from the inlet through the outlet sections. In Figure 4.10, ice profiles are given for

the inlet, middle and outlet card sections, at $t = 60$ min, 120 min, 240 min and 480 min.

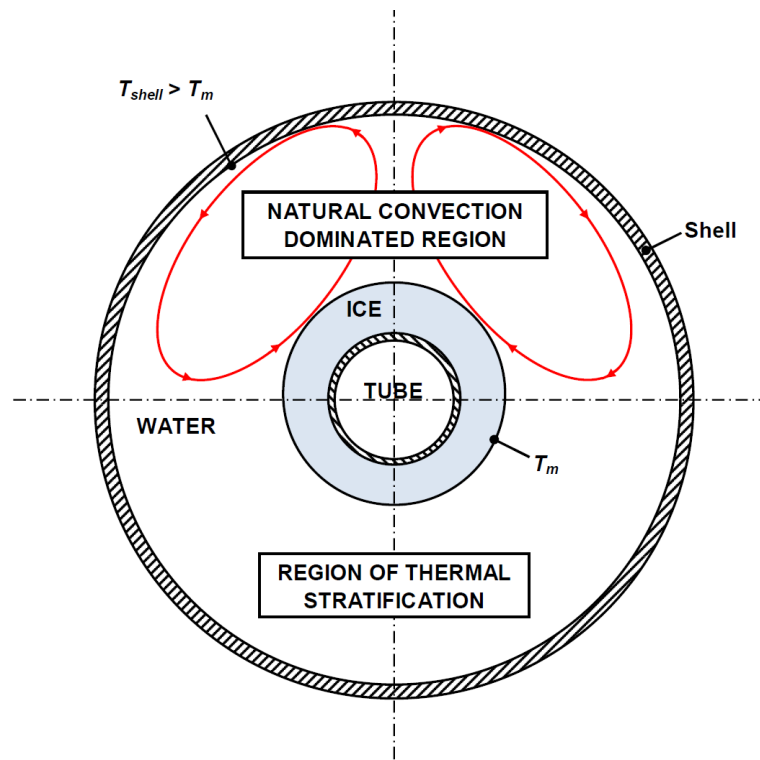


Figure 4.9 Illustration of thermal sub regions inside the annulus for solidification mode.

Similar to the solidification mode, the influence of natural convection on the melting process is examined with the aid of temperature distributions. The temperature counters and interface variations for the melting process are illustrated for a selected discharging experiment ($T_{in} = +5^{\circ}\text{C}$, $\dot{V} = 4$ l/min) in Figure 4.11. It is clear that ice melts both inward and outward directions in this experiment. While the hot tube causes outward melting, the heat gain from surroundings induces inward melting. Therefore, two different thermal sub regions occur inside the annulus. These sub-regions can be called as *outer* and *inner* regions, which take place between the outer surfaces of the outer interface and the shell, and between the surfaces of the tube and the inner interface, respectively. In the former one, natural convection mechanisms are similar with the solidification case. While at the top side of the outer region, natural convection dominant sub-region occurs, and at the bottom side of the outer region, relatively hot water forms thermal stratification. Hence, as seen from the temperature distributions given in Figure 4.11, in progressing time, inward

melting speed becomes higher at the bottom side, in comparison to the top side. On the other hand, for outward melting, the interface variation around the tube seems symmetrical for $t = 60$ min. In progressing time, interface becomes differ around the tube. While the melting speed slows down at the top side of the annuli, a thermal plume occurs at the bottom side of the tube. In Figure 4.12, the time wise variations of the interface positions for $\theta = 90^\circ$, $\theta = 0^\circ$ and $\theta = -90^\circ$ are given to clarify the interface variations around the tube. In contrast to the solidification mode, in melting mode, speed of phase change is higher at the bottom side of the tube. In Figure 4.13, melting profiles are given for inlet, middle and outlet card section at $t = 60$ min, 120 min, 240 min and 480 min. At the inlet, middle, and outlet sections of the tank, there occur thermal plume at the bottom side of the tube.

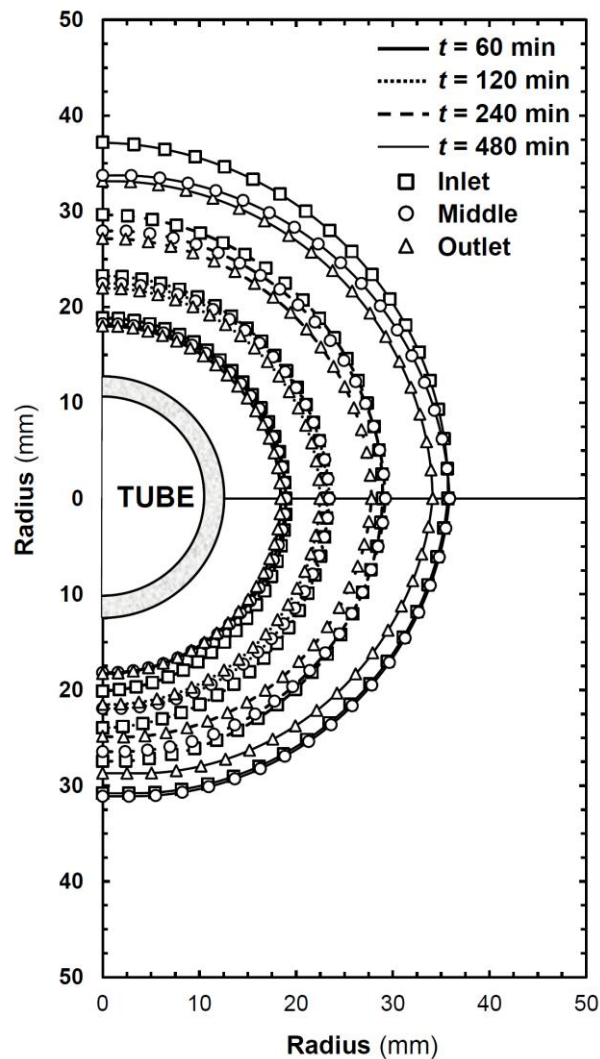
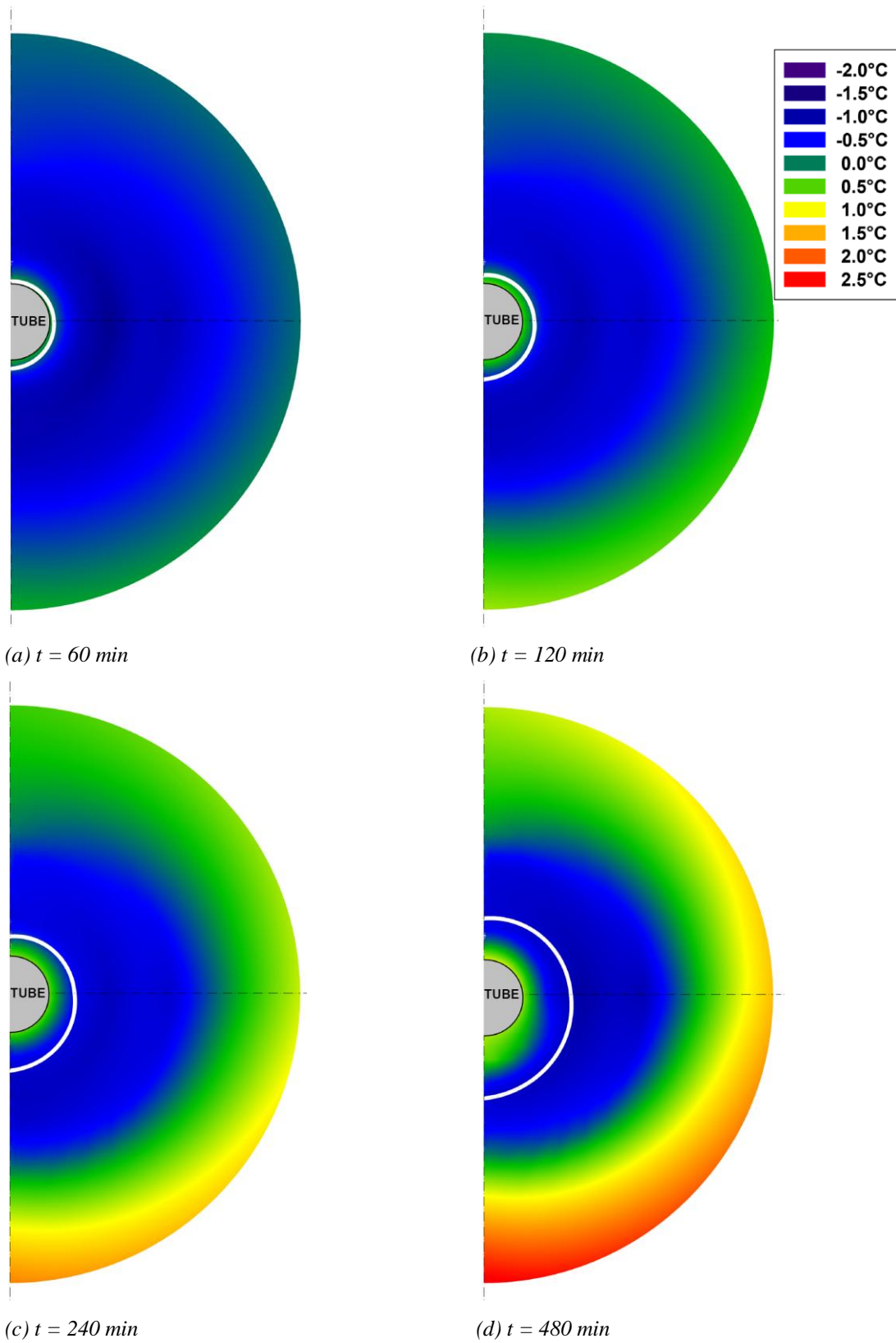
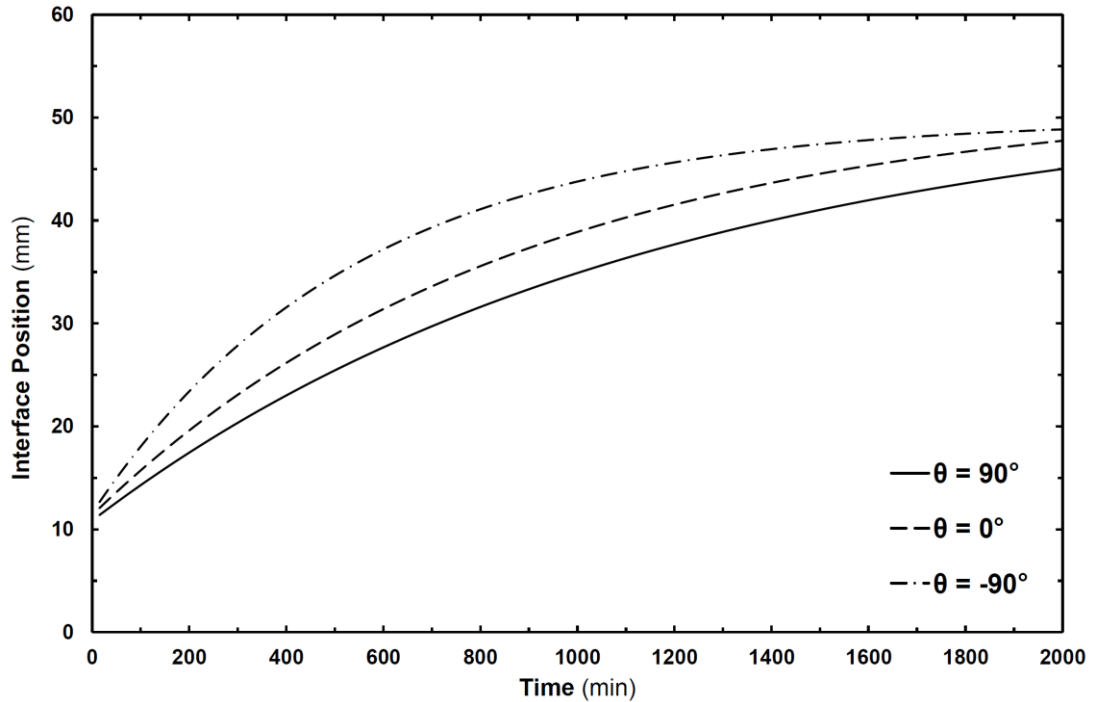


Figure 4.10 Interface variations around the tube and along the flow direction for solidification mode.



($D_{shell} = 190 \text{ mm}$, $T_{in} = +5^\circ\text{C}$ and $\dot{V} = 4 \text{ l/min}$)
 Figure 4.11 Temperature contours for melting mode.



($D_{shell} = 190$ mm, $T_{in} = +5^\circ\text{C}$ and $\dot{V} = 4$ l/min)

Figure 4.12 Time wise variation of the interface position around the tube for melting mode.

Because of the dominant heat conduction mechanism, the melting interface at the inner space of the ice is nearly symmetric at earlier times. Subsequently, natural convection effects become clear in progressing time. Because of the density variations inside the liquid water, two independent thermal sub-regions occur for the outward melting region. In Figure 4.14, these sub-regions are illustrated schematically. For the bottom side of the tube, while relatively hot water around the tube surface ($T_{tube} > T_m$) with higher density flows downwards through the interface (ice) surface. Relatively cold water near the ice surface with lower density moves upwards through the tube surface. This buoyancy effects shift the interface through the bottom of the tube ($\theta = -90^\circ$) and cause a thermal plume.

On the other hand, for the top side of the tube, relatively cold water with lower density stands at the top region of the tube ($\theta = 90^\circ$) and melting process slows down in this conduction dominated region.

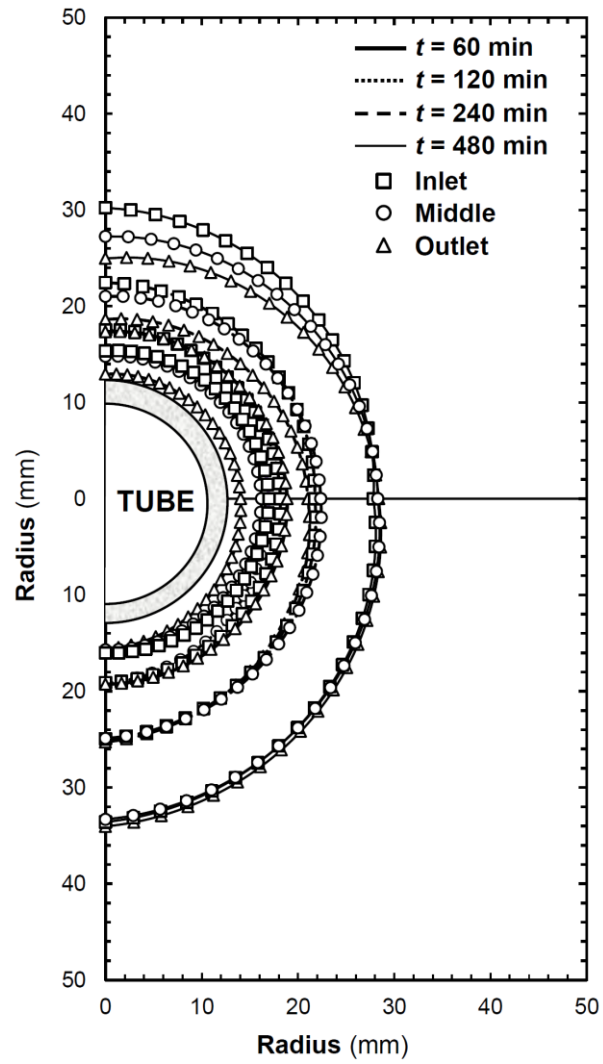


Figure 4.13 Interface variations around the tube and along the flow direction for melting mode.

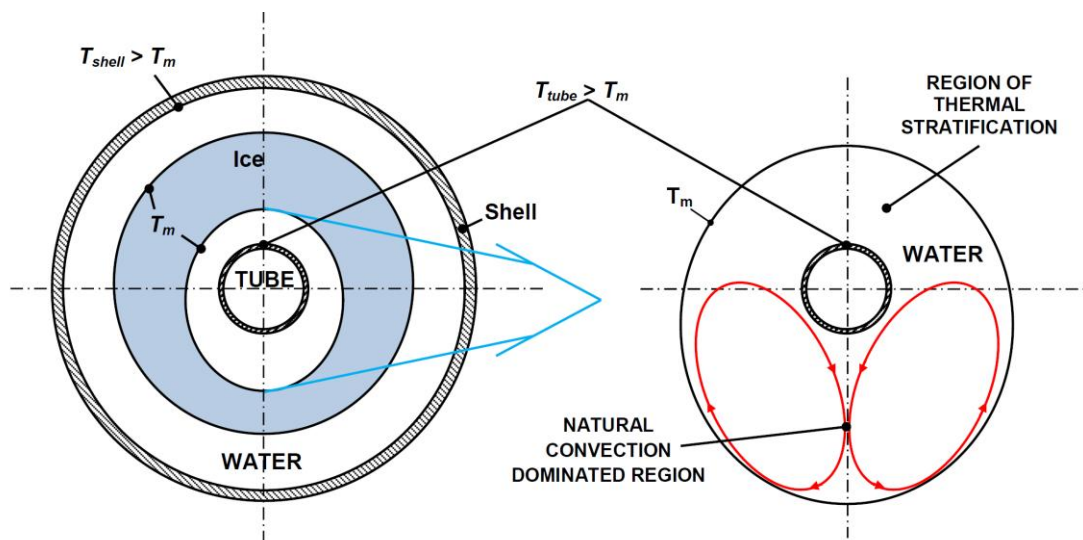


Figure 4.14 Illustration of thermal sub regions inside the annulus for melting mode.

4.1.3 Parametric Results of Shell-and-tube LHTES System

In this study, a total of 46 parametric experiments is carried out in the shell-and-tube type LHTES system. In Table 4.6, experimental parameters are given in terms of the inlet temperature and the flow rate values of the HTF and pipe materials. Flow rates are selected to be in laminar flow conditions and Re number varies between in the range of 250 to 1700, depending on the flow rate and viscosity of the HTF. While in Cases, #1, #2, and #3 the diameter of the shell is 114 mm, in the Case #4 diameter of the shell is 190 mm. In this section, parametric energy and exergy results are discussed for charging and discharging modes of the system.

Table 4.6 Experimental parameters for the shell-and-tube LHTES system

Case	Charging (Solidification)		Case	Discharging (Melting)	
	Flow rate	T_{in}		Flow rate	T_{in}
	(l/min)	(°C)		(l/min)	(°C)
#1 (S. Steel)					
#2 (Copper)	2 4 8	-5, -7.5, -10, -15	#4 (PE-32)	2 4	+5, +10
#3 (PE-32)					
#4 (PE-32)	2 4 8	-7.5, -10			

4.1.3.1 Influences of Flow Parameters of HTF on Charging

Charging experiments are carried out for four different inlet temperature values and three flow rates of the HTF to investigate their combine effect on the total stored energy. Figure 4.15 represents the time wise variations of the total stored energy, as functions of the inlet temperatures and flow rates, for Case #2. It is clear that, the total stored energy rises with decreasing the inlet temperature and increasing the flow rate of the HTF. The influence of the inlet temperature is more significant in comparison to the flow rate.

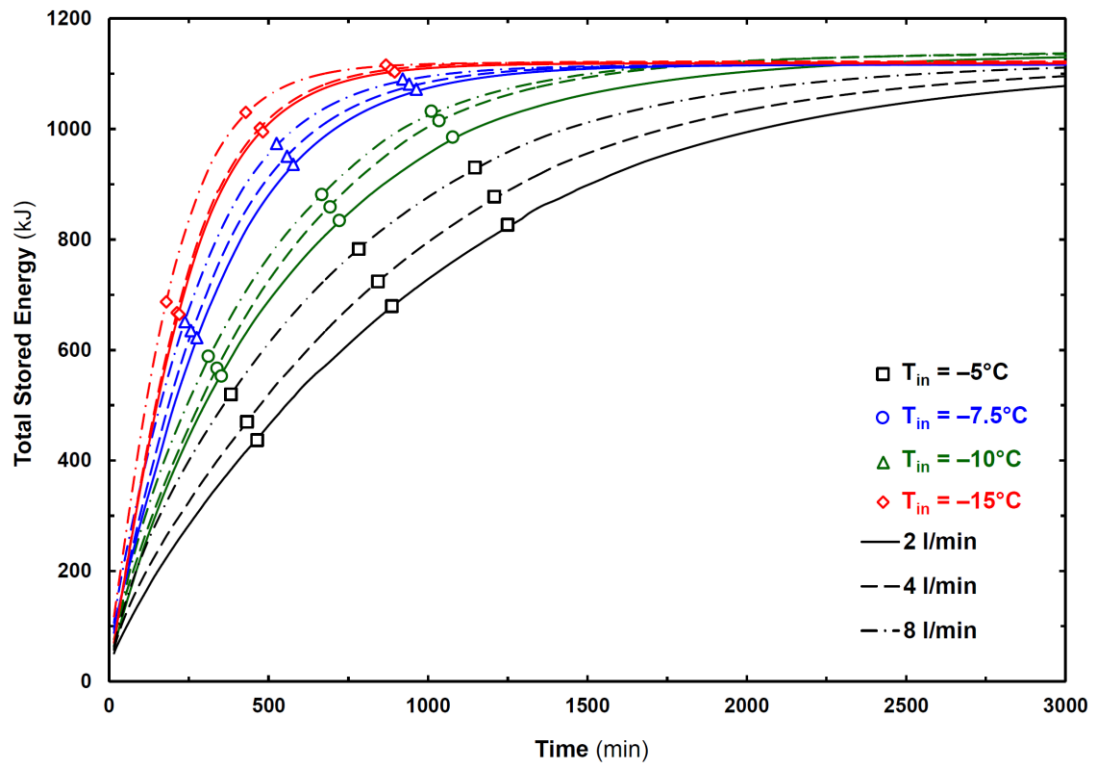


Figure 4.15 Influences of the inlet temperature and the flow rate of the HTF on the total stored energy.

On the other hand, it must be emphasized that, flow rate variations become more significant for relatively higher inlet temperature values of the HTF. As an instance, for $T_{in} = -5^{\circ}\text{C}$ and $T_{in} = -7.5^{\circ}\text{C}$, the flow rate seems to be more effective rather than the lower temperature values, such as $T_{in} = -10^{\circ}\text{C}$ and $T_{in} = -15^{\circ}\text{C}$.

Besides, influences of the inlet temperature and the flow rate of the HTF on the energy and exergy efficiencies are shown in Figures 4.16 and 4.17. Similar to the total stored energy variations, energy efficiency decreases with increasing the inlet temperature of the HTF; in contrast, energy efficiency increases with increasing the flow rate of the HTF. The influence of the inlet temperature on the energy efficiency is more significant. While the inlet temperature of the HTF increases through the phase change temperature of water, the effect of the flow rate becomes clearer. Besides, as seen from Figure 4.17, exergy efficiency increases with increasing the inlet temperature and flow rate. Similar to the energy efficiency, inlet temperature is deterministic parameter in comparison with the flow rate of the HTF. The effect of the flow rate becomes remarkable for the relatively higher inlet temperatures.

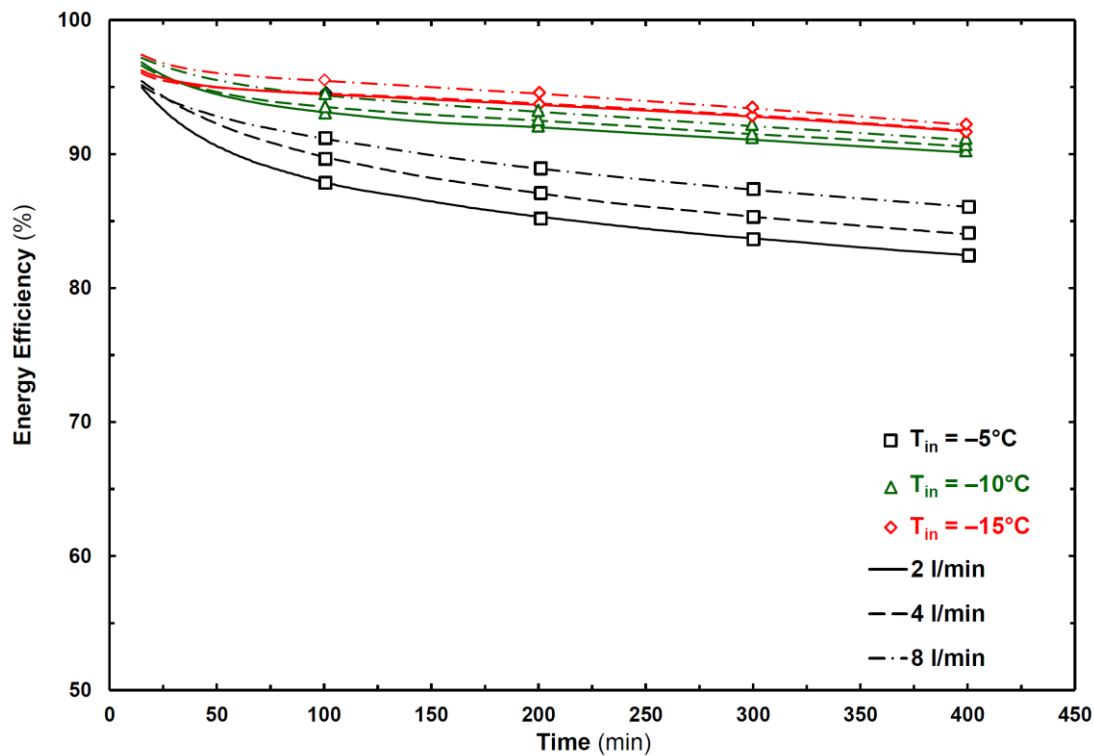


Figure 4.16 Influences of the inlet temperature and flow rate of the HTF on the energy efficiency for charging period.

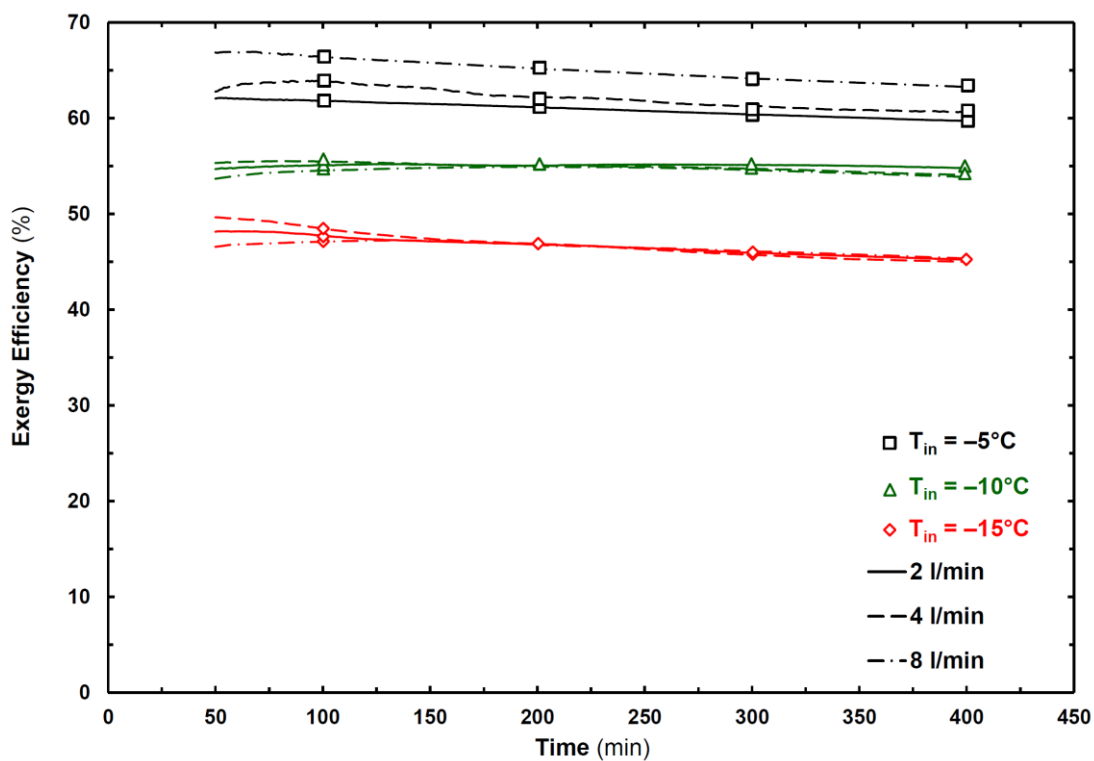


Figure 4.17 Influences of the inlet temperature and flow rate of the HTF on the exergy efficiency for charging period.

4.1.3.2 Influence of Tube Material on Charging

The influence of the tube material on the total stored energy is also investigated with three different tube materials: *copper*, *stainless steel*, and *PE-32(Polyethylene)*. Comparative experiments are conducted for $D_{shell} = 114$ mm and with the inlet temperature of $T_{in} = -10^{\circ}\text{C}$. Thermal conductivities of the tube materials are given in Table 4.7.

Table 4.7 Thermal conductivities of the tube materials.

Material	Thermal Conductivity
	(W/mK)
Copper	400
S. Steel	16
PE-32 (<i>Polyethylene</i>)	0.38

In Figure 4.18, the time wise variations of the total stored energies are given for three tube materials. In conjunction with the increase of the thermal conductivity, from the material of PE-32 to copper, the total stored energy becomes nearly double, especially at the beginning of the experiments. A quantitative comparison is also represented to show the difference of the total stored energies between each material type. The comparisons can be achieved for $t = 480$ min, since the nighttime low tariff duration in Turkey is eight hours. For the flow rate of $\dot{V} = 4$ l/min, the differences between the total stored energies in terms of copper/stainless-steel, stainless steel/PE-32 and copper/PE-32 are almost 30%, 130% and 200%, respectively. Similar to the variations of the total stored energy, energy efficiency also increases with increasing the thermal conductivity of tube material, as seen in Figure 4.19. The influence of the flow rate of the HTF on the total stored energy becomes relatively insignificant with increasing the thermal conductivity of the tube material.

On the other hand, exergy efficiency also increases with increasing the thermal conductivity as seen in Figure 4.20. It seems there is an inconsistency for the initial period of the PE-32 tube material and $\dot{V} = 8$ l/min experiment. The reason is that, total experimental durations for the PE-32 experiments are relatively too long in

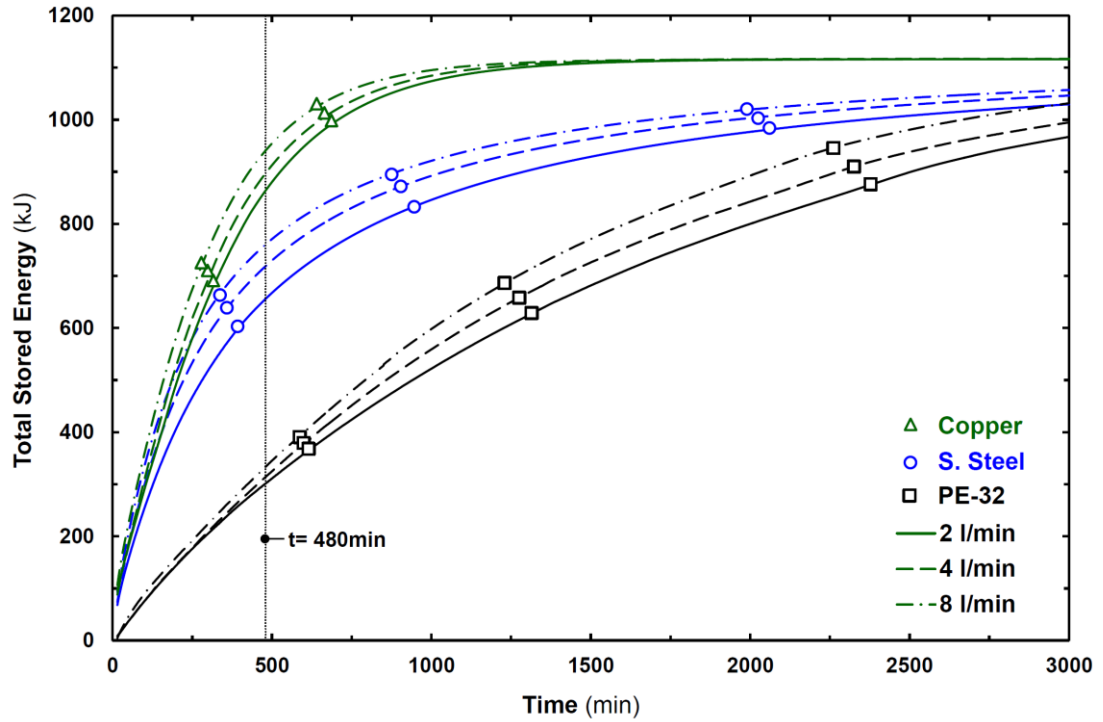


Figure 4.18 Influence of the tube material on the total stored energy for charging period.

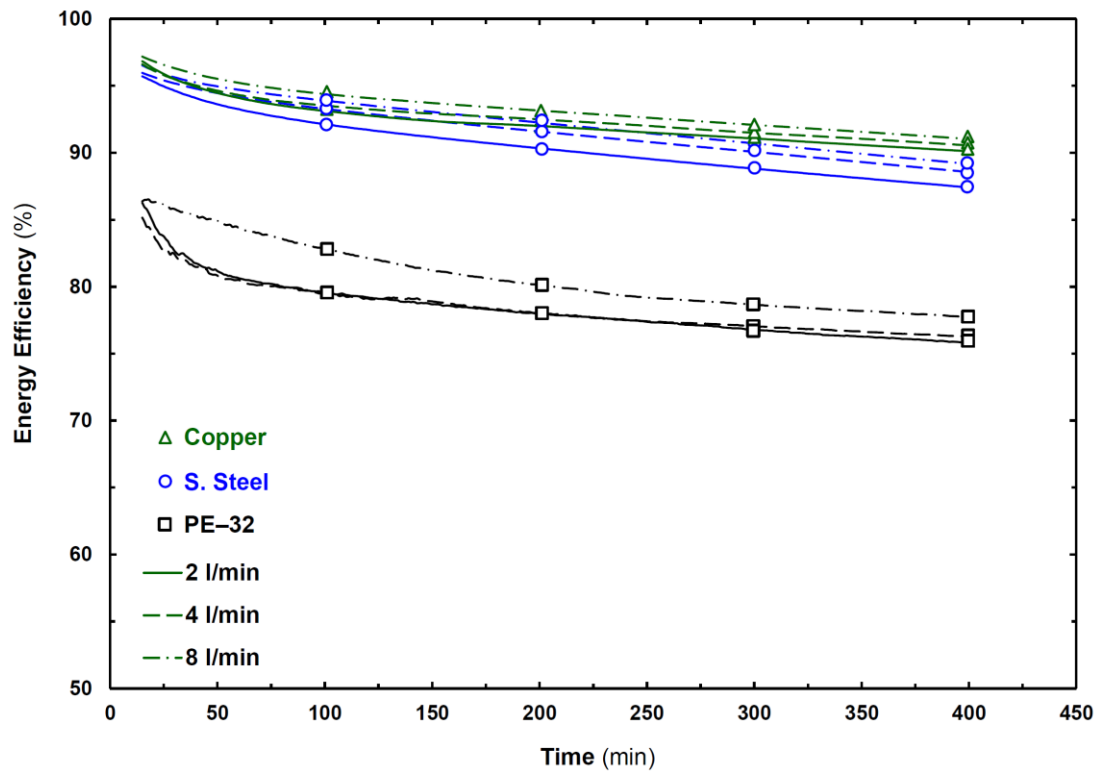


Figure 4.19 Influence of the tube material on energy efficiency for charging period.

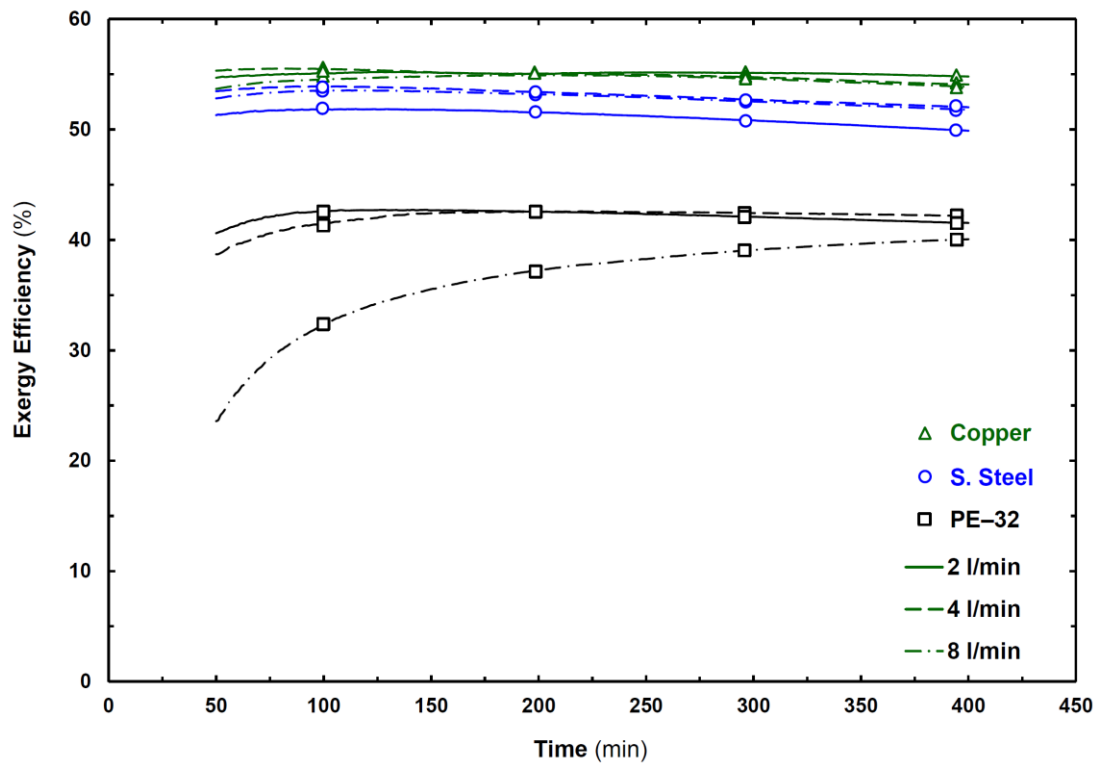


Figure 4.20 Influence of the tube material on exergy efficiency for charging period.

comparison with the stainless steel or copper tubes. The inconsistent behavior of $\dot{V} = 8$ l/min experiment refined after $t = 400$ min, as seen in Figure 4.24.

4.1.3.3 Influence of Shell Diameter on Charging

The shell diameter is also an important parameter for the shell-and-tube type LHTES systems, as it imposes the efficiency, such as the inlet temperature or flow rate of the HTF (Trp et al., 2006; Ereke & Dincer, 2008). Ereke & Dincer (2008) numerically investigated the influence of the shell diameter on the storage performance. They carried out analyses for three dimensionless radii, $R_{shell} = 2, 3$ and 5 , where the dimensionless parameter is defined as, $R_{shell} = r/D_o$. In this study, experimental comparisons are performed for two different shell diameters, which are selected as; $2 < R_{shell} < 3$ ($D_{shell} = 114$ mm) and $3 < R_{shell} < 5$ ($D_{shell} = 190$ mm), with the inlet temperature of $T_{in} = -10^\circ\text{C}$. The effect of the shell diameter on the total stored energy can be seen in Figure 4.21 for various flow rates. The total stored energy variations are nearly the same for the initial time of the experiments. Even though

the surface temperatures of tubes are nearly same for two cases, energy variations become differ. This difference can be discussed with introducing the thermal behavior inside these two shell geometries. In Figure 4.22, the temperature distributions are given at $t = 240$ min and $t = 480$ min for two different shell diameters with the flow parameters of, $T_{in} = -10^{\circ}\text{C}$, $\dot{V} = 2$ l/min. For the shell with the diameter of 114 mm, solidification speed becomes slow after the thermal stratification occurs. The reason is that, relatively hot water stratifies around the ice at the bottom side of the tube, and slows down the solidification speed. On the other hand, for the shell with the diameter of 190 mm, thermal stratification occurs in a relatively larger space, so water around the ice has relatively lower temperature compared with the small shell. Hence, the total stored energy increases with increasing the shell diameter from 114 mm to 190 mm. Besides, as seen from Figure 4.23, it is obvious that the shell diameter is inversely proportional to the energy efficiency. Here, the significant point is that, the slopes of the efficiency curves are different. While the solidification is almost complete at $t = 1800$ min for $D_{shell} = 114$ mm, the volumetric solidification fraction of $D_{shell} = 190$ mm is only 20%.

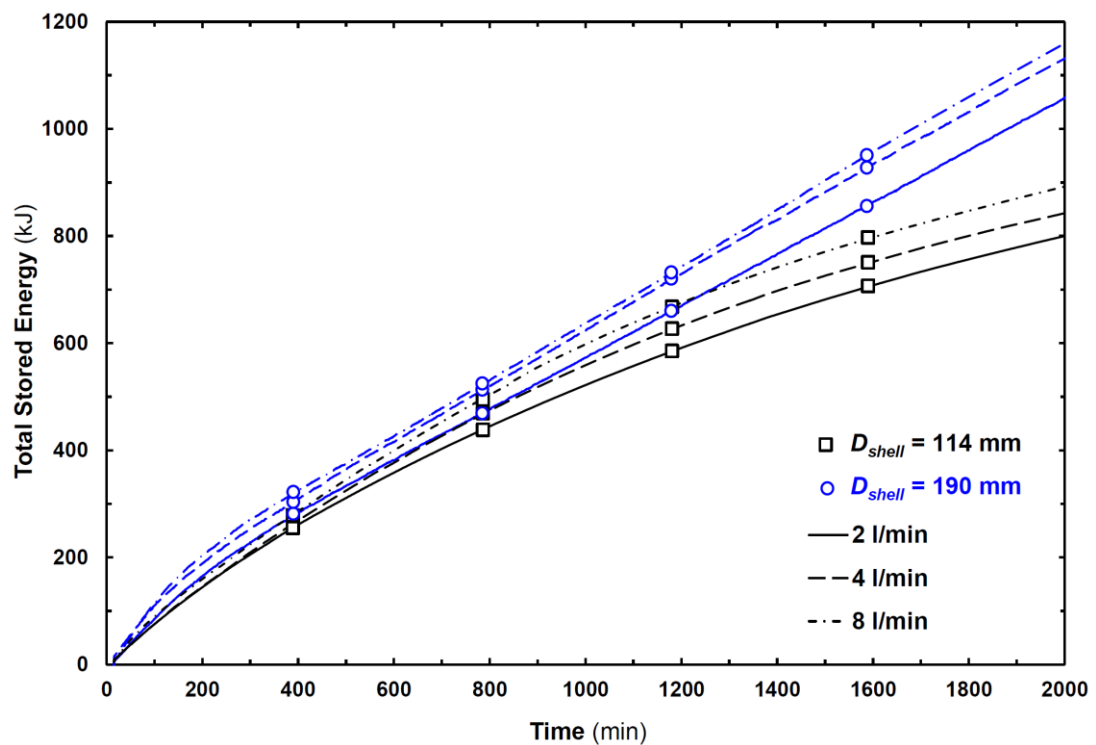


Figure 4.21 Influence of the shell diameter on the total stored energy for charging period.

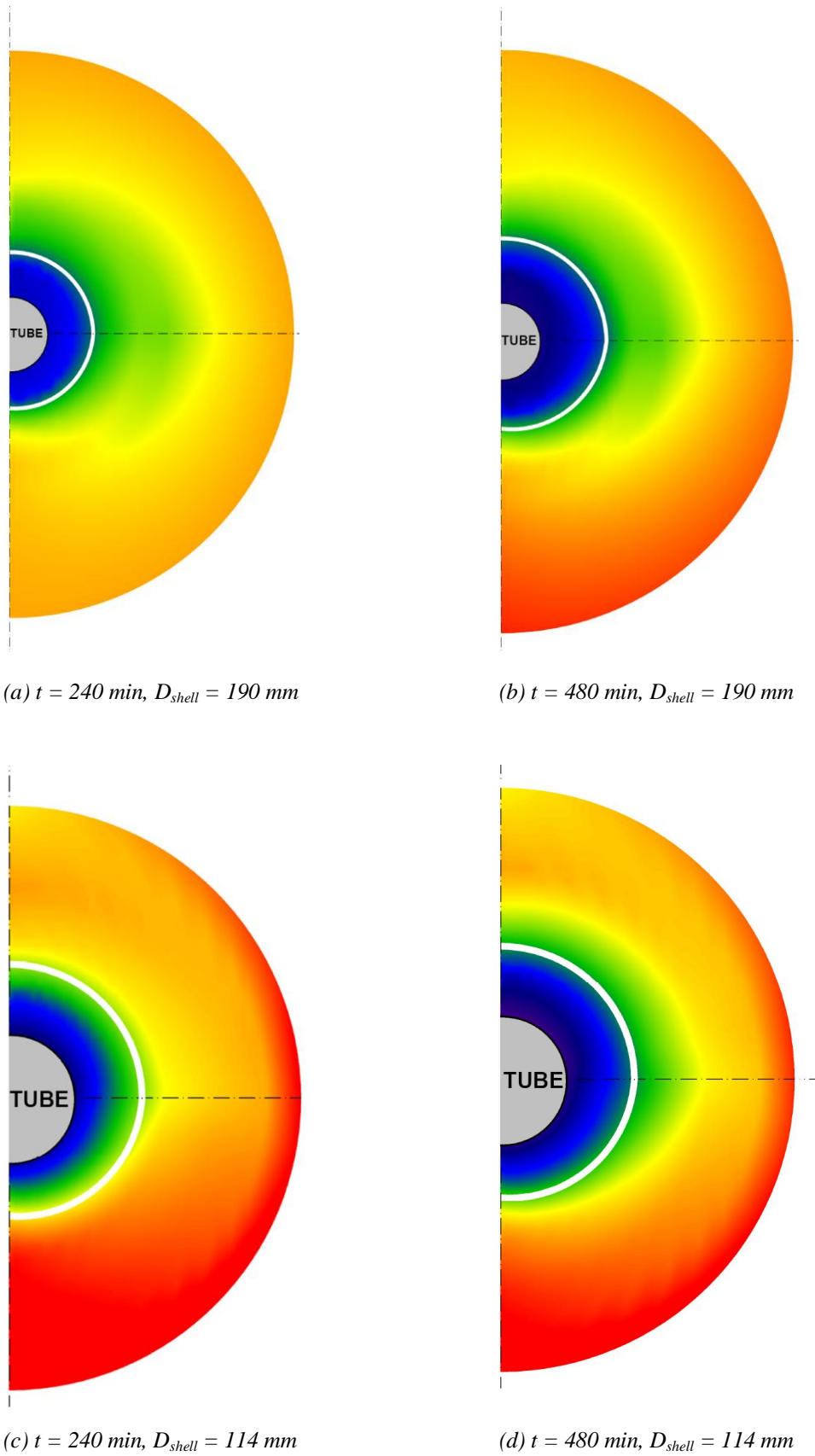


Figure 4.22 Influence of the shell diameter on temperature distributions.

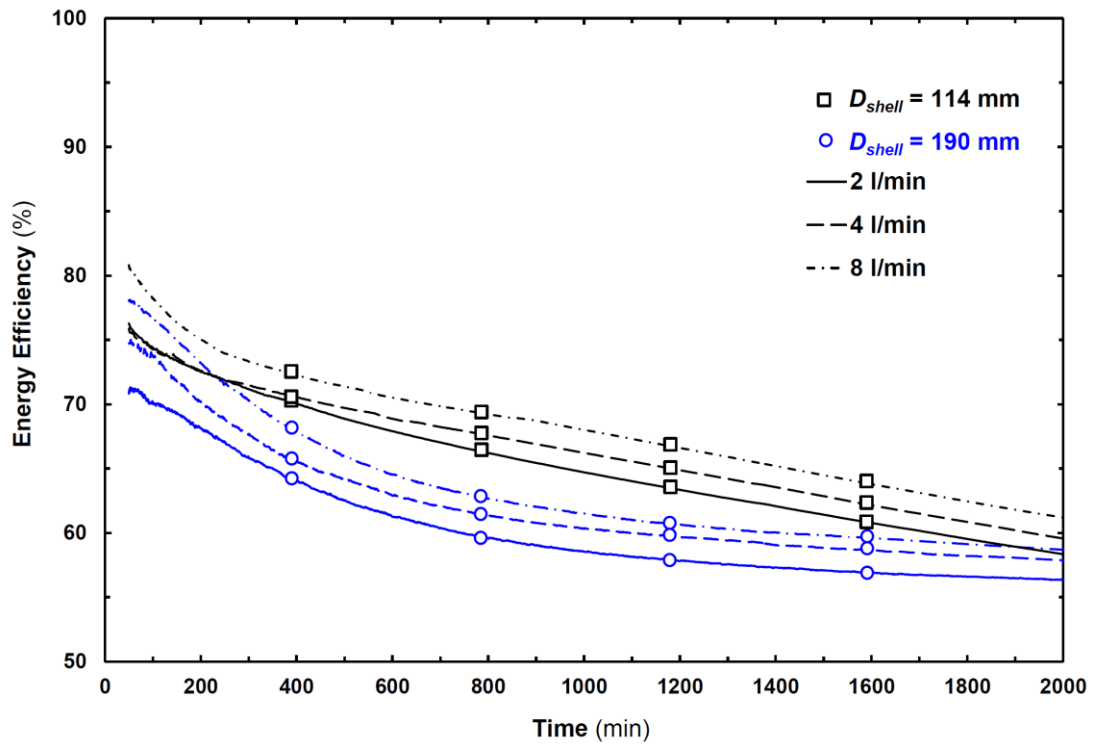


Figure 4.23 Influence of the shell diameter on energy efficiency for charging period.

Exergy efficiency of the system increases with increasing shell diameter, as seen in Figure 4.24. The difference between the efficiency values of these two cases increases in the progressing time.

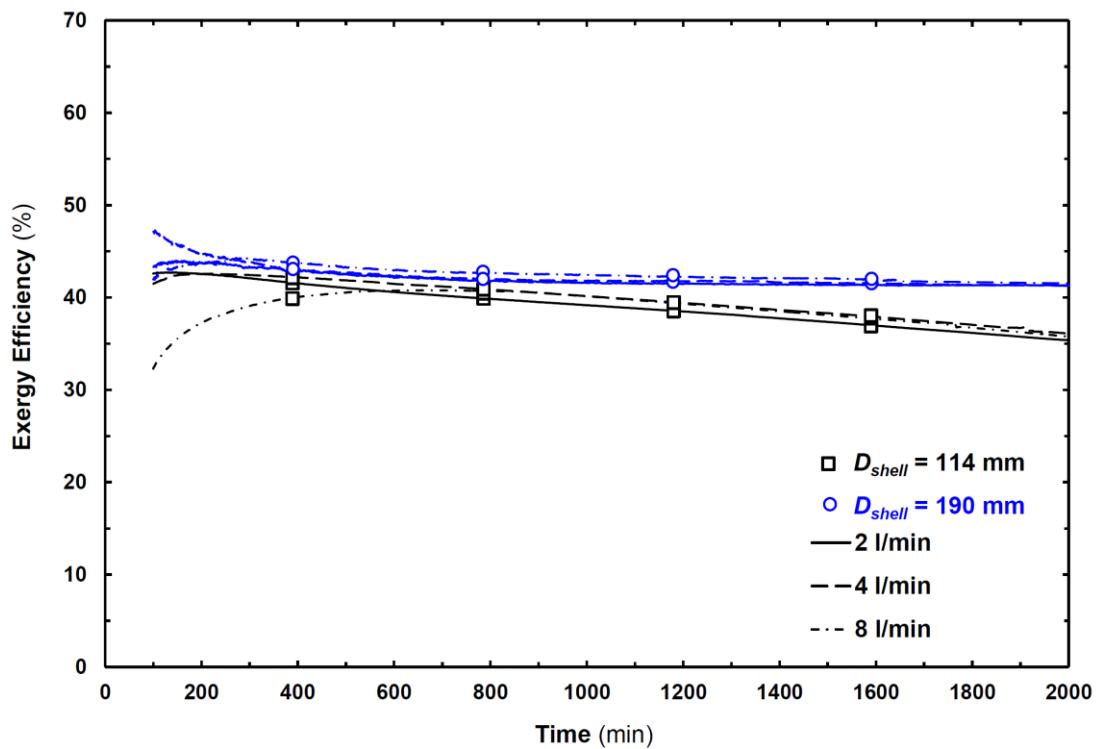


Figure 4.24 Influence of the shell diameter on exergy efficiency for charging period.

4.1.3.4 Influences of Flow Parameters of HTF on Discharging

In melting experiments, experiments are performed for two different inlet temperatures and flow rates of the HTF to observe the influence of the inlet temperature and flow rate of the HTF on the total rejected energy. Figure 4.25 represents the total rejected energy variations as functions of the inlet temperature and flow rate for Case #4. Here, it can be seen that for the selected parameters, the inlet temperature of the HTF is more significant than the flow rate, which has nearly no meaningful effect on the melting period. Surface temperature variations can be introduced to explain this situation. In Figure 4.26, time wise variations of the surface temperature values are given for each parameter. It is clear that with increasing the flow rate of the HTF from 2 l/min to 4 l/min, the surface temperature of the tube remains almost constant.

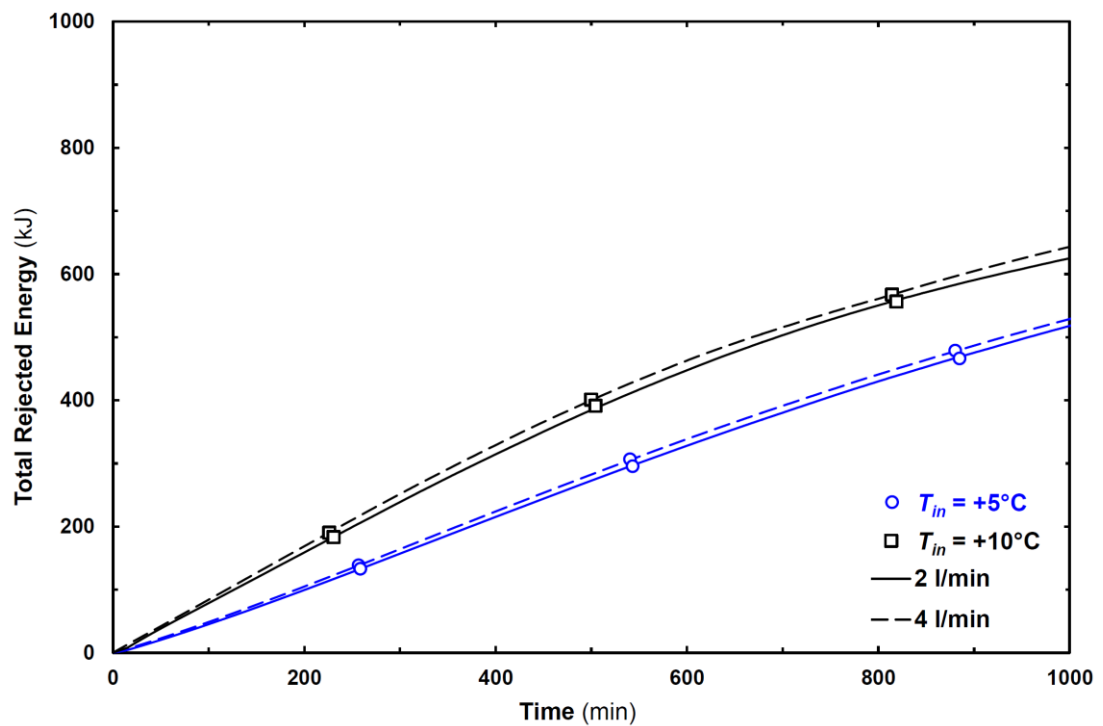


Figure 4.25 Influences of the inlet temperature and flow rate of the HTF on the total rejected energy.

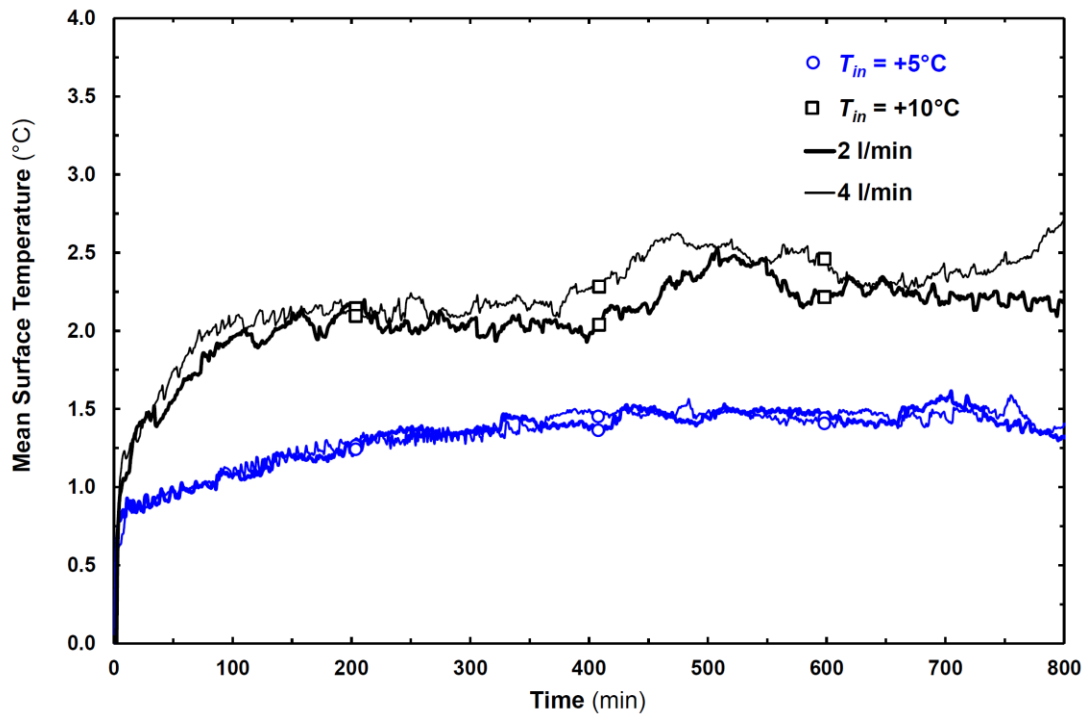


Figure 4.26 Time wise variations of the mean surface temperature of the tube for discharging period.

The influences of the inlet temperature and flow rate of the HTF on the energy efficiency of the system during discharging process are given Figure 4.27. Energy efficiency increases with increasing the inlet temperature and flow rate of the HTF. Similar to the charging experiments, inlet temperature of the HTF is more significant parameter rather than the flow rate. Besides, variations of exergy efficiencies are given in Figure 4.28. Irreversibility increases as the temperature difference between the phase change temperature of the PCM and, the inlet temperature of the HTF increases. Hence, exergy efficiency decreases with increasing the inlet temperature. The influence of the flow rate of the HTF on the exergy efficiency seems to be insignificant for selected parameters.

In Table 2.10, energy and exergy efficiencies of the system are given together with the total stored or rejected energy values. Here, a reference volumetric fraction is determined for charging and discharging cases to make comparisons for energy and exergy efficiencies for these experiments. These fractions are selected as 40% and 25% for charging and discharging experiments, respectively.

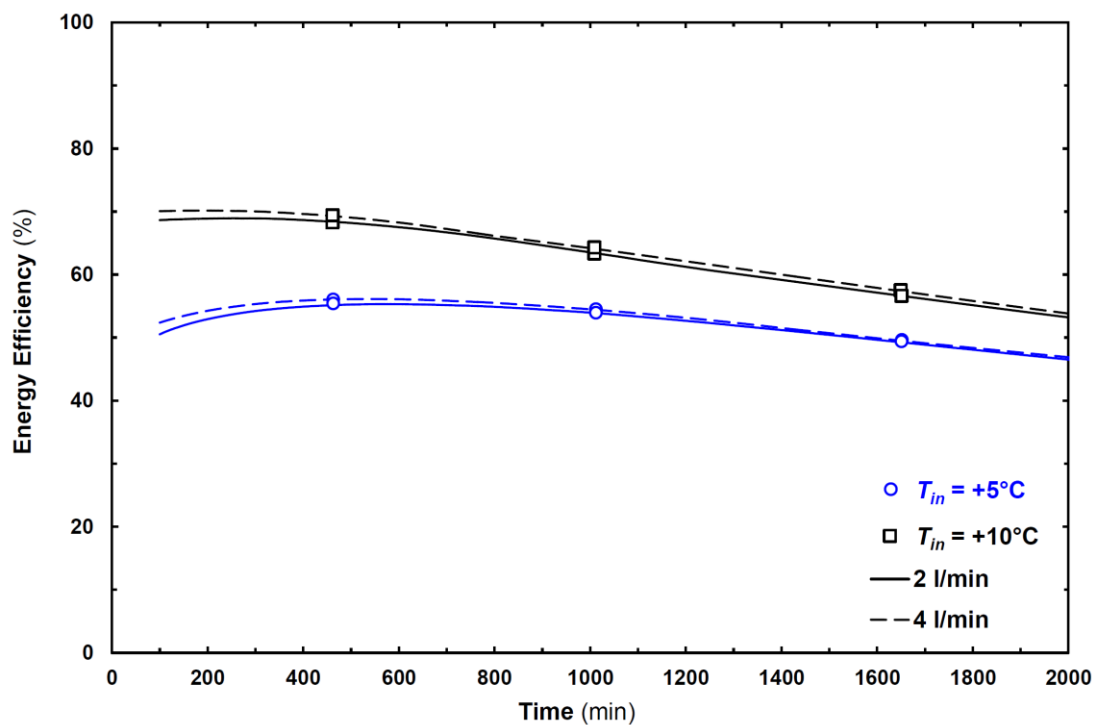


Figure 4.27 Influences of the inlet temperature and flow rate of the HTF on energy efficiency for discharging period.

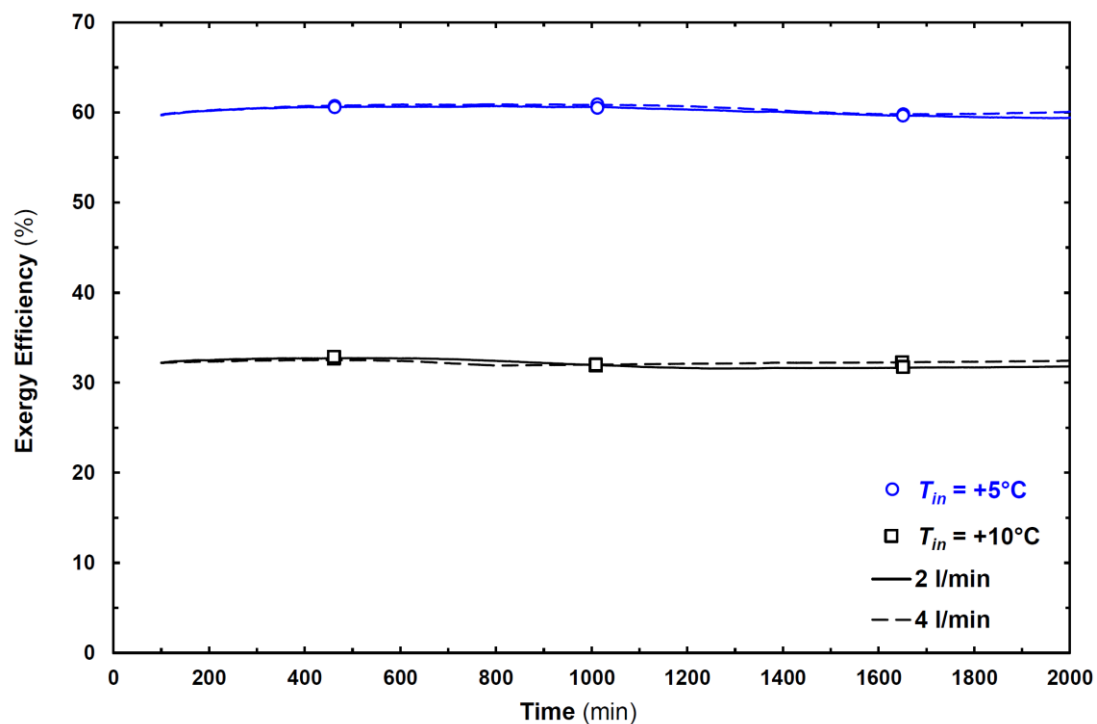


Figure 4.28 Influences of the inlet temperature and flow rate of the HTF on exergy efficiency for discharging period.

Table 4.8 Parametric results of the shell-and-tube type LHTES.

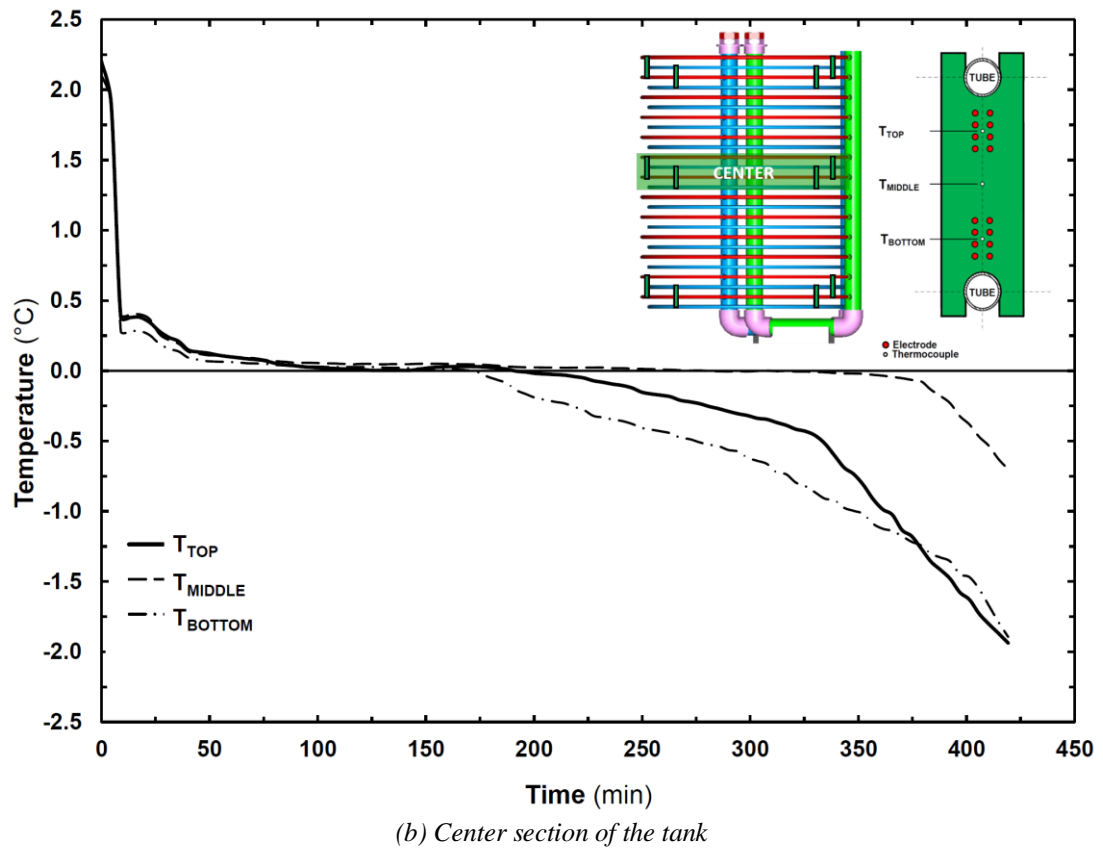
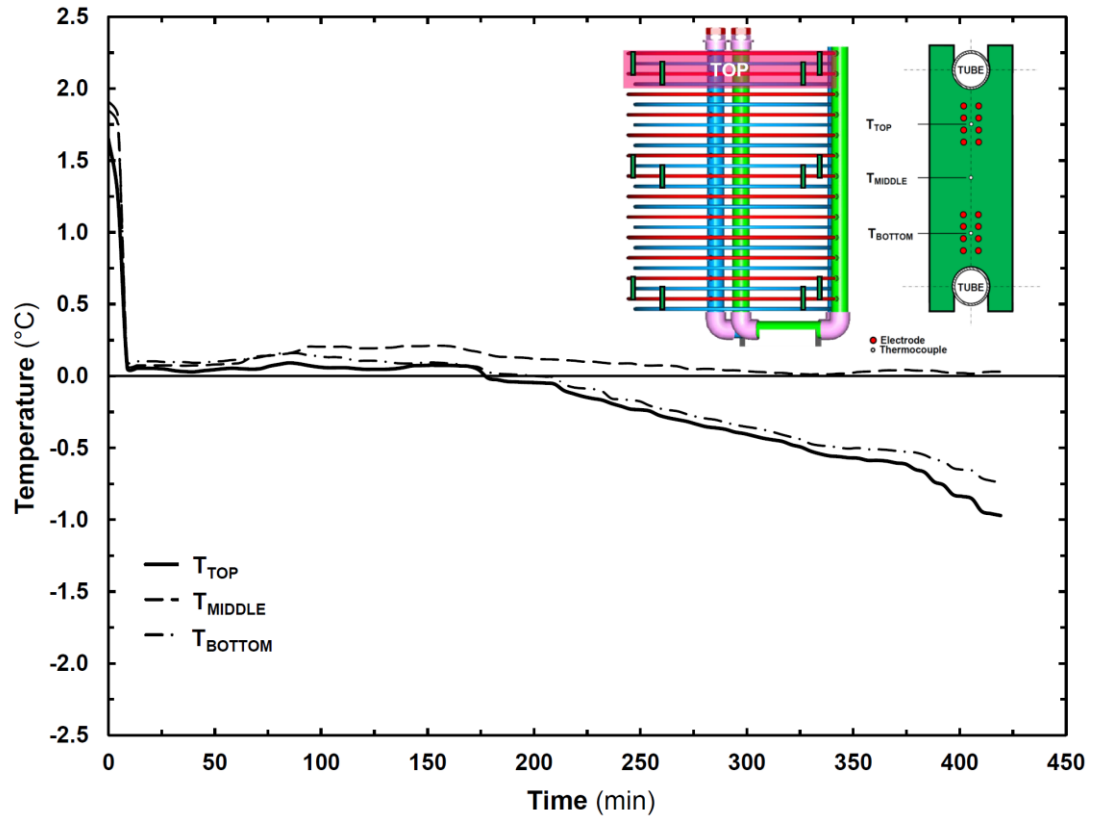
Mode	Shell Diameter	Tube Material	T_{in}	Flow rate	Time	Stored/Rejected Energy	Energy Efficiency	Exergy Efficiency
–	(mm)	–	(°C)	(l/min)	(min)	(kJ)	(%)	(%)
Charging	114	Copper	–5	2	497	474.4	81.4	58.9
				4	420	472.6	83.8	60.5
				8	323	471.6	87.0	64.0
			–10	2	189	478.3	92.1	55.0
				4	173	480.6	92.7	55.0
				8	148	482.4	93.7	54.7
		–15	2	138	484.6	94.2	47.1	
			4	135	484.1	94.3	47.5	
			8	108	486.0	95.4	47.1	
		Stainless Steel	–10	2	255	471.5	89.5	51.0
				4	199	476.6	91.7	52.4
				8	170	472.0	92.7	53.1
	PE-32	–10	2	853	478.3	65.8	39.7	
			4	782	477.8	67.7	40.9	
			8	711	478.6	69.8	40.8	
190	PE-32	–10	2	2779	1410.3	43.0	40.8	
			4	2589	1408.5	56.8	40.8	
			8	2523	1422.8	57.7	41.2	
Discharging	190	PE-32	5	2	2663	843.0	41.8	59.2
				4	2637	854.5	42.3	60.2
			10	2	2303	840.4	50.4	31.9
				4	2260	855.6	51.3	32.5

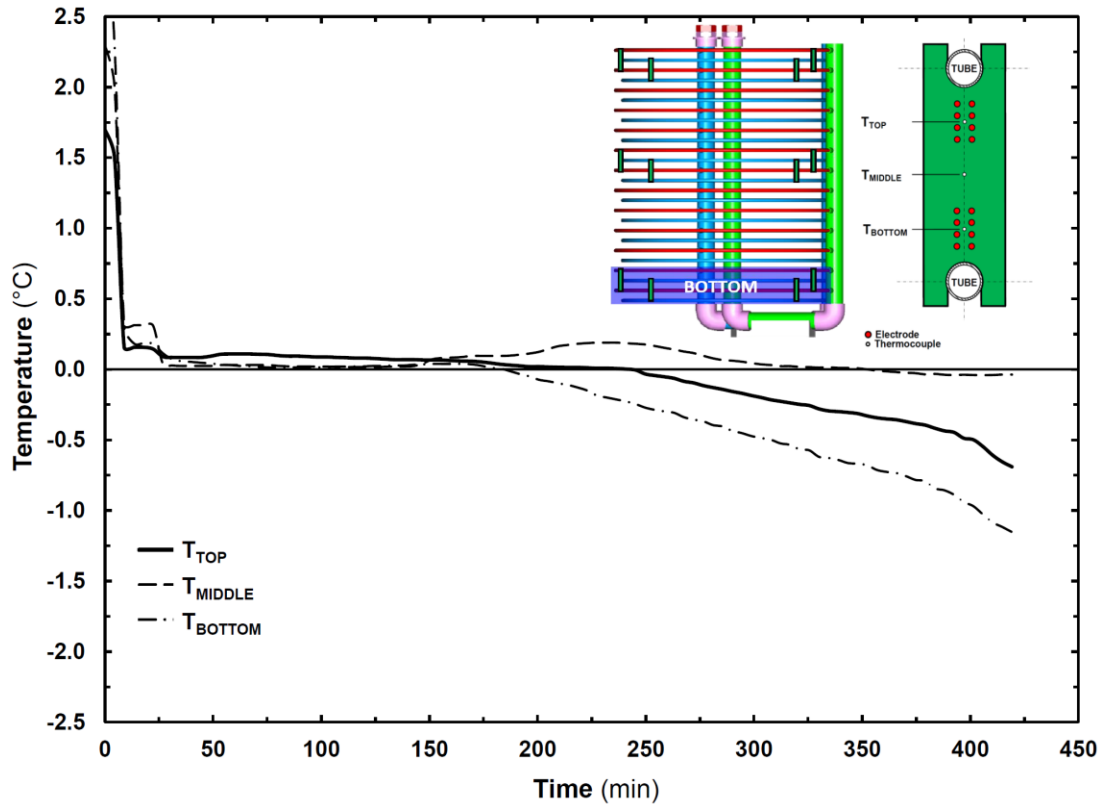
4.2 Experimental Results of Ice-on-coil Type LHTES System

Experimental results for charging and discharging periods of the ice-on-coil heat type LHTES system are represented in two subsections; *temperature-interface variation* and *parametric results of system*. In former one, temperature and interface variations are represented for solidification case. In the latter one, effects of the several working and, design parameters on the charging and discharging capability of the system are investigated.

4.2.1 Temperature and Interface Variations

Measurement cards are located at fifteen different locations inside the tank. Hence, it is possible to watch the variations of temperatures and interface positions for various sections of the tank. As an instance, in Figures 4.29 and 4.30, temperature and interface variation for three cards are illustrated for a selected experiment ($T_{in} = -8^{\circ}\text{C}$, $\dot{V} = 60 \text{ l/min}$). Figure 4.29 illustrates the temperature variations for three cards which are located at the *top-outer-inlet* (T-O-I), *center-outer-inlet* (C-O-I) and *bottom-outer-inlet* (B-O-I) sections of the tank. Thermocouples are settled on the cards at distances of $r_{top} = 22.5 \text{ mm}$, $r_{bottom} = 22.5 \text{ mm}$ and $r_{middle} = 45 \text{ mm}$ from the centers of the tubes. As seen from the figure, at the beginning of the experiment, the initial temperature of the water varies from 2°C to 2.5°C in the vertical direction. Afterwards, temperature value of the water drops under 0.5°C in less than 10 minutes. At the top section of the tank, temperature variations look similar for the bottom and top thermocouples. On the other hand, at the center and the bottom sections of the tank, bottom thermocouples are covered by ice slightly earlier times. This means that, for the center and the bottom sections of the tank, cooling speed is relatively faster for bottom thermocouples in comparison with the top thermocouples. Physical meaning for this slight difference may explain with considering the card section consisting of two tubes arranged in the vertical direction. For both upper and lower tubes, while relatively cold water with lower density flows through the up side, relatively hot water with higher density drops through down side. Hence, this effect





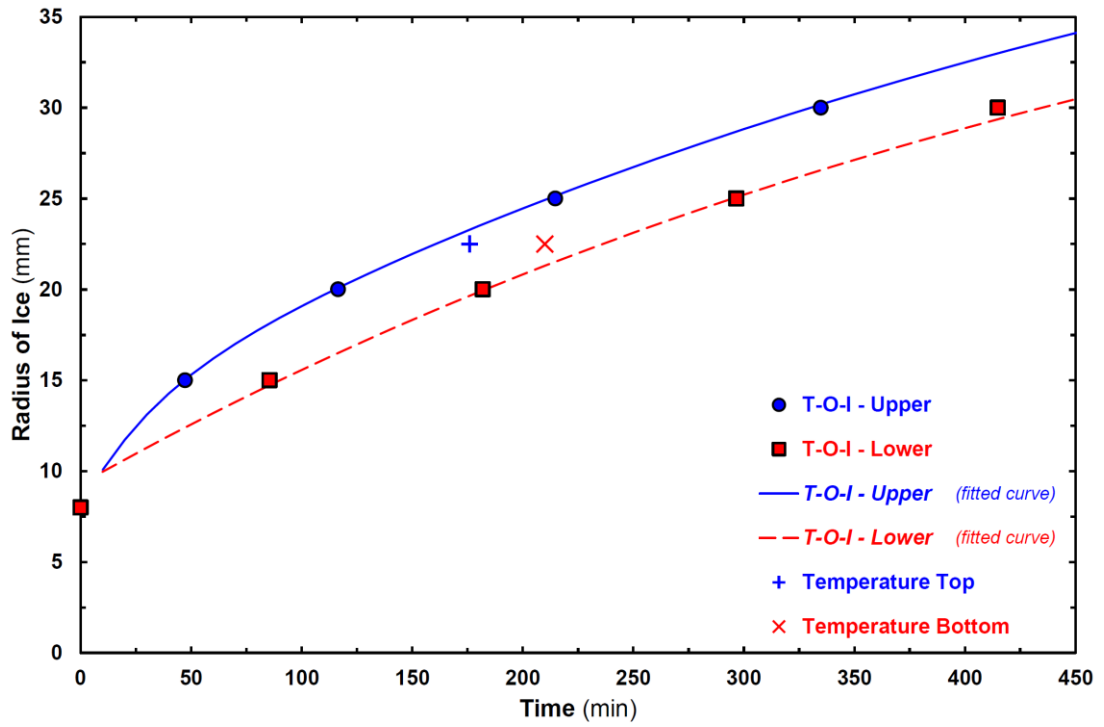
(c) Bottom section of the tank

($T_{in} = -8^{\circ}\text{C}$ and $\dot{V} = 60 \text{ l/min}$)

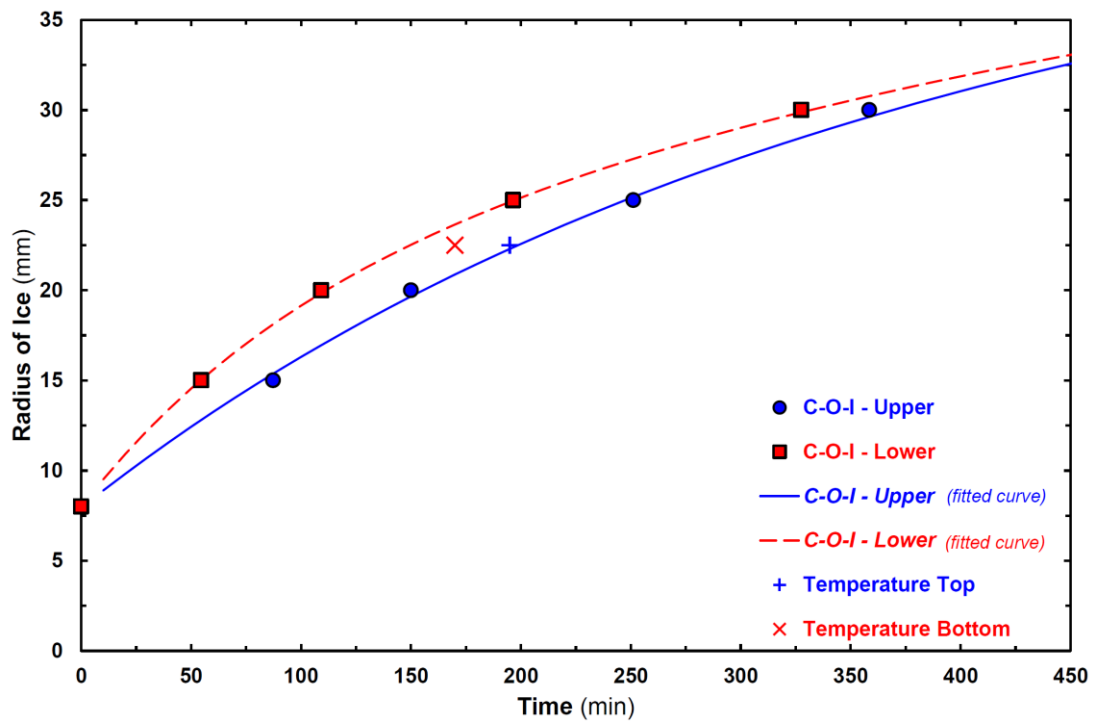
Figure 4.29 Temperature variations inside the tank.

may cause a natural convection dominated local regions around the top side of the lower tube. On the other hand, a thermal stratification dominated local region may occur at the bottom side of the upper tube. This thermal stratification slightly slows down the solidification for the upper tube. Besides, it can be seen that, from top to bottom of the tank, the temperature values vary in a small interval, and the temperature distribution is nearly homogenous.

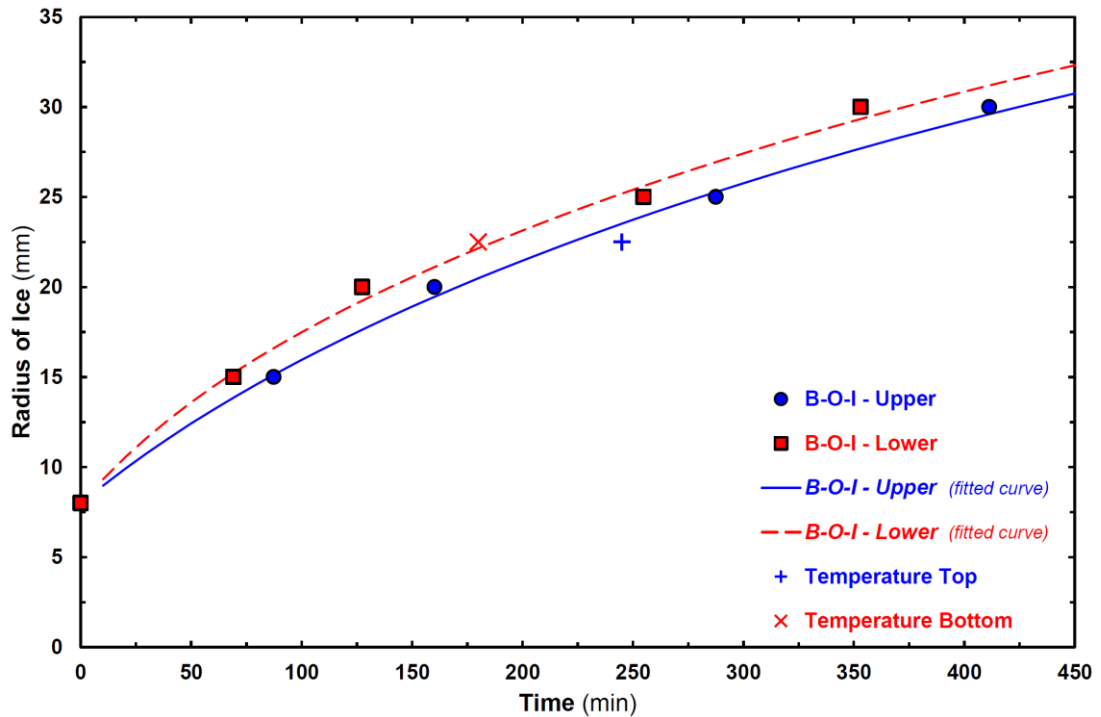
For the same experiment, interface variations for three card sections are also computed for both upper and lower tubes. In Figure 4.30, the time wise variations of the interfaces are illustrated for the top, center and bottom sections. For each card, growth of ice is given for the upper and the lower tubes. The solid circles and squares represent the solidification times of electrodes that are located near the upper and lower tubes, respectively. Electrodes are placed at $r_1 = 15 \text{ mm}$, $r_2 = 20 \text{ mm}$, $r_3 = 25 \text{ mm}$ and $r_4 = 30 \text{ mm}$ positions from the centers of the tubes. A dynamic curve fitting method (*Exponential Rise to Maximum – 5 Parameters*) is applied to five nodes of



(a) Top section of the tank



(b) Center section of the tank



(c) Bottom section of the tank

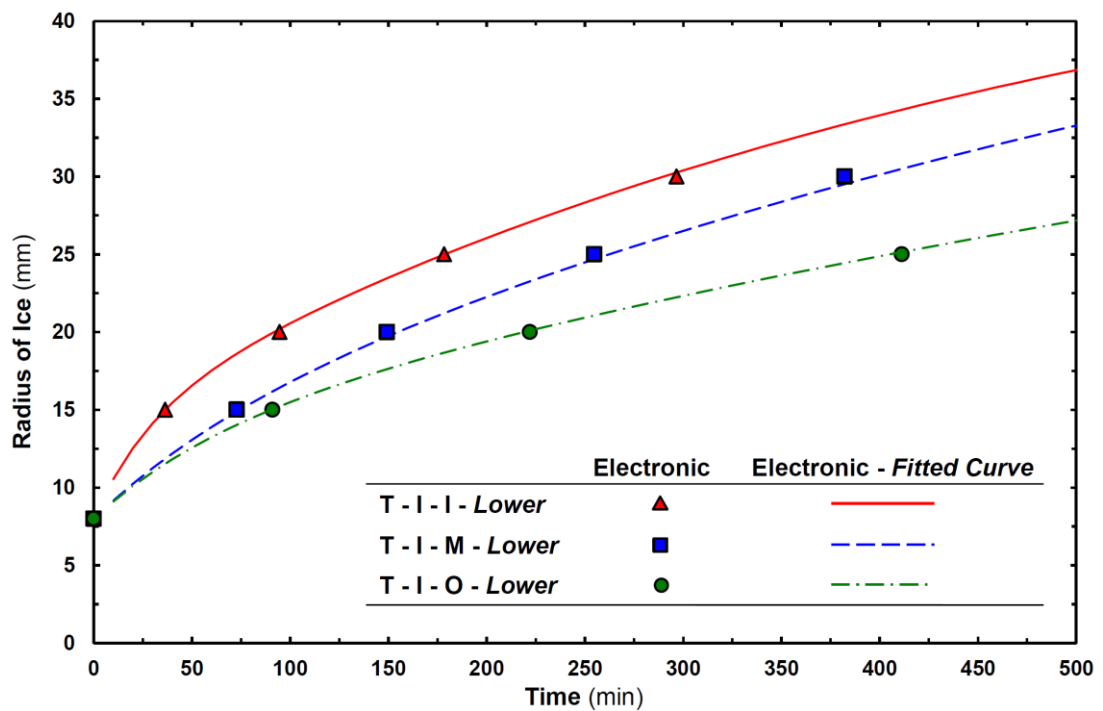
($T_{in} = -8^{\circ}\text{C}$ and $\dot{V} = 60 \text{ l/min}$)

Figure 4.30 Interface variations inside the tank.

the measurement card data to obtain the fitted curves. Fitted curves are shown with the dashed and straight lines for the upper and the bottom tubes, respectively. The fitted curves are defined as in the form of Eq. (4.1). In Figures, solidification times of the thermocouple positions are also illustrated. “+” and “x” symbols designate the time that T_{UPPER} and T_{BOTTOM} positions are covered by ice. It seems the thermocouple data and fitted curves have similar pathway. The mean difference between the radius values obtained from thermocouples and interface curves are nearly 3%. From the interface variations, we can say that solidification process takes place almost homogeneously through the vertical direction of the tank. Moreover, the radius of ice slightly differs for upper and bottom tubes. As indicated above, at the center and bottom parts of the tank, the deviation will occur between upper and lower tubes since the formation of local natural convection dominated regions. In contrast, at the top section of the tank, amount of ice radius is higher for upper tube. Even an opening covers the tank, the tank is not evacuated, and the tank consist air between water layer and the opening. Therefore, relatively hot air layer interacts with water,

and this interaction may cause natural convection effects at the top section of the tank.

Additionally, the solid/liquid interface variations through the flow direction are investigated. As seen in Figure 4.31, at the end of the experiment the radius of ice decreases nearly 25%, from the inlet to the outlet sections of the coil. As mentioned before, this effect is expected because of the increasing surface temperature of the tube. From this figure, it can be seen that, for $t = 480$ min, the radii of ice become nearly 35 mm and 25 mm, at the inlet and outlet sections of the HTF, respectively. It means that the pitch is totally covered with ice, with applying cross flow design.



($T_{in} = -8^{\circ}\text{C}$ and $\dot{V} = 60$ l/min)

Figure 4.31 Interface variations along the flow direction.

4.2.2 Parametric Results of Ice-on-coil LHTES System

In this study, two groups of experiments are performed. In the first group of experiments a total of 16 parametric experiments is carried out to compare the usage of the chiller control schemes. These control schemes are; (i) control with the evaporation temperature of R404A (ii) control with the HTF temperature at the outlet

section of the evaporator, (iii) control with the suction pressure of the compressor and (iv) on/off control. Experimental parameters for the first group of studies are given in Tables 4.9.

Table 4.9 Experimental conditions for each control scheme.

Control Schemes	Flow rate	T _{in}
	(l/min)	(°C)
Scheme #1	60	-7, -5
	70	-7, -5
Scheme #2	60	-7, -5
	70	-7, -5
Scheme #3	60	-7, -5
	70	-7, -5
Scheme #4	60	-7, -5
	70	-7, -5

In addition to that, after comparing these control schemes, further 19 experiments are conducted to observe the influences of the inlet temperature and flow rate of the HTF (*or* PCM) on the charging and discharging performances of the system.

For solidification case, experiments are carried out for four different flow rates and five different inlet temperatures of the HTF to investigate the charging behavior of the LHTES system. In order to introduce the discharging performance of the system, while the external melting experiments are performed for two different heat loads and flow rates, internal melting experiments are carried out for two heat loads and various inlet temperatures with two different flow rates. Experimental parameters for the second group of studies are given in Tables 4.10.

Besides, several selected experiments are also repeated to check the reproducibility of the experiments. It was observed that the results varies less than 3% for pair experiments.

Table 4.10 Experimental parameters for charging and discharging experiments.

Case	Flow rate (l/min)	Inlet Temperature (°C)		
Solidification (Charging)	70	-8, -7, -6, -5, -4		
	50	-8, -6		
	40	-8		
	30	-8, -6		
Melting (Discharging)	Melting Mode	Flow rate (l/min)	Inlet Temperature (°C)	
	<i>Internal</i>	50	+10, +12	
		75	+8, +10, +12	
		Flow rate (l/min)	Heat Load (kW)	
		<i>Internal</i>	60, 70	7, 9
		<i>External</i>	50, 70	7, 9

4.2.2.1 Influence of Control Schemes on Performance of System

Control schemes are compared in terms of the time wise variations of the inlet temperature of the HTF to the storage tank, energy efficiency of the storage tank and COP of the system.

In Figure 4.32, time wise variations of the inlet temperature of the HTF are represented for each control scheme. As is known, inlet temperature of the HTF has more influence on the energy storage quantity of the system rather than the flow rate of the HTF. Stable inlet temperature allows to determine the exact amount of the stored energy. As seen in Figure 4.32, it is clear that, Scheme (i) cannot provide a stable inlet temperature of the HTF. On the other hand, Scheme (ii) provides closer temperature to the set values for both -5°C and -7°C with very small temperature fluctuations. Scheme (iii) is not able to stabilize the inlet temperature of the HTF for the set value and large fluctuations are observed. Temperature fluctuations for the Schemes (i) and (iii) are related with the time delay between the variation of the inlet temperature of the HTF and the change in the evaporation temperature and, the suction pressure values, respectively. On the other hand, for on/off control scheme, it takes so long time to reach the set value because of the limiting the frequency at the 50 Hz. This initial period is about 50 minutes for the Schemes (i), (iii) and (iv) and

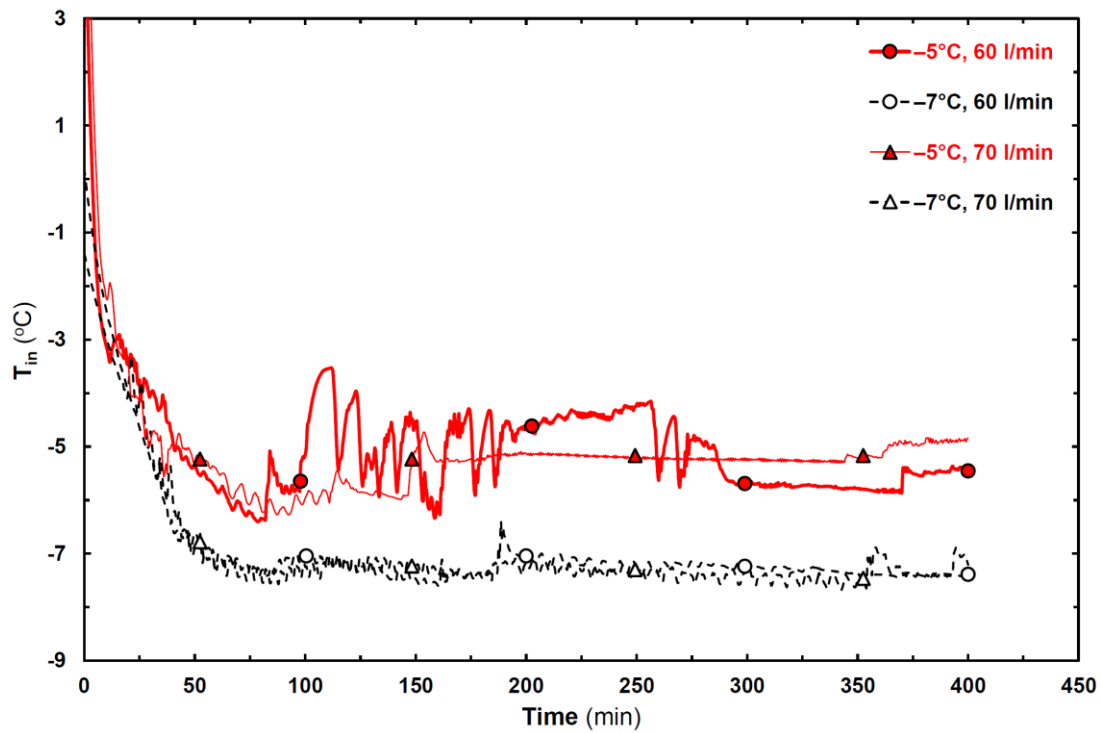
25 minutes for the Scheme (ii). After this long initial period, on/off control scheme has better stabilization in comparison with Schemes (i) and (iii).

Further comparisons are conducted in terms of the time wise variations of energy efficiencies. Energy efficiency of the system is related with the internal energy variation of the system and the enthalpy variation of the HTF. With considering the energy balance as given in Eq. (2.23), energy efficiency can be defined as a function of the heat gain from surroundings. Experimental results indicate that the heat gain from surroundings is almost constant for all experiments. Hence, the rate of enthalpy variation in the HTF is deterministic parameter for the energy efficiency. In Figure 4.33, variations of efficiencies are represented for various inlet temperatures and flow rates of the HTF with three different control schemes.

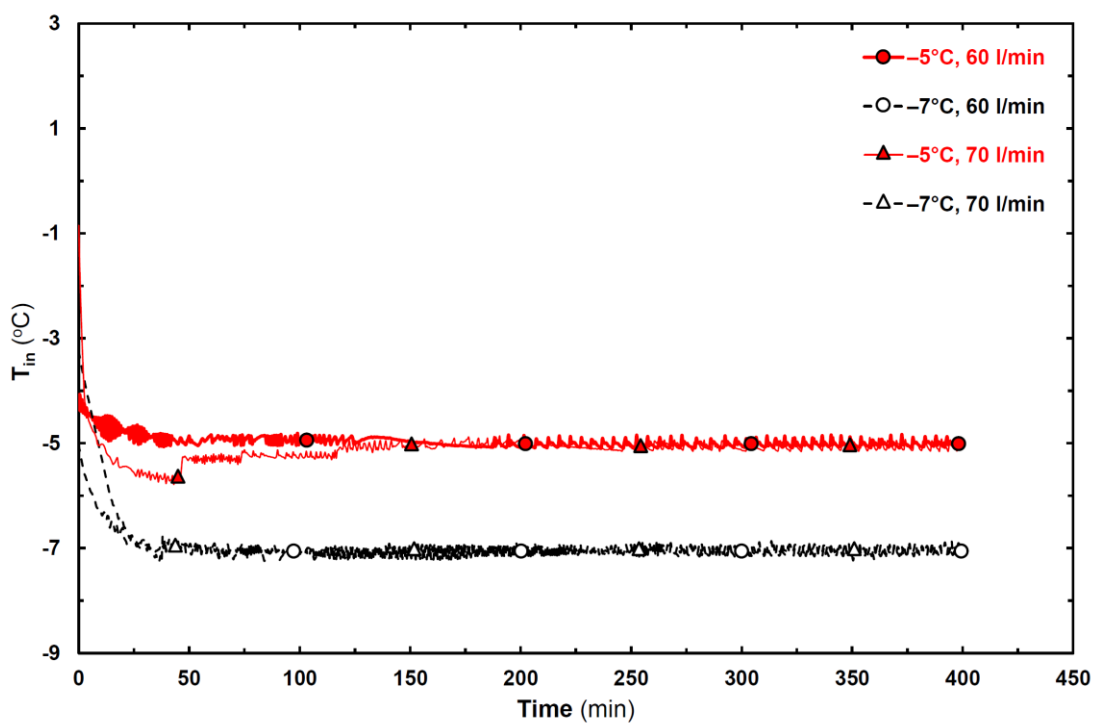
In Figure 4.33(a), time wise variations of energy efficiencies are illustrated for Scheme (i). Energy efficiency of the storage system varies between 97.1% and 98.2%. The highest energy efficiency value (98.2%) is obtained for $\dot{V} = 70$ l/min and $T_{in} = -7^{\circ}\text{C}$, and the lowest value (97.1%) is obtained for $\dot{V} = 60$ l/min with $T_{in} = -5^{\circ}\text{C}$.

Similarly, for the Scheme (ii), energy efficiency varies between 97.6% and 99.0%. The highest energy efficiency value (99.0%) is obtained for 60 l/min flow rate and -7°C inlet temperature of HTF. The lowest efficiency value (97.6%) is obtained for 60 l/min flow rate with -5°C inlet temperature of HTF. Schemes (i) and (iii) have almost the same energy efficiency values. In addition, energy efficiency values of Scheme (iv) is close to Scheme (i) and (iii) for all inlet temperatures of HTF.

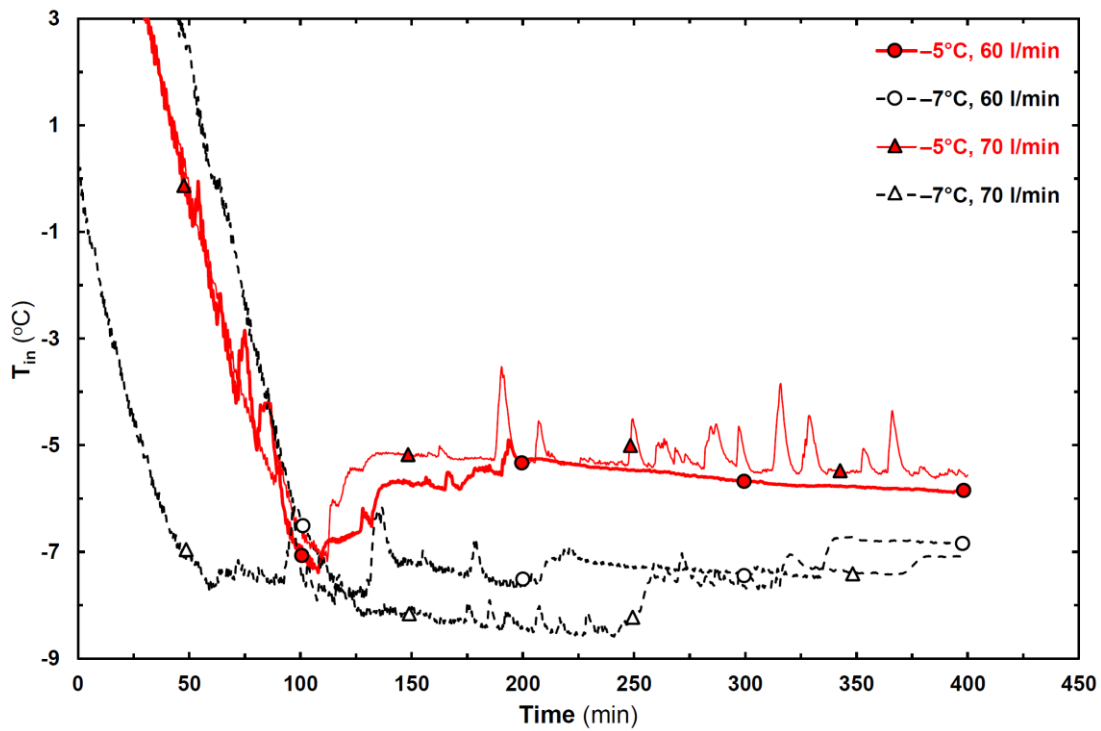
Energy efficiency starts from 100% and decreases in progressing time of the experiments until the solidification process is completed. Scheme (ii) provides the higher energy efficiency values (99.0%) than all of the other control cases. On the other hand, Scheme (iv) has the lowest efficiency values.



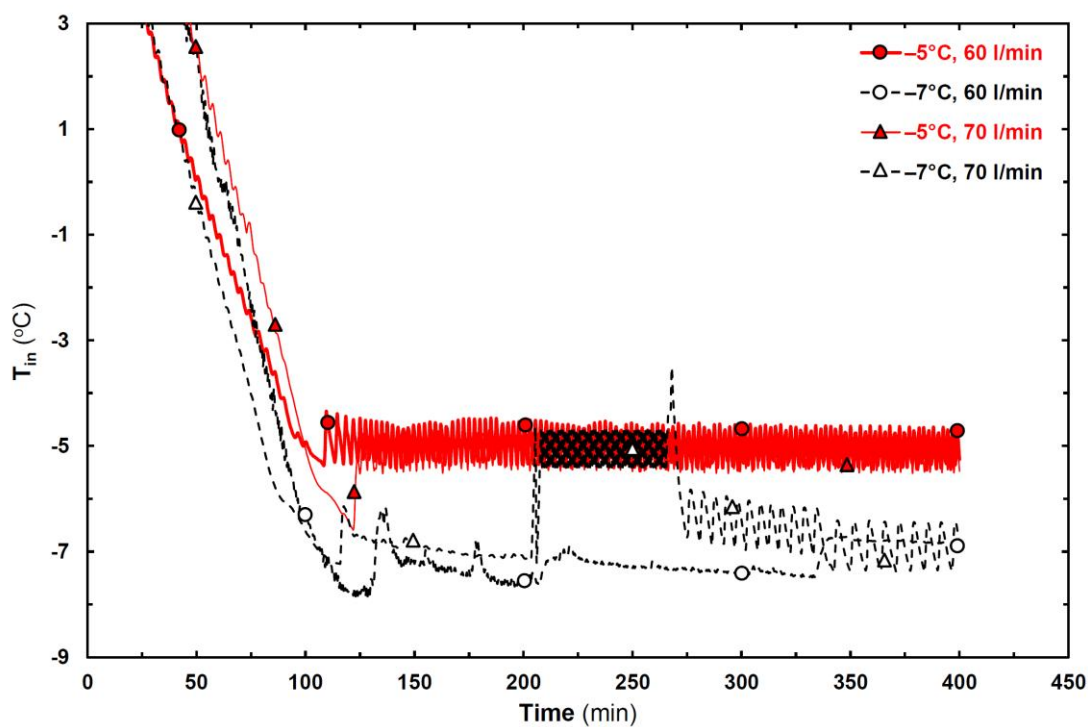
(a) Scheme (i)



(b) Scheme (ii)

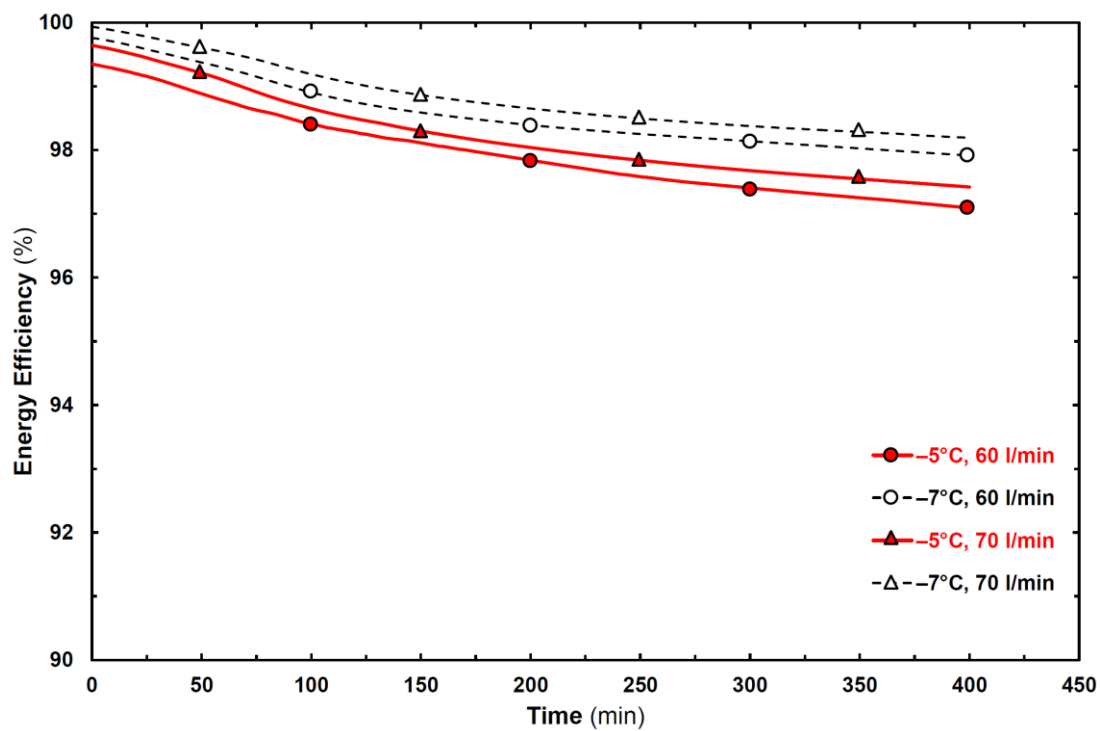


(c) Scheme (iii)

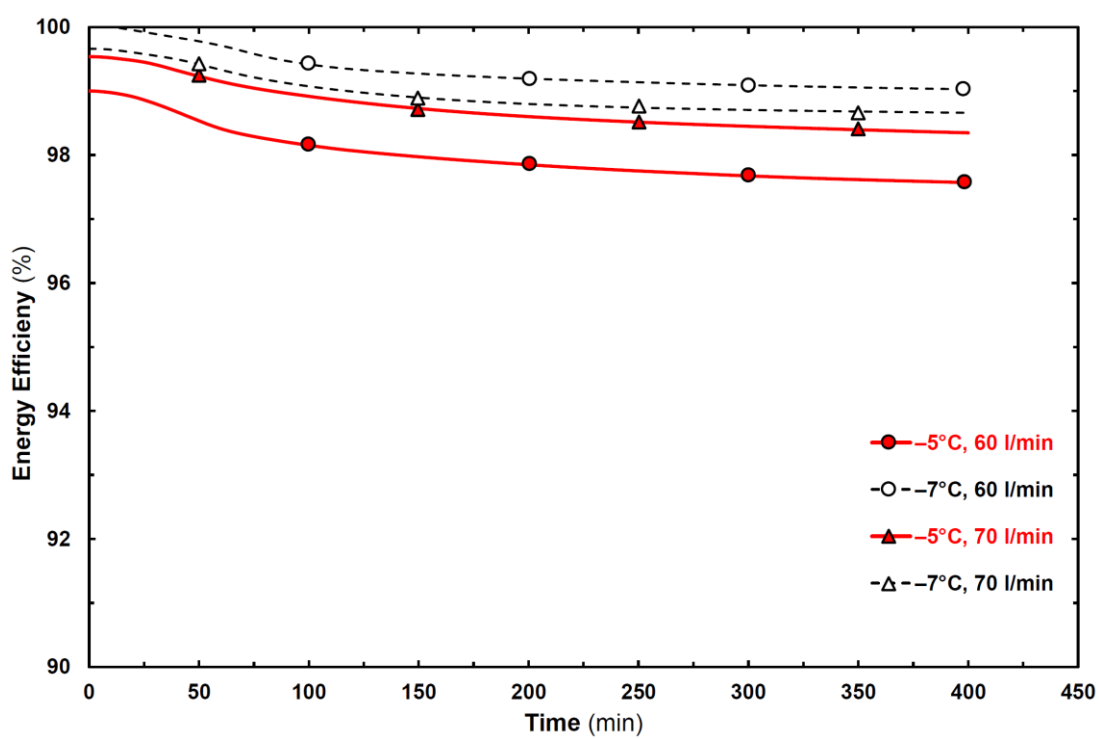


(d) Scheme (iv)

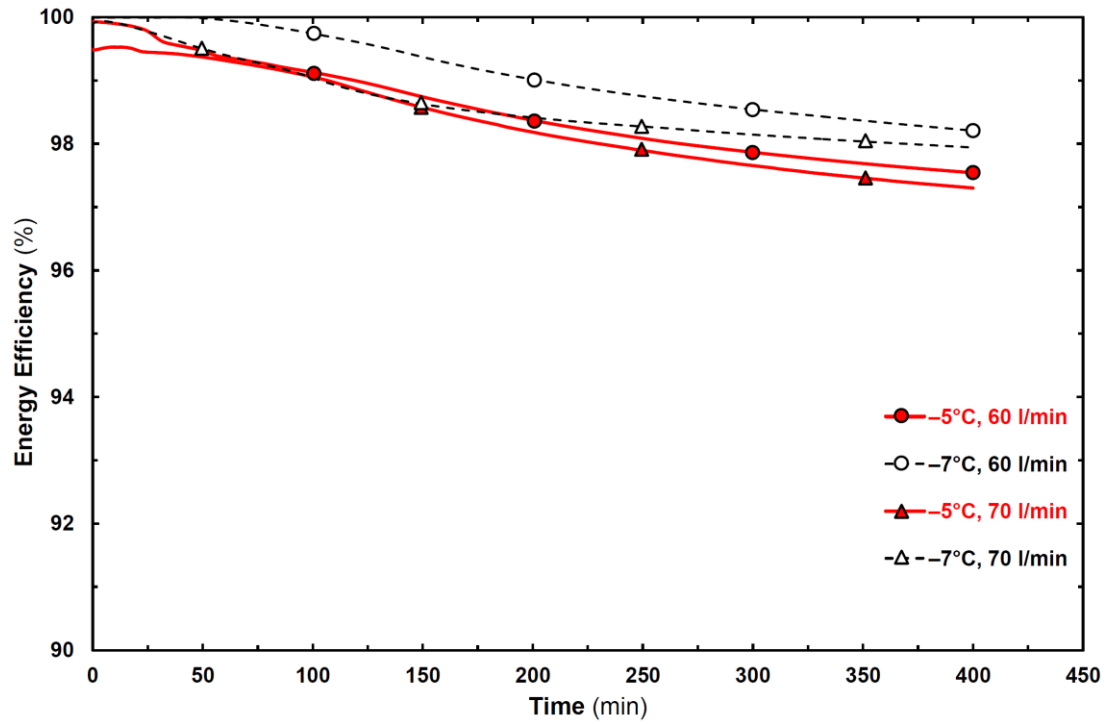
Figure 4.32 Time wise variations of the inlet temperature of the HTF for different control schemes.



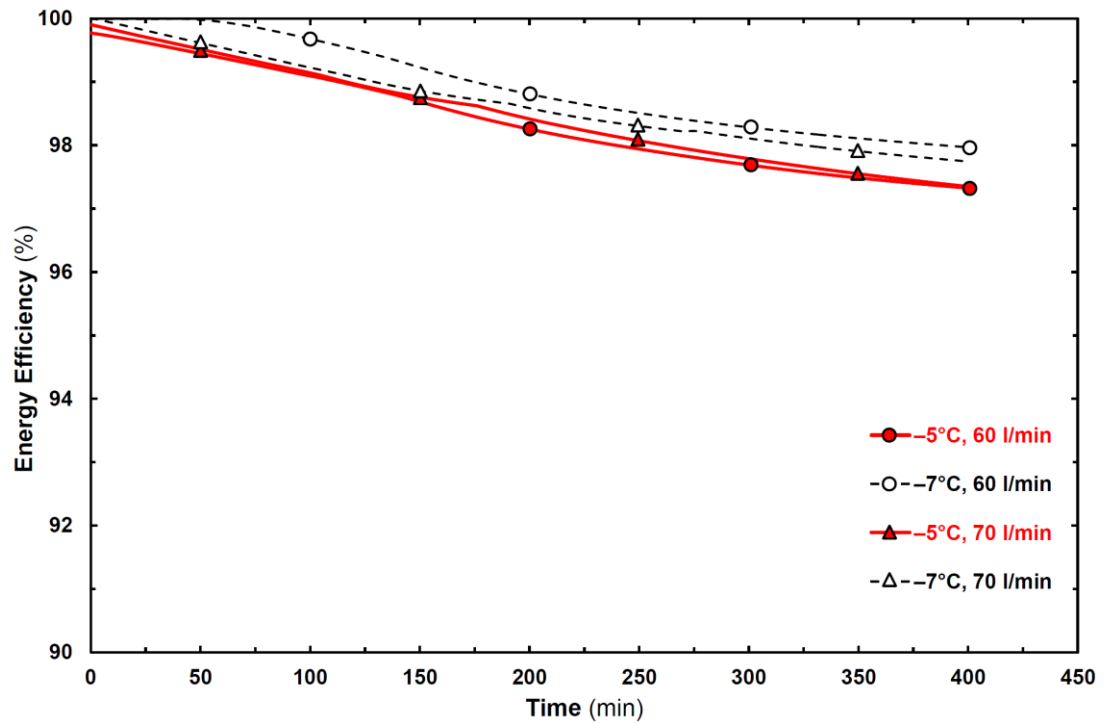
(a) Scheme (i)



(b) Scheme (ii)



(c) Scheme (iii)



(d) Scheme (iv)

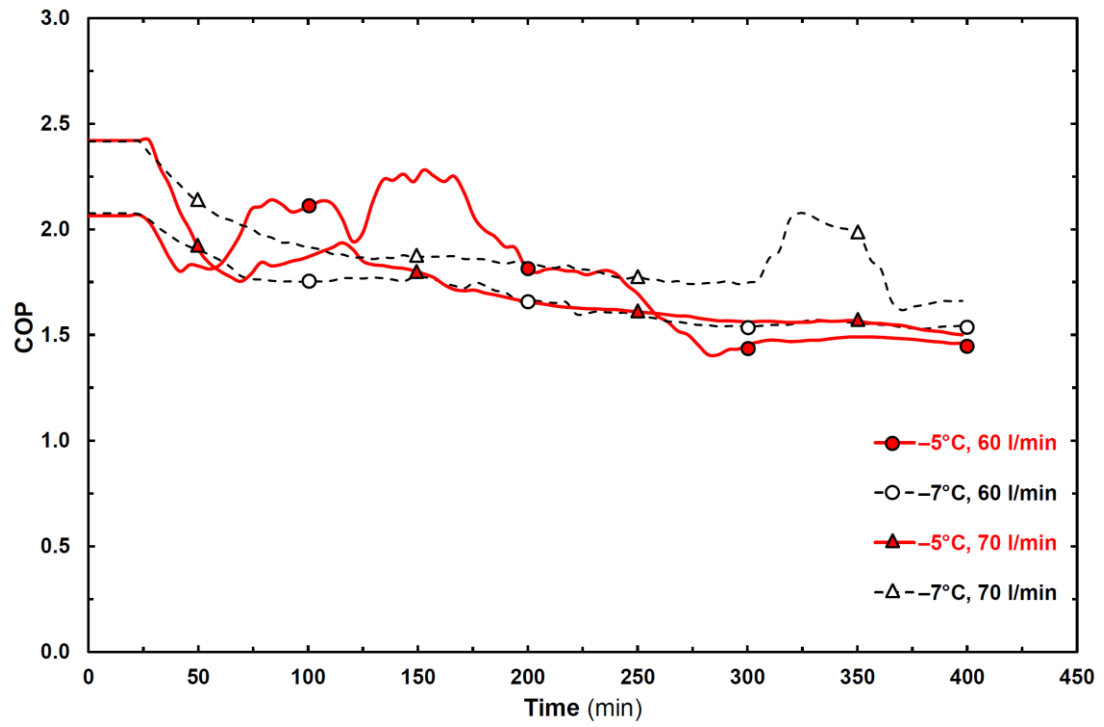
Figure 4.33 Time wise variations of energy efficiencies for different control schemes.

Another performance parameter for the LHTEs system is the coefficient of performance (COP). Figure 4.34 shows the time wise variations of the COP for different control schemes. It is clear that, for current experiments, COP varies around 2–2.5.

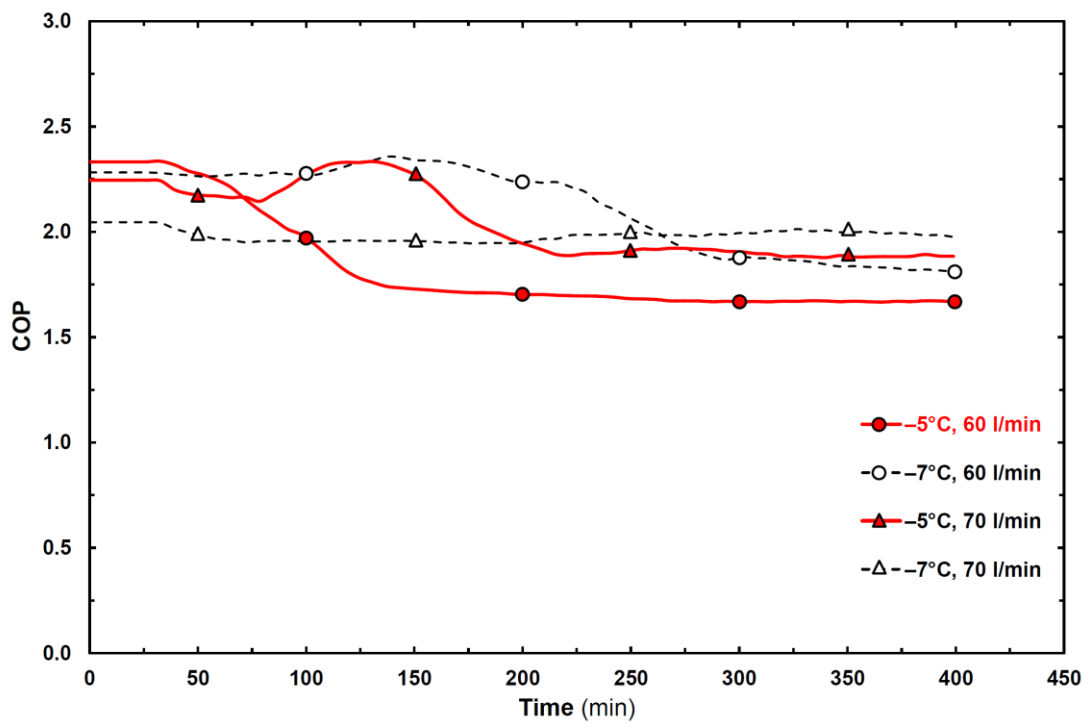
One can observe from Figure 4.34 that, at the beginning of the experiments, COP values are around 2.0 to 2.5, and nearly remain constant for 40 min. This period can be called as continues cooling, because the chiller works continuously until the inlet temperature of the HTF reaches the set value. While the inlet temperature of the HTF becomes closer to the set value, depending on scheme, either speed of the compressor varies or compressor goes on the off periods. Because of the varying compressor power consumption, COP values start fluctuation.

For current parameters, COP of the system increases with using the Scheme (ii) rather than using the control Schemes (i) and (iii). On the other hand, usage of on/off control scheme causes large fluctuations in the COP, because of the on and off periods of the compressor. On/off operation of the compressor provides a constant speed (50 Hz) at the start–up and operation periods. Besides, in Schemes (i) to (iii) frequency of the compressor varies between 20 to 80 Hz. When starting–up period occurs, compressor speed reaches to 80 Hz and COP tends to decrease. Therefore, with respect to these start–up periods, COP values become lower in Schemes (i) to (iii) in comparison to the Scheme (iv).

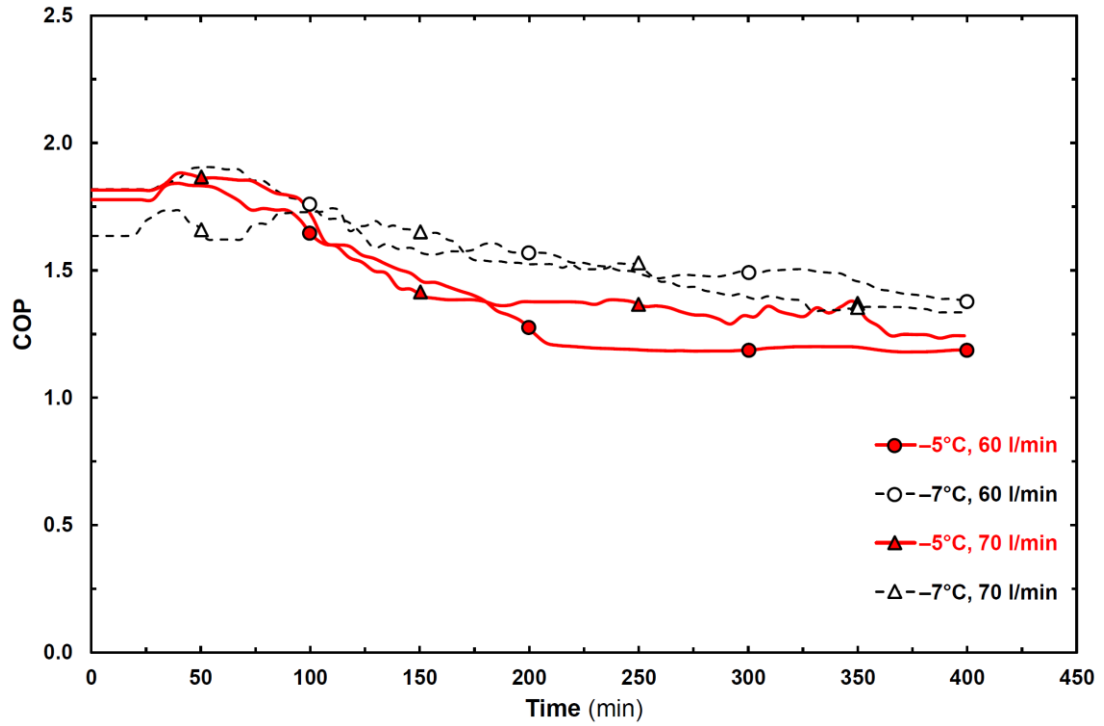
As a result, four different control schemes are tested to obtain a constant temperature value of the HTF at the inlet section of the storage tank. Results indicate that control Scheme (ii) fulfill this request that is specified aforementioned. In the following section, further parametric experiments are represented with using the control Scheme (ii).



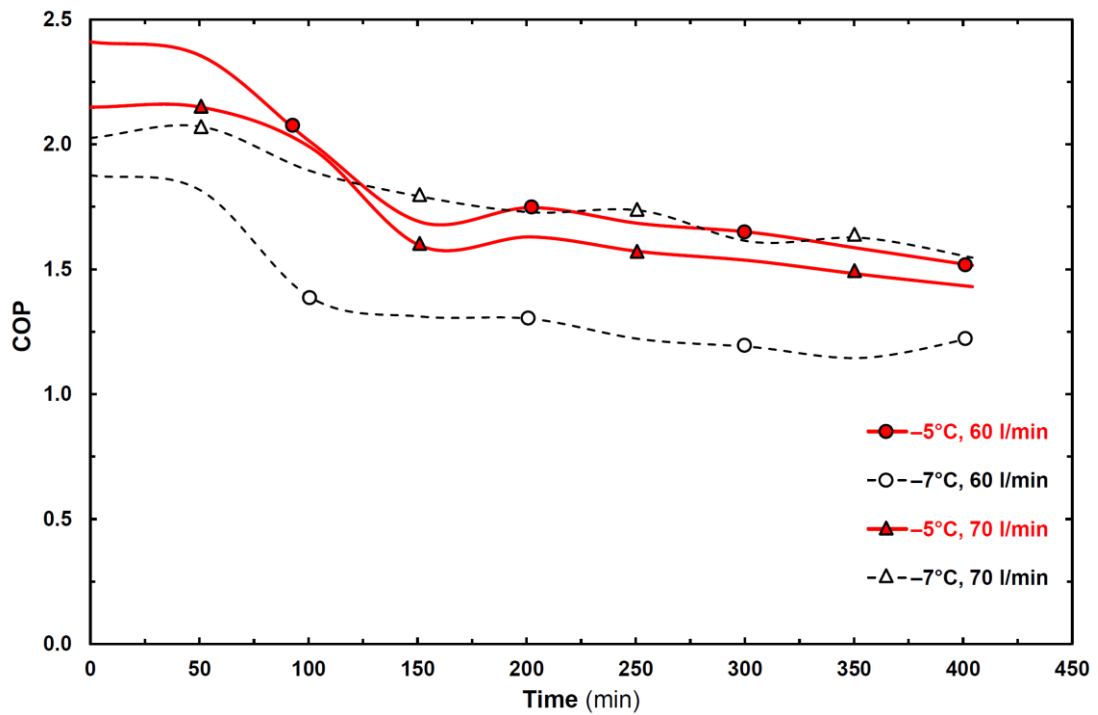
(a) Scheme (i)



(b) Scheme (ii)



(c) Scheme (iii)



(d) Scheme (iv)

Figure 4.34 Time wise variations of the COP for different control schemes.

4.2.2.2 Parametric Results for Charging (Solidification) Experiments

Solidification experiments are performed for five different inlet temperatures and four different flow rates of the HTF to investigate their combine effects on the total stored energy. Figures 4.35 and 4.36 represent the time wise variations of the total stored energy, in terms of various inlet temperatures and flow rates of the HTF. It is clear from the figures that with the decreasing the inlet temperature and increasing the flow rate, the total stored energy rises, as it is expected.

On the other hand, it must be emphasized that, for relatively lower inlet temperatures of the HTF, such as $T_{in} = -8^{\circ}\text{C}$, the flow rate of the HTF seems to be more effective than the higher inlet temperatures, such as $T_{in} = -6^{\circ}\text{C}$ (see Figure 4.36).

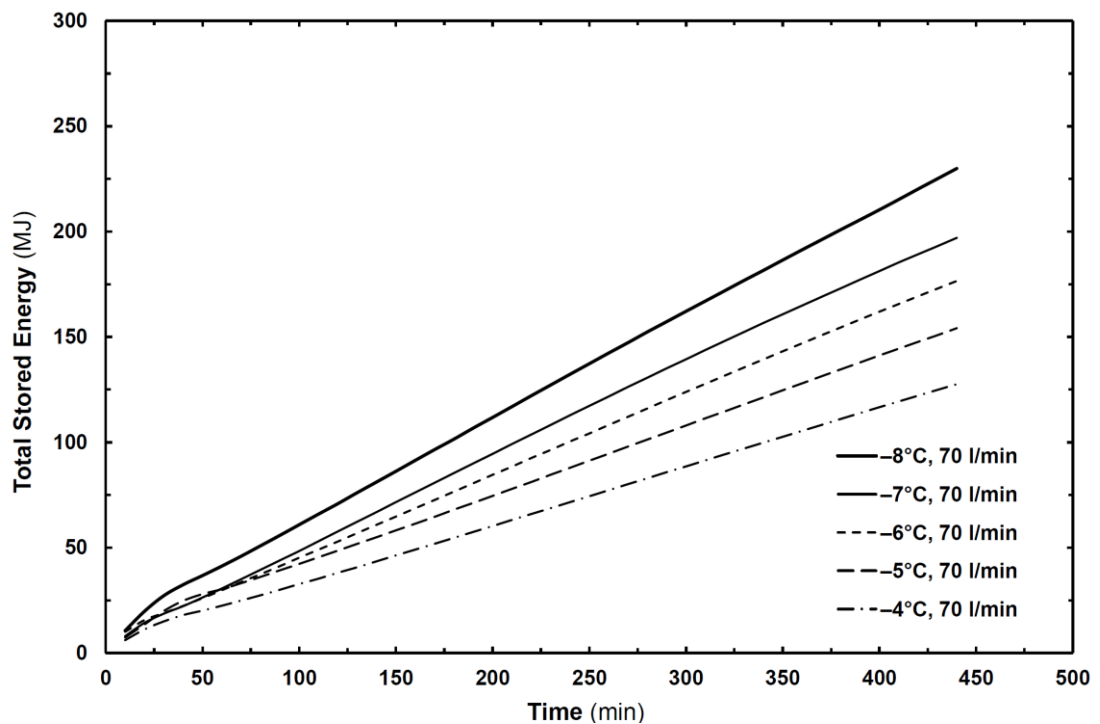


Figure 4.35 Influence of the inlet temperature of the HTF on the total stored energy.

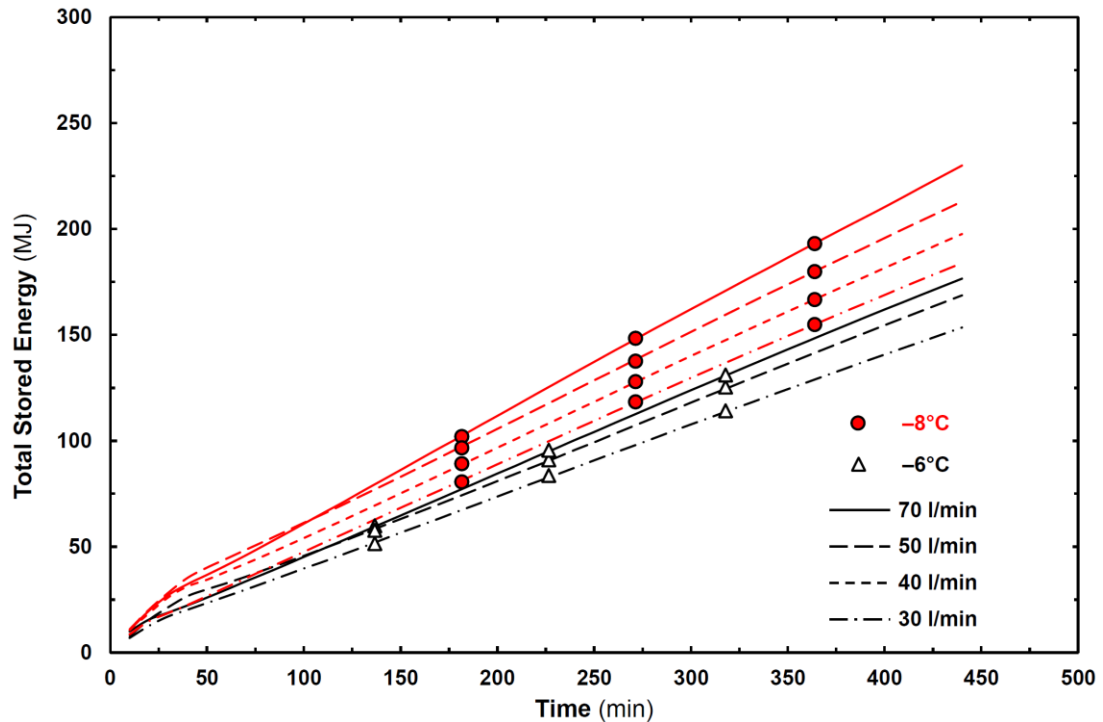


Figure 4.36 Influences of the flow rate and inlet temperature of the HTF on the total stored energy.

4.2.2.3 Parametric Results for Discharging (Melting) Experiments

Discharging experiments are carried out for internal and external melting modes.

4.2.2.3.1. Internal Melting Experiments. For internal melting mode, first, constant inlet temperature condition is investigated. In Figure 4.37, variations of temperature differences between the inlet and outlet sections of the tank are represented for five parameters. The temperature difference of the HTF increases with decreasing the flow rate or increasing the inlet temperature of the HTF. In the light of the temperature difference, it seems that the flow rate of the HTF is more effective than the inlet temperature. For current parameters, results designate that; the temperature drop in the system varies between 1.3°C and 2.5°C, depending on the parameters. System can supply this temperature drop for more than 400 minutes. With increasing the inlet temperature of the HTF, temperature difference rises with a decreasing tendency. Furthermore, for relatively higher inlet temperatures of the HTF, the influence of the flow rate becomes effective.

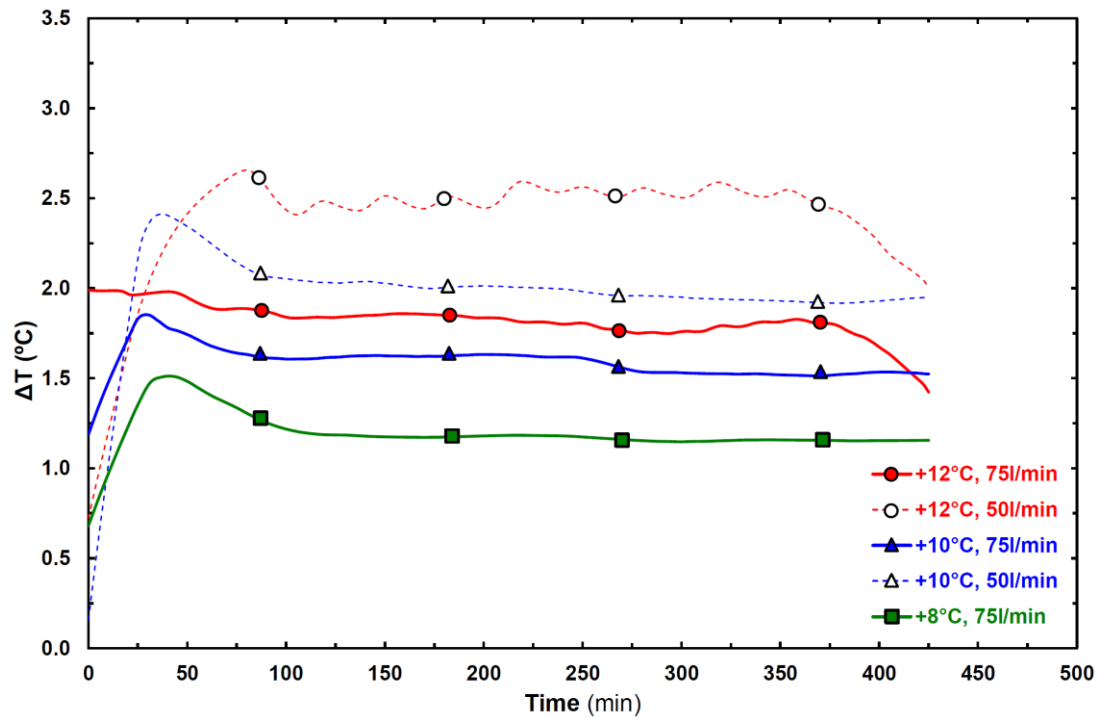


Figure 4.37 Time wise variations of the temperature difference for internal melting mode.

For the same parameters, time wise variations of the rejected energies are given in Figure 4.38. It can be seen that the total rejected energy rises via increasing the inlet temperature with a decreasing tendency. To explain this effect, time wise variations of the surface temperatures are also investigated. For the experiment with $T_{in} = +8^{\circ}\text{C}$ condition, the mean surface temperature of coils remain under 4°C . On the other hand, for $T_{in} = +10^{\circ}\text{C}$ and $T_{in} = +12^{\circ}\text{C}$ conditions, the mean surface temperatures of the coils reach to 5°C and 6°C , respectively. For the latter experiments, relatively higher surface temperatures increase the Rayleigh number; hence, the influence of natural convection becomes more effective. It is known that, for water, the direction of buoyancy forces inverse after 4°C and these cause more complex convection behavior inside the melted region. Considering these interactions, with increasing the inlet temperature of the HTF from $+8^{\circ}\text{C}$ to $+10^{\circ}\text{C}$, melted volume increases with a higher rate, in comparison with change from $+10^{\circ}\text{C}$ to $+12^{\circ}\text{C}$.

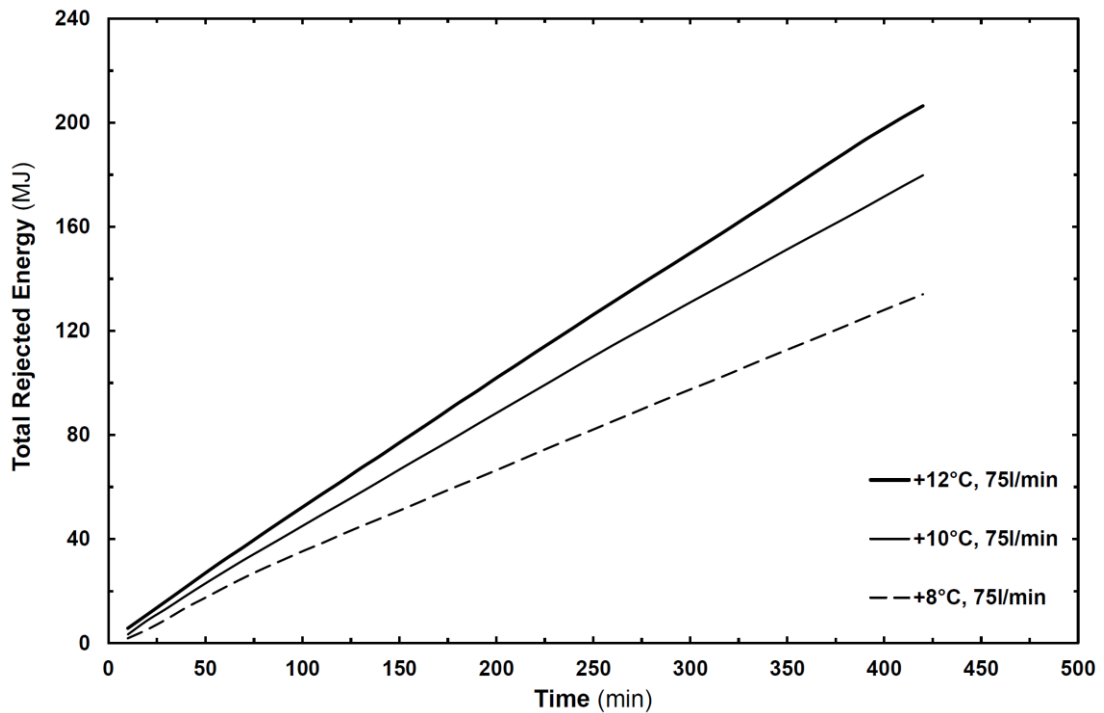


Figure 4.38 Influence of the inlet temperature on the total rejected energy for internal melting mode.

Besides, in Figure 4.39, time wise variations of the total rejected energies are given for two different flow rates and inlet temperatures of the HTF. For selected parameters, it can be seen that the flow rate of the HTF has nearly the same effect as the inlet temperature of the HTF. With increasing the inlet temperature or decreasing the flow rate of the HTF, total rejected energy increases.

Secondly, internal melting process is investigated for the constant heat load condition. In Figure 4.40, time wise variations of the inlet–outlet temperature values of the HTF are given together with the variations of temperature differences. From the figure, it can be seen that, the inlet temperature of the HTF rises with increasing the heat load and decreasing the flow rate. Parallel to this change, the temperature difference of the HTF rises with increasing the heat load and decreasing the flow rate. From Figure 4.40, it can be seen that, system supplies constant outlet temperature for nearly 350 min and 450 min under 9 kW and 7 kW heating loads, respectively. For 9 kW heating load condition, the outlet temperature of water is measured as 10°C. On the other hand, for 7 kW heating load condition, the outlet temperature of water is achieved as 7.5°C.

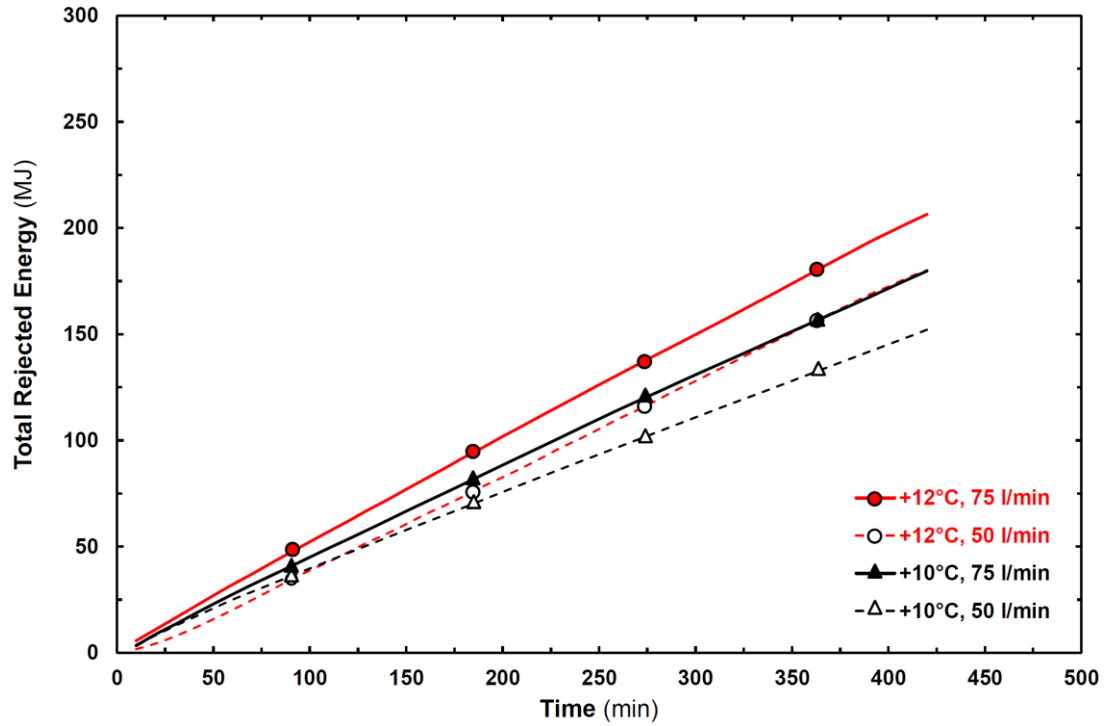


Figure 4.39 Influence of the flow rate on the total rejected energy for internal melting mode.

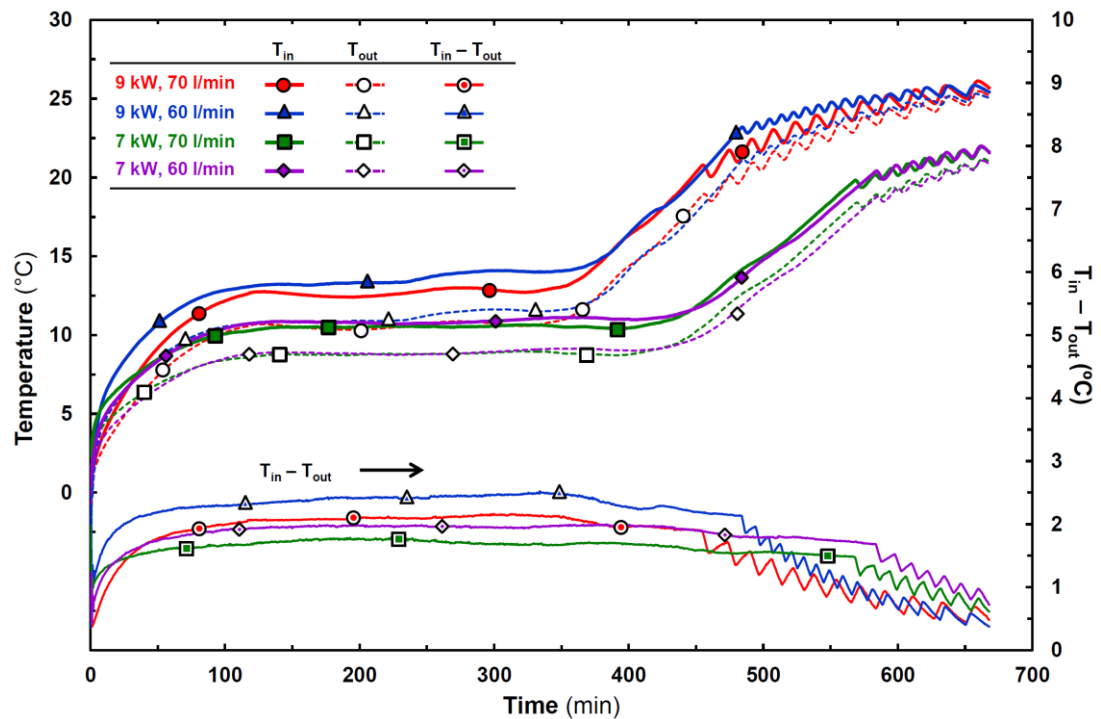


Figure 4.40 Time wise variations of inlet and outlet temperatures of HTF for various constant heat loads for internal melting mode.

Influences of working parameters on the total rejected energy can be seen in Figure 4.41. It is clear that, rejected energy rises with increasing the heat load. The rejected energy almost has no change with the change of the flow rate. Because, with increasing the flow rate, the temperature difference of the HTF decreases, and for selected parameters, these two variations have the same ratio. In the light of the total rejected energy variations, one can say that with using proper working conditions, more than 250 MJ cold energy can be reject in 10 hours, with using internal melting mode of current LHTES system.

4.2.2.3.2. External Melting Experiments. For the external melting mode, experiments are carried out for only constant heat load condition. In Figure 4.42, inlet–outlet temperature variations and temperature differences of the PCM are given for several heat loads and flow rates. It can be seen that, the inlet temperature and temperature difference of the PCM rises with increasing the heat load and decreasing the flow rate of the HTF. In external melting mode, the outlet temperature of water remains under 7.5°C for 7 kW heating load condition for nearly 500 minutes. On the other hand, for 9 kW heating load condition, outlet temperature of water measured as less than 10°C nearly 400 min. These results emphasize that, for current experimental conditions, external melting mode can supply relatively lower outlet temperatures for a long period, in comparison to the internal melting mode.

Lastly, in Figure 4.43 time wise variations of the total rejected energy values are represented. Similar to the internal melting mode, heat load is the deterministic parameter in comparison with the flow rate. Rejected energy increases with increasing the heat load and there is almost no change with the variation of the flow rate from 60 l/min to 70 l/min.

In the light of the total rejected energy variations, one can say that with using the proper working conditions, more than 200 MJ cold energy can be rejected in 500 minutes with using external melting mode of the current LHTES system.

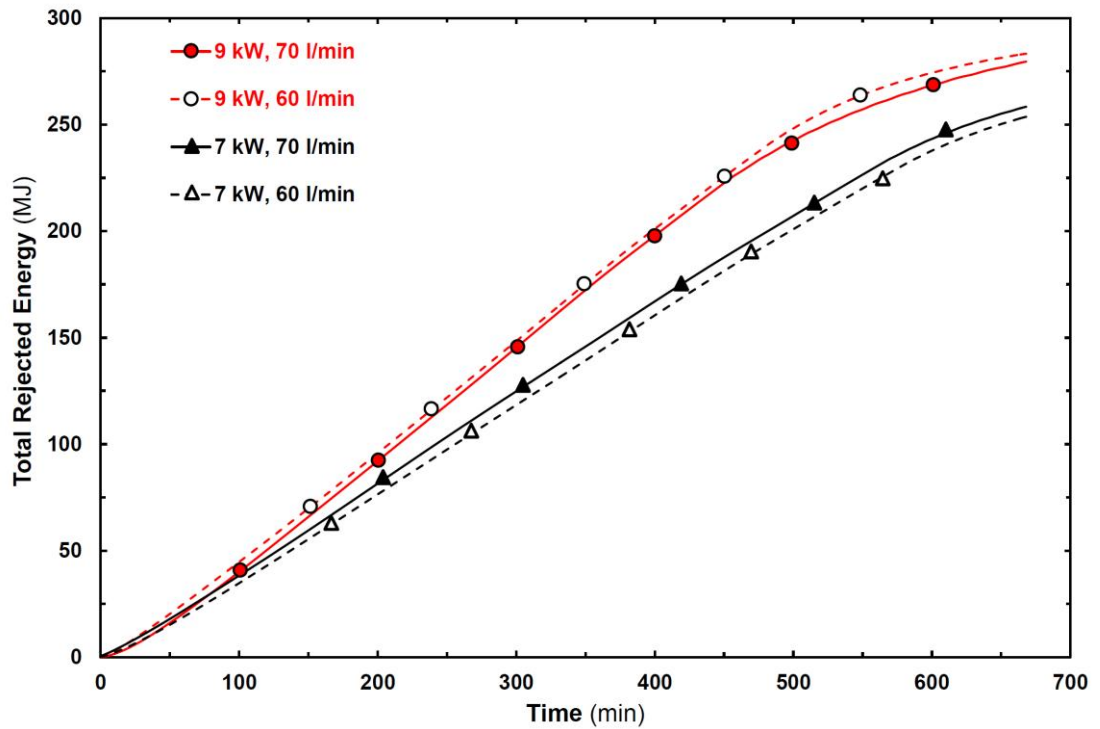


Figure 4.41 Influences of the heat load and flow rate on the total rejected energy for internal melting mode.

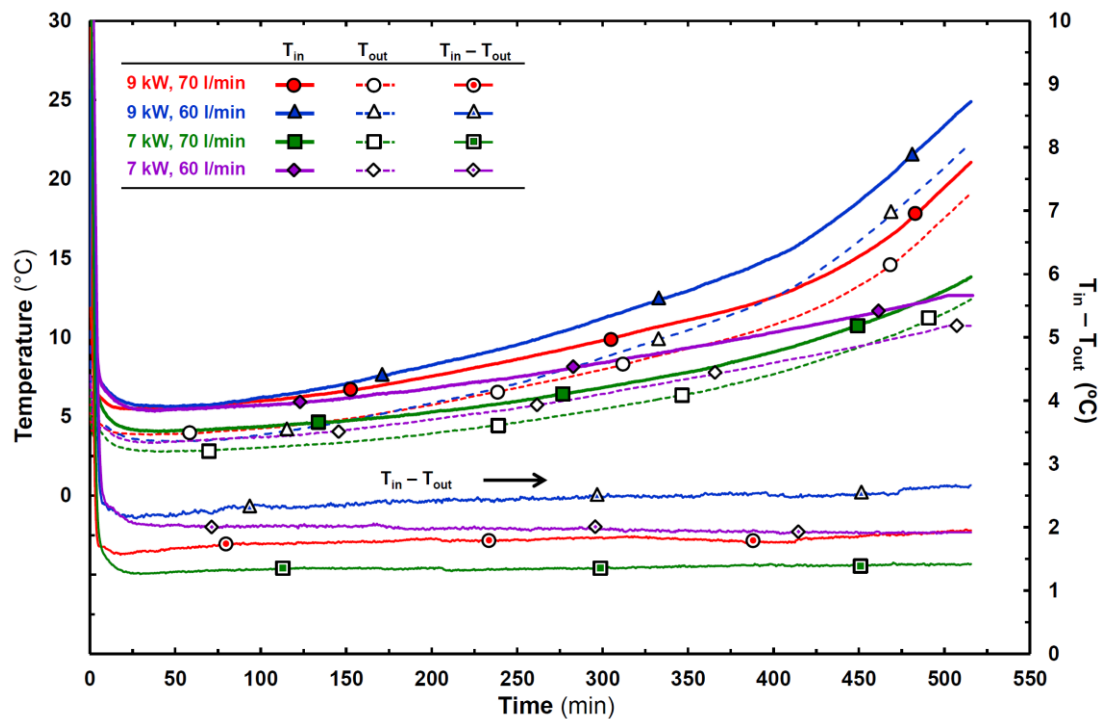


Figure 4.42 Time wise variations of the inlet and the outlet temperatures of the HTF for various constant heat loads, for external melting mode.

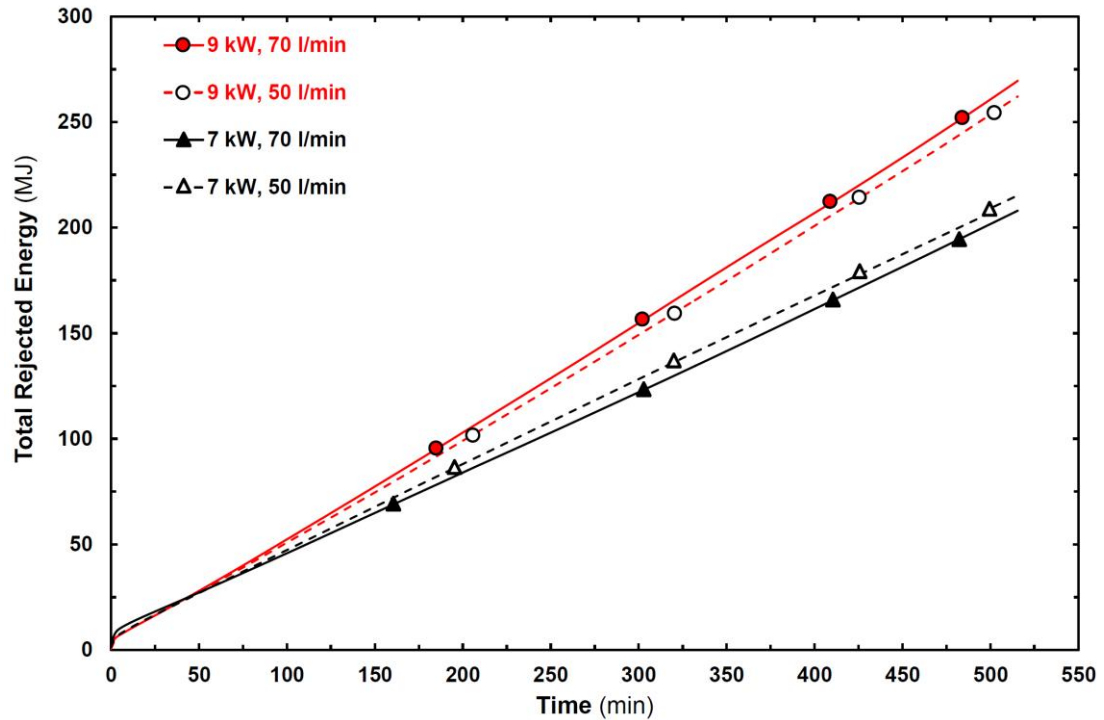


Figure 4.43 Influence of the heat load and the flow rate on the total rejected energy for external melting mode.

4.3 Numerical Results

In this part of dissertation, two sets of numerical results are represented. For consideration of natural convection dominated phase change problem, first, several case studies are tested to validate the numerical methodology. Second, experimental comparisons are performed. Finally, influence of the natural convection on solidification period around a tube is investigated. Time wise variations of the local entropy generation are represented for several initial temperatures. On the other hand, for the ice-on-coil LHTES system, the time-dependent variations of predicted total stored energy, mass of ice and outlet temperature of the HTF from the storage tank are compared with the experimental data. Afterwards, performance of the ice-on-coil LHTES system is investigated for several working and design parameters. The results of a comparative study are represented in terms of variations of the heat transfer rate, the total stored energy, dimensionless energetic and exergetic effectiveness, also, energy and exergy efficiency.

4.3.1 Natural Convection Dominated Phase Change

Two sets of analyses are conducted to investigate the influence of natural convection on phase change. First, four different preliminary cases are carried out to test the validity of the current numerical methodology,

- (i) One–dimensional conduction dominated solidification,
- (ii) Natural convection of water inside a rectangular cavity,
- (iii) Natural convection dominated melting of n –octadecane in a square cavity,
- (iv) Natural convection dominated solidification of water in a rectangular cavity.

In the following section, definitions of problems and comparisons of the current predictions with analytical, numerical, or experimental data are represented for each preliminary case study.

4.3.1.1 Case Studies

4.3.1.1.1 One Dimensional Solidification (Case #1). In this case, water fills a long and well–insulated cavity with an initial temperature of, $T_i = 273.65$ K. Then suddenly, the temperature of the left sidewall of the container drops under the phase change temperature of water, $T_{cold} = 270.15$ K. Thus, in time, there will be ice formation through the x –direction, as seen in Figure 4.44.

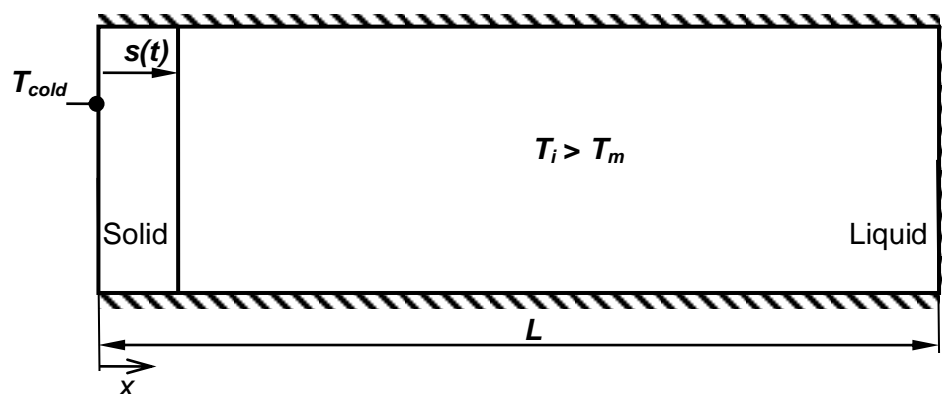


Figure 4.44 Description of the one–dimensional solidification problem.

Ozisik (1980) gives the analytical solution of this one-dimensional solidification problem. Temperature distributions inside the solid and liquid phases of water are defined as follows:

$$\text{Solid phase: } \frac{T_s(x,t) - T_{cold}}{T_m - T_{cold}} = \frac{\text{erf}\left[x/2(\alpha_s t)^{0.5}\right]}{\text{erf}(\lambda)} \quad (4.2)$$

$$\text{Liquid phase: } \frac{T_l(x,t) - T_i}{T_m - T_i} = \frac{\text{erfc}\left[x/2(\alpha_l t)^{0.5}\right]}{\text{erfc}\left[\lambda(\alpha_s/\alpha_l)^{0.5}\right]} \quad (4.3)$$

and the interface position is defined as

$$s(t) = 2\lambda\sqrt{\alpha_s t} \quad (4.4)$$

where λ can be obtained with the solution of the following equation:

$$\frac{e^{-\lambda^2}}{\text{erf}(\lambda)} + \frac{k_l}{k_s} \left(\frac{\alpha_s}{\alpha_l}\right)^{0.5} \frac{T_m - T_i}{T_m - T_{cold}} \frac{e^{-\lambda^2(\alpha_s/\alpha_l)}}{\text{erfc}\left[\lambda(\alpha_s/\alpha_l)^{0.5}\right]} = \frac{\lambda h_{sf} \sqrt{\pi}}{c_s (T_m - T_{cold})} \quad (4.5)$$

In numerical analysis, two-dimensional computational domain is created with length and height of 0.3 m and 0.1 m, respectively. Non-uniform mesh structure is applied near cold boundary and after making sensitivity analyses, the optimum time step size is found as $\Delta t = 2$ s. Iterations are continued unless the convergence criteria of $\varepsilon = 10^{-9}$ is satisfied for the energy equation, which yields at least 150 iterations for each time step.

Comparisons are performed in terms of temperature distributions for selected process times and, time wise variations of the interface position and the total energy variations. In Figure 4.45, temperature distributions are compared with the analytical results for six different times. Besides, time-wise interface variations are represented in Figure 4.46, together with analytical results and numerical predictions. Moreover, in Figure 4.46, the energy balance of the system is verified by comparing the total internal energy variation of the system with the total energy transferred from the cooling surface. These results show that there is a good agreement between the numerical and analytical temperature profiles and the interface positions.

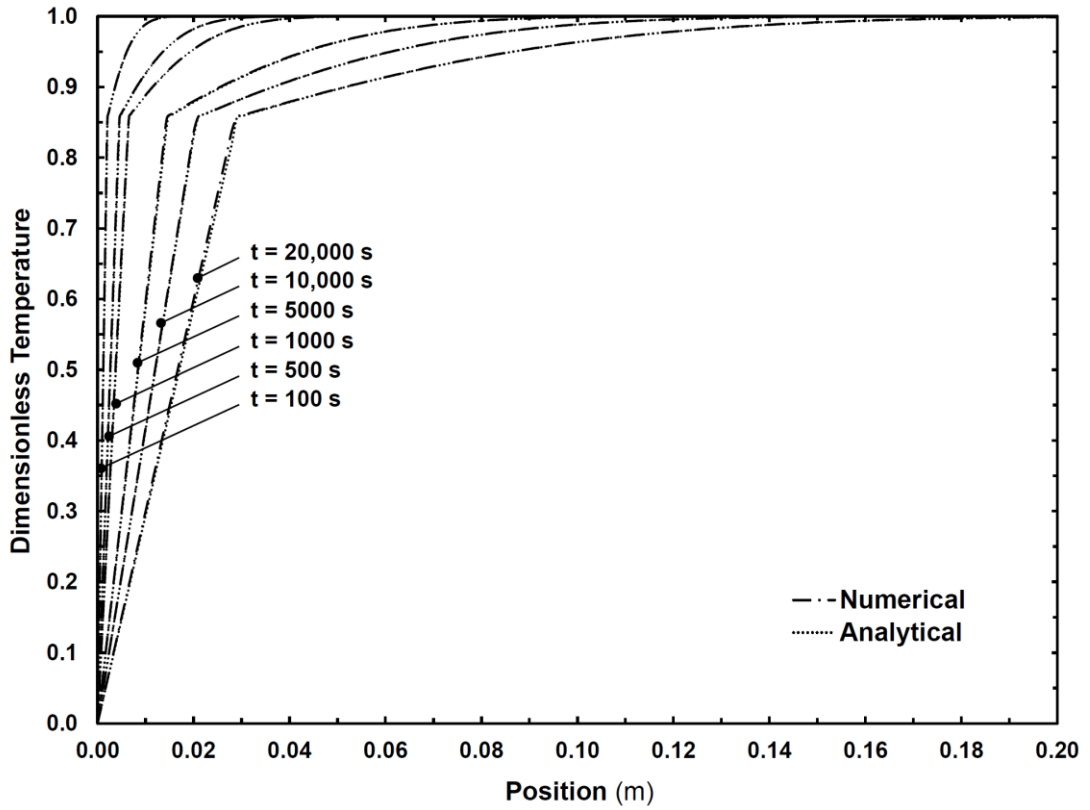


Figure 4.45 Comparison of the predicted and analytical temperature distributions.

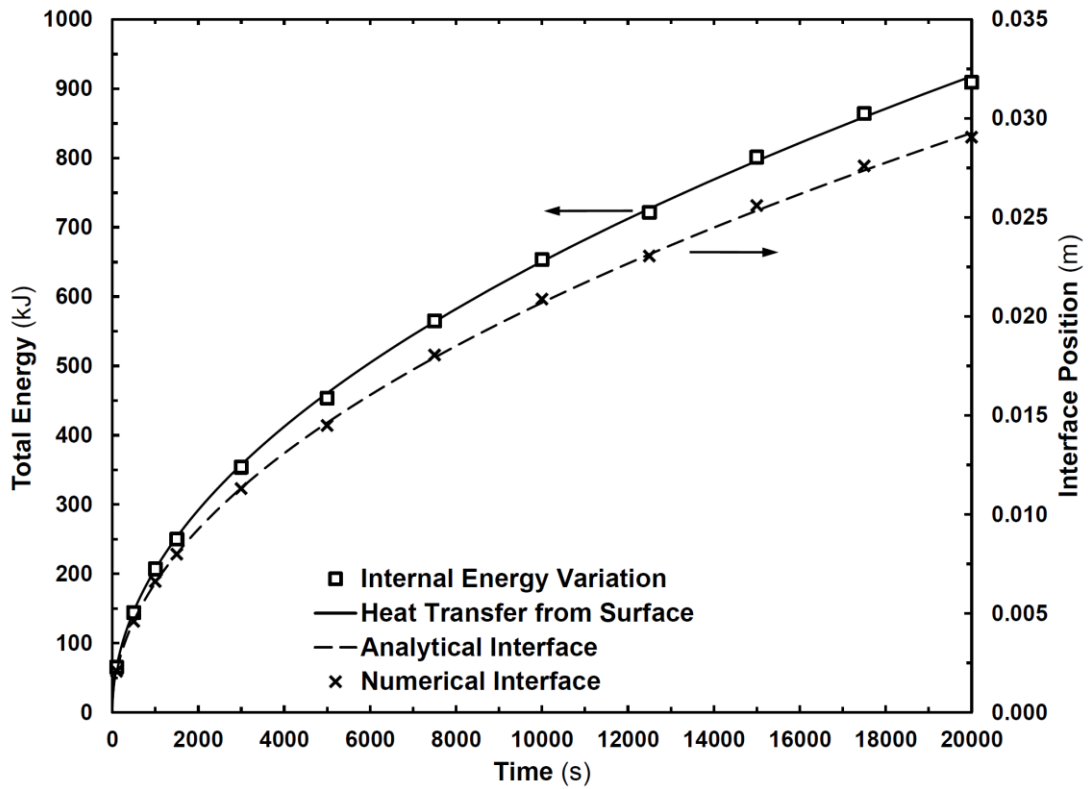


Figure 4.46 Comparisons of the predicted and analytical interface positions with energy balance.

4.3.1.1.2 *Natural Convection of Water (Case #2)*. This case study is based on the experimental investigations of Braga & Viskanta (1992a). In that study, a rectangular cavity ($L = 300$ mm, $H = 150$ mm) was filled with water at an initial temperature of, $T_i = 281.15$ K. The temperature of the left surface of the cavity was suddenly dropped to $T_{cold} = 273.15$ K, while the right side was kept at the initial temperature, $T_{hot} = 281.15$ K. Both the upper and bottom surfaces of the cavity were well-insulated and these surfaces can be assumed as adiabatic. Figure 4.47 illustrates the experimental domain and positions of the thermocouples. There are 15 thermocouples settled inside the cavity at five different axial positions and three different dimensionless heights, $Y_1 = 0.119$, $Y_2 = 0.503$ and $Y_3 = 0.902$. Further details about the experimental setup and procedure can be found in Braga & Viskanta (1992a).

In numerical analysis, non-uniform mesh structure is applied near the hot and cold boundaries. Moreover, gradient-based (*velocity*, *temperature*, and *density*) mesh adaption is performed in progressing time of the analyses, thus number of mesh varies from 67,000 to 115,000, depending on the progressing time. After making sensitivity analyses, the optimum time step size is found as $\Delta t = 4$ s. Iterations are continued unless the convergence criteria of $\varepsilon = 10^{-4}$ is satisfied for all transport equations, which needs at least 300 iterations for each time step.

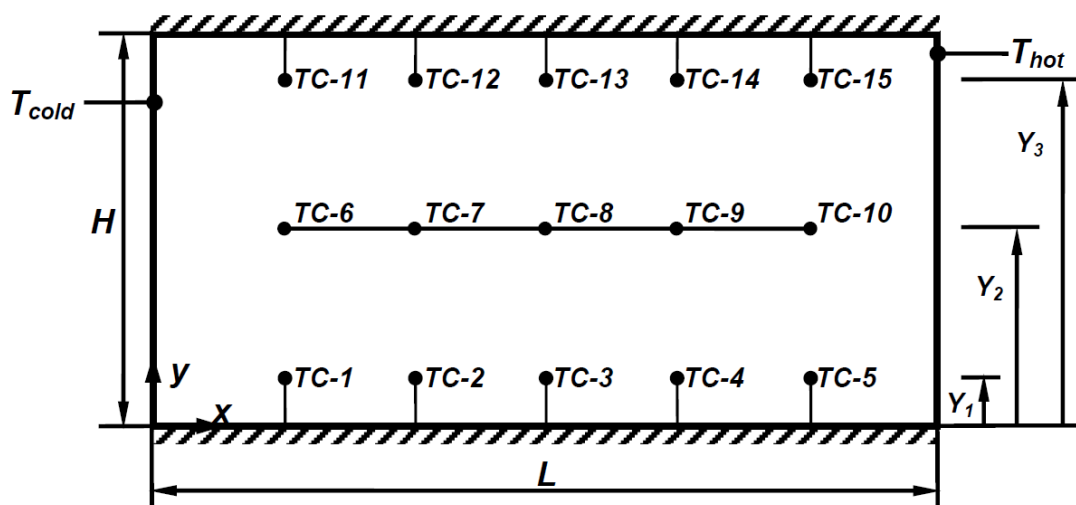


Figure 4.47 Experimental domain defined in Braga & Viskanta (1992a).

Comparisons are carried out qualitatively and quantitatively. Temperature predictions along x -axis are compared with the experimental results of Braga & Viskanta (1992a) for $t = 15$ min and $t = 30$ min. From Figure 4.48, it can be seen that the results have almost the same trends, except the deviation at the left side of the cavity at $t = 15$ min. This gap disappears on progressing time and the predictions become almost same with the experimental results. Further comparisons are performed for the isotherms and the streamlines inside the cavity. Figures 4.49 and 4.50 represent current numerical predictions together with the experimental results of Braga & Viskanta (1992a) and the numerical results of Kwak et al. (1998). Because of the density inversion at $T_{\rho, max} \approx 277.15$ K ($\theta = 0.5$), two discrete circulation cells observed inside the cavity. Between the temperature range of $T_m < T < T_{\rho, max}$ there appears a clockwise circulation cell (*left side of the cavity*) and for the interval of $T_{\rho, max} < T < T_{hot}$ there occurs counter-clockwise circulation cell (*right side of the cavity*). These separated circulation cells can clearly be seen in Figures 4.49, for $t = 15$ min and $t = 30$ min. As seen from these figures, for this case, predicted isotherms, and streamlines have an applicable agreement with the reference works.

After presenting the isotherms and streamlines, the discrepancies seen in Figure 4.48 can be explained in detail as follows. Owing to the formation of the separated circulation cells around the density inversion point, the higher temperature and velocity gradients occur around this critical temperature. Because of the higher velocity and temperature gradients, higher deviations should be expected near the density inversion point. For $t = 15$ min, the density inversion temperature of water is measured near the TC-1 thermocouple measurement point. The maximum deviation between the prediction and experimental measurement is obtained as nearly 1.3°C for this thermocouple data. On the other hand, for $t = 30$ min, the density inversion is observed near the TC-2 thermocouple measurement point, and the maximum deviation becomes nearly 0.55°C . In comparison with the temperature difference between the hot and the cold boundaries ($\Delta T = 8^\circ\text{C}$), such small local deviations are considered as acceptable for numerical studies.

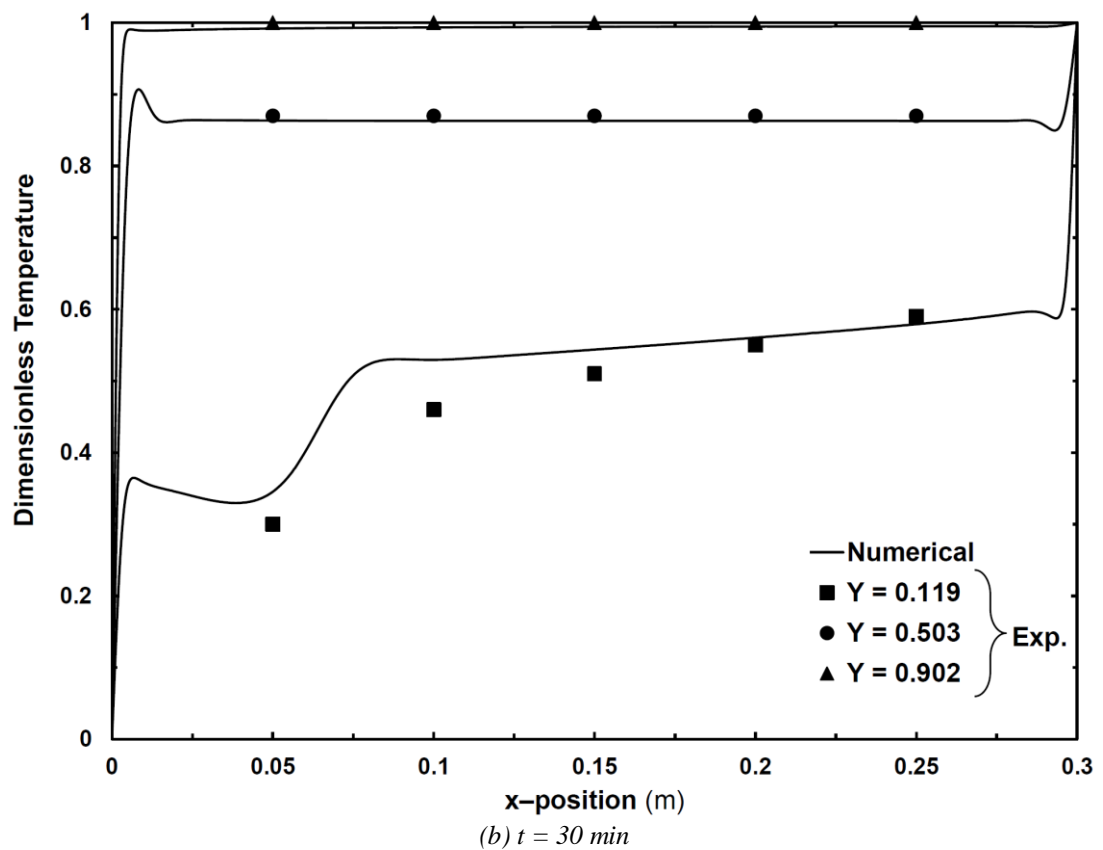
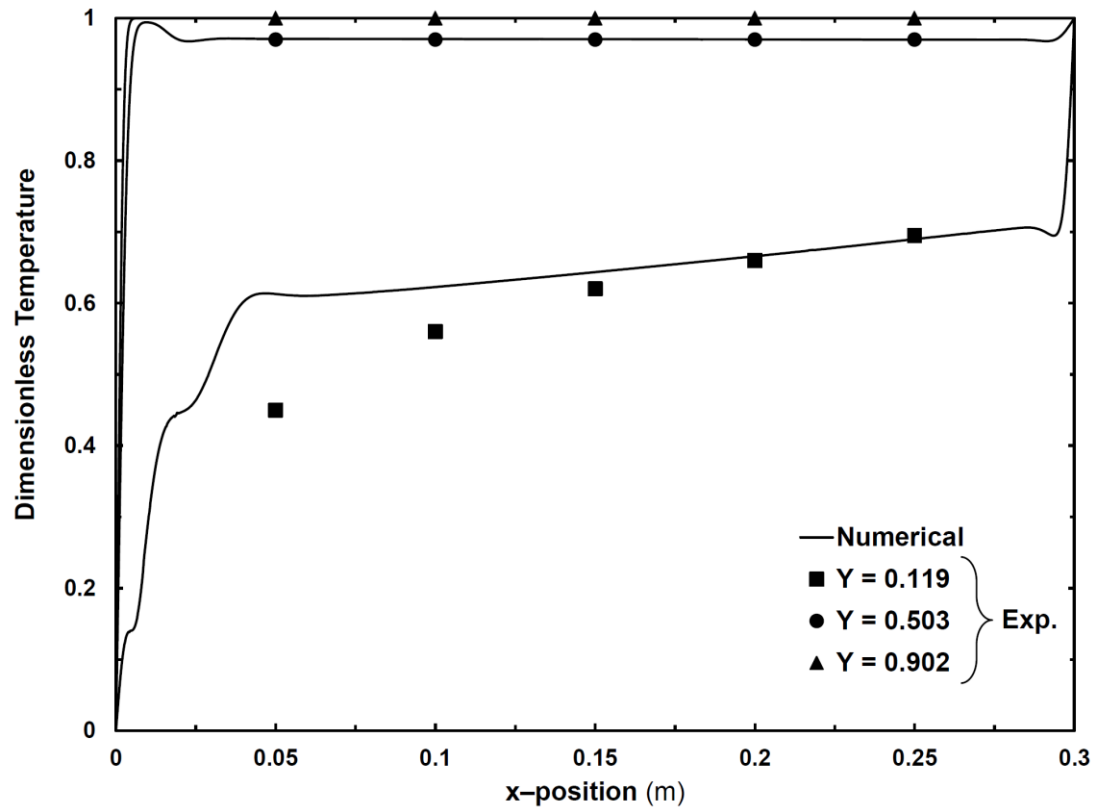
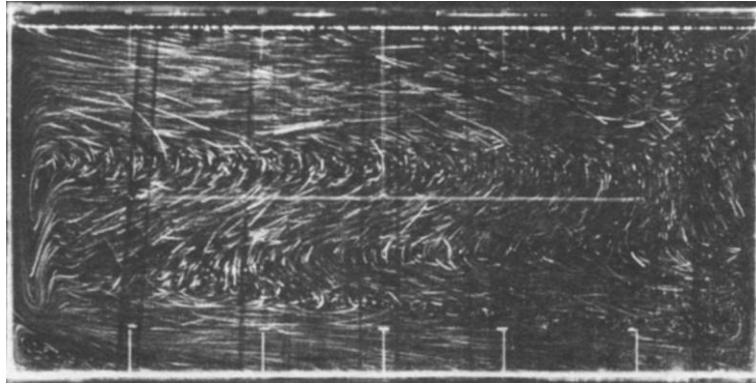
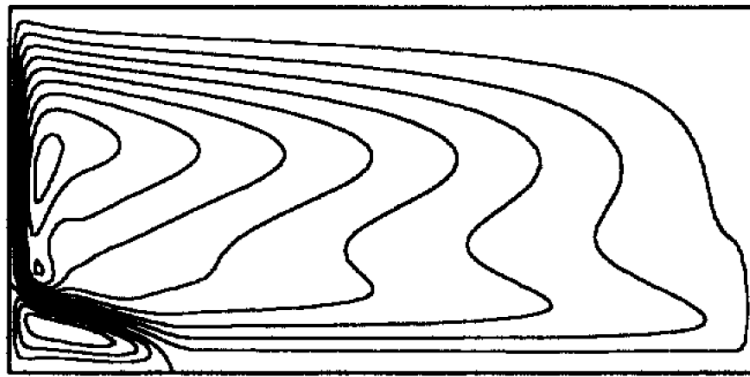


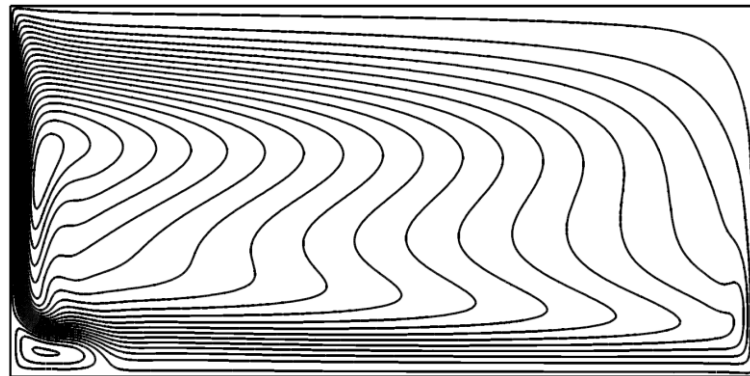
Figure 4.48 Temperature predictions in comparisons with the experimental results of Braga & Viskanta (1992a) (■, ● and ▲ symbols designate the experimental measurements).



Experimental results of Braga & Viskanta (1992a)

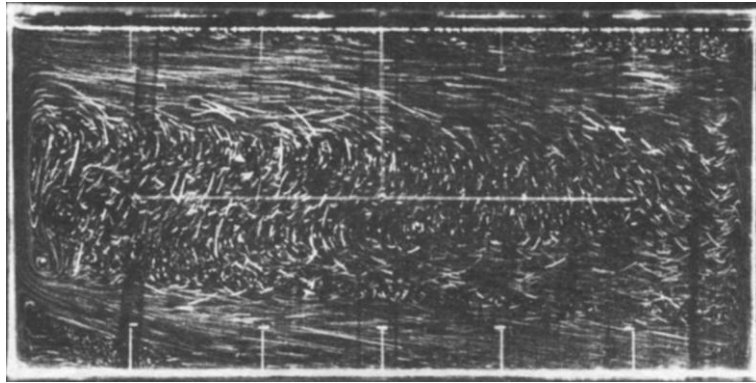


Numerical results of Kwak et al. (1998)

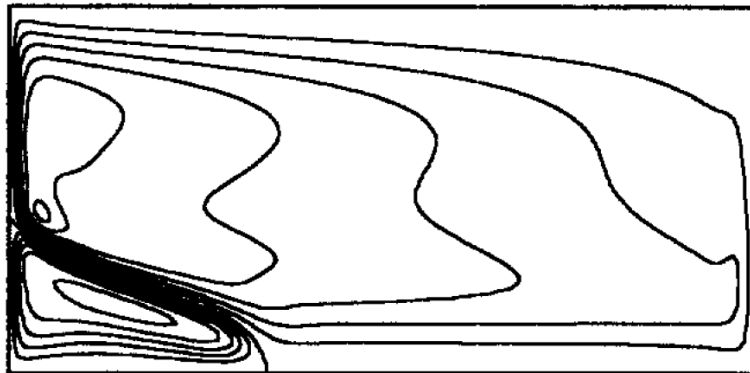


Current predictions

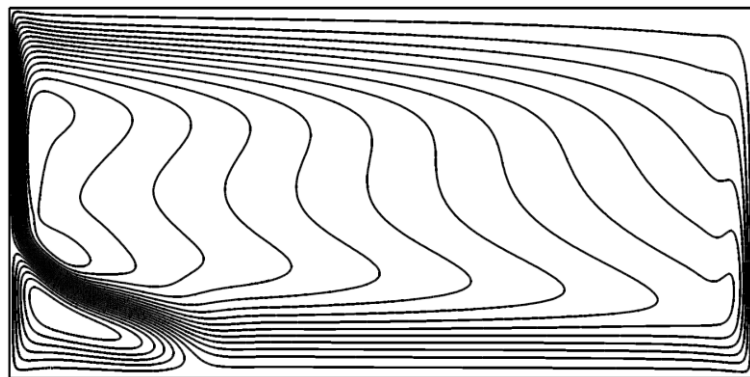
(a) $t = 15 \text{ min}$



Experimental results of Braga & Viskanta (1992a)



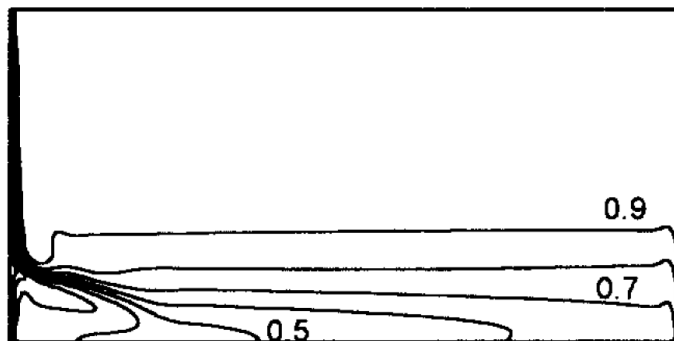
Numerical results of Kwak et al. (1998)



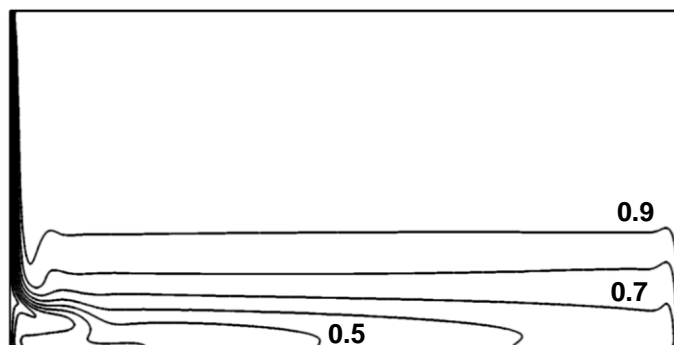
Current predictions

(b) $t = 30$ min

Figure 4.49 Predicted streamlines in comparison with the reference works – Case #2. (Clockwise circulation cell is at the left hand side and counter-clockwise circulation cell is at the right hand side).

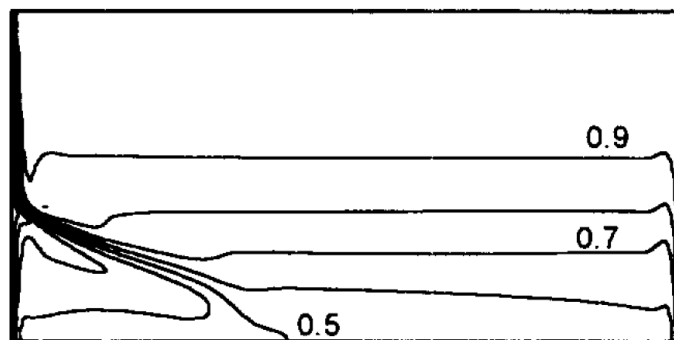


Numerical results of Kwak et al. (1998)

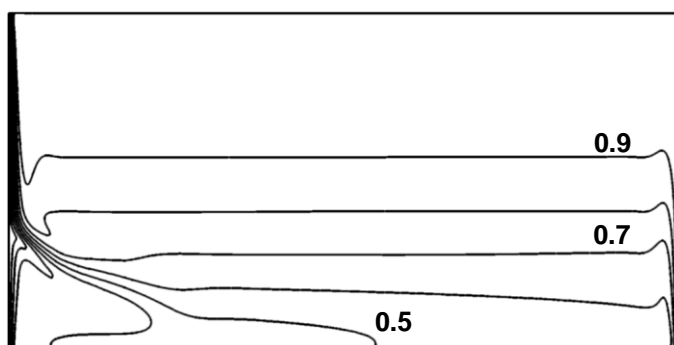


Current predictions

(a) $t = 15 \text{ min}$



Numerical results of Kwak et al. (1998)



Current predictions

(b) $t = 30 \text{ min}$

Figure 4.50 Predicted isotherms in comparison with the reference work – Case #2.

4.3.1.1.3 *Natural Convection Dominated Melting (Case #3)*. In this case, natural convection dominated melting period of *n*-octadecane is simulated in a square cavity. This study based on the numerical works of Gong & Mujumdar (1998). They simulated the melting problem with using the Streamline Upwind/Petrov Galerkin finite element method in combination with a fixed grid primitive variable method for various Rayleigh number.

In melting problem, pure *n*-octadecane is filled in a square enclosure with an initial dimensionless temperature of $\theta_i = -0.0256$. While the bottom surface is isothermal, remaining three surfaces of the enclosure are well insulated. Suddenly, the temperature of the bottom surface ($y = 0$) of the container increases to a dimensionless temperature of $\theta_{bottom} = 1$, which is above the melting temperature of the PCM. Therefore, in time, there will be inward melting in *y*-direction with both diffusion and convection dominated. Schematic representation of the problem is given in Figure 4.51 and the dimensionless thermo-physical and geometric parameters of the current problem are defined in Table 4.11.

In this problem, the dimensionless temperature, Rayleigh number, Fourier number, and Stefan number are defined as follows:

$$\theta = \frac{T - T_m}{T_{bottom} - T_m} \quad (4.6a)$$

$$Ra = \frac{\rho^2 c_l g \beta L^3 (T_{bottom} - T_m)}{\mu k_l} \quad (4.6b)$$

$$Fo = \frac{t \alpha_l}{L^2} \quad (4.6c)$$

$$Ste = \frac{c_l (T_{bottom} - T_m)}{h_{sf}} \quad (4.6c)$$

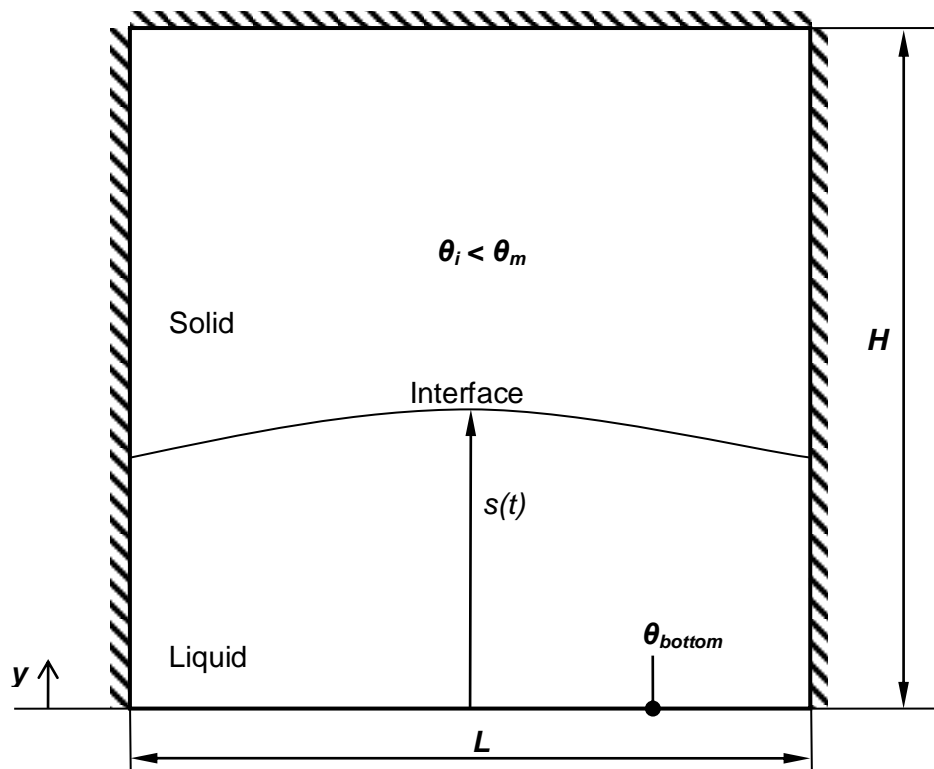


Figure 4.51 Illustration of the mathematical model for melting problem.

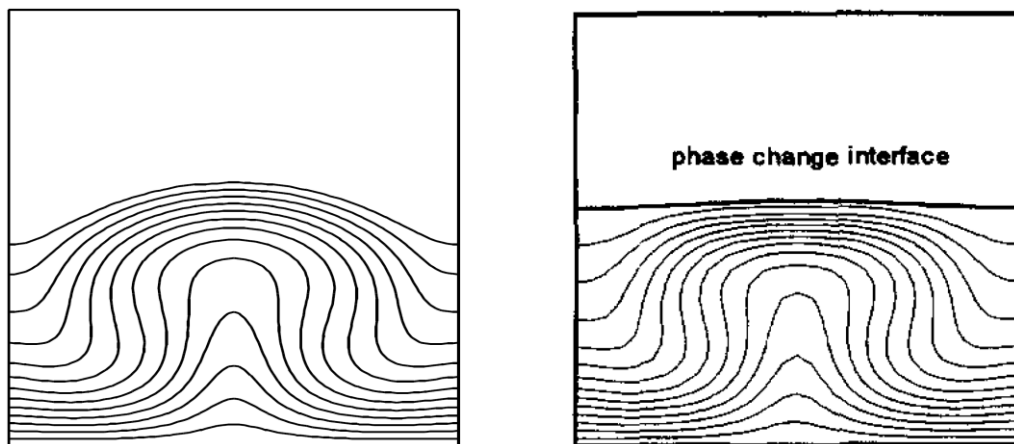
Table 4.11 Dimensionless parameters for Case #3.

Parameter	Definition	Value
R	Aspect ratio L/H	1.0
Ra	Rayleigh number	$2.844 \times 10^4 - 2.844 \times 10^5$
Pr	Prandtl number	46.1
Ste	Stefan number	0.138
c_s/c_l	Ratio of solid/liquid specific heat	0.964
k_s/k_l	Ratio of solid/liquid thermal conductivity	2.419
θ_i	Dimensionless initial temperature	-0.0256

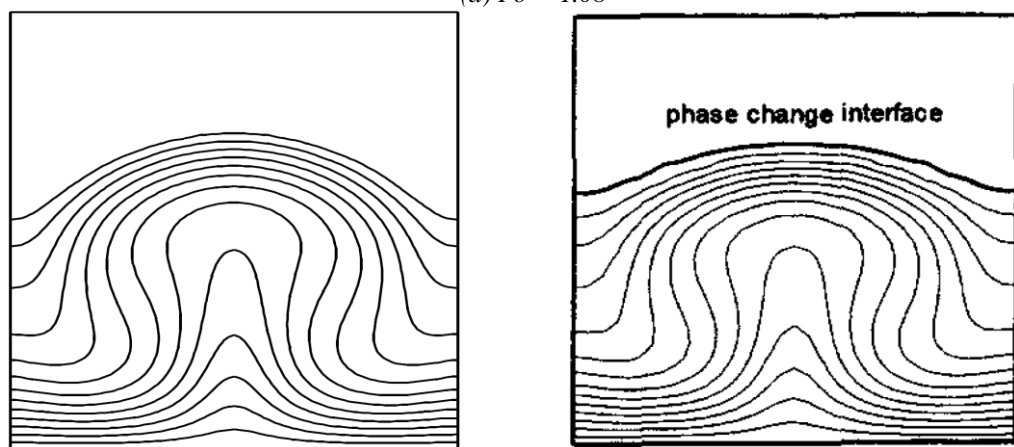
In numerical analysis, non-uniform mesh structure is applied near the bottom boundary with a total of 6400 computational elements. After making sensitivity analyses, the optimum time step size is found as $\Delta t = 0.1$ s. Iterations are continued unless the convergence criteria of $\varepsilon = 10^{-4}$ is satisfied for all transport equations, which needs at least 800 iterations for each time step.

Comparisons are carried out qualitatively. Temperature and streamline predictions along y -axis are compared with the numerical results of Gong & Mujumdar (1998), for two different values of Rayleigh number, 2.844×10^4 and 2.844×10^5 .

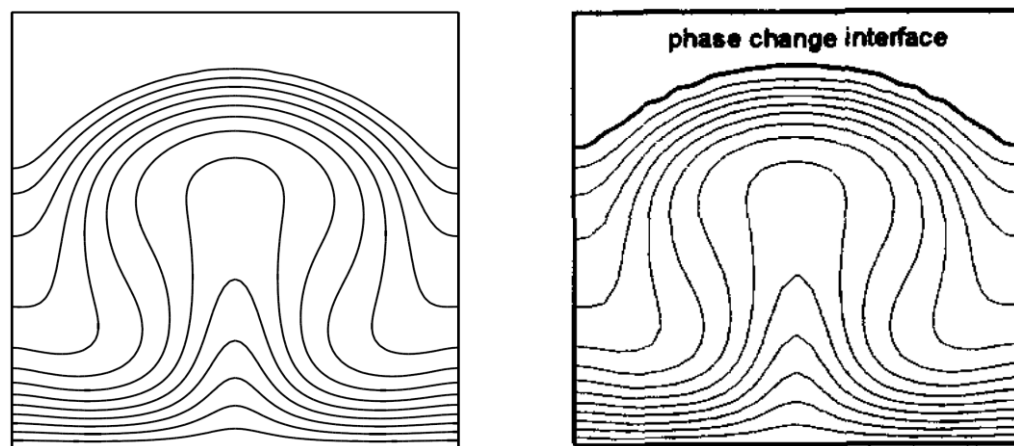
In Figures 4.52 and 4.53 predicted isotherms and streamlines are given together with the reference work for $Ra = 2.844 \times 10^4$ at three dimensionless Fo values: 1.08, 1.296 and 1.62. Numerical results indicate that buoyancy forces become clear after $Fo = 1.08$. In the earlier periods of melting, the solid-liquid interface moves as conduction dominated. This is because; the actual Rayleigh number is relatively small, since the small height of melted PCM. In time, with increasing height of melting, Rayleigh number increases. Two separated circulation cells are observed after $Fo = 1.08$ and in time, these circulation cells grow through upper direction. Flow directions of the left and the right circulation cells are counter-clockwise and clockwise, respectively. Owing to the formation of two separated circulation cells, in progressing time, solid-liquid interface becomes parabolic. Relatively hot fluid flows from the bottom to the upper side of the cavity and cause a plume at the center of the cavity. On the other hand, for $Ra = 2.844 \times 10^5$ comparative results are represented in Figures 4.54 and 4.55 at four dimensionless Fo values: 0.302, 0.454, 0.605 and 0.756. Due to the relatively higher Rayleigh number, natural convection develops much earlier times in comparison with the $Ra = 2.844 \times 10^4$. Four independent circulation cells are observed after $Fo = 0.302$ and in time, these circulation cells grow through upper direction. Owing to the formation of four separated circulation cells, two symmetrical cups form on the solid-liquid interface. These cups form because of the flow direction of the melted PCM. From left to right, flow cell directions varies as, clockwise and counter-clockwise. For the first circulation cell on the left hand side, hot fluid flows up in the clockwise direction and melts interface as plume near the wall. Unlike to the first circulation cell, in the second one, hot fluid flows up in the counter-clockwise direction and plume occurs at the center of the cavity. This effect can be seen from the isotherms in Figure 4.54. As a result, from the comparisons that are given in Figures 4.52 to 4.55, it is clear that predicted isotherms and streamlines have applicable agreement with the reference work.



(a) $Fo = 1.08$



(b) $Fo = 1.296$

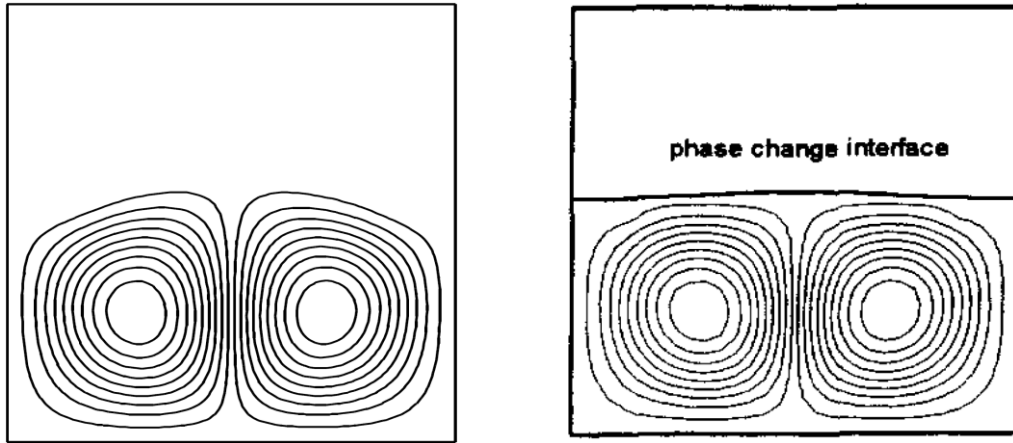
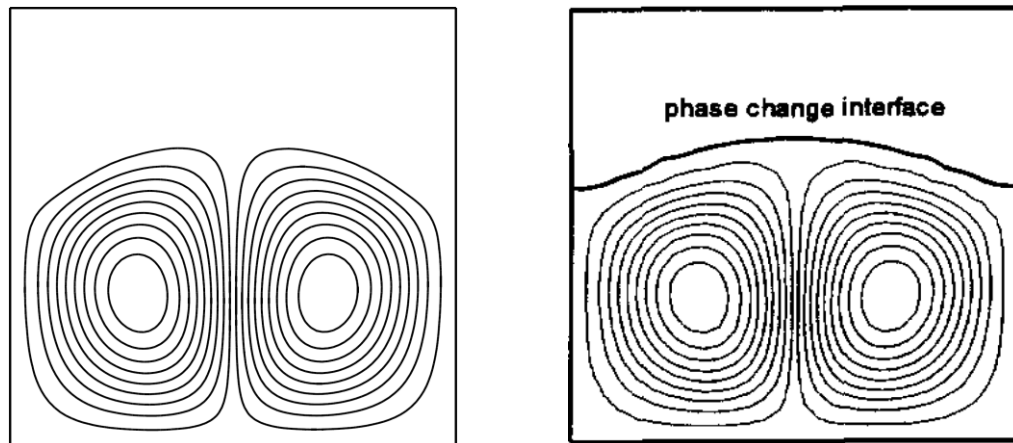
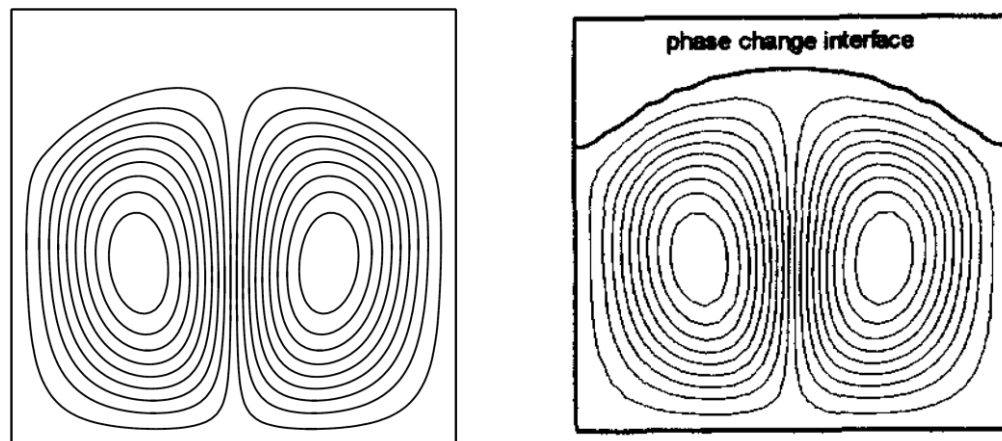


(c) $Fo = 1.62$

Current Predictions

Numerical Results of Gong & Mujumdar (1998)

Figure 4.52 Isotherms for $Ra = 2.844 \times 10^4$ – Case #3.

(a) $Fo = 1.08$ (b) $Fo = 1.296$ (c) $Fo = 1.62$

Current Predictions

Numerical Results of Gong & Mujumdar (1998)

Figure 4.53 Streamlines for $Ra = 2.844 \times 10^4$ – Case #3 (Counter-clockwise circulation cell is at the left hand side and clockwise circulation cell is at the right hand side).

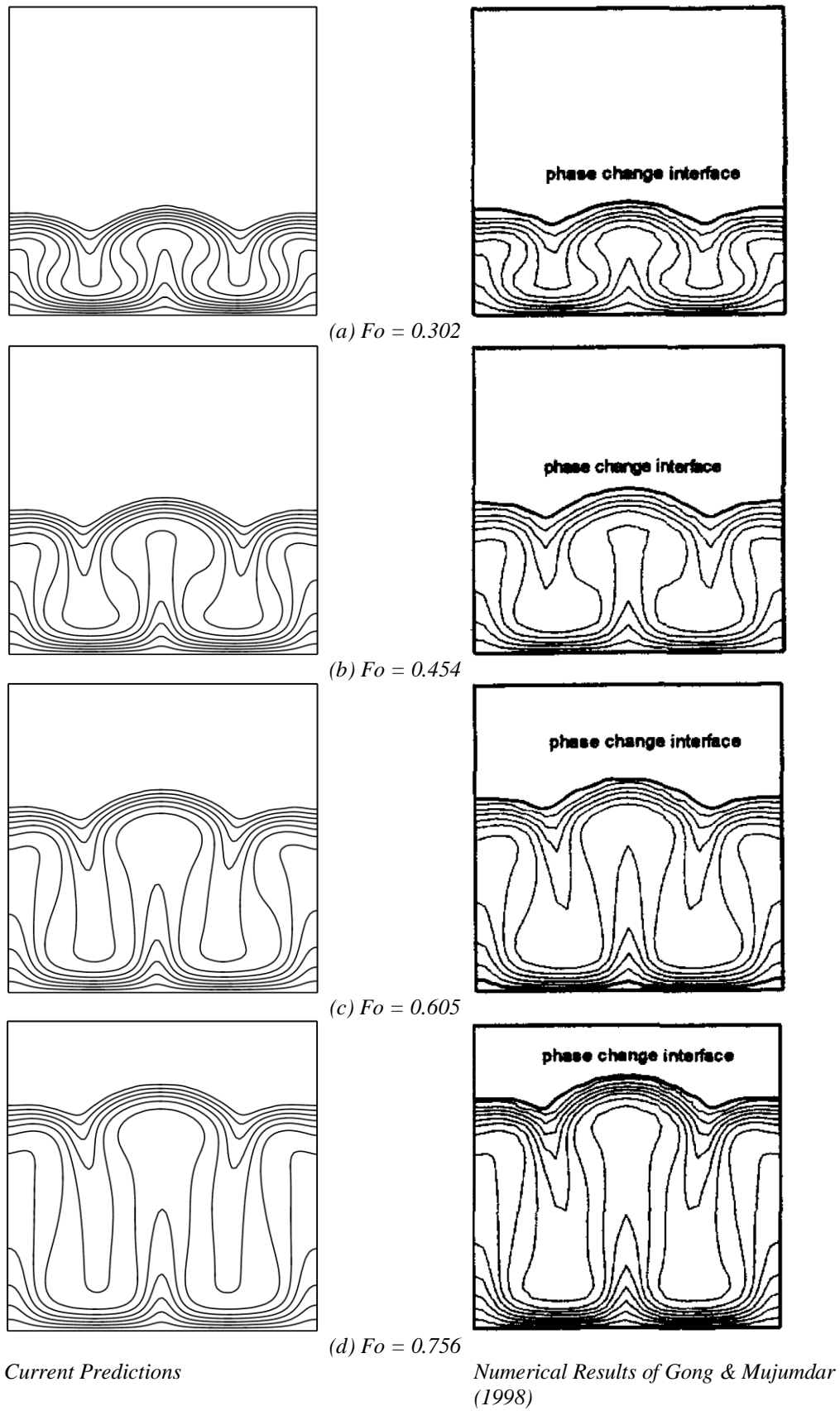
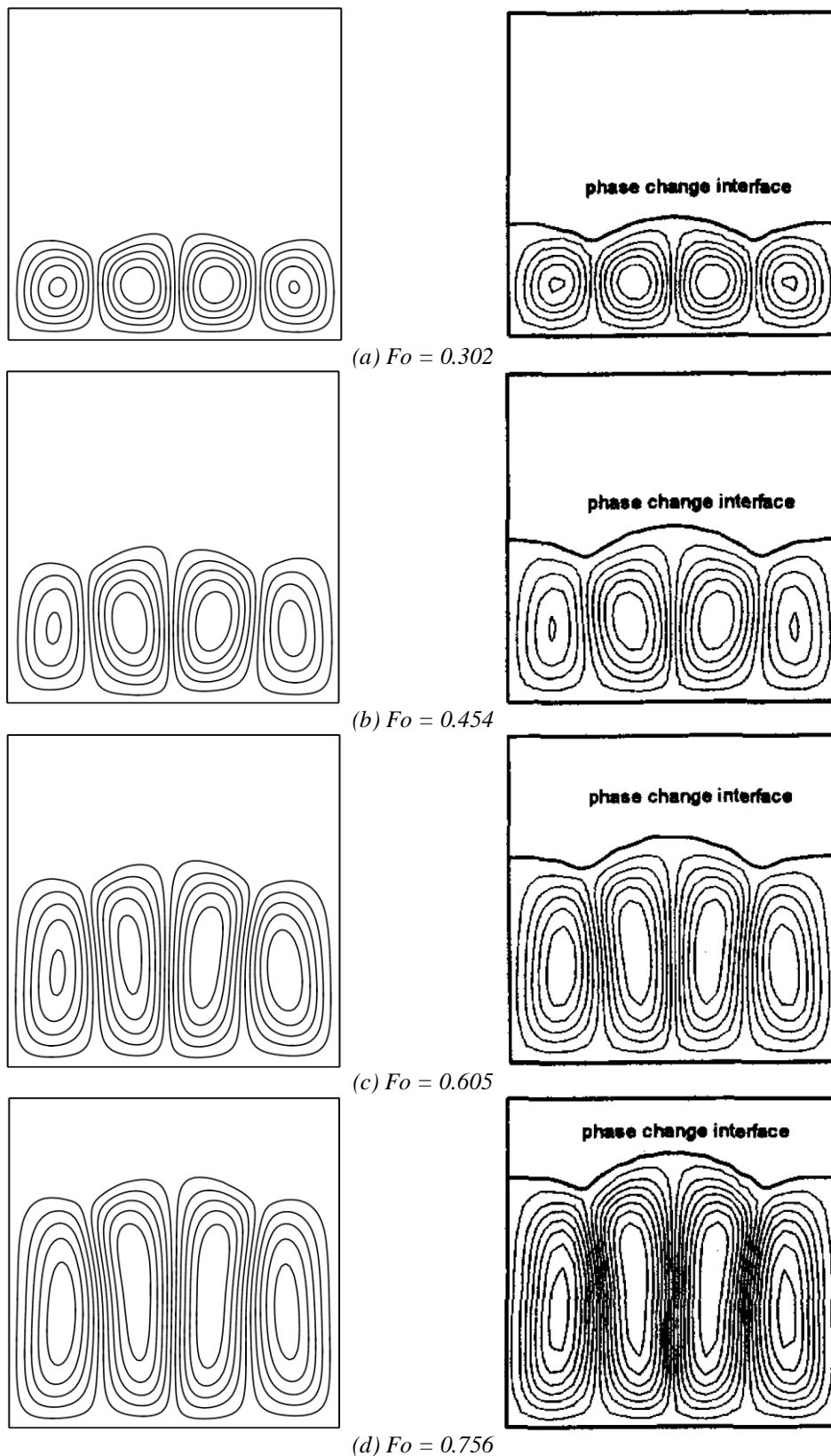


Figure 4.54 Isotherms for $Ra = 2.844 \times 10^5$ - Case #3.



Current Predictions

Numerical Results of Gong & Mujumdar (1998)

Figure 4.55 Streamlines for $Ra = 2.844 \times 10^5$ – Case #3.

4.3.1.1.4 *Natural Convection Dominated Solidification (Case #4)*. Natural convection dominated solidification problem inside a cavity is investigated in this case study. For the same experimental system given in Braga & Viskanta (1992a), they also extended their study to investigate the buoyancy–dominated solidification in Braga & Viskanta (1992b). In this particular case, the initial temperature of water is set as, $T_i = 283.35$ K. Then suddenly, the temperature of the left surface of the cavity is dropped at a temperature, which is less than fusion temperature of water, $T_{cold} = 263.15$ K. On the other hand, right side of the cavity is kept at the initial temperature, $T_{hot} = 283.35$ K. Non–uniform mesh structure is applied near the wall boundaries and gradient based (*velocity, temperature and density*) mesh adaption is performed in progressing time of analyses. Thus, the number of mesh varies from 67,000 to 115,000 depending on the progressing time. After making sensitivity analyses, the optimum time step size is found as $\Delta t = 4$ s. Iterations are continued unless the convergence criteria of $\varepsilon = 10^{-4}$ is satisfied for all transport equations, which needs at least 300 iterations for each time step.

For this case, comparisons are carried out qualitatively and quantitatively. Time wise variations of predicted temperatures are compared with the experimental measurements of Braga & Viskanta (1992b) at two specific locations (*for TC–1 and TC–8 in Figure 4.47*). The first selected thermocouple is located at the left corner of the cavity (at $x = 25$ cm, $y = 17.85$ cm), where the generation of small clockwise circulation cell is expected, as in Case #2. In addition, the second selected thermocouple is located at the center of the cavity (at $x = 150$ cm, $y = 75.45$ cm). Figure 4.56 represents that the predicted temperatures and experimental results of Braga & Viskanta (1992b) have the same trend for both TC–1 and TC–8. The numerical results have satisfying agreement for TC–1, where the density inversion and clockwise circulation cell appears. Besides, qualitative comparisons with the experimental streamline profiles obtained by Braga & Viskanta (1992b) are represented in Figure 4.57. Here it can be seen that, because of the density inversion at $T_{\rho, max} \approx 277.15$ K ($\theta \approx 0.7$), there appears a discrete small clockwise circulation cell at $t = 15$ min, at the left corner of the cavity and in time, it grows as in Case #2.

For this particular case, one can say that predicted temperature and streamline profiles have reasonable consistency with reference work.

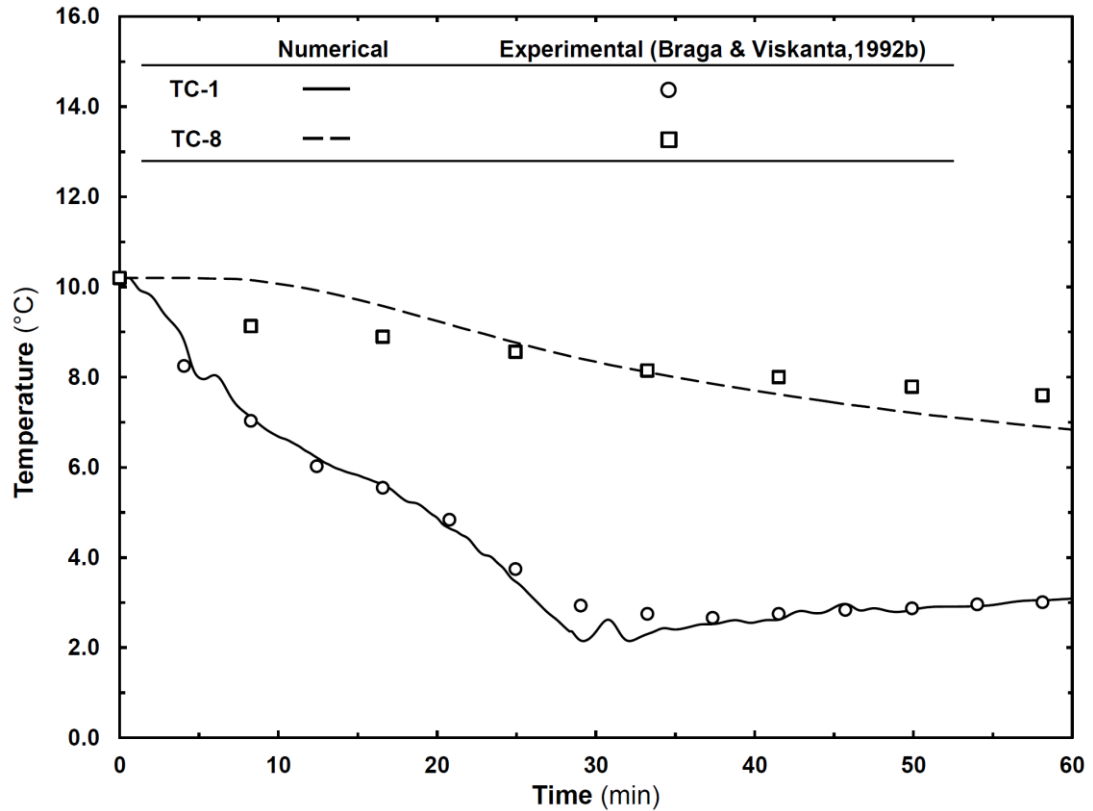
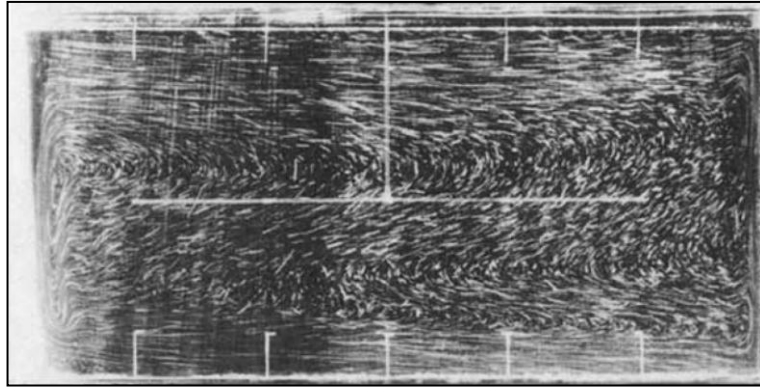
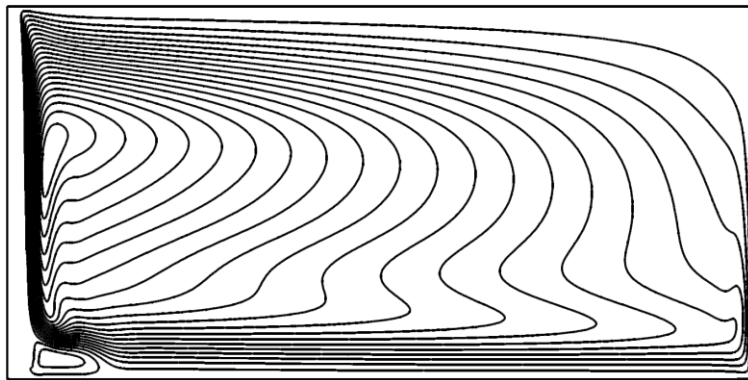


Figure 4.56 Comparisons of temperature variations with the experimental results of Braga & Viskanta (1992b) for two selected thermocouples – Case #4.

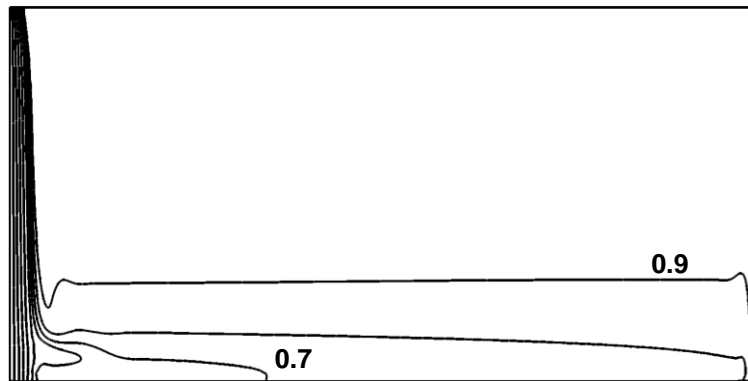
After validating the methodology, another set of numerical analyses are performed to investigate the influence of fins on the ice formation in a rectangular geometry. Analyses are carried out for two different fin arrangements for the same geometry given in Figure 4.47, with the same boundary and initial conditions as in un-finned model. Aluminum fins with the length of $H/2$ placed at the cold wall on the two identical vertical positions of $y = H/2$ (for single fin) and $y = H/3$ (for double fin) for different cases. In Figure 4.58, the solidification interfaces are shown for $t = 10$ min, 30 min and 60 min with the presence or absence of natural convection effects. Figure 4.58(a) represents the time wise variations of solidification interfaces for both bare- and finned-wall cases in the presence of convection. As illustrated in Figure 4.58(a), due to the formation of clockwise circulation cell at the left corner of the cavity, time wise solidification interfaces become distorted through y -axis, after



Experimental streamlines of Braga & Viskanta (1992b)

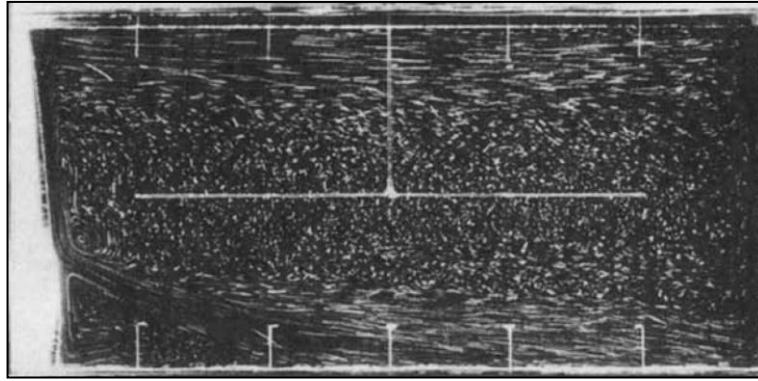


Predicted streamlines

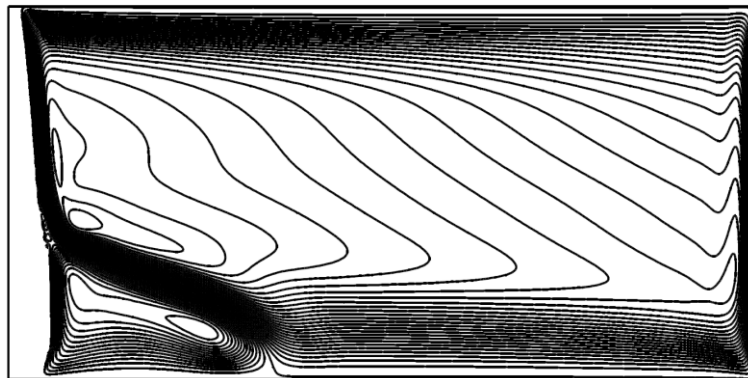


Predicted isotherms

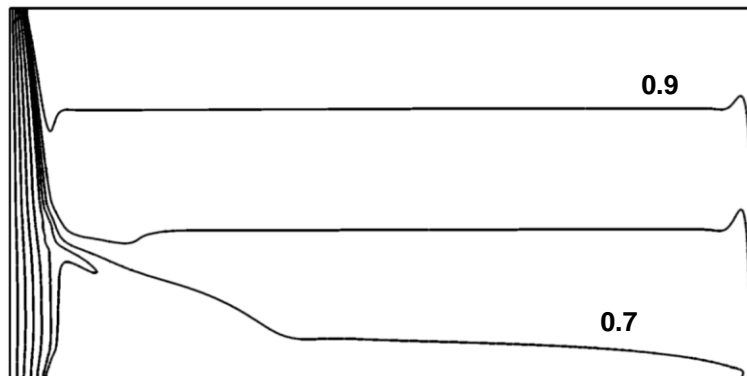
(a) $t = 15 \text{ min}$



Experimental streamlines of Braga & Viskanta (1992b)



Predicted streamlines



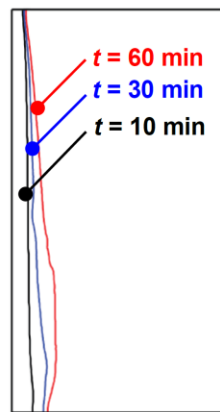
Predicted isotherms

(b) $t = 60 \text{ min}$

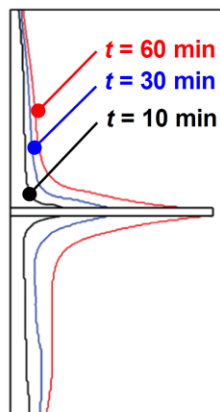
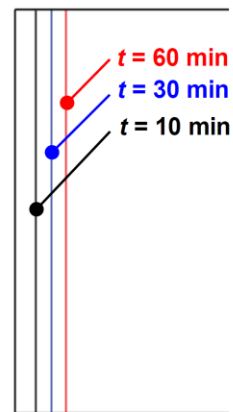
Figure 4.57 Predicted streamlines and isotherms in comparison with the experimental results of Braga & Viskanta (1992b) – Case #4 (Clockwise circulation cell is at the left hand side and counter-clockwise circulation cell is at the right hand side).

$t = 10$ min. Ice formation near the top and bottom surfaces nearly stops and solidification interface starts to grow through on diagonal directions in progressing time. In addition, for the same bare- and finned-wall models, further analyses are carried out with neglecting the buoyancy forces to introduce the difference between the convection and conduction driven conditions. Figure 4.58(b) represents solidification interfaces for conduction driven cases and it is clear that, the formation of ice is symmetrical through y -axis for all cases, as expected. In terms of the amount of ice formed inside the cavity, time wise variations of the ratio of solidified area (A_{ice} / A_{total}) are given in Figure 4.58(c). It is obvious that, the solidified area increases with fin addition. Moreover, with neglecting the buoyancy effects, the solidified areas become nearly doubled in this particular case.

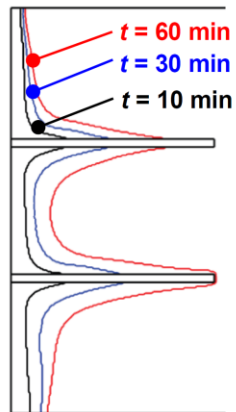
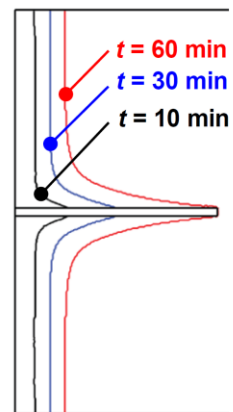
Furthermore, isotherms and streamlines inside the cavity are represented at several process times for single- and double-finned cases, in Figures 4.59 and 4.60, respectively. In both single- and double-finned cases, at the initial times, Figures 4.59(a) and 4.60(a), there are almost symmetric temperature gradients and streamline profiles occur around the fin/fins. After $t = 10$ min, because of the convective effects around fins, two different thermal regions take place at the top and bottom sides of the fin or fins, as shown in Figures 4.59(b) and 4.60(b). Temperature gradient increases with in progressing time, and after $t = 30$ min density inversion line becomes clearer in isotherms ($\theta \approx 0.7$), for both single and double finned cases. In Figure 4.59(c), the clockwise convection cell can be seen at the left corner of the cavity as in Case #2. On the other hand, from Figure 4.60(c), it can be seen that, for the double finned case, unlike to the single fin case, the small clockwise convection cell occurs in earlier time and has been growing through both x - and y -directions, because of the convective effect of upper fin. Finally, in Figures 4.59(d) and 4.60(d), it can be seen that the secondary convection cells grew through vertical and horizontal directions and totally covered the bottom of the fin. Moreover in Figure 4.60(d), with penetration of temperature gradient, another clockwise convection cell between the two fins appears.



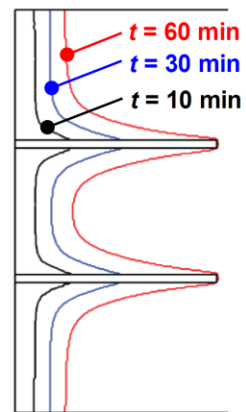
Bare-wall



Single Fin

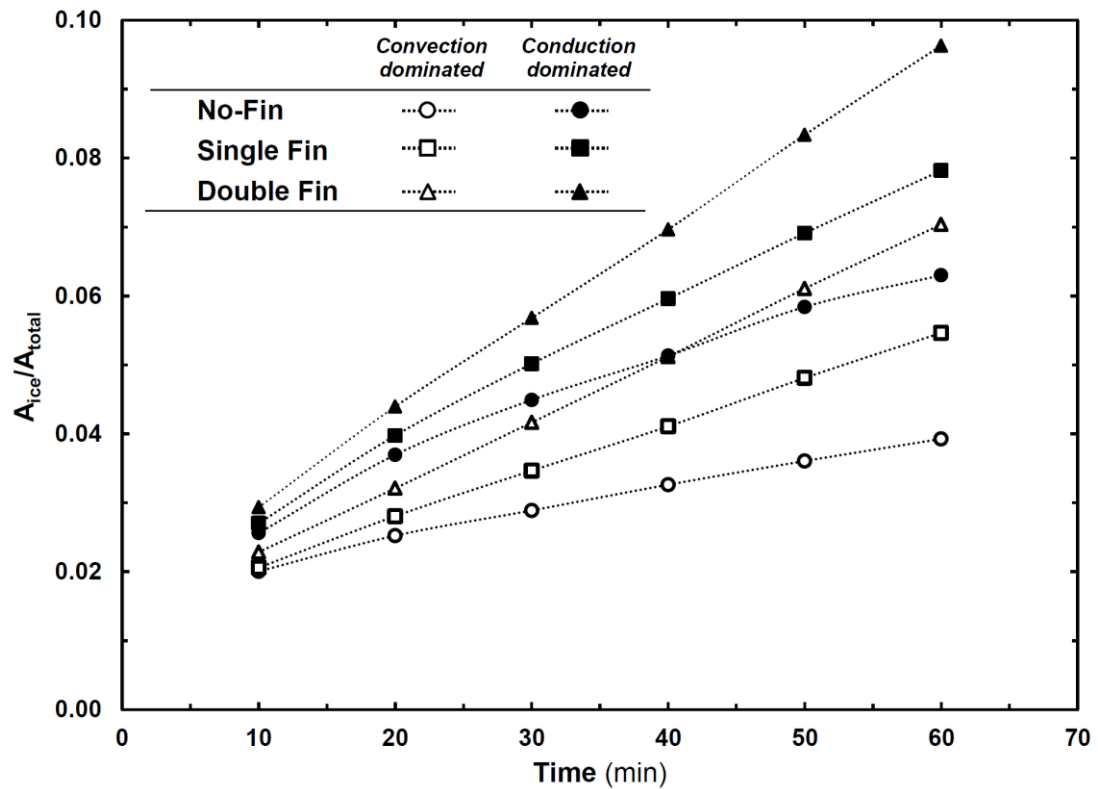


Double Fin



(a) Time-wise solidification interfaces – presence of the natural convection

(b) Time-wise solidification interfaces – absence of the natural convection

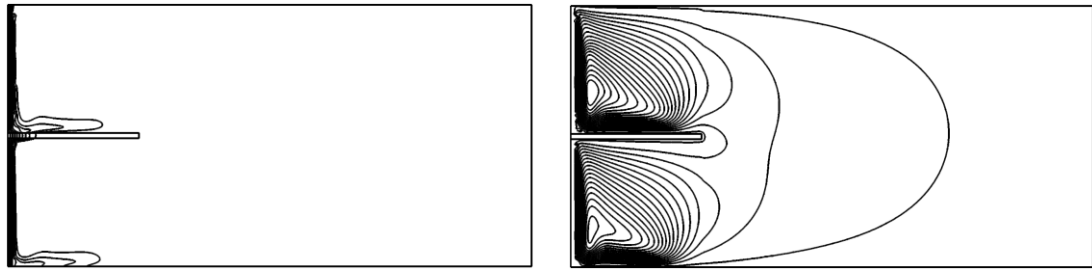


(c) Ratio of the solidified area – with/without buoyancy forces

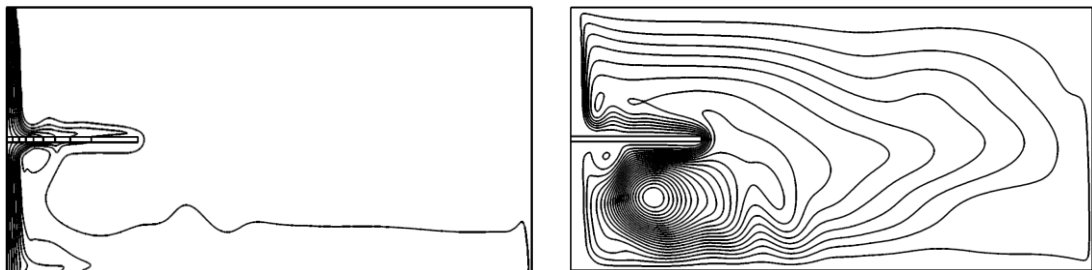
Figure 4.58 Effect of fins and natural convection on ice formation inside cavity – Case #4.

Based on the preliminary case studies, the following conclusions can be drawn,

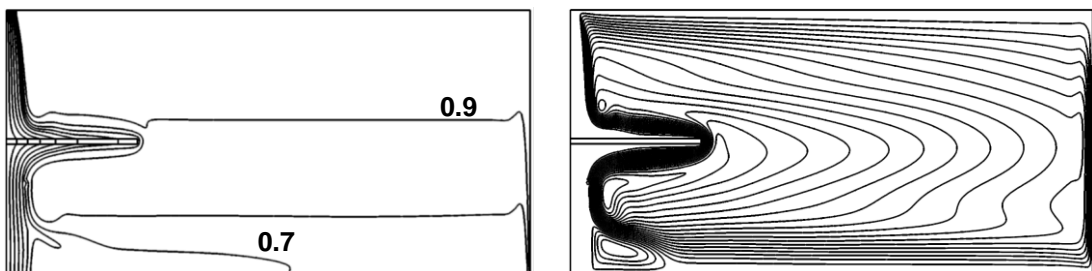
- The temperature transforming method is successfully applied to solve conduction/convection dominated solidification/melting problems. The current numerical methodology and models are validated with comparing available analytical, experimental, or numerical results.
- Although using extended surfaces improves the amount of ice, it increases the influence of natural convection inside cavity and causes larger discrete convection cells because of the density inversion temperature of water.
- The comparative results between natural convection dominated and conduction–dominated cases show that, the influence of natural convection is deterministic for solidification processes of water in the systems that the initial temperature of water is higher than its density maximum.



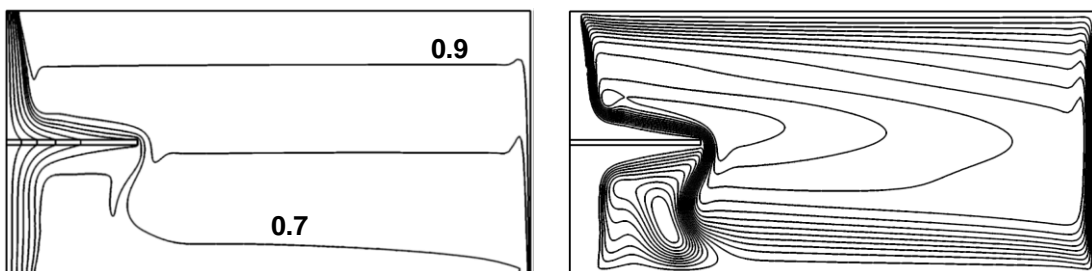
(a) $t = 1 \text{ min}$



(b) $t = 10 \text{ min}$

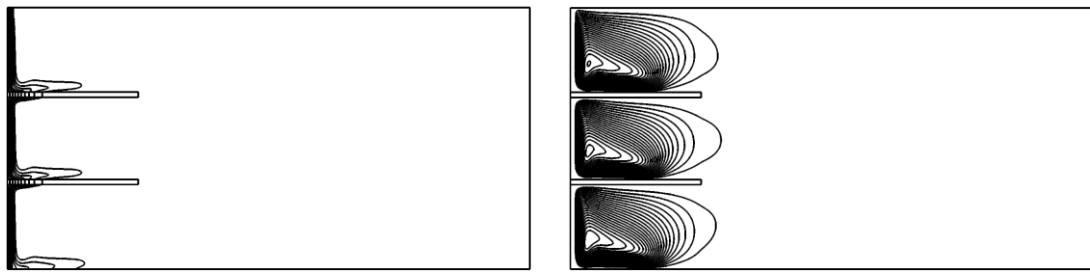
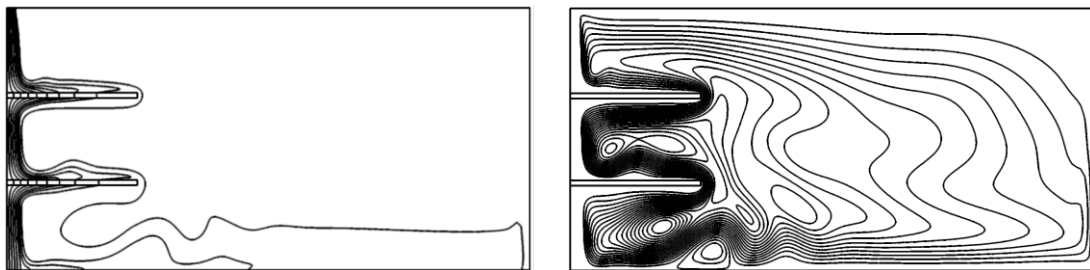
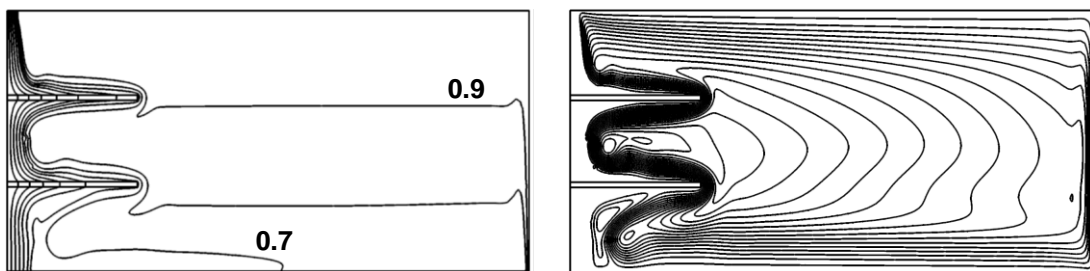
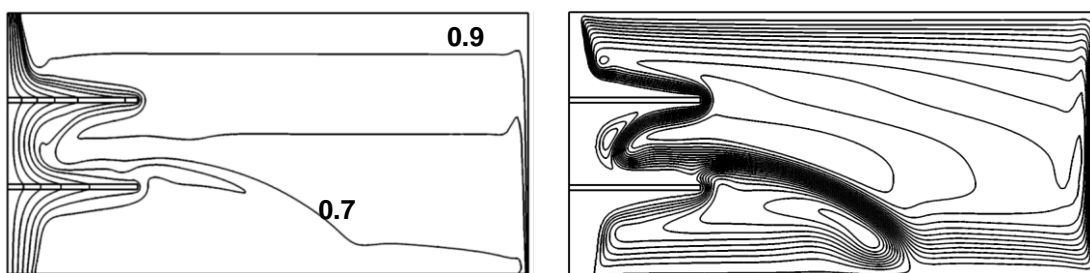


(c) $t = 30 \text{ min}$



(d) $t = 60 \text{ min}$

Figure 4.59 Isotherms (*left*) and streamlines (*right*) for single fin – Case #4.

(a) $t = 1$ min(b) $t = 10$ min(c) $t = 30$ min(d) $t = 60$ minFigure 4.60 Isotherms (*left*) and streamlines (*right*) for single fin – Case #4.

4.3.1.2 Natural Convection Driven Solidification around Tube

After carrying out preliminary tests for several case studies, solidification process around a tube in a cylindrical domain is analyzed in the presence of natural convection and heat gain from surroundings. Numerical validation of the model is performed with comparing the predictions with the current experimental results.

4.1.3.1.1 Description of Mathematical Model and Validation. First, a two-dimensional mathematical model is defined corresponding to the middle card section of the shell-and-tube type LHTES system. In this problem, water fills the annulus of the exchanger with an initial temperature of T_i , which is slightly higher than the melting temperature of water. At time $t = 0$ s, HTF suddenly started to flow inside the tube, so in time the surface temperature of the tube dropped below the phase change temperature of water, $T_{tube}(t)$, and solidification initiated around the tube. With assuming symmetrical temperature and velocity profiles along the vertical centerline of the annulus, half of the domain can be taken into account for analyses. In Figure 4.61, current mathematical model is represented. Here the inner radii of the shell and outer radii of the tube are, $r_{shell} = 95$ mm and $r_o = 12.5$ mm, respectively.

In experiments, even though double insulation layers cover the outer surface of the shell, there occurs heat gain from the surroundings. According to the experimental data, the outer surface temperature of the insulation remains almost constant during experiments. Thus, constant temperature definition is valid for the outer insulation surface to simulate the heat gain from surroundings. In the experimental system, from the inner surface of the shell to the outer surface of the insulation, the total thickness is measured as $\Delta r = 0.04$ mm and consists of three layers: wall thickness of shell, Armaflex and glass wool. In the mathematical model, instead of creating these three different types of layers the *wall thickness* definition in FLUENT is used. Because, creating the computational cells for that small volumes cause inconsistent grid structures which leads inessential computational effort in computations. With using the wall thickness definition, rather than solving two-dimensional conduction equation inside small volumes, one-dimensional heat

conduction equation is solved for related thermal conductivity and wall thickness value. Here, an equivalent thermal conductivity value is calculated by using the overall heat transfer coefficient, which is obtained experimentally as follows:

$$\bar{U}A(T_{outer} - T_{inner}) = k_{eq} (2\pi\ell) \frac{(T_{outer} - T_{inner})}{\ln(r_{insulation}/r_{shell})} \quad (4.7)$$

where k_{eq} represents the equivalent thermal conductivity value corresponding to the layers between the inner surface of the shell and the outer surface of the insulation. For the system with $D_{shell} = 190$ mm, equivalent thermal conductivity is computed as $k_{eq} = 0.03$ W/mK.

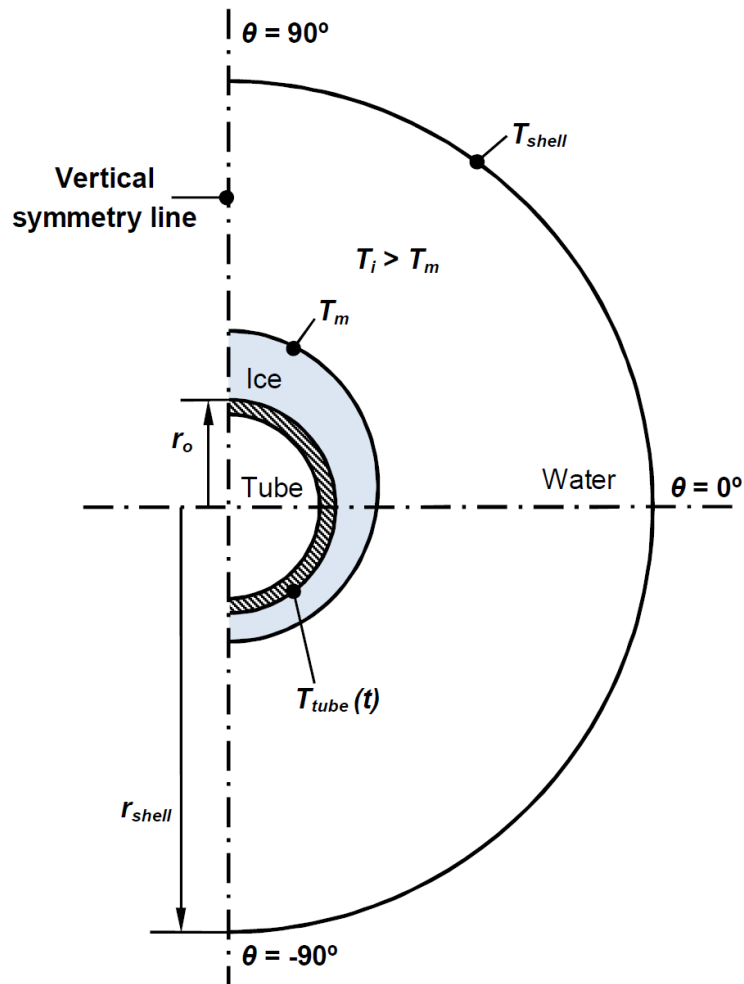


Figure 4.61 Mathematical model of solidification around tube.

Comparisons between the experimental results and the numerical predictions are carried out for $D_{shell} = 190$ mm with the flow parameters of $T_{in} = -10^\circ\text{C}$ and $\dot{V} = 8$ l/min. Because of the transient nature of the problem, the surface temperature of the tube varies with time. Thus, the time dependent surface temperature is defined at the wall temperature of the tube as, $T_{tube}(t)$ in order to use the same temperature boundary conditions as in experimental measurements. In Figure 4.62, the variations of the inlet and the outlet temperatures of the HTF are presented along with the variation of the surface temperature at the middle card section of the system. A dynamic curve fitting method (*Exponential Rise to Maximum – 5 Parameters*) is applied to the time wise variation of the surface temperature, to obtain a representative correlation for the problem. In Figure 4.62, this fitted curve is shown as a dashed line. An additional UDF (*User Defined Function*) is defined into FLUENT to apply this time dependent boundary condition. Moreover, based on the experimental data, the initial temperature of water is defined as $T_i = 0.5^\circ\text{C}$, and the surface temperature of the shell is set as $T_{shell} = 15^\circ\text{C}$.

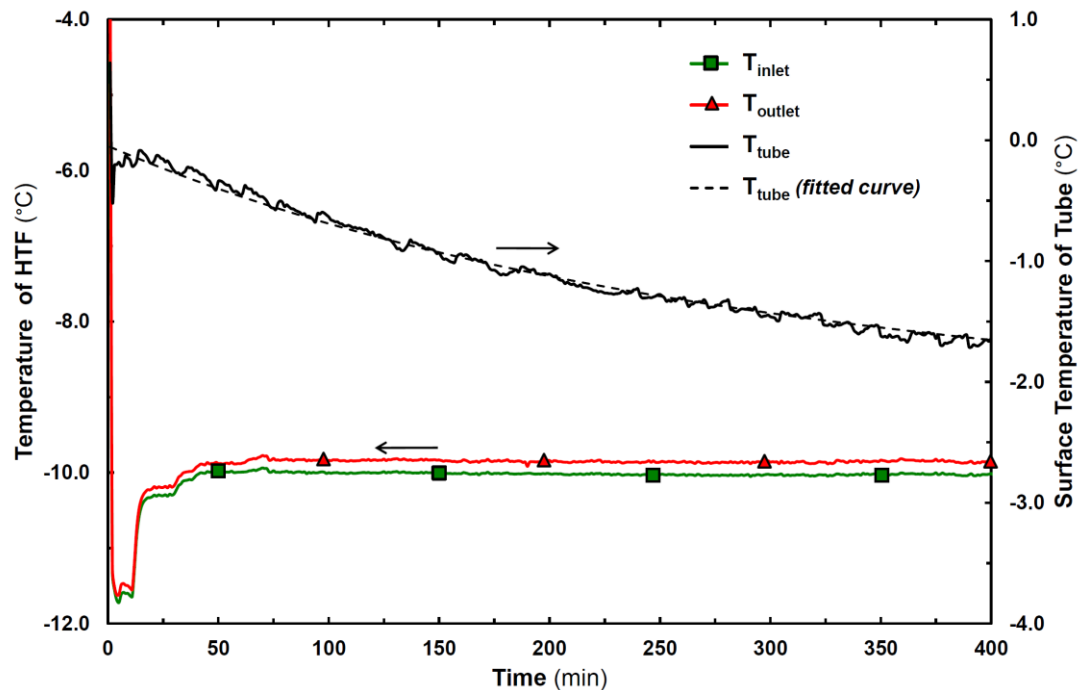


Figure 4.62 Time wise variations of the inlet, outlet, and surface temperatures.

As indicated in Section 2.1.1, phase change temperature range for water is selected as 0.51K with referring to Scanlon & Stickland (2004) with, $T_m - \delta T_m = 272.66$ K and $T_m + \delta T_m = 273.16$ K. The specific heat and thermal conductivity

values of water are defined as constants for the three regions. Density and viscosity of water are determined as temperature (K) dependent polynomial functions as in Seybert & Evans (2005). Thermo-physical properties of water used in current analyses are given in Table 4.1 for each phase. According to the experimental data, the initial temperature of water is defined as $T_i = 0.5^\circ\text{C}$ and the surface temperature of the shell is set as $T_{shell} = 15^\circ\text{C}$. Non-uniform mesh structure is applied around the tube surface to capture the higher temperature and velocity gradients. Domain is divided into 54,000 computational cells. After making sensitivity analyses, time intervals are set from $\Delta t = 1.5$ s to 5 s considering the convergence in the calculations. Iterations are continued unless the convergence criteria of $\varepsilon = 10^{-4}$ is satisfied for all transport equations, which needs at least 1,000 iterations for each time step. Because of the complex nature of the problem, the total computation time of each analysis is at least 3 weeks.

The comparisons between the numerical predictions and the experimental data are performed in terms of the time wise variations of the interface positions and temperature readings, for the top ($\theta = 90^\circ$) and the bottom ($\theta = -90^\circ$) sides of the tube. Figure 4.63 illustrates the time wise variations of the solidification front for top and bottom sides of the tube. In this Figure, while solid circles and triangles indicate the photography data, hollow ones with dashed lines indicate the numerical predictions for top and bottom directions, respectively. On the other hand, the time wise variations of predicted and measured temperature values are compared for two-selected thermocouple positions. In Figure 4.64, TC-1 and TC-4 indicate the first thermocouple positions at the top and bottom directions of the tube, $r_{tl} = 22.5$ mm. As it is clearly seen in Figures 4.63 and 4.64, the numerical results have the same trend with the experimental ones. The predicted solidification front variations for the top and bottom directions have close agreement with photography data. The maximum deviation between two results is less than 9% which is observed at $t = 210$ min for top side of the tube. On the other hand, the maximum deviation becomes less than 4% for the entire time range at the bottom side. In terms of absolute values, maximum deviations are approximately 2.4 mm and 1.2 mm for the top and bottom directions, respectively.

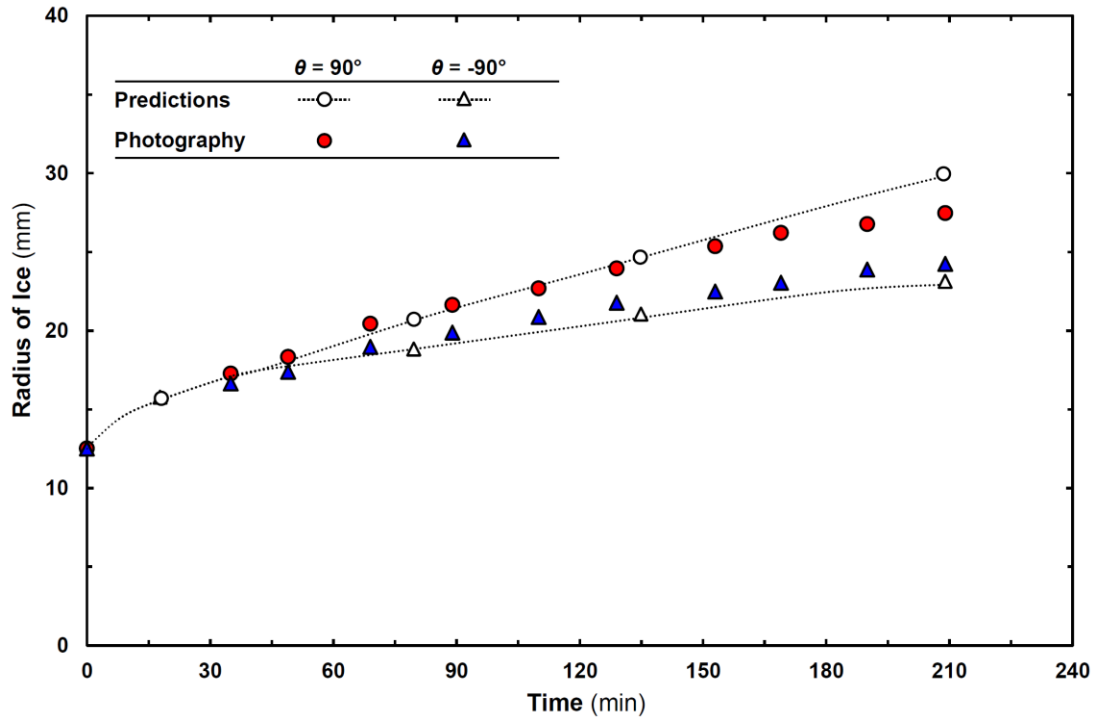


Figure 4.63 Comparison of time wise variations of predicted interface positions and photography data for top and bottom directions.

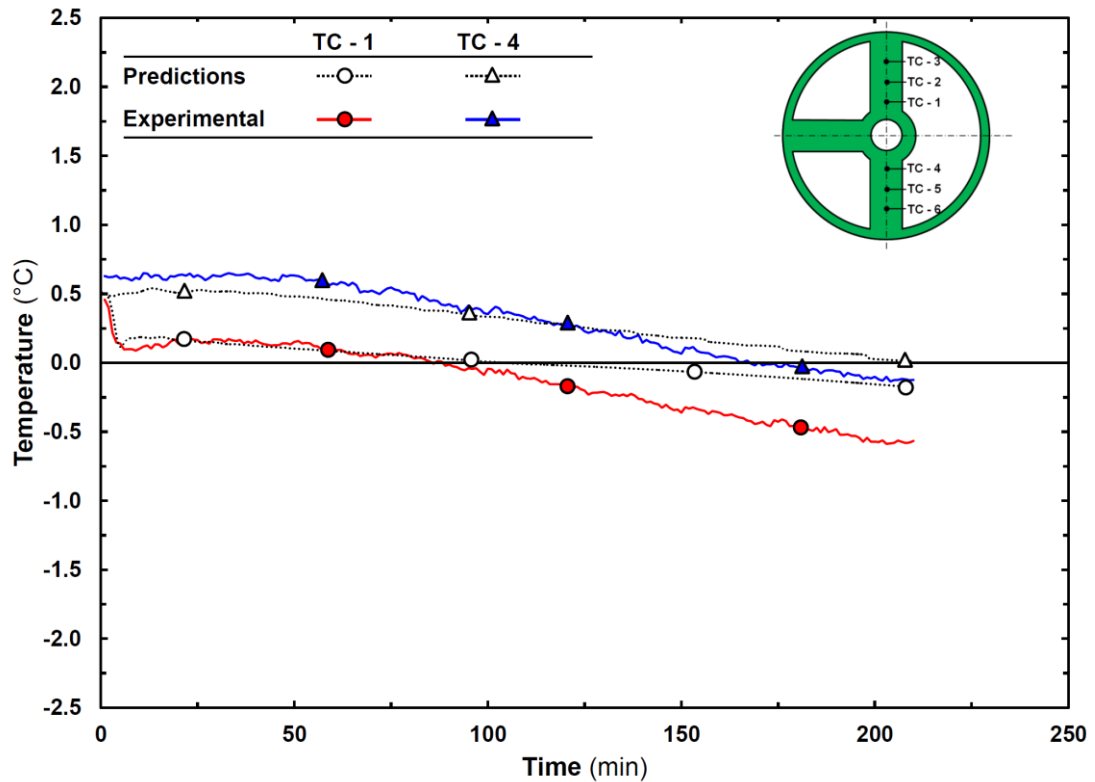


Figure 4.64 Comparison of time wise variations of predicted and measured temperature values two selected thermocouple positions.

Furthermore, as shown in Figure 4.64, the predicted temperature values are in well agreement with the experimental data employed until the phase change occurs on the thermocouple positions. After water turns into ice, the predicted temperature variations deviate from the experimental data. Therefore, the largest difference between the calculation results and experimental data becomes less than 0.4°C . This might be due to some measurement inaccuracies in experimental data and some assumptions or simplifications in the present model. Considering the nature of numerical assumptions, such as reducing the problem from three-dimensional to two-dimensional symmetric model and selecting constant thermal conductivities for solid and liquid phases could be the main source for deviations. In the experimental measurements, the thermocouples are fixed on the solid card body, although it is a hollow cylinder, and during the measurements, the thermocouples are affected by the phase change from liquid to solid, which cause some surface tension, and this affects the accuracy of experimental data. Under these circumstances, it can be concluded that the predicted numerical results are in considerably high agreement with the experimental data, and the present model is validated for simulating such a solidification process around tube with the presence of natural convection and heat gain from the surroundings.

Some further results are represented to introduce the influence of natural convection during solidification. In Figure 4.65, the isotherms and streamlines are given for $t = 60$ min, 120 min and 180 min. It is clear seen in the streamline patterns that the natural convection is dominant at the top side of the annulus. There occurs a clockwise circulation cell owing to the temperature difference between the hot shell surface ($T_{shell} > T_m$) and the cold ice surface ($T_m = 0$). Hot water with relatively higher density flows down through the interface surface and because of the cold ice surface, temperature of water decreases. With decreasing temperature, the density of water also decreases around interface and cold water with relatively low density, flows up through shell surface. This upward flow cause a thermal plume at the top side of the tube, as seen in isotherm patterns. On the other hand, the thermal stratification is formed at the bottom side of the tube, and the temperature gradient increases with time.

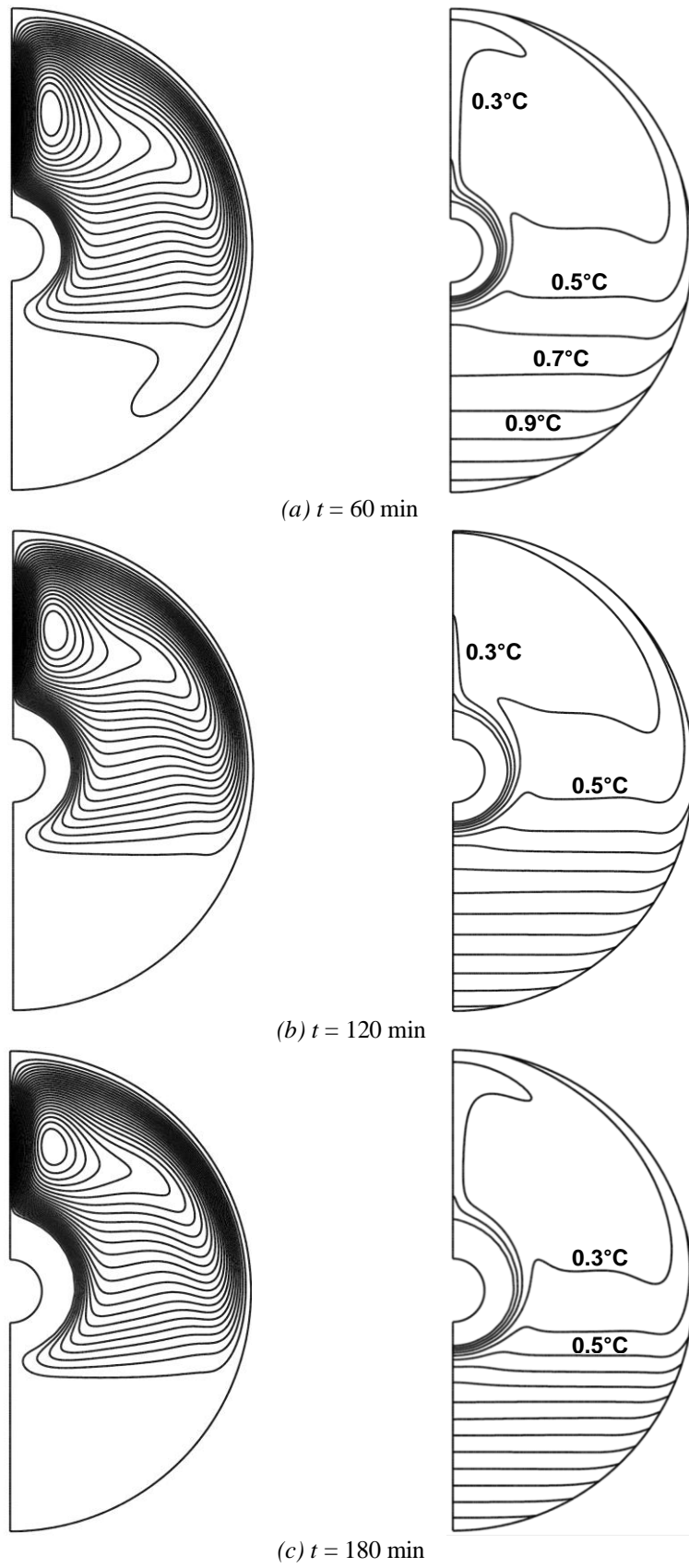


Figure 4.65 Isotherm (*right*) and streamline (*left*) patterns around tube during solidification in presence of heat gain.

4.1.3.1.2 *Case Studies.* After validating the numerical method for solidification process around the tube, some additional analyses are carried out to investigate the influence of the initial temperature on the heat transfer mechanism inside the annulus. In this part of the study, heat gain from the surroundings is neglected and adiabatic boundary conditions are considered for the shell surface. In addition, the tube temperature is taken as constant for the parametric studies. In this regard, three different cases are considered to introduce the influence of super heat factor (Sh) on the natural convection dominated solidification around tube. The dimensional and dimensionless quantities for each case are given in Table 4.12.

Table 4.12 Initial and tube temperature values for cases.

Case	Initial Temperature, T_i	Tube Temperature, T_{tube}	Superheat factor, Sh
	(°C)	(°C)	$(T_i - T_{tube}) / (T_m - T_{tube})$
#1	+0.5	-5.0	1.1
#2	+4.0	-5.0	1.8
#3	+8.0	-5.0	2.6

The comparisons of these three case studies are performed in terms of the time wise variations of the radius of ice, heat flux rejected from tube, temperature distributions, and local entropy generation associated with the heat transfer and the viscous flow. The local entropy generation definition is utilized to investigate the distribution of entropy generation (or *exergy destruction*) inside a specific domain.

For the solidification process with the presence of natural convection, the entropy generation is associated with the heat transfer and fluid flow inside the system. Bejan (1995) defined the local entropy generation as follows:

$$\dot{S}_{gen}^m = \frac{k}{T^2} \left[\left(\frac{\partial T}{\partial x} \right)^2 + \left(\frac{\partial T}{\partial y} \right)^2 \right] + \frac{\mu}{T} \left\{ 2 \left[\left(\frac{\partial u}{\partial x} \right)^2 + \left(\frac{\partial v}{\partial y} \right)^2 \right] + \left(\frac{\partial u}{\partial y} + \frac{\partial v}{\partial x} \right)^2 \right\} \quad (4.8)$$

In Section 3.1.3, the derivation of the local entropy generation is illustrated in detail, for two-dimensional conduction-convection heat transfer process. In Equation (4.8), the first bracket on the right-hand side represents the local entropy generation due to the heat transfer ($\dot{S}_{gen,heat}^m$) and the second one designates the local

entropy generation arises from the viscous effects of the flow ($\dot{S}_{gen,flow}^m$). Hence, local entropy generation can be written in terms of these two components as

$$\dot{S}_{gen}^m = \dot{S}_{gen,heat}^m + \dot{S}_{gen,flow}^m \quad (4.9)$$

The fraction of the heat transfer component to the total entropy generation is called as Bejan (*Be*) number (Bejan, 1995),

$$Be = \frac{\dot{S}_{gen,heat}^m}{\dot{S}_{gen}^m} \quad (4.10)$$

Bejan number determines the dominant component that causes irreversibilities. If $Be \gg 1/2$ irreversibilities arise from heat transfer is dominant to viscous effects. On the other hand, when *Be* number becomes $Be \ll 1/2$, it means that the irreversibilities arise from the viscous effects is more dominant. Eq. (4.8) adopted into FLUENT with defining two custom field functions to compute the heat transfer and flow components of the local entropy generation in terms of the velocity and the temperature gradients.

In Figure 4.66, the time wise variations of the radius of ice and heat flux are illustrated for three different *Sh* factors. With increasing *Sh* factor, or in other terms, increasing the initial temperature of water, it is clear that the growth of ice decreases, as it is expected. On the other hand, the amount of heat flux rejected from the tube surface slightly increases with *Sh* factor. This is due to the large temperature gradients at increasing *Sh* factors.

Furthermore, the time-dependent variations of point temperatures inside the annulus for each case are investigated. The temperature variations are then observed at the six different measurement points at $r = 22.5$ mm, 32.5 mm and 42.5 mm for both top ($\theta = 90^\circ$) and bottom ($\theta = -90^\circ$) directions of the tube. Thus, Figures 4.67 to 4.72 represent the time wise temperature variations with isotherms and streamline patterns at selected times for $Sh = 1.1$, 1.8 and 2.6.

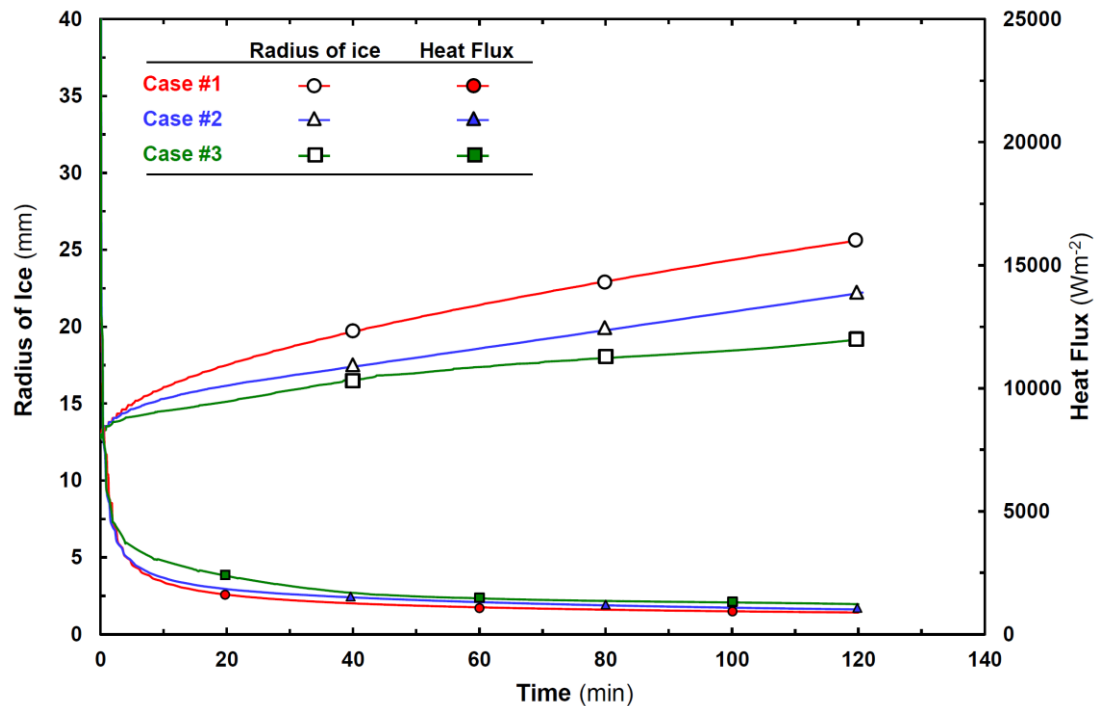


Figure 4.66 Time wise variations of radii of ice and heat flux values for three cases.

Figure 4.67, represents the time wise variations of temperature values for $Sh = 1.1$ (Case #1). It is apparent in the figure that the temperature values at the top side of the tube remain constant for a while in the beginning and then start decreasing sharply to reach a local minimum value at approximately $t \approx 10$ min. Since, the buoyancy forces arise with the formation of temperature distribution inside the annulus after a short conduction dominated heat transfer period. The buoyancy forces help to move the cold water around the tube through the shell surface. Thus, temperature values at the top side of the tube decrease rapidly. After a transitional period, the temperature values tend to decrease with a nearly constant slope until the solidification takes place. On the other hand, for the bottom side of the tube, it is clear that, natural convection affected only the first measurement point, $r = 22.5$ mm, and the temperature value of that point slightly decreases likely to the top side of the tube. For the remaining two measurement points at $r = 32.5$ mm and 42.5 mm, heat transfer is dominated by conduction, so, temperature values remain constant for about 40 minutes and then tends to decrease. To clarify these heat transfer mechanisms, isotherm and streamline patterns are given in Figure 4.68 for $Sh = 1.1$ at $t = 30$ min, 60 min, 90 min and 120 min. The streamlines indicate that there occurs a

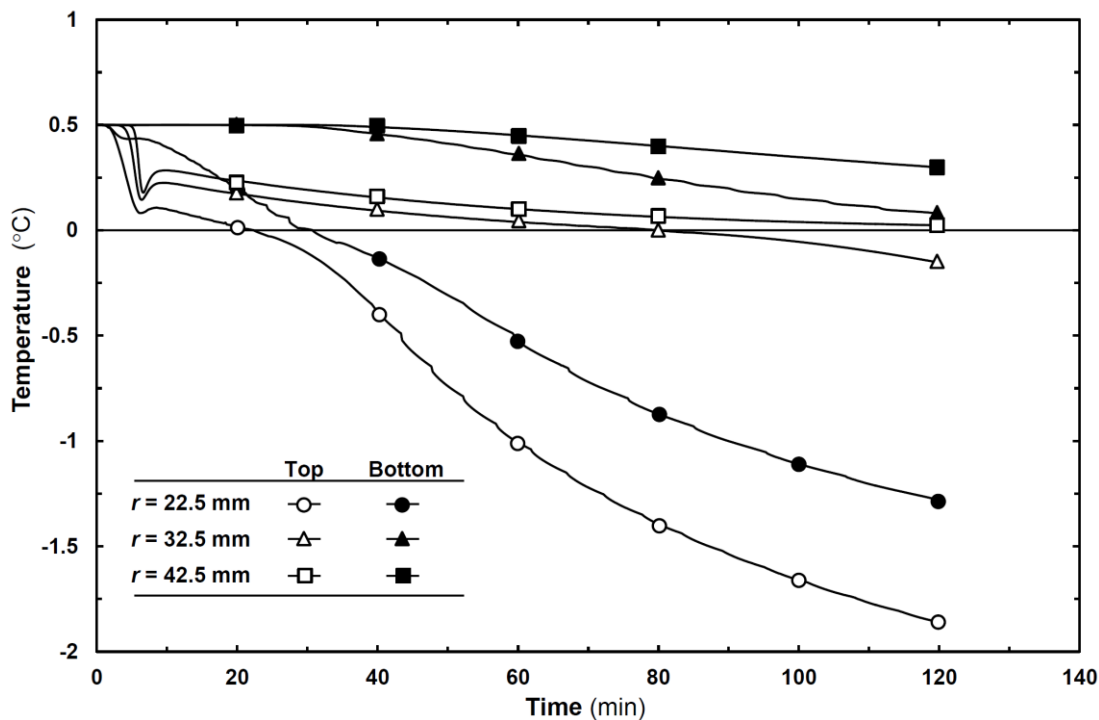


Figure 4.67 Time wise temperature variations inside the annulus for $Sh = 1.1$ (*Case #1*).

clockwise circulation cell dominated especially at the top side of the tube. In addition, the isotherms show that, thermal stratification takes place at the bottom side region of the tube while the temperature rapidly decreases for the top.

Figure 4.69 illustrates the time–dependent variation of the temperature values for $Sh = 1.8$ under *Case #2*. Similar to $Sh = 1.1$, the temperature values decrease rapidly after a short constant temperature period, at the top region. In comparison to the previous case, the temperature values drop down in a relatively shorter period. In less than 5 minutes, the temperature values decrease nearly 3°C . Because of the relatively higher temperature difference between the tube surface (or *interface surface*) and water temperature, the buoyancy forces becomes more dominant in comparison to the *Case #1*. Disregarding the rapid temperature drop for the top measurement points, the remaining process becomes similar to the *Case #1*.

Besides, it can be seen that, temperature values make small fluctuations for the measurement point located at $r = 22.5$ mm, at the bottom side. These fluctuations

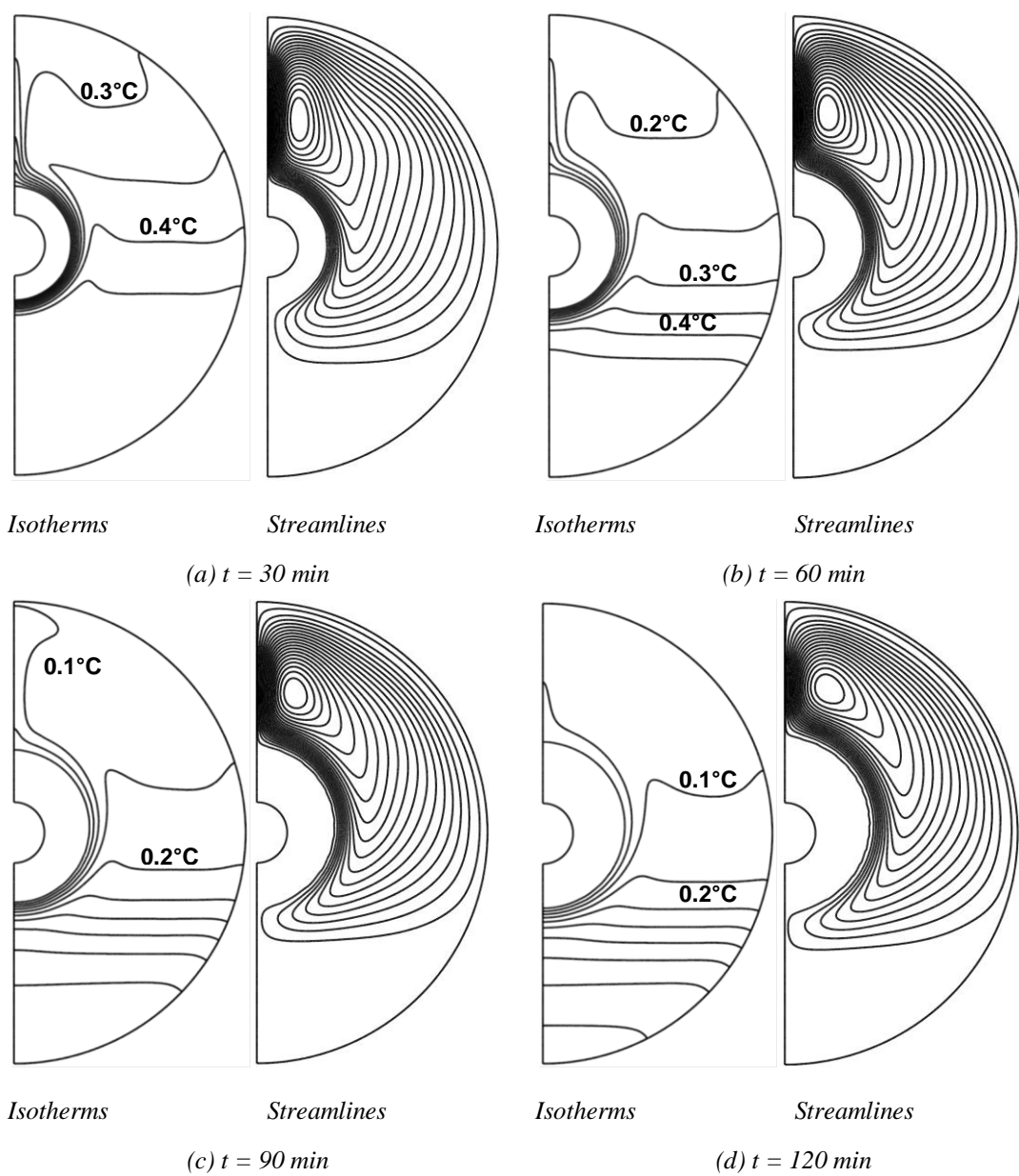


Figure 4.68 Isotherm and streamline patterns around the tube for $Sh = 1.1$ (Case #1).

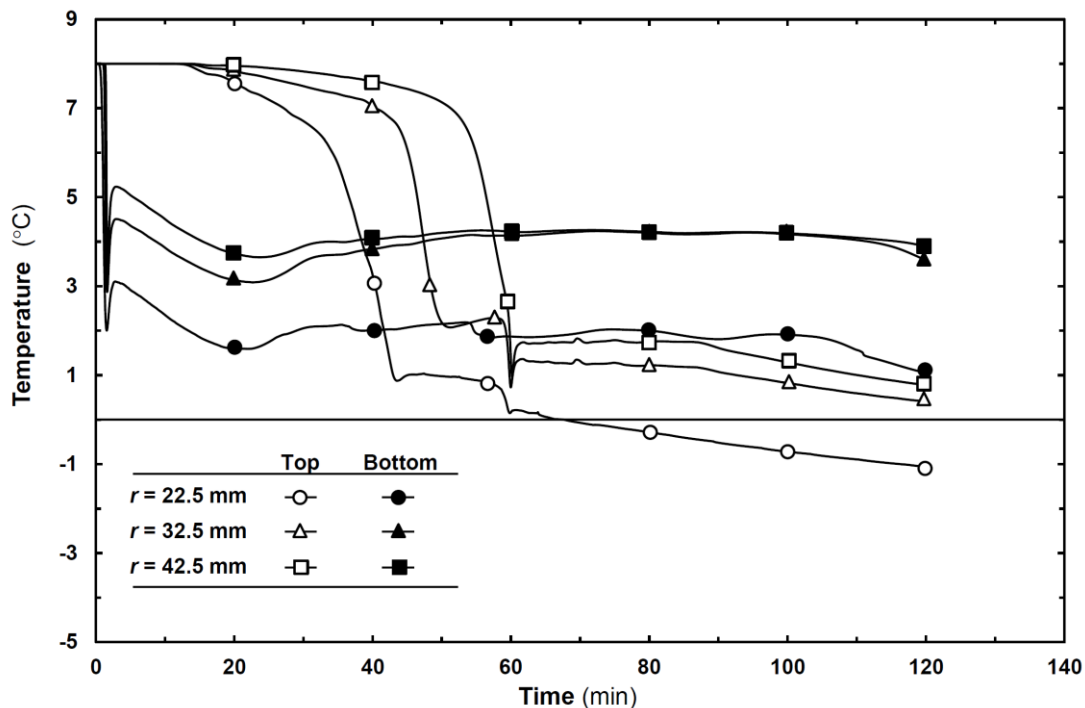


Figure 4.69 Time wise temperature variations inside the annulus for $Sh = 1.8$ (Case #2).

can be explained with examining the isotherm and the streamline patterns. In Figure 4.70, the isotherms and streamlines are given for $Sh = 1.8$ at $t = 30$ min, 60 min, 90 min and 120 min. The streamline patterns show that at the initial period of the analysis, natural convection cell shifts from the bottom to top side of the annulus. This transient behavior of the convection cell may affect the first temperature measurement point settled under the tube. On the other hand, the influence of the natural convection at the top side of the tube can be clearly seen. The temperature of water rapidly drops below 1°C in 90 min for the top region and thermal stratification occurs at the bottom side of the annulus. Thus, the ice formation around the tube turns into asymmetric and for $t = 180$ min, the difference between the top and bottom radii becomes nearly twice.

Figure 4.71 represents the time wise variation of temperature values for $Sh = 2.6$ (Case #3). The initial temperature of water is set as 8°C , which is higher than density inversion point of water ($T_{\rho,max} = 4^{\circ}\text{C}$). Hence, two separated convection cells and inversion of circulation direction in the progressing time should be expected.

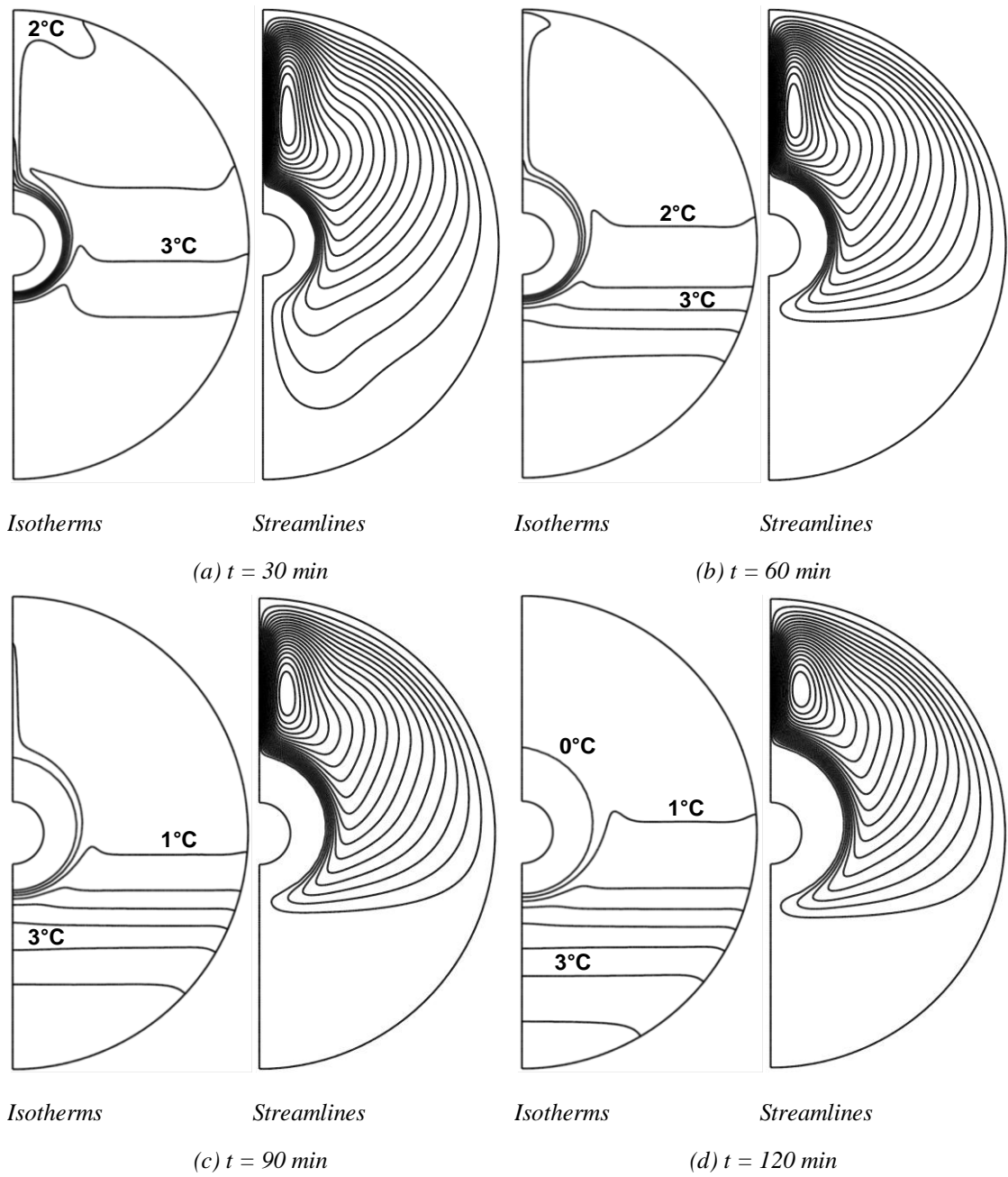


Figure 4.70 Isotherm and streamline patterns around the tube for $Sh = 1.8$ (Case #2).

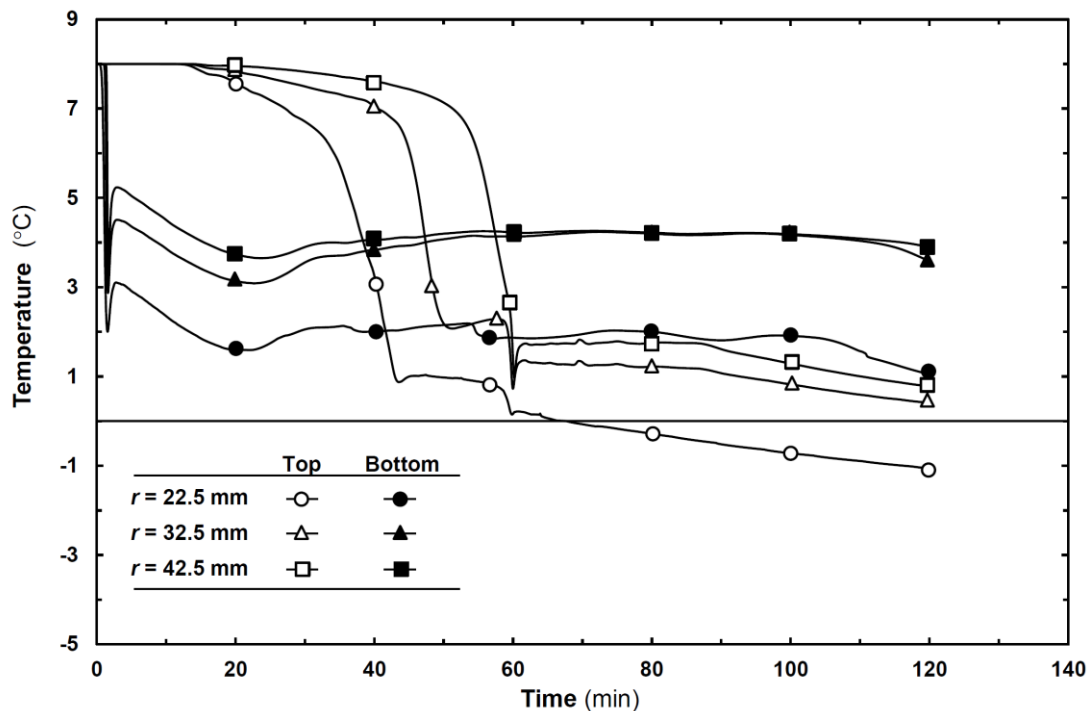


Figure 4.71 Time wise temperature variations inside the annulus for $Sh = 2.6$ (Case #3).

In this figure, it can be understood that the temperature values at the bottom side of the tube decrease rapidly and reach a local minimum value at approximately 2 minutes in the beginning of the analysis. Because of a higher temperature difference, the buoyancy forces arise at the beginning of the process and the cold water drops down from the tube surface through the shell surface. Thus, the temperature values at the bottom side of tube decrease rapidly. On the other hand, the temperature values remain almost constant until the inversion takes place on the top side. To analyze the temperature variations more clearly, the isotherm and streamline patterns should also take into account. In Figure 4.72, the isotherms and streamlines are given for $Sh = 2.6$ at $t = 30 \text{ min}$, 60 min , 90 min and 120 min . At $t = 30 \text{ min}$, two separated circulation cells are observed. Between the temperature range of $T_{\rho,max} < T < T_i$ there appears counter-clockwise circulation cell at the bottom side of tube and for the interval of $T_m < T < T_{\rho,max}$ there occurs clockwise circulation cell at the inner region. As seen in Figure 4.71, owing to the natural convection dominated heat transfer at the bottom side of the tube, temperature values rapidly drop around 4°C in the first 30 min. For $t = 60 \text{ min}$, the flow direction of the circulation cell starts to inverse up side of the tube, as seen in isotherms. After $t = 60 \text{ min}$, the clockwise circulation cell forms at

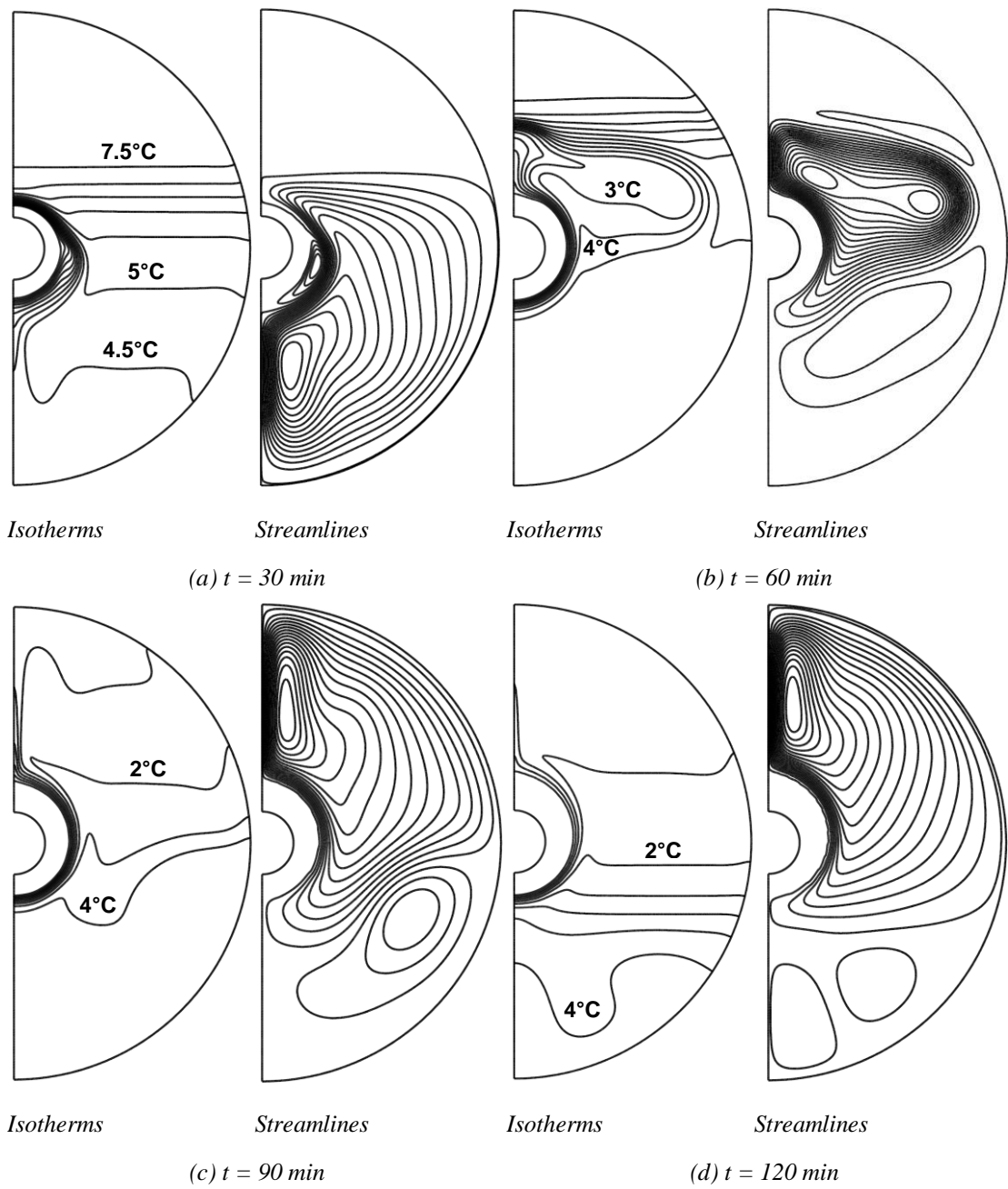


Figure 4.72 Isotherm and streamline patterns around the tube for $Sh = 2.6$ (Case #3).

the top region and drops down the temperature values under 4°C . This rapid change in temperature values can be seen in Figure 4.71. After $t = 90$ min, the isotherm and streamline profiles become similar to the ones given in Cases #1 and 2 for the top region. At the bottom region, small counter-clockwise circulation cell can be observed for $t = 90$ min and this cell separates into two parts after $t = 120$ min. These small reverse circulation cells are observed, where the temperature above than $T_{\rho,max}$.

Besides, additional comparisons are carried out in terms of time wise variations of the mean volumetric entropy generations, related with the heat transfer and viscous flow in Figure 4.73. Here, the mean volumetric entropy generation terms are computed in terms of the volumetric average of the local entropy generation values in the domain.

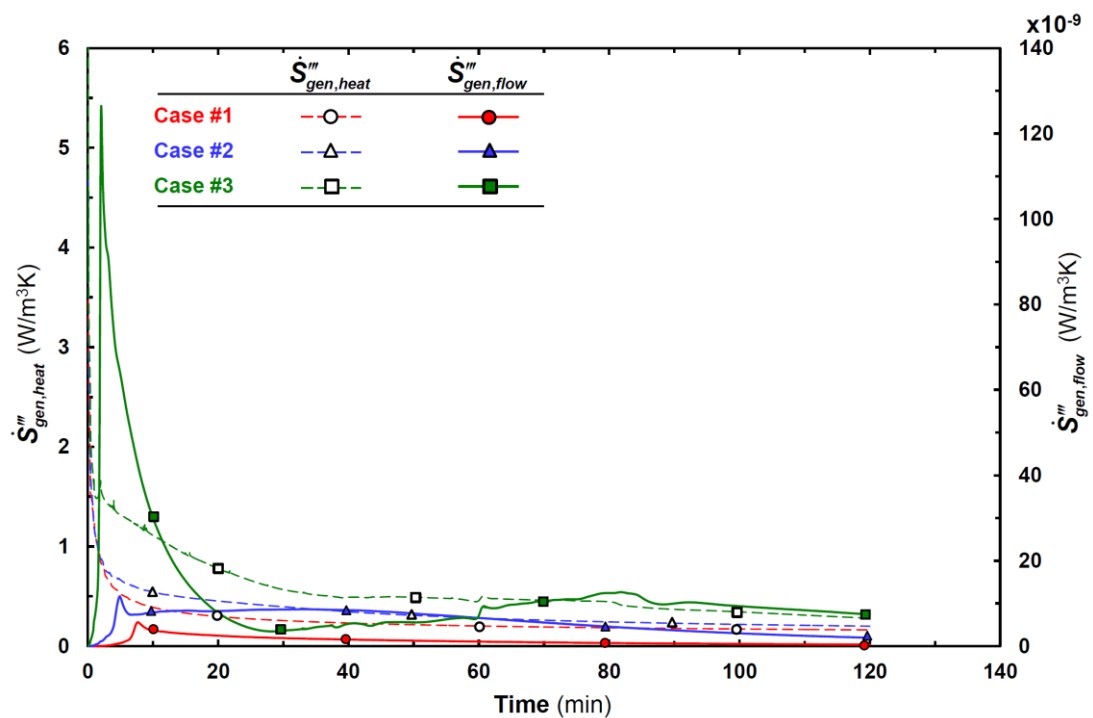


Figure 4.73 Time wise variations of mean entropy generations related to heat transfer and viscous flow.

It can be seen in Figure 4.73 that, the entropy generation rate related with the heat transfer is dominant in all cases and Be number is almost unity. With increasing super heat factor, entropy generation rate related with the heat transfer increases

because of the increasing temperature gradients inside the annulus. The heat transfer component tends to decrease in processing time, as the heat flux and temperature gradients decrease in time. On the contrary, the entropy generation rates related with the viscous flow make picks at the initial periods of the analyses. Because, influences of the natural convection arise at these periods and then the velocity gradients relatively decrease, in progressing time. For Case #1, the local maximum observed at $t \approx 10$ min, afterwards, the entropy generation rate related with the viscous effects tends to decrease. Since, the influence of the natural convection decreases in time. For Case #2, the variation of the entropy generation rate of flow, has similar trend as in Case #1. Owing to the higher temperature difference and super heat factor, the local maximum value is slightly higher than the previous case and takes place at $t \approx 5$ min. For Case #3, because of the formation of two separated circulation cells inside the annulus, velocity gradients should be higher than former cases. From this figure, it can be clearly that the peak value for Case #3 is nearly six times higher than the former cases. The entropy generation rate of viscous flow tends to decrease until the flow direction inverses to the top side. Because of the higher temperature gradients at the top region, the rate of entropy generation slightly increases after $t = 60$ min. Finally, as the temperature distribution inside the annulus turns into homogenous, velocity gradients and the rate of entropy generation of viscous flow tends to decrease after $t = 90$ min.

For Case #3, the maps of the local rate of entropy generation related with the viscous flow, are illustrated in Figure 4.74, for $t = 2$ min, 30 min, 60 min and 90 min. As seen here, for $t = 2$ min, the local entropy generation occurs mostly at the bottom side of the annuli and around the tube. On the other hand, for $t = 30$ min, because of the formation of the separated circulation cells, the rate of entropy generation arises mostly near the interface. In the progressing time, the maximum value of rate of entropy generation increases at $t = 60$ min and $t = 90$ min. Entropy generation occurs near the interface surface for $t = 60$ min. On the other hand, at $t = 90$ min, with shifting the convective cell through the top region of the tube, the rate of entropy generation arise at the top side of the annulus.

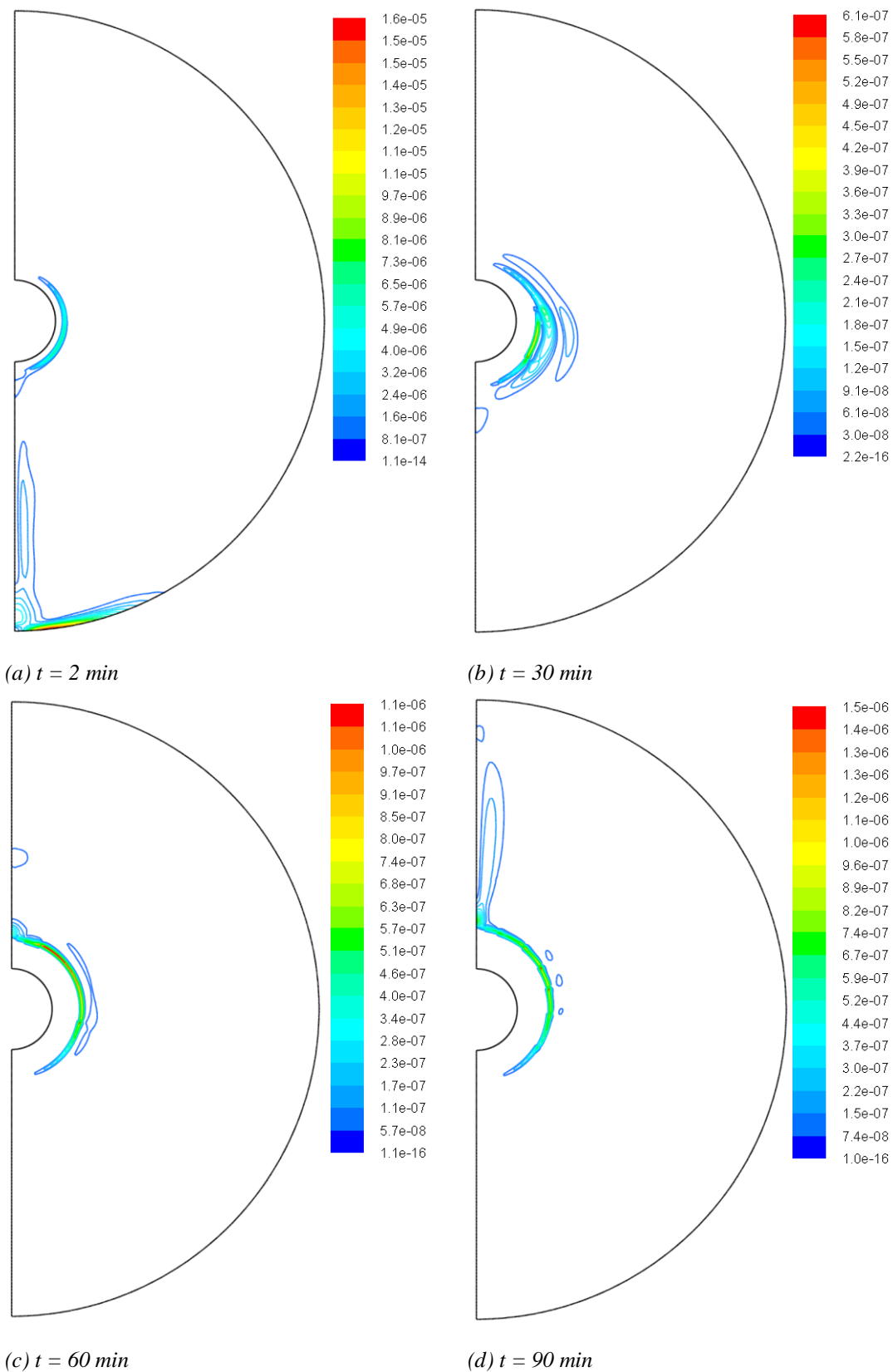


Figure 4.74 Maps of local rate of entropy generation related to viscous flow.

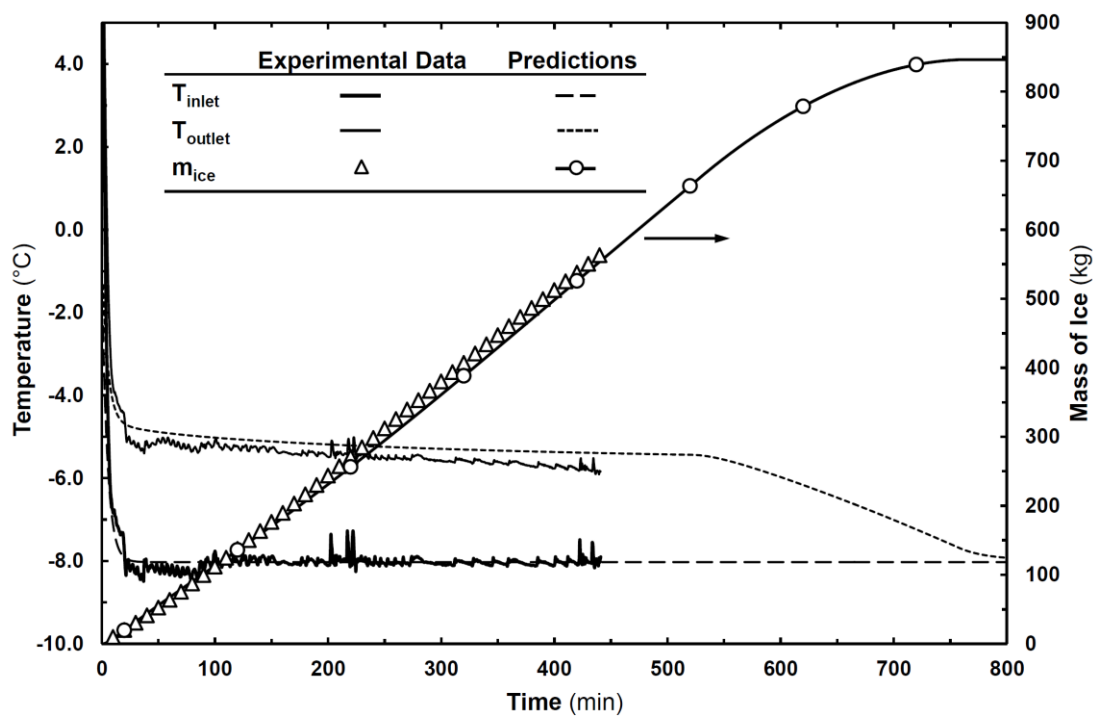
4.3.2 Numerical Investigation of Ice-on-coil LHTES System

First, numerical model is validated by comparing the predictions with the experimental results. Afterwards, performance assessment of the ice-on-coil LHTES system is investigated for several working and design parameters, in terms of; heat transfer rate, total stored energy, dimensionless energetic and exergetic effectiveness, also, energy and exergy efficiency.

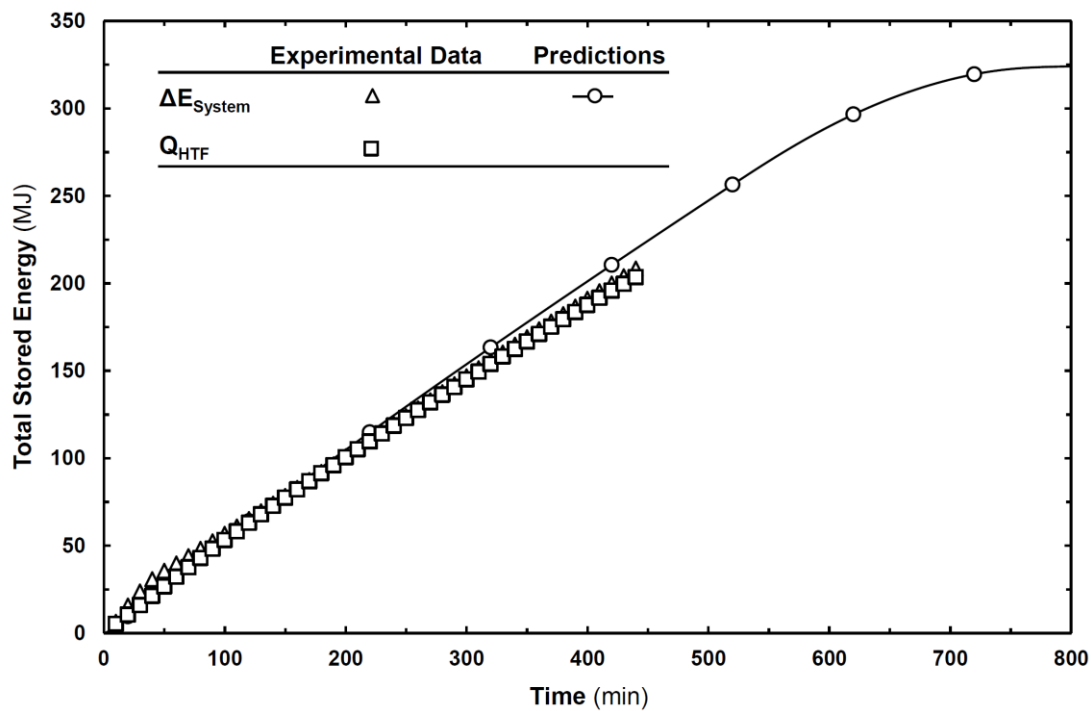
4.3.2.1 Model Validation

The validity of the model is tested by comparing the predicted results with the current experimental data. Time wise variations of the predicted outlet temperature, total amount of ice and total stored energy variations are compared with experimental results. Figures 4.75 and 4.76 represent the predicted results together with the experimental data for two different volumetric flow rates of $T_{in} = -8^{\circ}\text{C}$.

In Figures 4.75(a) and 4.76(a), bold straight lines designate the inlet temperature of the HTF to the storage tank. It can be seen that the inlet temperature values of the HTF have transient behavior at the initial periods of experiments and reach the set temperature nearly in 20 min. Thus, the inlet temperatures are defined as time dependent functions in the numerical analyses, in order to obtain the same inlet temperature boundary conditions as in experimental measurements. A dynamic curve fitting method (*Exponential Rise to Maximum – 5 Parameters*) is applied to the time wise variations of the inlet temperatures to obtain functions. In Figures 4.75(a) and 4.76(a), fitted curves are illustrated with dashed lines and the forms of the functions are given in Eq. (4.1). Moreover, the initial temperature values of water and heat gain from surroundings are set to the corresponding experimental data. At the beginning of the experiments, the mean temperature values of water are measured as 5°C and 3°C for $\dot{V} = 50$ l/min and $\dot{V} = 70$ l/min experiments, respectively. On the other hand, the experimental results are indicated that heat gain is independent of the experimental parameters and almost constant during experiments.

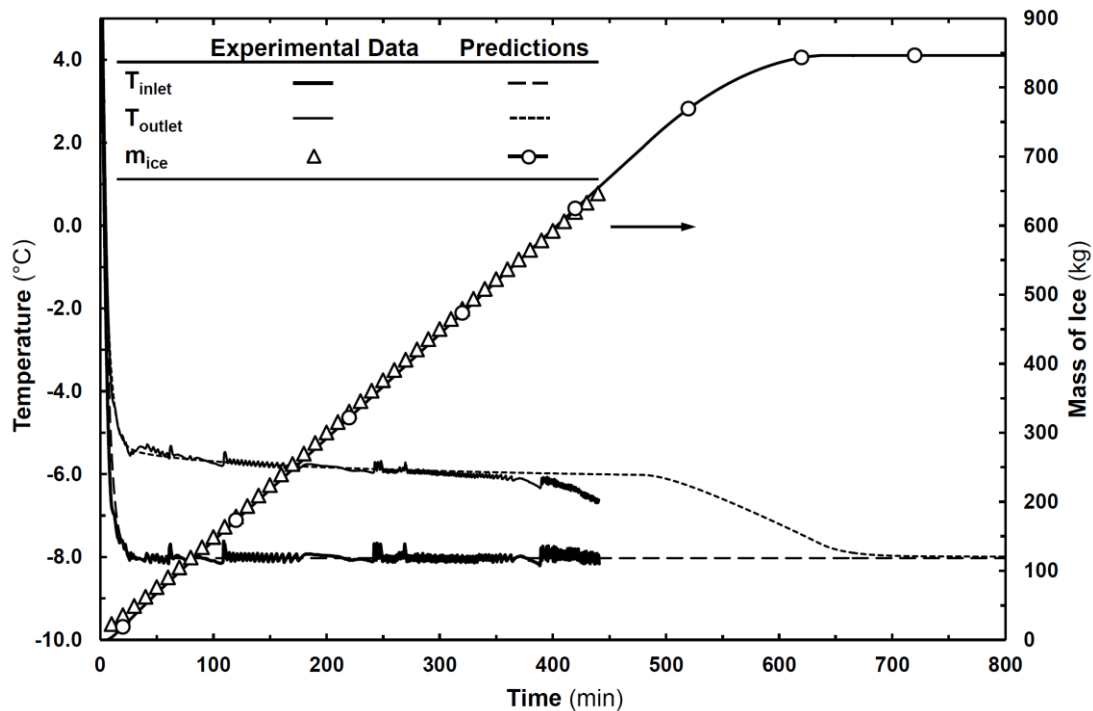


(a) Variations of inlet–outlet temperatures of HTF with total mass of ice

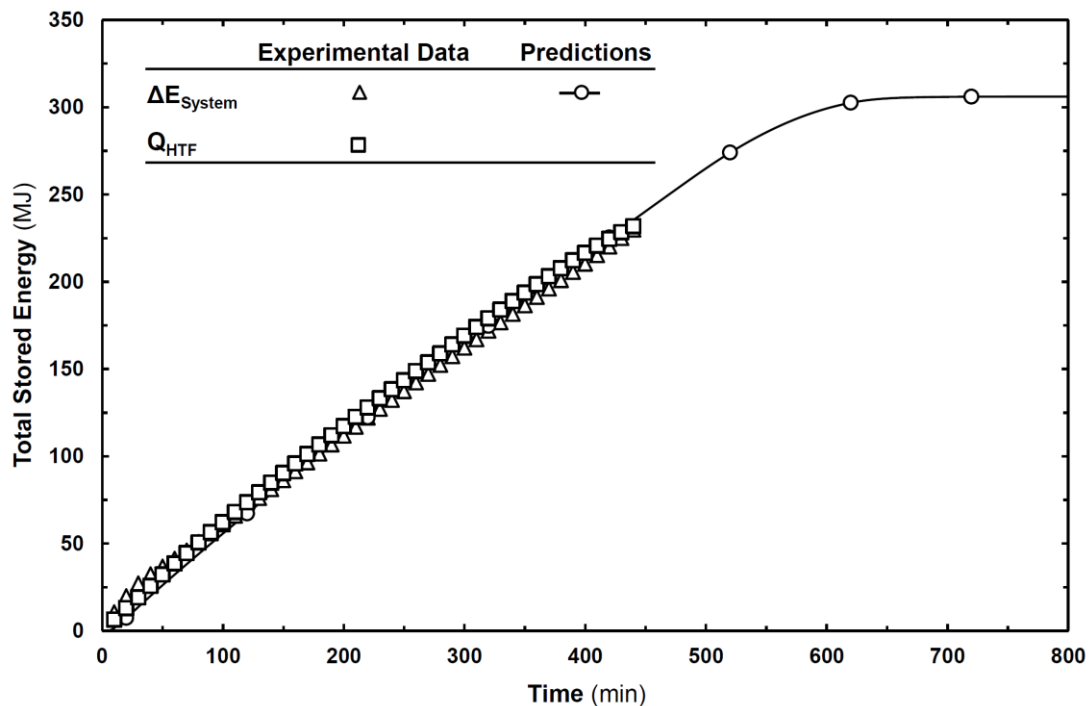


(b) Variations of total stored energy

Figure 4.75 Comparisons of experimental and predicted results – $T_{in} = -8^{\circ}\text{C}$, $\dot{V} = 50 \text{ l/min}$.



(a) Variations of inlet–outlet temperatures of HTF with total mass of ice



(b) Variations of total stored energy

Figure 4.76 Comparisons of experimental and predicted results – $T_{in} = -8^{\circ}\text{C}$, $\dot{V} = 70 \text{ l/min}$.

In Figures 4.75(a) and 4.76(a), time wise variations of the predicted outlet temperature of the HTF and the total amount of the mass of ice are given together with the experimental results. While dashed lines designate the predicted outlet temperature values of the HTF, straight lines indicate the experimental temperature readings at the outlet section of the tank. On the other hand, straight lines with hollow circles and triangles correspond to the variations of the total mass amount of ice for numerical predictions and experimental measurements, respectively.

Results show that there is a good agreement between the predicted and experimental data in terms of the temperature and the amount of mass of ice comparisons. Temperature and mass variations have the same trend until the unconstrained ice formation period finalize. Then, predicted outlet temperature of the HTF deviate from the experimental results with the initiation of the constrained ice formation period. In contrast, predicted mass amount of ice values have a good agreement for whole range. Further comparisons are performed in terms of the total stored energies.

In Figures 4.75(b) and 4.76(b), variations of predicted total stored energy values are given together with the experimental results. In experiments, the total stored energy is computed in two different ways; from the internal energy variation of the PCM and from the enthalpy variation of the HTF with considering the heat gain from surroundings. Energy variations indicate that the predicted total stored energy values have good agreement with the experimental data, unlike the temperature variations. In the light of these comparisons, it can be concluded that the predicted results have reasonable consistency with the experimental data, and the present numerical method is valid for simulating the solidification process inside an ice-on-coil LHTES tank.

4.3.2.2 Parametric Energy and Exergy Based Analyses

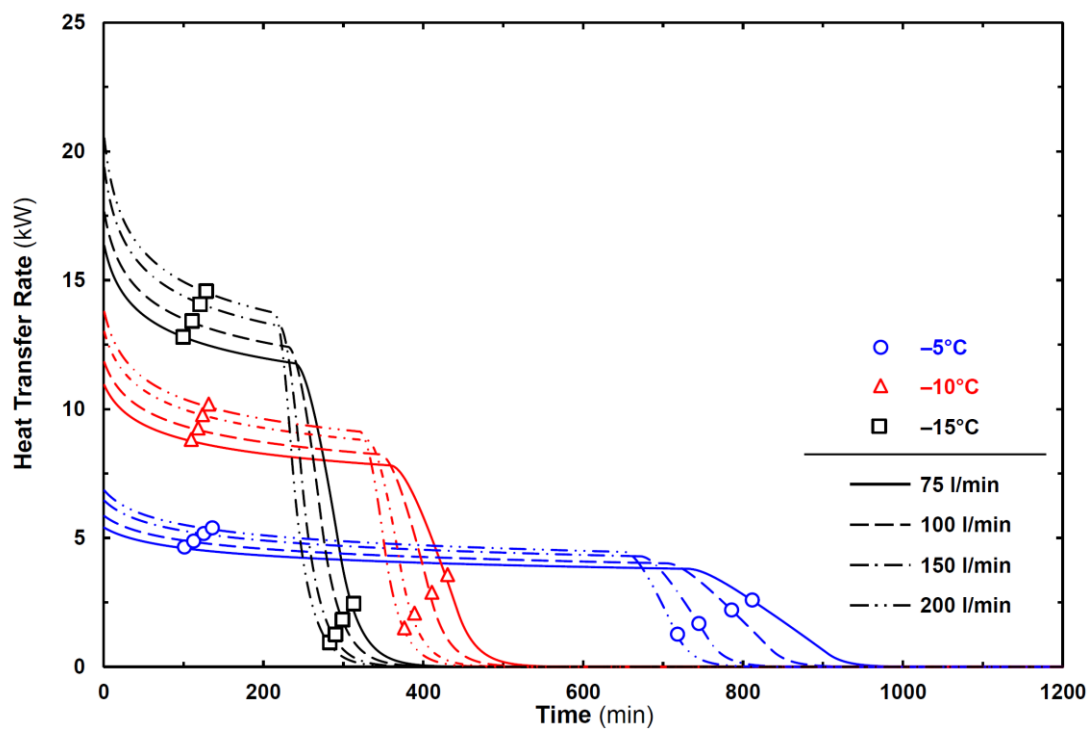
In this study, a total of 48 parametric analyses is conducted to investigate the thermal characteristic of the storage system in the light of the various working and design parameters. Numerical parameters used in the current analyses are given in

Table 4.13. Parametric results are obtained in terms of the time wise variations of the heat transfer rate, total stored energy, dimensionless energetic and exergetic effectiveness, also, energy and exergy efficiency.

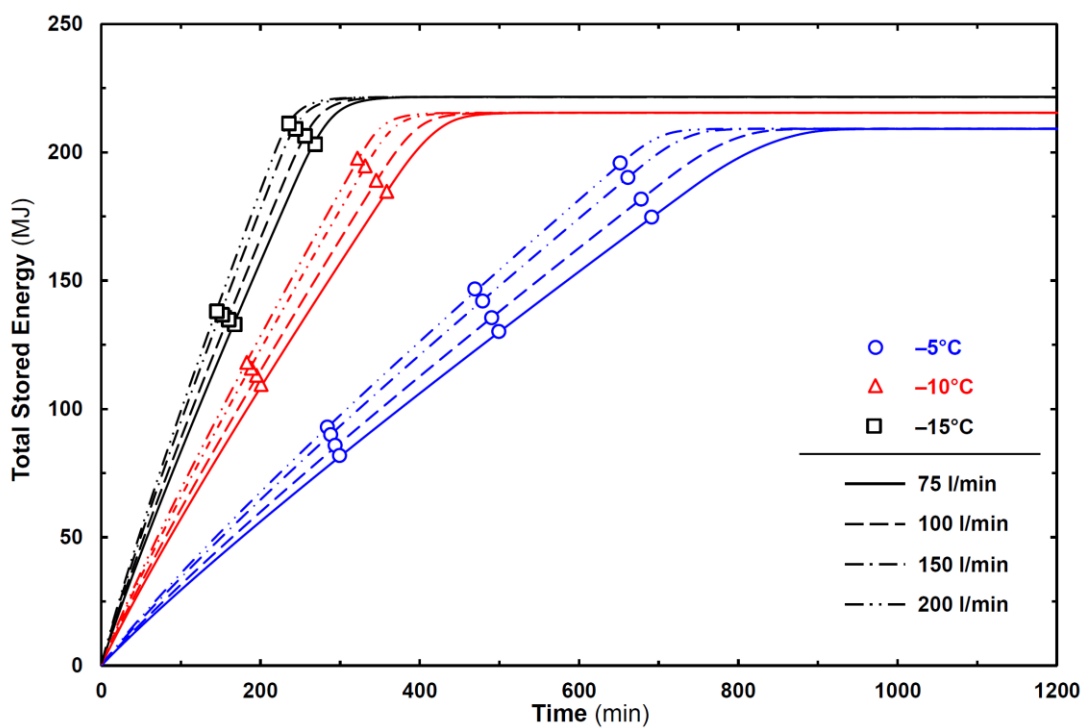
Table 4.13 Design and working parameters for numerical analyses of the ice-on-coil LHTES system.

Length of tube, ℓ	Inlet temperature of HTF, T_{in}	Flow rate of HTF, \dot{V}	Heat gain from surroundings, \dot{Q}_{gain}	Tube Material
(m)	(°C)	(l/min)	(kW)	-
10				
15	-5, -10, -15	75, 100, 150, 200	0.25	PE-32, S.Steel, Copper
20				
25				

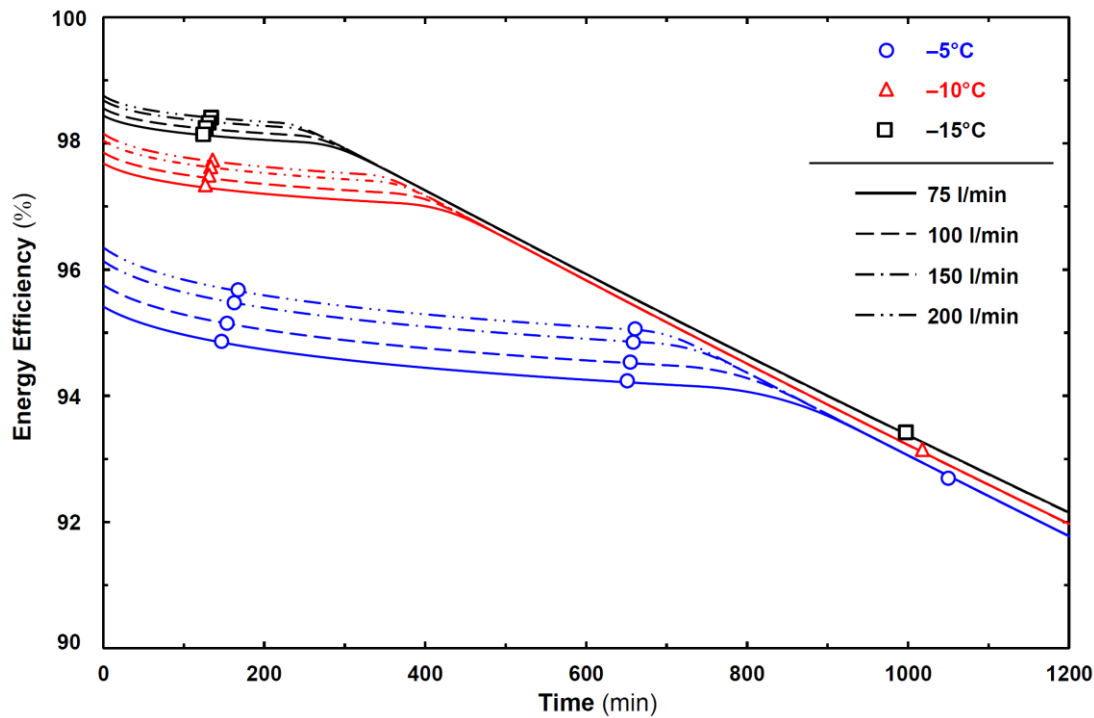
In Figure 4.77, time wise variations of the heat transfer rate, total stored energy, and exergy efficiency are represented for various inlet temperature and flow rate values of the HTF. From Figures 4.77(a) and (b), it can be seen that the total stored energy and heat transfer rate increase with increasing the flow rate and decreasing the inlet temperature of the HTF. Owing to the great value of the temperature difference between water and the HTF, at the beginning of the analyses the heat transfer rate has maximum values, and tends to decrease in time. For relatively lower inlet temperature values of the HTF, the heat transfer rates rapidly decrease and reach to minimum. On the other hand, for the higher inlet temperature cases, after a sudden decreasing period heat transfer rates keep almost constant until the radius of ice reaches the pitch value. Besides, the time wise variation of the heat transfer rate is sharper for the lower inlet temperature value in the sensible cooling period of ice. As seen in Figure 4.77(b) and (c), the influence of the inlet temperature is more deterministic on the stored energy and energy efficiency. Flow rate becomes effective for relatively higher inlet temperature values such as $T_{in} = -5^{\circ}\text{C}$. On the other hand, total solidification time decreases nearly half with decreasing the inlet temperature of the HTF from -5°C to -15°C . Furthermore, Figure 4.77(d) designates that exergy efficiency increases with increasing inlet temperature of the HTF. Exergy efficiency increases with increasing the inlet temperature from -15°C to -5°C approximately from 60% to 80%. Because, irreversibility increases and in contrast the exergy efficiency decreases with increasing the temperature difference between the phase change temperature of water and the inlet temperature of the HTF.



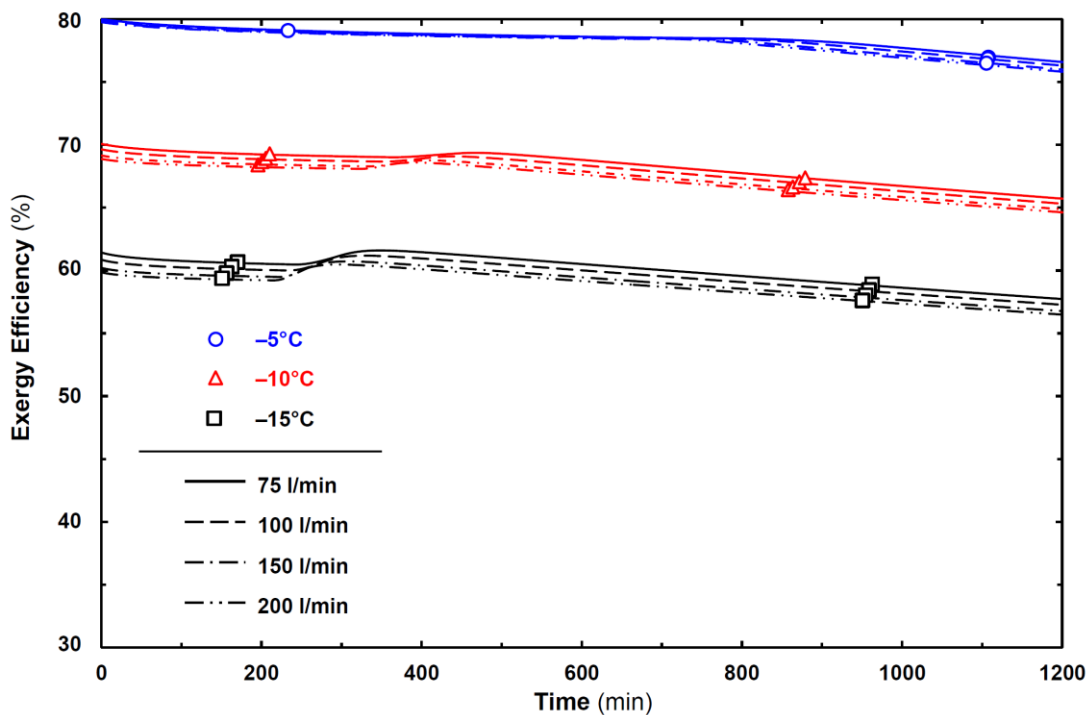
(a) Heat transfer rate



(b) Total stored energy



(c) Energy efficiency



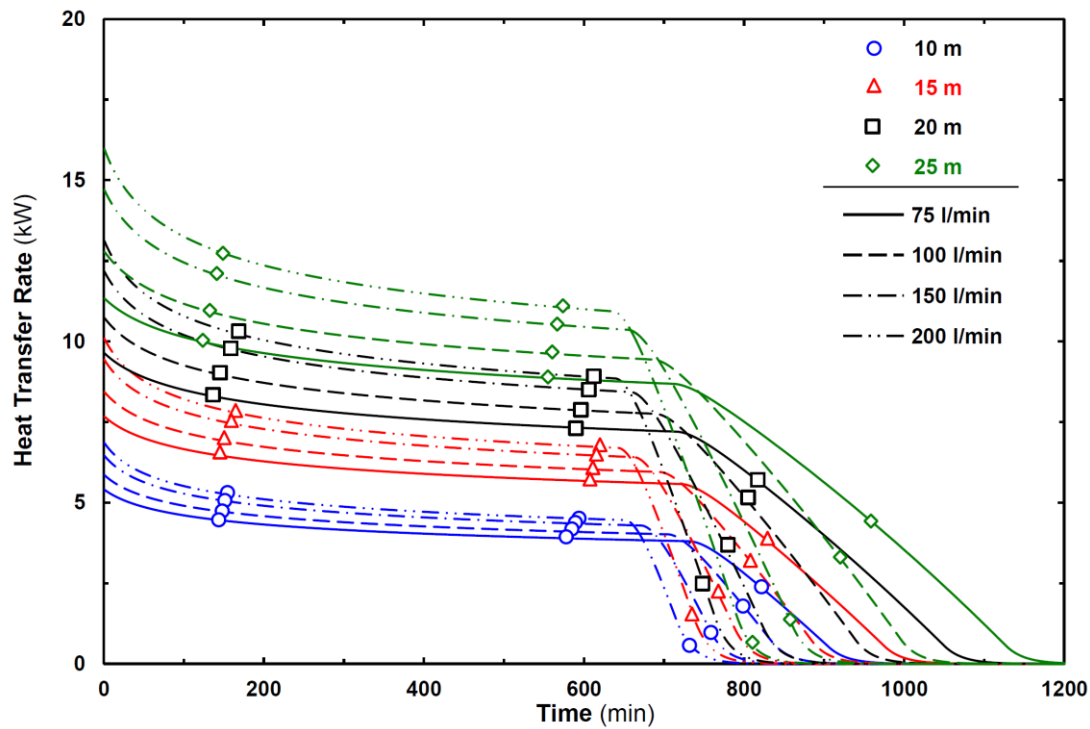
(d) Exergy efficiency

Figure 4.77 Influences of inlet temperature and flow rate of HTF on (a) Heat transfer rate, (b) Total stored energy (c) Energy efficiency and (d) Exergy efficiency – $\ell = 10$ m, PE-32.

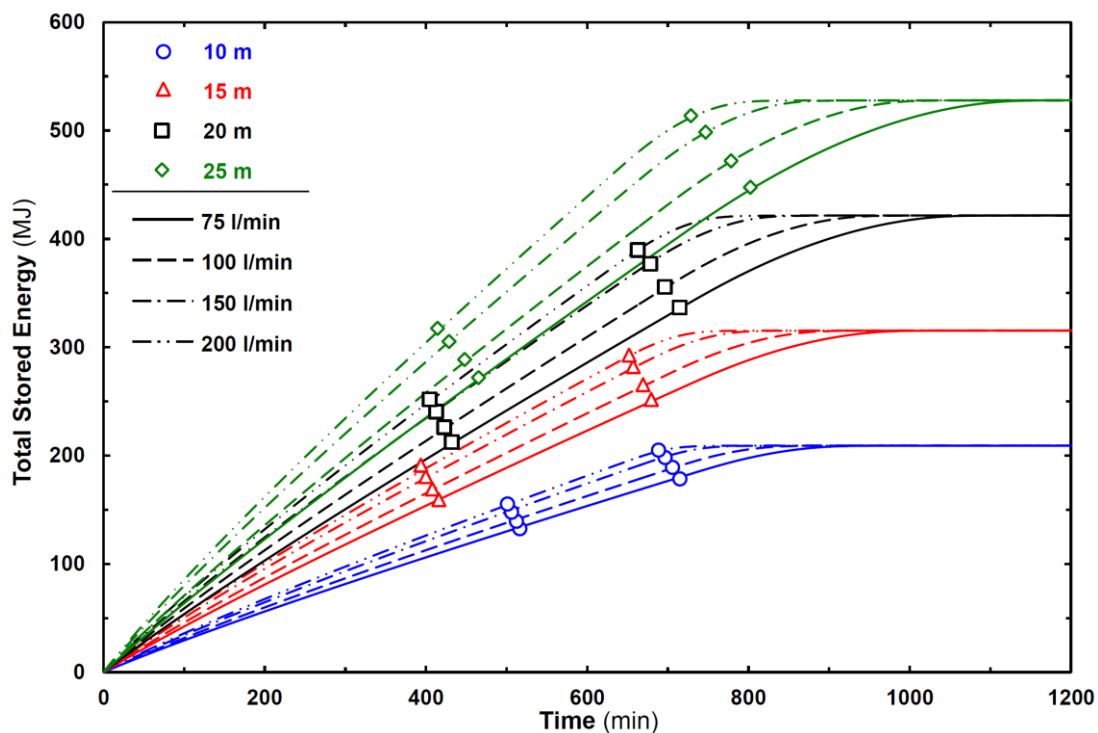
Similar to the energy variations, the inlet temperature of the HTF is more deterministic on the exergy efficiency. The influence of the flow rate becomes clear for relatively lower inlet temperatures of the HTF, (*such as* $T_{in} = -15^{\circ}\text{C}$) unlike to the energy variations.

In Figure 4.78, time wise variations of the heat transfer rate and total stored energy are given for different values of the tube lengths and flow rates for $T_{in} = -5^{\circ}\text{C}$. The rate of heat transfer and total process time increases with increasing the length of the tube as seen in Figure 4.78(a). Figure 4.78 (b) illustrates the variations of total stored energy for four different values of the tube length and several of the flow rate of the HTF. It is clear that, total stored energy increases with increasing the length of the tube. To investigate these variations in a non-dimensional scale, time wise variations of energetic/exergetic effectiveness values are represented with energy/exergy efficiency variations for two different lengths of the tube in Figure 4.79. From Figure 4.79(a) and (b), it can be seen that, energetic and exergetic effectiveness decreases with increasing the length of the tube. For relatively higher temperatures or lower flow rates of the HTF, this effect becomes clearer. Besides, there is a similarity between energetic and exergetic effectiveness results, because the storage behaviors of energy and exergy are similar in the current system. Finally, variations of energy and exergy efficiencies are illustrated in Figure 4.79(c) and (d) for various flow rate and inlet temperature values of the HTF with two lengths of the tube. Similar to the total stored energy variations, with increasing the length of the tube, energy and exergy efficiencies increase. Furthermore, influence of the flow rate on the exergy efficiency becomes clearer with increasing the tube length. It should be emphasized that, even though the effectiveness of the system increases with decreasing the inlet temperature of the HTF from $T_{in} = -5^{\circ}\text{C}$ to $T_{in} = -15^{\circ}\text{C}$, exergy efficiency decreases significantly with decreasing the inlet temperature of the HTF.

In Figure 4.80, time wise variations of the heat transfer rate, total stored energy, and energy and exergy efficiencies are represented for three different tube materials and two different values of the tube length. Thermal conductivity values for each material are given in Table 4.7. As seen in Figure 4.80(a) and (b), the rate of heat

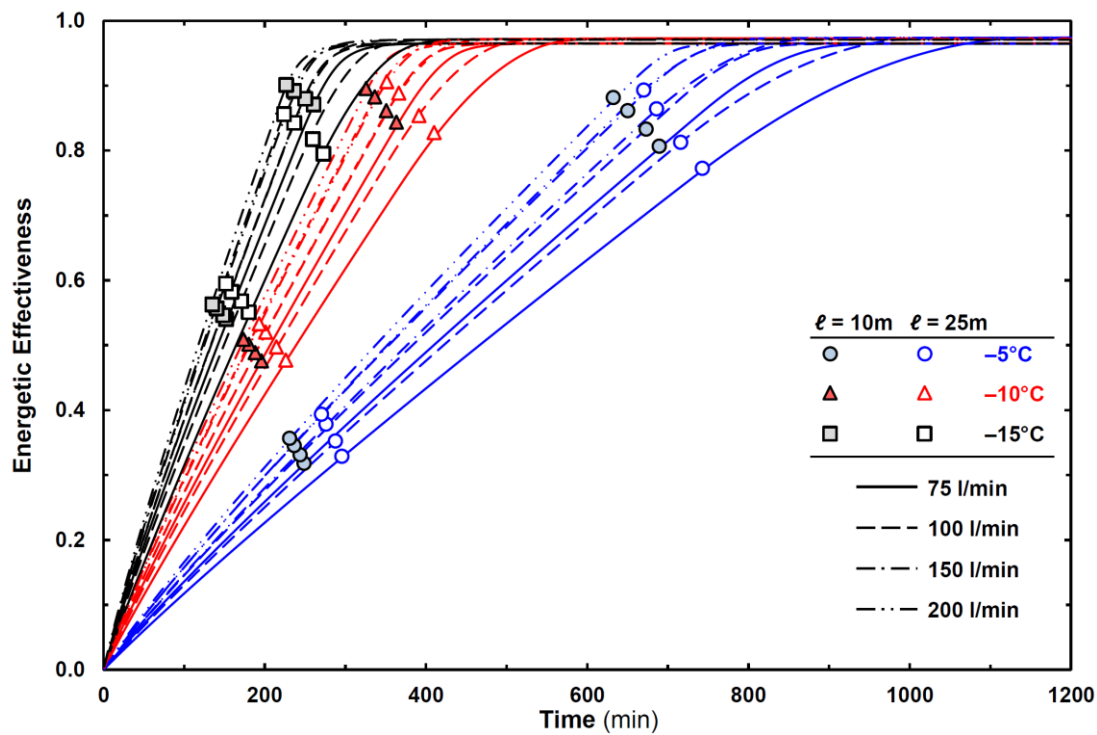


(a) Heat transfer rate

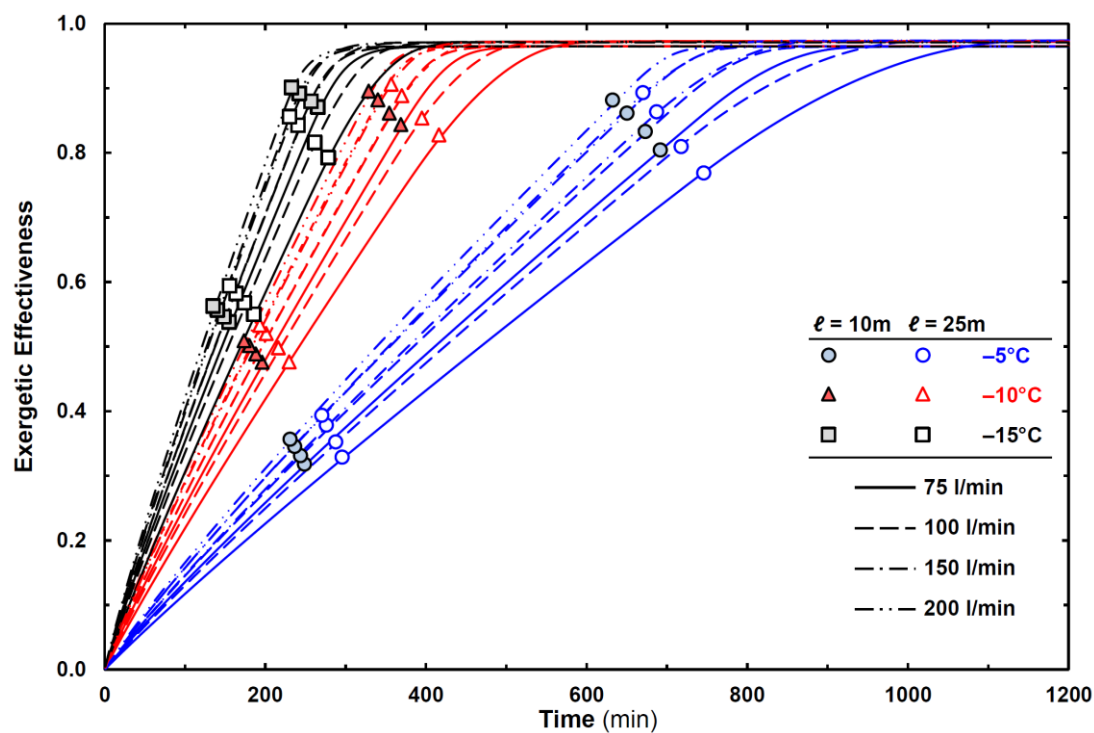


(b) Total stored energy

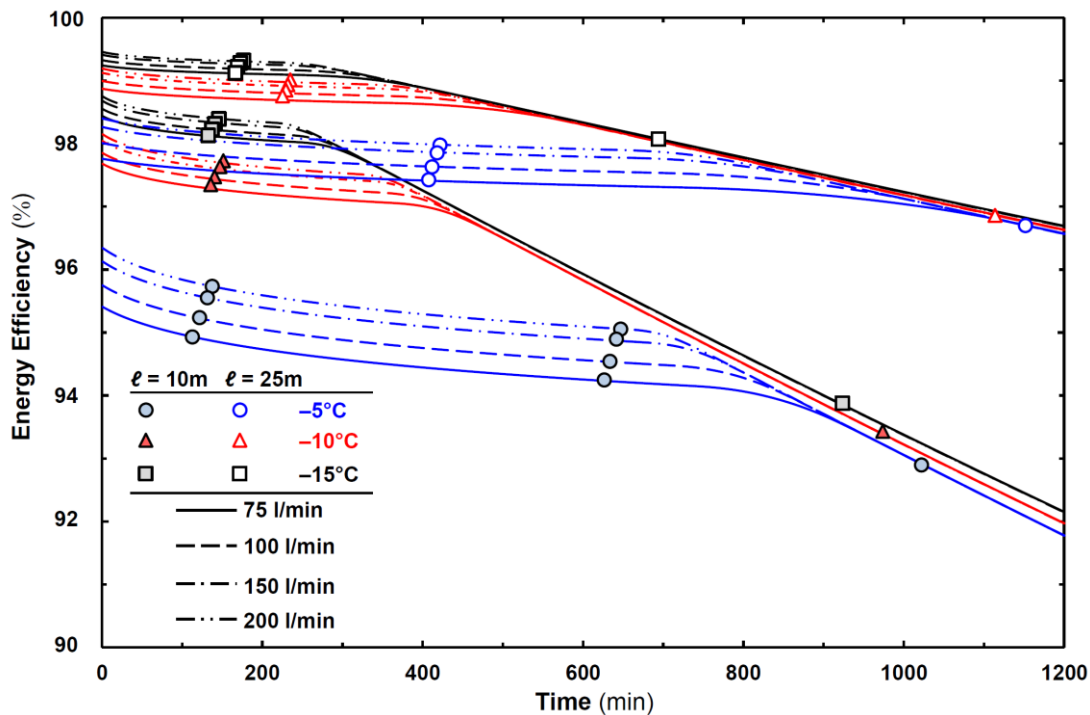
Figure 4.78 Influences of tube length and flow rate of the HTF on (a) Heat transfer rate and (b) Total stored energy – $T_{in} = -5^{\circ}\text{C}$, PE-32.



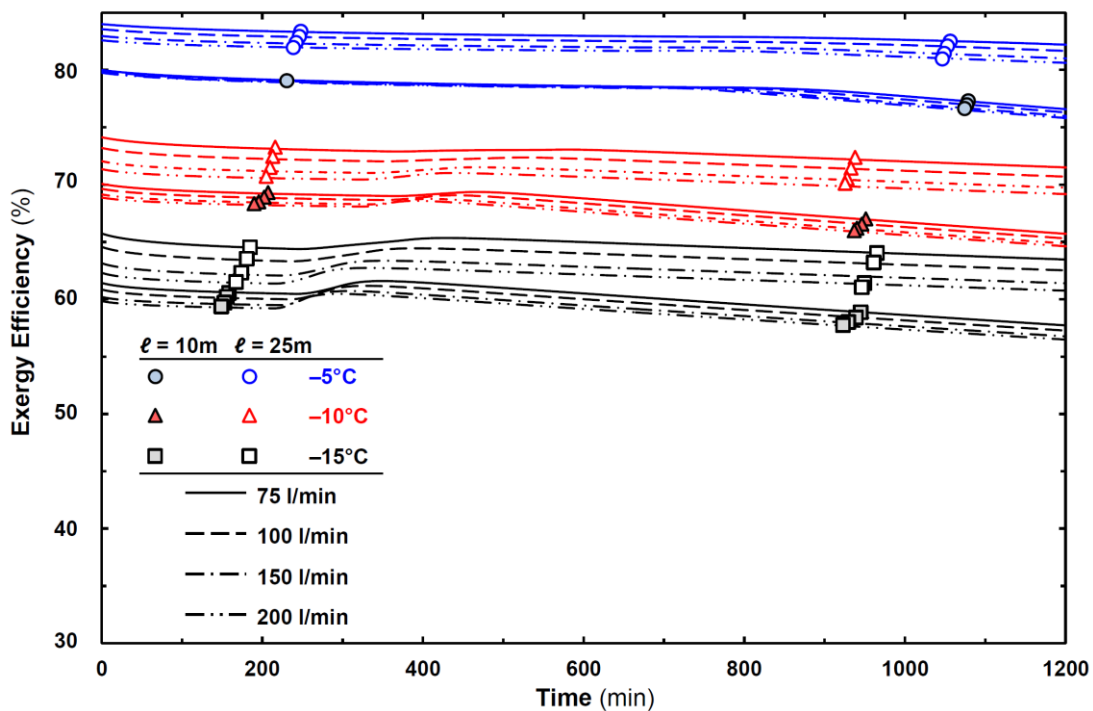
(a) Energetic effectiveness



(b) Exergetic effectiveness



(c) Energy efficiency

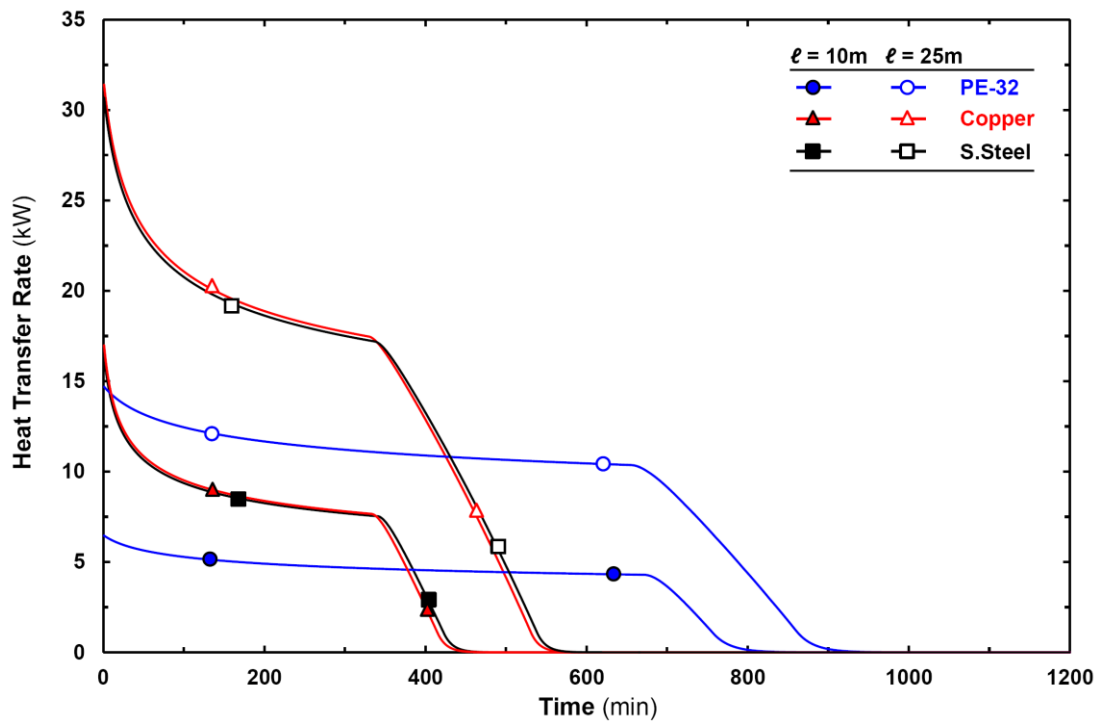


(d) Exergy efficiency

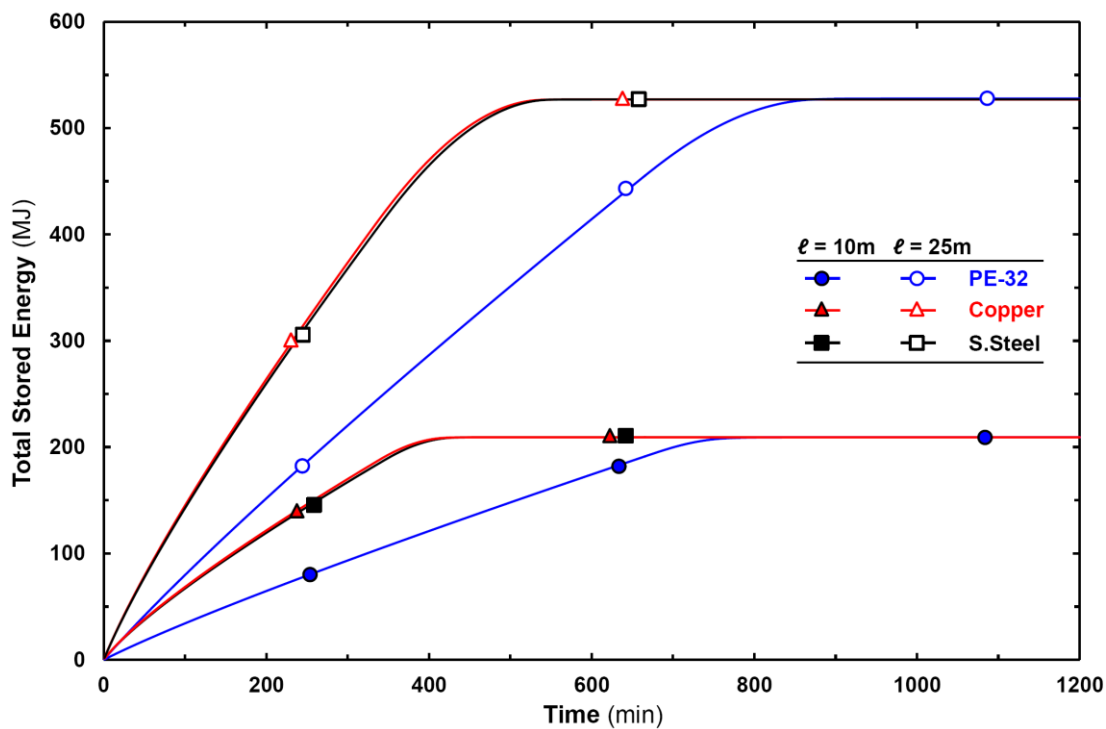
Figure 4.79 Influences of tube length and flow rate of the HTF on (a) Energetic effectiveness, (b) Exergetic effectiveness, (c) Energy efficiency, and (d) Exergy efficiency – PE-32.

transfer and total stored energy increase with increasing the thermal conductivity of the tube material. In contrast, the total process time decreases with increasing the thermal conductivity of the tube material. From Figure 4.80(c) and (d), it can be seen that, energy and exergy efficiencies increases with increasing the thermal conductivity of the tube material. Results indicate that, with increasing the thermal conductivity of the tube material from 0.38 W/mK (PE-32) to 16 W/mK (S.Steel), efficiencies, total stored energy, and rate of heat transfer values increase considerably. On the other hand, with increasing the thermal conductivity of tube material from 16 W/mK (S.Steel) to 400 W/mK (Copper), there is no significant variation. This effect can be explained with considering the heat transfer between the HTF and the PCM as a thermal resistance network. With increasing the thermal conductivity of the tube material, the thermal resistance of the tube material decreases and in contrast, the heat transfer increases. However, when the thermal conductivity reaches relatively higher values, in comparison with the thermal resistivity of the HTF, the thermal resistivity of the tube material becomes insignificant on the overall heat transfer coefficient. For the current materials, even though the difference of the thermal conductivities between S.Steel and Copper is 25 nearly times, the variation between the heat transfer rate and the total stored energy is only 1%. As a conclusion, for specifying the tube material, considering only the thermal conductivity of the tube material may not be sufficient. The influence of the thermal resistance for conduction on the overall heat transfer coefficient should be considered.

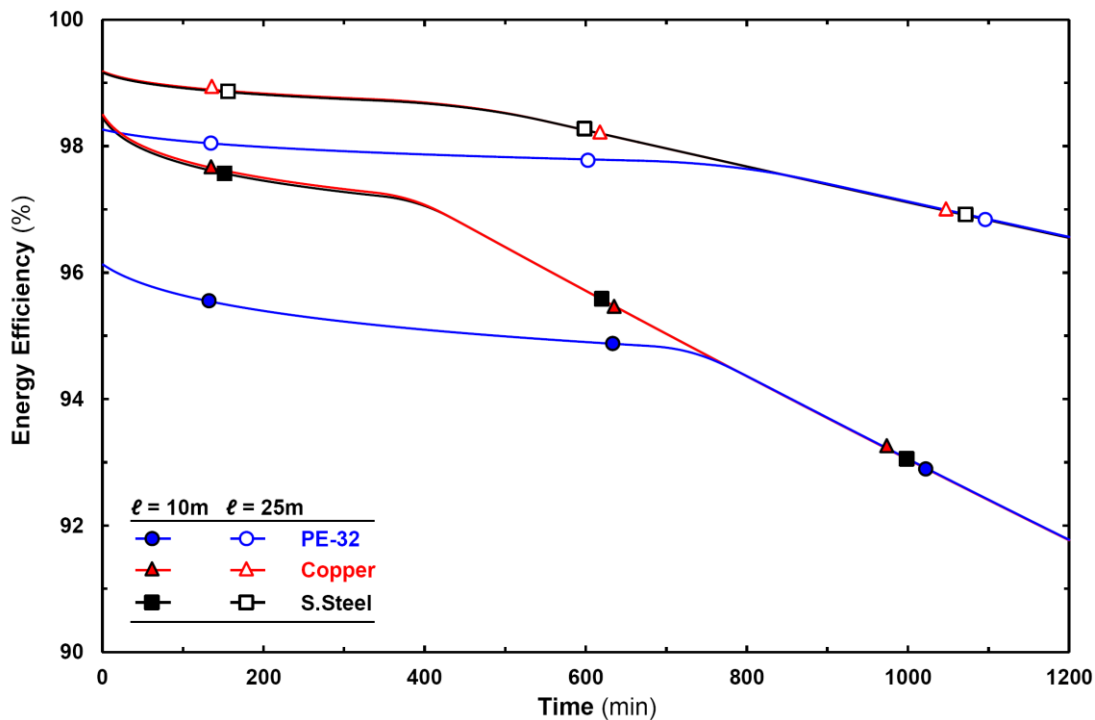
As an overview, in Table 4.14, some selected results are given to compare the influences of the flow and design parameters on energy/exergy efficiencies and total time for completion the heat transfer processes.



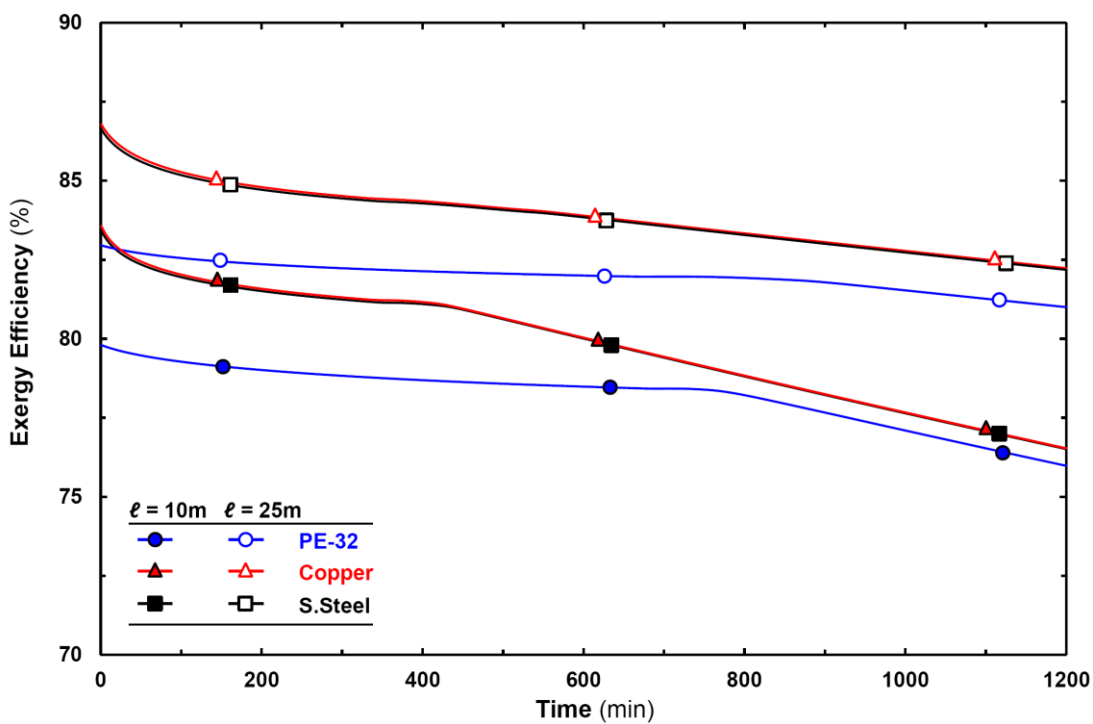
(a) Heat transfer rate



(b) Total stored energy



(c) Energy efficiency



(d) Exergy efficiency

Figure 4.80 Influences of tube material on (a) Heat transfer rate, (b) Total stored energy, (c) Energy efficiency, and (d) Exergy efficiency – $T_{in} = -5^{\circ}\text{C}$, $\dot{V} = 150\text{ l/min}$

Table 4.14 Parametric results of numerical analyses for ice-on-coil type LHTES system.

Length of tube	Inlet temperature of HTF	Flow rate of HTF	Exergy efficiency	Energy efficiency	Total time for completion of process
(m)	(°C)	(l/min)	(%)	(%)	(min)
10	-5	75	76.6	91.8	1110
		100	76.3	91.8	992
		150	76.0	91.8	949
		200	75.8	91.8	902
	-10	75	65.7	92.0	654
		100	65.3	92.0	596
		150	64.9	92.0	568
		200	64.6	92.0	542
	-15	75	57.7	92.1	511
		100	57.3	92.1	481
		150	56.8	92.1	446
		200	56.5	92.1	428
25	-5	75	82.2	96.6	-
		100	81.7	96.6	1194
		150	81.0	96.6	1053
		200	80.6	96.6	977
	-10	75	71.5	96.6	775
		100	70.7	96.6	703
		150	69.7	96.6	627
		200	69.2	96.6	587
	-15	75	63.5	96.7	595
		100	62.5	96.7	545
		150	61.4	96.7	490
		200	60.8	96.7	461

CHAPTER FIVE

CONCLUSIONS AND RECOMMENDATIONS

In the current dissertation, solid–liquid phase change process of water is investigated. Two different types of latent heat thermal energy storage systems are designed and fabricated. In–depth experimental and numerical investigations are carried out for these two different types of the latent heat thermal energy storage systems, which are named as *shell–and–tube type LHTES system* and *ice–on–coil type LHTES system*.

Main findings for the shell–and–tube type LHTES system can be listed as follows:

For charging period:

- Parametric results indicate that the flow rate, inlet temperature, shell diameter, and thermal conductivity of the tube material have considerable effects on the charging capability of the system. The influence of the inlet temperature is more significant in comparison to the flow rate.
- With decreasing the inlet temperature and increasing the flow rate of the HTF, the total stored energy rises. On the other hand, it must be emphasized that, for relatively higher inlet temperature of the HTF values, the flow rate variations become more significant.
- Similar to the total stored energy variations, energy efficiency decreases with increasing the inlet temperature of the HTF; in contrast, energy efficiency increases with increasing the flow rate of the HTF. The influence of the inlet temperature on the energy efficiency is more significant,
- Exergy efficiency increases with increasing the inlet temperature and flow rate of the HTF. Similar to the energy efficiency, the inlet temperature of the HTF is deterministic parameter in comparison with the flow rate of the HTF. The effect of the flow rate becomes remarkable for relatively higher inlet temperatures,
- In conjunction with the increase of the thermal conductivity, from the material of PE–32 to copper, the total stored energy becomes nearly double, especially at the beginning of the experiments. Similar to the variations of the total stored energy,

energy efficiency also increases with increasing the thermal conductivity of the tube material. Besides, with increasing the thermal conductivity, exergy efficiency also increases,

- With increasing the shell diameter from 114 mm to 190 mm, total stored energy increases. Besides, the shell diameter is inversely proportional to the energy efficiency. Exergy efficiency of the system increases with increasing the shell diameter.

For discharging period:

- For the selected parameters, the inlet temperature of the HTF is more significant than the flow rate. The flow rate of the HTF has nearly no meaningful effect on the melting period,
- Energy efficiency increases with increase of the temperature and flow rate of the HTF. Similar to the charging experiments, inlet temperature of the HTF is more significant parameter rather than the flow rate. Energy efficiency increases with increasing the temperature and flow rate of the HTF. Irreversibility increases as the temperature difference between the phase change temperature of the PCM and the inlet temperature of the HTF increases. Hence, exergy efficiency decreases with increasing the inlet temperature.

Main findings for the ice-on-coil type LHTES system can be listed as follows:

For charging period:

- Conservation of energy is verified with comparing the energy variations for the storage tank, compressor, and evaporator. Results indicate that mean difference between the total stored energy and the energy computed from the flow side is less than 5%. Besides, the variations of the compressor and evaporator capacities have good agreement with the measurements and the energy variation in the HTF, respectively,
- More stable inlet temperature of the HTF is observed for the control with the outlet temperature of the HTF from the evaporator,
- The total stored energy rises with decreasing the inlet temperature and increasing the flow rate of the HTF. On the other hand, it must be emphasized that, for

relatively lower inlet temperatures of the HTF, the flow rate of the HTF seems to be more effective than the high inlet temperature.

For discharging period:

- For internal melting experiments, temperature difference rises with a decreasing tendency with increasing the inlet temperature of the HTF. Furthermore, for relatively higher inlet temperatures of the HTF, the influence of the flow rate becomes effective. The temperature difference of the HTF increases with decreasing the flow rate or increasing the inlet temperature of the HTF. In the light of the temperature difference, it seems that the flow rate of the HTF is more effective than the inlet temperature,
- For the current parameters, results designate that; temperature drop inside the system varies between 1.3°C and 2.5°C, depending on the parameters. System can supply this temperature drop for more than 400 minutes. The total rejected energy rises with increasing the inlet temperature with a decreasing tendency. With increasing the inlet temperature of the HTF from +8°C to +10°C, melted volume increases with a higher rate, in comparison with change from +10°C to +12°C. Because, for +10°C and +12°C experiments, surface temperature of the tube reaches to 5°C and 6°C, so density inversion and more complex natural convection interactions may occur for these cases. Furthermore, the flow rate of the HTF has nearly same effect as the inlet temperature of the HTF. Total rejected energy increases with increasing the inlet temperature or decreasing the flow rate of the HTF,
- Internal melting process is investigated for the constant heat load condition. The inlet temperature of the HTF rises with increasing the heat load and decreasing the flow rate. Parallel to this change, the temperature difference of the HTF rises with increasing the heat load and decreasing the flow rate. System supplies constant outlet temperature for nearly 350 min and 450 min under 9 kW and 7 kW heating loads, respectively. For 9 kW heating load condition, the outlet temperature of water is measured as 10°C. On the other hand, for 7 kW heating load condition, the outlet temperature of water is achieved as 7.5°C. Results indicate that, more

than 250 MJ cold energy can be reject in 10 hours, with using internal melting mode of the current LHTES system,

- In external melting mode, the outlet temperature of water remains under 7.5°C for 7 kW heating load condition for nearly 500 minutes. On the other hand, for 9 kW heating load condition, the outlet temperature of water measured as less than 10°C nearly 400 min. These results emphasize that, for the current experimental conditions, the external melting mode can supply relatively lower outlet temperatures for longer period, in comparison with the internal melting mode.

Main findings for the numerical results can be listed as follows:

- Temperature transformation method is applied into FLUENT CFD code to simulate the natural convection dominated phase change. Special UDF and UDS sub-routines are coded into FLUENT software. The current numerical methodology and models are validated with comparing available analytical, experimental, or numerical results.

For rectangular cavity:

- Although using extended surfaces improve the amount of ice, it increases the influence of natural convection inside cavity and causes larger discrete convection cells because of the density inversion temperature of water. The comparative results between the natural convection dominated and conduction-dominated cases show that, the influence of the natural convection is deterministic for the solidification processes of water in the systems that the initial temperature of water higher than its density maximum.

For around tube:

- The present model is validated by comparing the predictions with the current experimental data. In terms of the absolute values of the ice radii, the maximum deviations are obtained as about 2.4 mm and 1.2 mm for the top and the bottom directions, respectively,
- Numerical analyses are conducted for three different initial temperatures of water as $T_{in} = 0.5^\circ\text{C}$, 4°C and 8°C . For $T_{in} = 0.5^\circ\text{C}$ and 4°C the clockwise circulation cell

is observed at the upper side of the tube, and thermal stratification occurs at the bottom side. For $T_{in} > 4^{\circ}\text{C}$, at the beginning of the analysis, the counter-clock wise circulation cell is also observed at the bottom side of the tube. As time progresses, two separated circulation cells are formed. Due to the density inversion of water, the circulation cell shifts to the upper side of the tube,

- The local entropy generation increases with increasing the initial temperature of water. In comparison with the viscous effects, the entropy generation caused by the heat transfer is found the dominant for the parameters studied. For $T_{in} = 8^{\circ}\text{C}$, the entropy generation associated with the viscous term becomes six times larger than the ones for $T_{in} = 0.5^{\circ}\text{C}$ and $T_{in} = 4^{\circ}\text{C}$.

For Ice-on-coil LHTES System:

- Time wise variations of the total stored energy, mass of ice and outlet temperature of the HTF are compared and reasonable agreements are achieved. The maximum deviations are observed as 5% and 2% in terms of the total mass of ice for two different experiments.
- Thermal and flow parameters of the HTF are key factors for determining the performance of an ice-on-coil LHTES system. With decreasing the inlet temperature and increasing the flow rate of the HTF, the heat transfer rate, energy efficiency, also energetic and exergetic effectiveness values increase.
- Even though the effectiveness and total stored energy values of the system increases with decreasing the inlet temperature of the HTF from $T_{in} = -5^{\circ}\text{C}$ to $T_{in} = -15^{\circ}\text{C}$, the exergy efficiency decreases significantly with decreasing the inlet temperature. The irreversibility rate increases with increasing the temperature difference between the melting temperature of the PCM and the inlet temperature of the HTF,
- Comparative results showed that for specifying the tube material considering only the thermal conductivity of the tube material may not be sufficient. The influence of the thermal resistance for conduction on the overall heat transfer coefficient should be considered.

REFERENCES

- Abhat, A. (1983). Low temperature latent heat thermal energy storage: Heat storage materials. *Solar Energy*, *30*, 313–332.
- Agyenim, F., Eames, P., & Smyth, M. (2009). A comparison of heat transfer enhancement in a medium temperature thermal energy storage heat exchanger using fins. *Solar Energy*, *83*, 1509–1520.
- Agyenim, F., Eames, P., & Smyth, M. (2010). Heat transfer enhancement in medium temperature thermal energy storage system using a multitube heat transfer array. *Renewable Energy*, *35*, 198–207.
- Agyenim, F., Eames, P., & Smyth, M. (2011). Experimental study on the melting and solidification behaviour of a medium temperature phase change storage material (Erythritol) system augmented with fins to power a LiBr/H₂O absorption cooling system. *Renewable Energy*, *36*, 108–117.
- Agyenim, F., & Hewitt, N. (2010). The development of a finned phase change material (PCM) storage system to take advantage of off-peak electricity tariff for improvement in cost of heat pump operation. *Energy and Buildings*, *42*, 1552–1560.
- Agyenim, F., Hewitt, N., Eames P., & Smyth M. (2010). A review of materials, heat transfer and phase change problem formulation of latent heat thermal energy storage system (LHTESS). *Renewable and Sustainable Energy Reviews*, *14*, 615–628.
- Akgün, M., Aydın, O., & Kaygusuz, K. (2008). Thermal energy storage performance of paraffin in a novel tube-in-shell system. *Applied Thermal Engineering*, *28*, 405–413.

- ASHRAE, (1997). *Physical Properties of Secondary Coolants (Brines)*, ASHRAE Handbook Fundamentals. Chapter 20.
- ASHRAE, (1999). *Thermal Storage*, ASHRAE Handbook HVAC Applications. Chapter 33.
- Assis, E., Katsman, L., Ziskind, G., & Letan, R. (2007). Numerical and experimental study of melting in a spherical shell. *International Journal of Heat and Mass Transfer*, 50, 1790–1804.
- Assis, E., Katsman, L., Ziskind, G., & Letan, R. (2009). Numerical and experimental study of solidification in a spherical shell. *ASME Journal of Heat Transfer*, 131, 024502–2 – 024502–5.
- Baltimore, (n.d.). *Cooling Towers, Closed Circuit Cooling Towers, Evaporative Condensers, Aircoil Evaporators, Ice Thermal Storage Systems*, Retrieved 20/05/2011, from <http://www.baltimoreaircoil.com>.
- Banaszek, J., Domanski, R., Rebow, M., & El-Sagier, F. (1999). Experimental study of solid–liquid phase change in a spiral thermal energy storage unit. *Applied Thermal Engineering*, 19, 1253–1277.
- Banaszek, J., Jaluri, Y., Kowalewski, T. A., & Rebow, M. (1999). Semi–implicit FEM analysis of natural convection in freezing water. *Numerical Heat Transfer, Part A*, 36, 449–472.
- Bathelt, A. G., & Viskanta, R. (1980). Heat transfer at the solid–liquid interface during melting from a horizontal cylinder. *International Journal of Heat Mass Transfer*, 23, 1493–1503.
- Bejan, A. (1995). *Entropy Generation Minimization*. New York: CRC Press.

- Betzel, T., & Beer, H. (1986). Experimental investigation of heat transfer during melting around a horizontal tube with and without axial fins. *International Communications in Heat and Mass Transfer*, 13, 639–649.
- Braga, S. L., & Viskanta, R. (1992a). Transient natural-convection of water near its density extremum in a rectangular cavity. *International Journal of Heat and Mass Transfer*, 35, 861–875.
- Braga, S. L., & Viskanta, R. (1992b). Effect of density extremum on the solidification of water on a vertical wall of a rectangular cavity. *Experimental Thermal and Fluid Science*, 5, 703–713.
- Brewster, R. A., & Gebhart, B. (1988). An experimental study of natural convection effects on downward freezing of pure water. *International Journal of Heat Mass Transfer*, 31, 331–348.
- Calmac, (n.d.). *Thermal Energy Storage, Off-Peak Co.*, Retrieved 20/05/2011, from <http://www.calmac.com>.
- Cao, Y., & Faghri, A. (1990). A numerical-analysis of phase-change problems including natural convection. *ASME Journal of Heat Transfer*, 112, 812–816.
- Cao, Y., & Faghri, A. (1991). Performance characteristics of a thermal energy storage module: a transient PCM/forced convection conjugate analysis. *International Journal of Heat Mass Transfer*, 34, 93–101.
- Cao, W. Z., & Poulidakos, D. (1991). Experiments on the transient freezing of water in an inclined rectangular cavity. *International Journal of Heat and Fluid Flow*, 12, 116–121.
- Castell, A., Solé, C., Medrano, M., Roca, J., Cabeza, L. F., & Garcia, D. (2008). Natural convection heat transfer coefficients in phase change material (PCM)

- modules with external vertical fins. *Applied Thermal Engineering*, 28, 1676–1686.
- Chen, C. T., & Millero, F. J. (1976). The specific volume of sea water at high pressures. *Deep–Sea Research*, 23, 595–612.
- Costa, M., Oliva, A., & Pérez–Segarra, C. D. (1997). Three–dimensional numerical study of melting inside an isothermal horizontal cylinder. *Numerical Heat Transfer, Part A: Applications*, 32, 531–553.
- Daily, W., & Ramirez, A. (2004). Electrical resistance tomography. *The Leading Edge*, 23, 438–442.
- De Jong, E., Ballantyne, A. K., Cameron, D. R., & Read, D. W. L. (1979). Measurement of Apparent Electrical Conductivity of Soils by an Electromagnetic Induction Probe to Aid Salinity Surveys. *Soil Sci. Soc. Am. J.*, 43, 810–812.
- Dincer, I., & Rosen, M. A. (2002). *Thermal Energy Storage: Systems and Applications*. London: John Wiley & Sons.
- Drees, K. H., & Braun, J. E. (1995). Modeling of area–constrained ice storage tanks. *HVAC&R Research*, 1, 143–158.
- El–Dessouky, H., & Al–Juwayhel, F. (1997). Effectiveness of a thermal energy storage system using phase change materials. *Energy Conversion and Management*, 38, 601–617.
- Erek, A. (1999). Phase change around finned horizontal cylinder: A conjugate problem. Ph.D. thesis. Graduate School of Natural and Applied Sciences of Dokuz Eylul University, Izmir, Turkey.

- Erek, A., & Dincer, I. (2008). An approach to entropy analysis of a latent heat storage module. *International Journal of Thermal Sciences*, 47, 1077–1085.
- Erek, A., & Dincer, I. (2009). A new approach to energy and exergy analyses of latent heat storage unit. *Heat Transfer Engineering*, 30, 506–515.
- Erek, A., & Ezan, M. A. (2007). Experimental and numerical study on charging processes of an ice-on-coil thermal energy storage system. *International Journal of Energy Research*, 31, 158–176.
- Erek, A., İlken, Z., & Acar, M. A. (2005). Experimental and numerical investigation of thermal energy storage with a finned tube. *International Journal of Energy Research*, 29, 283–301.
- Ermis, K., Erek, A., & Dincer, I. (2007). Heat transfer analysis of phase change process in a finned-tube thermal energy storage system using artificial neural network. *International Journal of Heat and Mass Transfer*, 50, 3163–3175.
- Ettouney, H., El-Dessouky, H., & Al-Ali, A. (2005). Heat transfer during phase change of paraffin wax stored in spherical shells. *Journal of Solar Energy Engineering*, 127, 357–365.
- Evapco, (n.d.). *Thermal Ice Storage | Evapco.com*, Retrieved 20/05/2011, from <http://www.evapco.com>.
- Farid, M. M., Khudhair, A. M., Razack, S. A. K., & Al-Hallaj, S. (2004). A review on phase change energy storage: materials and applications. *Energy Conversion and Management*, 4, 1597–1615.
- ANSYS Inc. (2009). *ANSYS Fluent user's guide, Version 12*. ANSYS Inc.
- Fukusako, S., & Yamada, M. (1999). Melting heat transfer inside ducts and over external bodies. *Experimental Thermal and Fluid Science*, 19, 93–117.

- Fukusako, S., Yamada, M., & Kim, M. H. (1998). Numerical and experimental study on melting heat transfer of liquid ice in a rectangular cavity. *International Journal of Fluid Mechanics Research*, 25, 568–577.
- Gebhart, B., & Mollendorf, J. C. (1977). A new density relation of pure and saline water. *Deep-Sea Research*, 24, 831–848.
- Gong, Z. X., & Mujumdar, A. S. (1998). Flow and heat transfer in convection-dominated melting in a rectangular cavity heated from below. *International Journal of Heat and Mass Transfer*, 41, 2573–2580.
- Habeebullah, B. A. (2007). An experimental study on ice formation around horizontal long tubes. *International Journal of Refrigeration*, 30, 789–797.
- Hamada, Y., Ohtsu, W., & Fukai, J. (2003). Thermal response in thermal energy storage material around heat transfer tubes: effect of additives on heat transfer rates. *Solar Energy*, 75, 317–328.
- Hasan, A. (1994). Phase change material energy storage system employing palmitic acid. *Solar Energy*, 52, 143–154.
- Hasnain S. M. (1998a). Review on sustainable thermal energy storage technologies, Part I: Heat storage materials and techniques. *Energy Conversion and Management*, 39, 1127–1138.
- Hasnain, S. M. (1998b). Review on sustainable thermal energy storage technologies, Part II: Cool thermal storage. *Energy Conversion and Management*, 39, 1139–1153.
- He, A., Qian, H., Hu, Z., & Zhou, Z. (2001). Study of heat transfer in ice-storage tank. *Journal of Thermal Sciences*, 10, 357–362.

- Hepbasli, A., & Akdemir, O. (2004). Energy and exergy analysis of a ground source (geothermal) heat pump system. *Energy Conversion and Management*, 45, 737–753.
- Ho, C. J., & Viskanta, R. (1984). Heat transfer during inward melting in a horizontal tube. *International Journal of Heat Mass Transfer*, 27, 705–716.
- Ho, C. J., & Chen, S. (1986). Numerical simulation of melting of ice around a horizontal cylinder. *International Journal of Heat Mass Transfer*, 29, 1359–1369.
- Ho, C. J., & Tu F. J. (2001). Visualization and prediction of natural convection of water near its density maximum in a tall rectangular enclosure at high Rayleigh numbers. *ASME Journal of Heat Transfer*, 123, 84–95.
- Holman, J. P. (2011). *Experimental methods for engineers*. New York: McGraw–Hill.
- Hori, T., Kako, M., & Hayashi, H. (2006). Relationship between static electrical conductivity and unfrozen water content in food products. *Journal of Food Science*, 47, 1254–1256.
- Hossain, Md. A., & Rees, D. A. S. (2005) Natural convection flow of water near its density maximum in a rectangular enclosure having isothermal walls with heat generation. *Heat and Mass Transfer*, 41, 367–374.
- Incropera, F. P., & DeWitt, P. D. (2002). *Fundamentals of Heat and Mass Transfer*. John Wiley and Sons.
- Ismail, K. A. R., Alves, C. L. F., & Modesto, M. S. (2001). Numerical and experimental study on the solidification of PCM around a vertical axially finned isothermal cylinder. *Applied Thermal Engineering*, 21, 53–77.

- Ismail, K. A. R., & Gonçalves, M. M. (1999). Thermal performance of a PCM storage unit. *Energy Conversion & Management*, *40*, 115–138.
- Ismail, K. A. R., Henriquez, J. R., Moura, L. F. M., & Ganzarolli, M. M. (2000). Ice formation around isothermal radial finned tubes. *Energy Conversion & Management*, *41*, 585–605.
- Ismail, K. A. R., & da Silva, M. G. E. (2003). Melting of PCM around a horizontal cylinder with constant surface temperature. *International Journal of Thermal Sciences*, *42*, 1145–1152.
- Jay, H., & Lehr, J. K. (2005). *Water Encyclopedia*. John Wiley & Sons.
- Jegadheeswaran, S., Pohekar, S. D., & Kousksou, T. (2010). Exergy based performance evaluation of latent heat thermal storage system: A review. *Renewable and Sustainable Energy Reviews*, *14*, 2580–2595.
- Jekel, T. B., Mitchell, J. W., & Klein, S. A. (1993). Modeling of ice-storage tanks. *ASHRAE Transactions*, *99*, 1016–1024.
- Jian-you, L. (2008). Numerical and experimental investigation for heat transfer in triplex concentric tube with phase change material for thermal energy storage. *Solar Energy*, *82*, 977–985.
- Kell, G. S. (1967). Precise representation of volume properties of water at one atmosphere. *Journal of Chemical and Engineering Data*, *12*, 66–69.
- Kestin, J. (1980). Availability: the concept and associated terminology. *Energy*, *5*, 679–692.
- Khillarkar, D. B., Gong, Z. X., & Mujumdar, A.S. (2000). Melting of a phase change material in concentric horizontal annuli of arbitrary cross-section. *Applied Thermal Engineering*, *20*, 893–912.

- Khodadadi, J. M., & Zhang, Y. (2001). Effects of buoyancy-driven convection on melting within spherical containers. *International Journal of Heat Mass Transfer*, *44*, 1605–1618.
- Knight, P. C., & Cox, G. A. (2006). The Electrical Conductivity and Crystal Phase Change in d-Camphor. *Physica Status Solidi (b)*, *37*, K39–K41.
- Kowalczyk, W., Hartmann, Chr., & Delgado, A. (2004). Modelling and numerical simulation of convection driven high pressure induced phase changes, *International Journal of Heat Mass Transfer*, *47*, 1079–1089.
- Kowalewski, T. A., & Rebow, M. (1999). Freezing of Water in a Differentially Heated Cubic Cavity. *International Journal of Computational Fluid Dynamics*, *11*, 193–210.
- Kwak, H. S., Kuwuhara, K., & Hyun, J. (1998). Convective cool-down of a contained fluid through its maximum density temperature. *International Journal of Heat and Mass Transfer*, *41*, 323–333.
- Lacroix, M. (1993). Numerical simulation of a shell-and-tube latent heat thermal energy storage unit. *Solar Energy*, *50*, 357–367.
- Lamberg, P., & Sirén, K. (2003). Approximate analytical model for solidification in a finite PCM storage with internal fins. *Applied Mathematical Modelling*, *27*, 491–513.
- Lee, A. H. W., & Jones, J. W. (1996). Modeling of an ice-on-coil thermal energy storage system. *Energy Conversion and Management*, *37*, 1493–1507.
- Li, Q., Li, T., & Wu, J. (2001). Electrical Conductivity of Water/Sodium Bis(2-ethylhexyl) Sulfosuccinate/n-Heptane and Water/Sodium Bis(2-ethylhexyl) Phosphate/n-Heptane Systems: The Influences of Water Content, Bis(2-

- ethylhexyl) Phosphoric Acid, and Temperature. *Journal of Colloid and Interface Science*, 239, 522–527.
- Light, T. S., Licht, S., Bevilacqua, A. C., & Morash, K. R. (2005). The fundamental conductivity and resistivity of water. *Electrochem. Solid–State Lett.* 8, E16–E19.
- Lin, D. S., & Nansteel, M. W. (1987). Natural–convection heat transfer in a square enclosure containing water near its density maximum. *International Journal of Heat and Mass Transfer*, 30, 2319–2329.
- Makhanlall, D., & Liu, L. H. (2010). Second law analysis of coupled conduction–radiation heat transfer with phase change. *International Journal of Thermal Sciences*, 49, 1829–1836.
- Mark B. (1999). A technique for in situ measurement of the conductivity of water in triple point of water cells. *Measurement Science and Technology*, 10, L33–L36.
- McDonough, M. W., & Faghri, A. (1994). Experimental and numerical–analyses of the natural–convection of water through its density maximum in a rectangular enclosure. *International Journal of Heat and Mass Transfer*, 37, 783–801.
- McPhee, D., & Dincer, I. (2009). Thermodynamic analysis of freezing and melting processes in a bed of spherical PCM capsules. *Journal of Solar Energy Engineering*, 131, 031071–1 – 031071–11.
- Medrona, M., Yilmaz, M. O., Nogués, M., Martorell, I., Rocai, J., & Cabeza, L. F. (2009). Experimental evaluation of commercial heat exchangers for use as PCM thermal storage systems. *Applied Energy*, 86, 2047–2055.
- Morgan, K. (1981). A numerical analysis of freezing and melting with convection. *Computer Methods in Applied Mechanics and Engineering*, 28, 275–284.

- Nagano, K., Ogawa, K., Mochida, T., Hayashi, K., & Ogoshi, H. (2004). Performance of heat charge/discharge of magnesium nitrate hexahydrate and magnesium chloride hexahydrate mixture to a single vertical tube for a latent heat storage system. *Applied Thermal Engineering*, *24*, 209–220.
- Nelson, D. J., Vick, B., & Yu, X. (1996). Validation of the algorithm for an ice-on-pipe brine thermal storage systems. *ASHRAE Transactions*, *102*, 55–62.
- Neto, J. H. M., & Krarti, M. (1997a). Deterministic model for an internal melt ice-on-coil thermal energy storage tank. *ASHRAE Transactions*, *103*, 113–124.
- Neto, J. H. M., & Krarti, M. (1997b). Experimental validation of a numerical model for an internal melt ice-on-coil thermal energy storage tank. *ASHRAE Transactions*, *103*, 125–138.
- Ng, K. W., Gong, Z. X., & Mujumdar, A. S. (1998). Heat transfer in free convection-dominated melting of a phase change material in a horizontal annulus. *International Communications in Heat and Mass Transfer*, *25*, 631–640.
- Nguyen, T. H., Vasseur, P., & Robillard, L. (1982). Natural convection between horizontal concentric cylinders with density inversion of water for low Rayleigh numbers. *International Journal of Heat and Mass Transfer*, *25*, 1559–1568.
- Nishimura, T., Fujiwara, N. H., & Hisashi, M. (1991). Temperature visualizations by use of liquid crystals of unsteady natural convection during supercooling and freezing of water in an enclosure with lateral cooling. *International Journal of Heat and Mass Transfer*, *34*, 2663–2668.
- Nomura, T., Okinaka, N., & Akiyama, T. (2010). Technology of latent heat storage for high temperature application: A review. *ISIJ International*, *50*, 1229–1239.

- Orhan, M. F., Ereke, A., & Dincer, I. (2009). Entropy generation during a phase-change process in a parallel plate channel. *Thermochimica Acta*, 489, 70–74.
- Ozisik, M. N. (1980). *Heat Conduction*. New York: John Wiley & Sons.
- Palleschi, G., & Biagiotti, V. (2008). Study of amperometric sensors for the determination of nitrite and ammonia in drinking water, Ph.D. thesis, Università degli Studi di Roma.
- Patankar, S. V. (1980). *Numerical Heat Transfer and Fluid Flow*. New York: Hemisphere.
- Patankar, S. V., & Spalding, D. B. (1972). A calculation procedure for heat, mass and momentum transfer in three-dimensional parabolic flows. *International Journal of Heat Mass Transfer*, 15, 1787–1806.
- Pinelli, M., & Piva, S. (2003). Solid/Liquid phase change in presence of natural convection: A thermal energy storage case study. *ASME Journal of Energy Resources*, 125, 190–198.
- Proakis, J. G., & Manolakis, D. G. (1996). *Digital signal processing: principles, algorithms, and applications*. Macmillan.
- Rieger, H., Projahn, U., & Beer, H. (1982). Analysis of the heat transport mechanisms during melting around a horizontal circular cylinder. *International Journal of Heat Mass Transfer*, 25, 137–147.
- Saitoh, T., & Hirose, K. (1984). Characteristics of latent heat thermal energy storage around a horizontal cylinder. *Technology Reports of Tohoku University*, 49, 17–27.

- Sari, A., & Kaygusuz, K. (2002). Thermal performance of a eutectic mixture of lauric and stearic acids as PCM encapsulated in the annulus of two concentric pipes. *Solar Energy*, 72, 493–504.
- Sasaguchi, K., Kusano, K., Kitagawa, H., & Kuwabara, K. (1997). Effect of density inversion on cooling of water around a cylinder in a rectangular cavity. *Numerical Heat Transfer, Part A: Applications*, 32, 131–148.
- Sasaguchi, K., Kusano, K., & Viskanta, R. (1997). A numerical analysis of solid–liquid phase change heat transfer around single and two horizontal, vertically spaced cylinders in a rectangular cavity. *International Journal of Heat and Mass Transfer*, 40, 1343–1354.
- Sasaguchi, K., Kuwabara, K., Kusano, K., & Kitagawa, H. (1998). Transient cooling of water around a cylinder in a rectangular cavity – a numerical analysis of the effect of the position of the cylinder. *International Journal of Heat and Mass Transfer*, 41, 3149–3156.
- Scanlon, T. J., & Stickland, M. T. (2004). A numerical analysis of buoyancy–driven melting and freezing. *International Journal of Heat and Mass Transfer*, 47, 429–436.
- Seban, R. A., & McLaughlin, E. F. (1963). Heat transfer in tube coils with laminar and turbulent flow. *International Journal of Heat and Mass Transfer*, 6, 387–395.
- Seeniraj, R. V., Velraj, R., & Narasimhan, N. L. (2002). Thermal analysis of a finned–tube LHTS module for a solar dynamic power system. *Heat and Mass Transfer*, 38, 409–417.
- Seybert, C. D., & Evans, J. W. (2005). PIV measurements of velocity of water in the presence of ice and comparison with calculated values. *International Journal of Heat and Mass Transfer*, 48, 67–73.

- Sharma, S. D., & Sagara, K. (2005). Latent heat storage materials and systems: A review. *International Journal of Green Energy*, 2, 1–56.
- Sharma A., Tyagi, V. V., Chen, C. R., & Buddhi, D. (2009). Review on thermal energy storage with phase change materials and applications. *Renewable and Sustainable Energy Reviews*, 13, 318–345.
- Shi, W., Wang, B., & Li, X. (2005). A measurement method of ice layer thickness based on resistance–capacitance circuit for closed loop external melt ice storage tank. *Applied Thermal Engineering*, 25, 1697–1707.
- Shih, Y. C., & Chou, H. L. (2005). Numerical study of solidification around staggered cylinders in a fixed space. *Numerical Heat Transfer: Part A – Applications*, 48, 239–260.
- Sözen, A., Arcaklioglu, E., & Menlik, M. (2010). Derivation of empirical equations for thermodynamic properties of a ozone safe refrigerant (R404A) using artificial neural network. *Expert Systems with Applications*, 37, 1158–1168.
- Stickland, M. T., Scanlon, T. J., & MacKenzie, J. (2007). An experimental investigation of natural convection with solidification in a differentially heated cavity. *International Journal of Heat Mass Transfer*, 50, 36–44.
- Stillman, D. E., & Grimm, R. E. (2007). Laboratory Measurements of the Electrical Properties of Water Ice–Silicate Mixtures and Implications for Dielectric Spectroscopy and Radar on Mars, *Seventh International Conference on Mars*, 3311–3314, Pasadena, California.
- Strub, F., & Bedecarrats, J. P. (1999). Numerical second law analysis of a refrigeration phase change storage. *International Journal of Applied Thermodynamics*, 2, 133–138.

- Sugawara, M., & Beer, H. (2009). Numerical analysis for freezing/melting around vertically arranged four cylinders. *Heat Mass Transfer, 45*, 1223–1231.
- Sugawara, M., Komatsu, Y., & Beer, H. (2008). Melting and freezing round a horizontal cylinder placed in a square cavity *Heat Mass Transfer, 45*, 83–92.
- Sugawara, M., Komatsu, Y., Makabe, T., & Beer, H. (2010). Three dimensional freezing around a coolant-carrying tube. *Heat Mass Transfer, 46*, 1307–1314.
- Tan, F. L., Hosseinizadeh, S. F., Khodadadi, J. M., & Fan, L. (2009). Experimental and computational study of constrained melting of phase change materials (PCM) inside a spherical capsule. *International Journal of Heat Mass Transfer, 52*, 3464–3472.
- Tankin, R. S., & Farhadieh, R. (1971). Effects of thermal convection currents on formation of ice. *International Journal of Heat and Mass Transfer, 14*, 953–961.
- Tanchev, R. T., Mackenzie, J. A., Scanlon, T. J., & Stickland, M. T. (2005). Finite element moving mesh analysis of phase change problems with natural convection. *International Journal of Heat and Fluid Flow, 26*, 597–612.
- Tong, W., & Koster, J. N. (1994). Density inversion effect on transient natural-convection in a rectangular enclosure. *International Journal of Heat and Mass Transfer, 37*, 927–938.
- Trp, A., Lenic, K., & Frankovic, B. (2006). Analysis of influence of operating conditions and geometric parameters on heat transfer in water-paraffin shell-and-tube latent thermal energy storage unit. *Applied Thermal Engineering, 26*, 1830–1839.
- Tu, J., Yeoh, G. H., & Liu, C. (2008). *Computational fluid dynamics: A practical approach*. Butterworth-Heinemann.

- Vasseur, P., & Robillard, L. (1980). Transient natural convection heat transfer in a mass of water cooled through 4°C. *International Journal of Heat and Mass Transfer*, 23, 1195–1205.
- Velraj, R., Seeniraj, R. V., Hafner, B., Faber, C., & Schwarzer, K. (1999). Heat transfer enhancement in a latent heat storage system. *Solar Energy*, 65, 171–180.
- Versteeg, H. & Malalasekera, W. (2007). *An introduction to computational fluid dynamics: The Finite Volume Method* (2nd ed.). Prentice Hall.
- Vick, B., Nelson, D. J., & Yu, X. (1996). Model of an ice-on-pipe brine thermal storage component. *ASHRAE Transactions*, 102, 45–54.
- Viskanta, R. (1985). Natural Convection in Melting and Solidification. In S. Kakaç, W. Aug & R. Viskanta (Eds.), (845–877). *Natural Convection: Fundamentals and Applications*, Washington: Hemisphere.
- Wang, S. M., Faghri, A., & Bergman, T. L. (2010). A comprehensive numerical model for melting with natural convection. *International Journal of Heat and Mass Transfer*, 53, 1986–2000.
- Wang, B., Zhang, M., Li, X., & Yang, X. (2003). Experimental investigation of discharge performance and temperature distribution of an external melt ice-on-coil ice storage tank. *HVAC&R Research*, 9, 291–308.
- West, J., & Braun, J. E. (1999). Modeling partial charging and discharging of area-constrained ice storage tanks. *HVAC&R Research*, 5, 209–228.
- Xiaoping, S., Spitzer, P., & Sudmeier, U. (2007). Novel method for bulk resistance evaluation in conductivity measurement for high-purity water. *Accreditation and Quality Assurance*, 12, 351–355.

- Yamada, M., Fukusako, S., Kawanami, T., & Watanabe, C. (1997). Melting heat transfer characteristics of a horizontal ice cylinder immersed in quiescent saline water. *International Journal of Heat Mass Transfer*, *40*, 4425–4435.
- Yimer, B., & Adami, M. (1997). Parametric study of phase change thermal energy storage systems for space application. *Energy Conversion and Management*, *38*, 253–262.
- Zalba, B., Marin, J. M., Cabeza, L. F., & Mehling, H. (2003). Review on thermal energy storage with phase change: materials, heat transfer analysis and applications. *Applied Thermal Engineering*, *23*, 251–283.
- Zhu, Y., & Zhang, Y. (2001). Modeling of thermal processes for internal melt ice–on–coil tank including ice–water density difference. *Energy and Building*, *33*, 363–370.

APPENDIX

A. Nomenclature

A	area (m^2)
B	source term coefficient in momentum equations ($\text{kgm}^{-3}\text{s}^{-1}$)
c	specific heat capacity ($\text{Jkg}^{-1}\text{K}^{-1}$)
C	heat capacity ($\text{Jm}^{-3}\text{K}^{-1}$) or thermal capacitance (W)
D	diameter (m) or diffusion flux ($\Gamma/\delta x$)
e	specific energy (Jm^{-3})
E	energy (J)
\dot{E}_x	rate of exergy (W)
f	ice fraction or Darcy–Weisbach friction factor
F	convective mass flux (ρu)
g	gravitational acceleration (ms^{-2})
h	height of tank (m), specific enthalpy (Jkg^{-1}) or heat transfer coefficient ($\text{Wm}^{-2}\text{K}^{-1}$)
h_{sf}	latent heat (Jkg^{-1})
H	height of cavity (m) or enthalpy (Jkg^{-1})
k	thermal conductivity (WmK^{-1})
ℓ	length of tube (m)
L	length of cavity (m)
m	mass (kg)
\dot{m}	mass flow rate (kgs^{-1})
N_s	entropy generation number (–)
$N_{segment}$	number of segments (–)
Nu	Nusselt number (hD_{in}/k)
Q	total heat transfer (J)
Q_{gain}	heat gain from surroundings (J)
\dot{Q}	heat transfer rate (W)
p	pressure (Pa)
Pr	Prandtl number ($c\mu/k$)
r, x	radial and axial coordinates (m)
r	radius (m)
R	thermal resistance (KW^{-1}) or dimensionless radial coordinate (r/D_o)
Ra	Rayleigh number ($g\beta\Delta T D_{ice}^3 Pr/\nu^2$)
Re	Reynolds number ($4\dot{m}/\pi D\mu$)
s	source term in energy equation (Jkg^{-1})
S	total entropy (JK^{-1}) or source term in energy equation (Jm^{-3})
\dot{S}	rate of entropy (WK^{-1})

\dot{S}_{gen}	rate of entropy generation (WK^{-1})
t	time (s)
T	temperature ($^{\circ}\text{C}$ or K)
\bar{T}	mean temperature ($^{\circ}\text{C}$ or K)
\bar{U}	overall heat transfer coefficient ($\text{Wm}^{-2}\text{K}^{-1}$)
u, v	velocity components (ms^{-1})
x, y	coordinates (m)
V	volume (m^3)
\dot{V}	volumetric flow rate (lmin^{-1})
Y	dimensionless vertical coordinate (y/H)
y_0, a, b, c, d	equation constants

Greek Symbols

α	thermal diffusivity
Δ	difference
$2\delta T_m$	phase change temperature range ($^{\circ}\text{C}$ or K)
ε	convergence criteria or effectiveness
η	energy efficiency
ϕ	generic variable
Γ	diffusion coefficient
φ	source term in momentum equations ($\text{kgm}^{-2}\text{s}^{-2}$)
ρ	density (kgm^{-3})
μ	dynamic viscosity ($\text{kgm}^{-1}\text{s}^{-1}$)
θ	dimensionless temperature $(T - T_{cold}) / (T_{in} - T_{cold})$ or polar coordinate
ψ	exergy efficiency

Subscripts

$comp$	compressor
cr	critical
d	destruction
e	electrode
en	energy
$evap$	evaporator
ex	exergy
f	fluid
i	inner diameter of the tube, initial time or number of segment
in	inlet
l	liquid phase
m	melting point or mushy phase
ρ, max	maximum density

<i>o</i>	outer diameter of the tube <i>or</i> dead state
<i>ref</i>	reference <i>or</i> refrigerant
<i>s</i>	solid phase
<i>sen</i>	sensible
<i>t</i>	thermocouple

Superscripts

<i>n</i>	time step
<i>o</i>	previous time step

Abbreviations

<i>ANN</i>	artificial neural network
<i>CFD</i>	computational fluid dynamics
<i>COP</i>	coefficient of performance
<i>EEV</i>	electronic expansion valve
<i>HTF</i>	heat transfer fluid
<i>LHTES</i>	latent heat thermal energy storage
<i>QUICK</i>	quadratic upstream interpolation for convective kinetics
<i>PCM</i>	phase change material
<i>PE-32</i>	polyethylene-32
<i>PID</i>	proportional-integral-derivative
<i>PIV</i>	particle-image-velocimetry
<i>PRESTO</i>	pressure staggering option
<i>PWM</i>	pulse-width-modulated
<i>SHTES</i>	sensible heat thermal energy storage
<i>SIMPLE</i>	semi-implicit method for pressure-linked equations
<i>TES</i>	thermal energy storage
<i>TC</i>	thermocouple
<i>UDF</i>	user defined function
<i>UDS</i>	user defined scalar
<i>VBA</i>	visual basic application